# Investigation of Magneto-Optical and Photonic Properties of Plasmonic Tungsten Oxide and Alkali Tungsten Bronze Nanocrystals

by

Gyorgy J. Jaics

A thesis
presented to the University of Waterloo
in fulfillment of the
thesis requirement for the degree of
Doctor of Philosophy
in
Chemistry

Waterloo, Ontario, Canada, 2026

© Gyorgy J. Jaics 2026

**Examining Committee Membership**

The following served on the Examining Committee for this thesis. The decision of the Examining Committee is by majority vote.

External Examiner: **Dr. Jongwook Kim**,
Title: Assistant Professor,
Dept. of Physics, Ecole Polytecnique, Paris, France

Supervisor(s): **Dr. Pavle V. Radovanovic**,
Title: Professor,
Dept. of Chemistry, University of Waterloo, ON, Canada

Internal Member: **Dr. Rodney D. L. Smith**,
Title: Associate Professor,
Dept. of Chemistry, University of Waterloo, ON, Canada

Internal-External Member: **Dr. Zbigniew Wasilewski**,
Title: Professor,
Dept. of Electrical and Computer Engineering,
Dept. of Physics and Astronomy,
University of Waterloo, ON, Canada

Other Member(s): **Dr. Aicheng Chen**
Title: Professor,
Dept. of Chemistry, University of Guelph, ON, Canada

## Author's Declaration

This thesis consists of material all of which I authored or co-authored: see Statement of Contributions included in the thesis. This is a true copy of the thesis, including any required final revisions, as accepted by my examiners.

I understand that my thesis may be made electronically available to the public.

## Statement of Contribution

The work presented in **Chapter 3** is adapted with permission from the paper published in the Journal of Physical Chemistry C (see below), where I am a co-first author with equal contribution. For copyright permission from American Chemical Society, see **Letters of Copyright Permission section** on page 131.

**Aaron Kenny-Wilby,**† **Gyorgy Jaics**,† Chenwei Zhang, Penghui Yin, and Pavle V. Radovanovic*, Revisiting Plasmonic Properties of Complex Semiconductor Nanocrystals Using Magnetic Circular Dichroism Spectroscopy: A Cautionary Tale, J. Phys. Chem. C, 2023, 127, 1087-1096, Link

In this paper, we re-examine the magneto-optical properties of compositionally and electronically complex semiconductor nanocrystals (e.g., gallium iron oxide or GFO, copper iron chalcogenide or $Cu_xFe_xS_{2-z}Se_z$, oxygen-deficient tungsten oxide $WO_{3-x}$) that have recently been reported to exhibit unique and promising plasmonic properties, using magnetic circular dichroism (MCD) spectroscopy. My contributions to this paper include all the experimental work related to $WO_{3-x}$ nanocrystals: the synthesis and characterization of $WO_{3-x}$ nanocrystals, involving the structural, electronic, magnetic, optical, magneto-optical (*i.e.*, variable-field and variable-temperature MCD) measurements. Furthermore, I performed the corresponding data analysis, data plotting, and wrote all the corresponding sections of the manuscript.

The work presented in **Chapter 4** is adapted with permission from the paper published in Chemistry of Materials (see below), where I am the sole first-author. For copyright permission from American Chemical Society, see **Letters of Copyright Permission section** on page 132.

**Gyorgy Jaics**†, Aaron Kenny-Wilby, Emilly S. Wedde, Riad H. Rakib, Bharat Tandon, Shoronia N. Cross, and Pavle V. Radovanovic*, Aspect-Ratio-Controlled Excitonic Zeeman Effects in Alkali Tungsten Bronze Nanocrystals Revealed by Magnetic Circular Dichroism Spectroscopy, Chem. Mater., 2025, 37, 13, 4768-4777, Link

In this paper, I investigated the aspect-ratio-controlled modulation of magnetic- field-induced exciton polarization in oxygen-deficient plasmonic hexagonal cesium-doped tungsten oxide (hex-Cs:$WO_{3-x}$) nanocrystals, using variable-field and variable-temperature MCD spectroscopy measurements. My contributions to this paper include all the experimental work, including the synthesis, structural, electronic, optical and magneto-optical (variable-field and variable-temperature MCD) measurements with the corresponding data

analysis and plotting, and writing the manuscript. (The other authors in the paper are acknowledged for the experimental assistance during variable-field and variable-temperature MCD measurements.)

The work presented in **Chapter 5** is adapted with permission from the paper published in IOP Nanotechnology (see below), where I am a co-author. For copyright permission from IOP Nanotechnology, see **Letters of Copyright Permission section** on page 133.

Zach D. Merino, Gyorgy Jaics, Andrew W. M. Jordan, Arjun Shetty, Penghui Yin, Man C. Tam, Xinning Wang, Zbig R. Wasilewski, Pavle V. Radovanovic, and Jonathan Baugh*, Enhancement of Photoresponse for InGaAs Infrared Photodetectors Using Plasmonic $WO_{3-x}$ /Cs$yWO_{3-x}$ Nanocrystals, Nanotechnology, 36 (2025) 015201, Link

In this paper, we investigated plasmonic non-stoichiometric $WO_{3-x}$ and Cs:$WO_{3-x}$ nanocrystals as photoactive materials in epitaxially-grown planar InGaAs MSM photodetectors operating in the near-infrared (NIR) spectral region. My contributions to this paper include the synthesis and characterization of nanocrystals, corresponding data analysis, and writing the corresponding sections of the manuscript. Furthermore, at the early phase of the project, I also participated in optoelectronic characterization of devices. (Contribution of other authors: Zach D. Merino performed the experimental work characterizing photodetectors and NC solutions for drop casting, data analysis and plotting, and led the writing of the manuscript. Andrew W. M. Jordan fabricated the photodetectors. Arjun Shetty conducted initial photodetector fabrication and characterization. Penghui Yin conducted initial nanocrystal synthesis and characterization. Man C. Tam grew the InGaAs wafer. Xinning Wang performed optical measurement work. Jonathan Baugh and Pavle V. Radovanovic supervised the project and contributed to writing the manuscript. All authors reviewed the manuscript.)

The work presented in **Chapter 6** is currently in a progressing manuscript where I am the leading shared-first author (see below):

Decoupling Molecular Surface Adsorption and Plasmonic Photocatalysis on $WO_{3-x}$ Nanocrystals – A Spectroscopic Investigation, **Gyorgy Jaics**,†, **Emily S. Wedde**,†, Pavithra Partiban, Wenhuan Lu, and Pavle V. Radovanovic*, *Manuscript in preparation*

In this work, we investigate the plasmonic photocatalytic activity of colloidally-synthesized substoichiometric $WO_{3-x}$ nanocrystals using Rhodamine 6G dye as a model system. The primary goal is to understand how surface chemistry and the concentration of native defect

(oxygen vacancy) influence photocatalytic performance. I demonstrate that the removal of the oleic acid ligand shell from the surface of the colloidal nanocrystals significantly enhances their photocatalytic activity by increasing the accessibility of catalytically active sites. In addition, this work explores the effect of the concentration of the native oxygen vacancy on photocatalytic efficiency, which is systematically varied *via* post-synthesis annealing in air. The work presented in this chapter specifically aims to study the contribution of adsorption process to the overall photocatalytic activity, providing a clearer understanding of how surface properties and morphological changes influence the observed behavior of $WO_{3-x}$ NCs. My contributions to this paper include the synthesis, structural and optical characterization of NCs, photocatalysis and adsorption measurements, and corresponding data analysis and plotting, and writing the manuscript. (Contribution of other authors: Emily S. Wedde performed ESI-MS measurements, Emily S. Wedde and Pavithra Partiban participated in writing sections of the manuscript, Wenhuan Lu is acknowledged for preliminary photocatalysis measurements, Pavle V. Radovanovic supervised the project.)

## Abstract

Emerging quantum phenomena in multifunctional materials are reshaping the conceptual and technological foundations of modern condensed matter physics, driving the rapid adoption of plasmonic materials within quantum, optoelectronic, and photonics industries. Plasmonic semiconductor nanocrystals, characterized by collective charge carrier oscillations that are intrinsically linked to their electronic structure, provide a powerful platform for exploring quantum and photonic functionalities beyond conventional noble metal-based plasmonics. After introducing the fundamental principles of localized surface plasmon resonances (Chapter 1) and experimental methodologies (Chapter 2), in this dissertation, I experimentally examined the electronic structure, magneto-optical properties, and photonic applications of oxygen-deficient, doped plasmonic semiconductor metal oxide nanocrystals (NCs), using magnetic circular dichroism (MCD) spectroscopy.

First, I investigated the electronic structure of compositionally and electronically complex semiconductor NCs, focusing on oxygen-deficient tungsten oxide ($WO_{3-x}$) NCs. The motivation of this study (presented in Chapter 3) was to revisit and elucidate the electronic structure of plasmonic compound semiconductor nanostructures that have recently been reported to exhibit unique and promising plasmonic properties based solely on conventional optical absorption data. Unlike conventional optical absorption spectroscopy, MCD spectroscopy, which utilizes excitation by circularly polarized light in an external magnetic field, enables spectral specificity and sensitive detection of plasmon resonances. Using variable-field and variable-temperature MCD spectroscopy, I demonstrated that the broad optical absorption bands (visible-to-near infrared region) of colloidal plasmonic $WO_{3-x}$ NCs originate from intraionic $W^{5+}$ ligand-field transitions at higher energies (visible region) and free-carrier-related plasmonic absorption at lower energies (near infrared region), which spectrally overlap despite fundamentally different electronic origin. The results of this study demonstrated that caution must be exercised when assigning the absorption spectra of complex semiconductor NCs, particularly those containing transition-metal ions, to LSPR. Consequently, a sizeable portion of the literature on plasmonic semiconductor NCs should be re-examined and their conclusions revisited. With that, MCD spectroscopy is also demonstrated to serve as an effective methodology for reliable assignment and detailed investigation of LSPR in NCs.

Importantly, owing to their electronic band structure, plasmonic semiconductor NCs support the coexistence and interaction of plasmonic oscillation with other quasiparticles, enabling intrinsic (interface-free) interactions such as plasmon-exciton, plasmon-spin,

plasmon-phonon, and plasmon-magnon coupling. Owing to the non-resonant nature of plasmonic and interband (excitonic) absorption in doped plasmonic semiconductor NCs, realization and modulation of intrinsic plasmon-exciton coupling are challenging. In Chapter 4, I investigated the impact of NC geometry on the intrinsic plasmon-exciton interactions, using colloidal Cs-doped non-stoichiometric tungsten oxide (Cs:$WO_{3-x}$) hexagonal nanoprisms. With the aid of variable-field and variable-temperature MCD spectroscopy, I observed that NC aspect ratio as controlled geometric parameter enables the modulation of excitonic Zeeman splitting mechanism in the presence of external magnetic fields. Specifically, while for low-aspect-ratio nanostructures (nanoplatelets) the splitting of excitonic states are dictated by the spin of localized carriers (anomalous Zeeman splitting), the high-aspect-ratio nanostructures (nanorods) exhibit free-carrier-induced splitting (normal Zeeman splitting) of the NC excited states. The results of this study demonstrate that manipulation of the aspect ratio of degenerately doped semiconductor NCs can allow for unique control of their excitonic magneto-optical properties, providing promising opportunities for further fundamental investigations and potential applications of this phenomenon in quantum technologies.

Owing to their highly tunable free carrier densities and thus plasmon energies, plasmonic semiconductor NC enable a plethora of technologically relevant photonic and optoelectronic applications. In this context, we investigated the applicability of plasmonic colloidal $WO_{3-x}$ and Cs:$WO_{3-x}$ NCs for near-infrared sensing in metal-semiconductor-metal (MSM) photodetector devices, as presented in Chapter 5. The NCs, as photoactive components, were drop-cast on the active region of the detector. In the presence of the NCs, significant enhancements of photoresponse (by up to a factor of $\sim$2.5) were observed. The results of this work demonstrated the potential for a cost-effective and scalable method exploiting tailored plasmonic semiconductor NCs to improve the performance of NIR optoelectronic devices, such as enhanced speed and sensitivity of receivers in optical fiber communications or increased range and reliability of light detection for autonomous vehicles.

Owing to their unique electronic band structures, plasmonic semiconductor nanocrystals can harness visible-NIR light to facilitate chemical reactions with high efficiency. Upon resonant photon absorption, their localized plasmon resonances generate strong electromagnetic near-field enhancement and energetic charge carriers, which enhance light absorption, foster charge carrier separation and injection, and promote surface reaction processes. This combination of optical and electronic effects allows for a precise control over photocatalytic activity, making these nanocrystals highly tunable platform for visible- and

NIR-light-driven chemical transformations. In Chapter 6, I investigated the plasmonic photocatalytic activity of post-synthetically surface-modified $WO_{3-x}$ NCs, using Rhodamine 6G (Rh6G) dye as model compound. In this study, we observed an approximately 3.3 times improvement in the plasmonic photocatalytic activity of ligand-free $WO_{3-x}$ compared to the as-synthesized oleic-acid-capped $WO_{3-x}$ NCs, attributed to a higher surface accessibility of Rh6G dye. Through post-synthetic annealing in air at elevated temperatures (350-800°C), we modulated the oxygen-deficiency (and thus the free carrier density and plasmon resonance) of the NCs. As a result of the high temperature treatment, we observed sintering and large specific surface area of NCs, as evidenced by scanning electron micrographs and BET analysis, respectively. However, in nanostructures with large specific surface area, adsorption processes are inevitable and can co-exist with photocatalytic degradation processes, which, in the literature, is often not accurately accounted for. In this study, we used a combination of electronic absorption spectroscopy, surface area analysis, and electrospray ionization mass spectrometry, and examined the coupling between the adsorption and plasmonic catalytic activity. The results of this work show that the contribution from adsorption processes can be modulated *via* post-synthetic annealing while retaining coupling with the photocatalysis.

**Acknowledgements**

It would not have been possible for me to stand where I am today without the eternal support of my **Family**, teachers, and friends–each of whom has accompanied me on this journey from the very beginning. Above all, I thank my **Parents** and **Grandparents** for their boundless love and immense support. Your belief in me has been the foundation of everything I have achieved.

A very special thanks goes to **Dr. James Conway**, **and Adam B.**, and **T.J.**, for your huge support and friendship over the years. I am profoundly grateful to Jesse Elliot for the countless hours of conversation, exploration, and "window math" during our doctoral program. Your presence, curiosity, and openness made those years infinitely richer. You all helped shape me not just as a researcher, but as a person—and for that, I am eternally thankful.

I extend my sincere appreciation to the Graduate Coordinators and Advisors at the University of Waterloo's Department of Chemistry: **Madeline Blauel**, **Catherine "Cathy" van Esch**, **Kim Rawson**, and **Prof. Thorsten Dieckmann**. Thank you for your invaluable administrative support throughout my doctoral studies. I am also grateful to **Agnieszka "Aga" Wolczuk** for the exceptional EMLS 602R academic English course for international graduate students—your dedication to clear and effective communication made a lasting impact on my academic development.

My thanks go as well to **Dr. Jonathan Baugh**, and **Dr. Zachary "Zach" Merino** for the insightful collaboration on the infrared photodetector project. Visiting your lab at the Research Advancement Centre (RAC) was not only intellectually inspiring, but also a place where I found cherished friends—**Zach**, **Camille Lacroix**, and **Boghdan Kromets**–who made life in Waterloo all the more vibrant and joyful.

To **Dr. Germán Sciaini**, thank you for the stimulating conversations on spectroscopy, and to **Dr. Kostyantyn Pichugin**, for your generous technical support during our ultrafast laser alignments. I also extend my gratitude to **Dr. Holger Kleinke's** and **Dr. Rodney Smith's** research groups for allowing me access to essential instrumentation, even during your busiest times. Likewise, I thank **Dr. Faten Salim**, and **Dr. Charles dal Castel** of the Analytical Laboratory Facilities in the Department of Chemical Engineering for their critical training and support.

To all my friends and fellow Ph.D. students at the Quantum-Nano Centre–for the many intellectually stimulating conversations!

**Dr. Howard Siu**, I cannot thank you enough for being an outstanding teaching assistant mentor. Your infectious enthusiasm for education, your ability to bring a team of TAs together, and your genuine care for our academic growth made each lab session something to look forward to. Your encouragement, especially during our MCD sessions, helped many of us push through experimental roadblocks. It has truly been a privilege to work alongside you.

Being a part of the Radovanovic Research Group has been one of the most formative experiences of my academic life. I am grateful to all past and present members with whom I've had the pleasure to collaborate. In particular, I owe heartfelt thanks to **Wilson Kagabo**, **Emily Wedde**, **Prof. Bharat Tandon**, **Shoronia Cross**, **Riad Hussain Rakib**, **Aaron Kenny-Wilby**, **Olexiy Balitskii**, **Pavithra Parthiban**, **Scott Zorn**, **Khue "Louis" Nguyen**. Thank you for the thousands of hours spent brainstorming research, and more importantly, for the moral support and countless moments of shared laughter that made graduate life unforgettable. A special note of thanks to **Dr. Victor Galievsky** for your mentorship in laser setups and spectroscopy—your expertise and practical guidance were instrumental in the lab.

Finally, I wish to express my deepest gratitude to my doctoral advisor, **Prof. Pavle V. Radovanovic**. Thank you for accepting me into your research group in January 2021 during the height of the global COVID-19 pandemic—a decision that changed the course of my life. Your academic support, mentorship, and passion for spectroscopy and nanoscience have greatly influenced me. Whether in group meetings, research discussions, late-night MCD experiments, or casual hallway chats, your insight and encouragement have continually inspired me and helped me grow as a researcher and individual. It has been an honor to be your student and mentee!

*It's been a fantastic journey! And I thank you all once again!*

"*The two most important days in your life are the day you were born and the day you found why.*" (Mark Twain)

## Dedication

I would like to dedicate this thesis to my parents for their eternal support and love.

# Table of Contents

**Examining Committee Membership** ii

**Author's Declaration** iii

**Statement of Contribution** iv

**Abstract** vii

**Acknowledgements** x

**Dedication** xii

**List of Figures** xviii

**List of Tables** xxxi

**List of Abbreviations** xxxiii

**1 Introduction** 1

1.1 Physical Principles of Localized Surface Plasmon Resonances . . . . . 2

1.1.1 Optical Modelling of Plasmonic NCs . . . . . 3

1.1.1.1 Mie Scattering Theory . . . . . 4

1.1.1.2 Gans Theory . . . . . 5

1.1.1.3 Drude-Lorentz Free Electron Model . . . . . 6

1.2 Plasmonic Compound Semiconductor NCs . . . . . 8
1.2.1 Generating LSPR in Plasmonic Semiconductor Metal Oxide NCs . 10
1.2.1.1 Non-Stoichiometry . . . . . 10
1.2.1.2 Interstitial Doping . . . . . 12
1.2.1.3 Aliovalent Doping . . . . . 16
1.2.2 Static Modulation of LSPR in Plasmonic Semiconductor Metal Oxide NCs . . . . . 18
1.2.2.1 Impact of Spatial Distribution of Dopants in NCs . . . . . 18
1.2.2.2 Impact of Nanocrystal Geometry . . . . . 19
1.3 Magneto-Optical Properties of Plasmonic Semiconductor NCs . . . . . 20
1.3.1 Magnetic Circular Dichroism Spectroscopy of LSPR . . . . . 20
1.3.1.1 Intrinsic Plasmon-Exciton Interactions . . . . . 23
1.3.1.2 Magnetic Circular Dichroism and Excitonic Interactions of Localized Charge Carriers . . . . . 26
1.4 Photonic Applications of Plasmonic Semiconductor Metal Oxide NCs . . . 29
1.4.1 Semiconductor-Based Photodetectors . . . . . 29
1.4.1.1 Structure and Operation Principle of Conventional MSM Photodetectors . . . . . 29
1.4.1.2 Plasmon-Enhanced NIR-MIR Photodetectors . . . . . 31
1.4.2 Plasmonic Photocatalysis Using Metal Oxide NCs . . . . . 33
1.5 Motivation and Scope of this Thesis . . . . . 36

**2 Experimental Section** **38**
2.1 Nanocrystal Syntheses . . . . . 38
2.1.1 Materials . . . . . 38
2.1.2 Synthesis of Colloidal $WO_{3-x}$ NCs . . . . . 38
2.1.3 Ligand Stripping of As-synthesized Colloidal $WO_{3-x}$ NCs . . . . . 39
2.1.4 Post-Synthesis Annealing of As-Synthesized $WO_{3-x}$ NCs . . . . . 39
2.1.5 Synthesis of Colloidal Cs:$WO_{3-x}$ NCs . . . . . 40

2.2 Characterization . . . . . 40
2.2.1 X-Ray Diffraction . . . . . 40
2.2.2 Transmission Electron Microscopy . . . . . 41
2.2.3 Scanning Electron Microscopy . . . . . 41
2.2.4 UV-visible-NIR Absorption Spectroscopy . . . . . 41
2.2.5 Photoluminescence Emission Spectroscopy . . . . . 41
2.2.6 X-Ray Photoelectron Spectroscopy . . . . . 41
2.2.7 Raman Spectroscopy . . . . . 42
2.2.8 Fourier-Transform Infrared Spectroscopy . . . . . 42
2.2.9 Specific Surface Area Measurements . . . . . 42
2.2.10 Adsorption and Photocatalytic Measurements . . . . . 43
2.2.10.1 Photocatalysis Using Sacrificial Agents . . . . . 43
2.2.10.2 Recyclability Measurements . . . . . 44
2.2.11 Magnetic Circular Dichroism (MCD) Spectroscopy . . . . . 45

**3 Revisiting Plasmonic Properties of Complex Semiconductor Nanocrystals Using Magnetic Circular Dichroism Spectroscopy: A Cautionary Tale 48**

3.1 Introduction . . . . . 49
3.2 Results and Discussion . . . . . 51
3.2.1 Structural and Optical Characterization . . . . . 51
3.2.2 Magneto-Optical Properties of Colloidal $WO_{3-x}$ NCs . . . . . 56
3.2.3 Revisiting Optical Extinction Spectrum and Free Carrier Density of Colloidal $WO_{3-x}$ NCs . . . . . 58

**4 Aspect-Ratio-Controlled Excitonic Zeeman Effects in Alkali Tungsten Bronze Nanocrystals Revealed by Magnetic Circular Dichroism Spectroscopy 63**

4.1 Introduction . . . . . 64
4.2 Results and Discussion . . . . . 66

4.2.1 Structural and Optical Characterization of Cs:$WO_{3-x}$ NCs . . . . . 66
4.2.2 Magneto-optical properties of Cs:$WO_{3-x}$ NCs . . . . . 74
4.3 Conclusions . . . . . 81

**5 Enhancement of Photoresponse for InGaAs Infrared Photodetectors Using Plasmonic $WO_{3-x}$/Cs:$WO_{3-x}$ Nanocrystals 82**
5.1 Introduction . . . . . 83
5.2 Experimental Section . . . . . 85
5.2.1 Photodetector Device Fabrication . . . . . 85
5.2.2 Photocurrent Measurement Setup . . . . . 86
5.2.3 Photoresponsivity Measurements . . . . . 87
5.3 Results . . . . . 88
5.3.1 Photodetector Characterization . . . . . 92
5.3.2 Photodetector Device Performance . . . . . 95
5.4 Discussion . . . . . 99
5.5 Conclusions . . . . . 100

**6 Decoupling Molecular Surface Adsorption and Plasmonic Photocatalysis on $WO_{3-x}$ Nanocrystals – A Spectroscopic Investigation 101**
6.1 Introduction . . . . . 102
6.2 Results and Discussion . . . . . 104
6.2.1 Structural and Optical Characterization . . . . . 104
6.2.2 Investigation of Photocatalytic Activity of $WO_{3-x}$ NCs . . . . . 106
6.2.3 Investigating the Correlation between Adsorption and Photocatalytic Activity . . . . . 112
6.2.4 Adsorption and Kinetic Studies . . . . . 115
6.2.4.1 Adsorption Equilibrium Studies . . . . . 119
6.2.5 ESI-MS Study . . . . . 122
6.2.6 Conclusion . . . . . 124

**7 Conclusions and Future Work** **125**

7.1 Conclusions . . . . . 125

7.2 Future Work . . . . . 127

**Letters of Copyright Permission** **130**

**References** **134**

**APPENDICES** **158**

**A Chapter 3** **159**

A.1 Stead-State Photoluminescence of $WO_{3-x}$ NCs . . . . . 159

A.2 Variable-Temperature MCD Spectra of $WO_{3-x}$ NCs . . . . . 160

A.3 Low-Temperature CD Extinction Spectra of $WO_{3-x}$ NCs . . . . . 161

A.4 Magnetization Measurements of $WO_{3-x}$ NCs . . . . . 162

**B Chapter 4** **163**

B.1 Optical Extinction Spectra of Cs:$WO_{3-x}$ Nanoplatelets . . . . . 163

**C Chapter 5** **164**

C.1 Spectral Responsivity Normalization and Incident Power . . . . . 164

C.2 Enhancement of Photoresponse for InGaAs Infrared Photodetectors . . . . 165

**D Chapter 6** **167**

D.1 Recycling of Plasmonic $WO_{3-x}$ NC Photocatalysts . . . . . 167

D.2 BET Specific Surface Area Measurements . . . . . 168

D.3 XRD Patterns of Annealed $WO_{3-x}$ NCs . . . . . 169

# List of Figures

1.1 Schematic representation of (a) propagating surface plasmon polaritons along the metal-dielectric interface, and (b) dipolar localized surface plasmon resonance confined to a nanosized plasmonic particle. (a: Reprinted with permission from Aftab et al.,[1] Copyright (2023) Springer Nature. b: Reprinted with perission from Masson[2] Copyright (2020), Royal Society of Chemistry). 3

1.2 Free carrier density and LSPR frequency range for plasmonic materials. (Reprinted with permission from Luther et al.,[3] Copyright (2011) Springer Nature.) . . . . . 7

1.3 LSPR absorption of various n- and p-type semiconductor NCs. (Reprinted with permission from Agrawal et al.,[4] Copyright (2018) American Chemical Society.) . . . . . 9

1.4 (a) Crystallographic unit cell of various Magnéli phases of tungsten oxide. (b) Total and projected density of states (DOS) of $W_{18}O_{49}$, showing the orbital composition of valence and conduction bands. (c–f) Electronic band structures of $W_{18}O_{49}$ nanowires (c) with no oxygen vacancy, (d) with one oxygen vacancy in the $1h$ Wyckoff position, (e) with oxygen vacancy in the $2n$ position, and (f) in the $2m$ position. (Red dashed line corresponds to Fermi level). (Adapted with permission from Migas et al.,[5] Copyright (2010) AIP Publishing.) . . . . . 11

1.5 (a) Schematic representation of the basal plane (top panel) and prismatic plane (bottom panel) of *hex*-Cs:$WO_{3-x}$ NCs with hexagonal (blue), tetragonal (green), and trigonal (yellow) interstitial voids, respectively. Oxygen, cesium, and tungsten atoms are depicted as red, purple, and gray spheres, respectively. (b) AR-dependent LSPR band-splitting in *hex*-Cs:$WO_{3-x}$ nanoplatelets (top panel), iso-prisms (middle panel), and rods (bottom panel). (a: Reprinted with permission from Zydlewsky et al.,[6] Copyright (2022) American Chemical Society. b: Reprinted with permission from Kim et al.,[7] Copyright (2016) American Chemical Society.) . . . . . 14

1.6 (a) Deconvolution of optical extinction spectrum of oxygen-deficient $Cs_{0.30}WO_{3-x}$ NCs exhibiting plasmonic band-splitting in the visible–NIR region with $LSPR_{\perp}$ and $LSPR_{\parallel}$ modes and polaronic (P) contributions. (b) Electron density distribution in the unit cell of $Cs_{0.30}WO_{2.67}$ NCs. (c) Total DOS of stoichiometric $Cs_{0.30}WO_3$ and (d) oxygen-deficient $Cs_{0.30}WO_{2.83}$ NCs. Red dashed line indicates Fermi level. (e) Scheme depicting the hybridization of W–d and O–p orbitals projected onto the $x$–$z$ plane in a [$WO_6$] octahedron. (f) Molecular orbital diagrams of $Cs_{0.30}WO_3$ (left panel) and oxygen-deficient $Cs_{0.30}WO_{2.83}$ (right panel) NCs showing the W–d orbitals accommodating the $V_o$- and $Cs^+$-donated electrons. (a: Adapted with permission from Machida et al.,[8] Copyright (2019) AIP Publishing. c-f: Repreinted with permission from Machida et al.,[9] Copyright (2024) Springer Nature.) 15

1.7 (a) Schematic representation of the CB filling (and Burstein-Moss shift) of degenerately-doped semiconductor NCs. (b) Modulation of free carrier density and thus LSPR energy of Sn:$In_2O_3$ NCs. (c) Impact of various aliovalent dopant ions ($In^{3+}$, $Sn^{4+}$, $Al^{3+}$, and $Ga^{3+}$) on the LSPR energy of CdO NCs. (a: Adapted with permission from,[10] Copyright (2023) Elsevier. b: Reprinted with permission from Agrawal et al.,[11] Copyright (2017) Annual Reviews. c: Reprinted with permission from Diroll et al.,[12] Copyirght (2014) American Chemical Society.) . . . . . 17

1.8 (a) Cartoon depicting the cyclotron free carrier oscillations generated by the sequential absorption of LCP (blue spiral arrows) and RCP light (red spiral arrows) propagating parallel to a nonzero, homogeneous, uniform external magnetic field ($\vec{B} \neq 0$). (b) Schematic representation of the derivative-shape MCD spectral response arising from cyclotron free carriers in $\vec{B} \neq 0$. (Reprinted with permission from Yin et al.,[13] Copyright (2018) Springer Nature.) . . . . . 21

1.9 Normalized variable-field MCD spectra of the LSPR region of n-ZnO (d=3.1 nm), n-ITO (d=5.5 nm), p-$Cu_{2-x}Se$ (d=16.9 nm), Au (d=12.8 nm), and Ag (d=50 nm) NCs. Inset: MCD crossover energies plotted as a function of absorption peak energies. (Reprinted with permission from Hartstein et al.,[14] Copyright (2017) American Chemical Society.) . . . . . 22

1.10 (a) Excitonic absorption spectrum (300 K, 0 T) of plasmonic 10% Sn:$In_2O_3$ NCs (blue trace, top panel) with corresponding variable-field MCD spectra collected between 1–7 T range at 5 K (bottom panel); and MCD spectrum of plasmonic $In_2O_3$ NCs collected at 300 K, 7 T (middle panel). (b) Plot of monochromatic excitonic MCD peak intensities (from (a)) as a function of magnetic field strength. Solid line (blue trace) and dashed curve (red trace) correspond to linear and Brillouin fitting, respectively. (c) Variable-temperature MCD spectra of 10% Sn:$In_2O_3$ NCs, showing the temperature independent nature of plasmon-induced excitonic MCD signals. (d) Schematic depiction of the cyclotron free carrier-induced excitonic Zeeman splitting mechanism, with $M_j = \pm 1$ excited states. (Reprinted with permission from Yin et al.,[13] Copyright (2018) Springer Nature.) . . . . . 24

1.11 (a) Excitonic MCD bands of colloidal n-type plasmonic InN, 5% Sn:$In_2O_3$, 15% Sn:ZnO, and p-type $Cu_{2-x}Se$ NCs. Under the same magnetic field orientation, the excitonic MCD signals are oppositely polarized for p and n-type plasmonic semiconductor NCs depending on the charge of the majority charge carrier (*i.e.*, $q_e = -|e|$, and $q_h = +|e|$). (b) Schematic representation of the cyclotron free carrier-induced excitonic Zeeman splitting in n-type (left) and p-type (right) plasmonic semiconductor NCs. (Reprinted with permission from Yin et al.,[15] Copyright (2022) American Chemical Society.) 26

1.12 (a) Scanning electron micrograph of colloidal IMO NCs (inset: lattice resolved TEM micrograph). (b) Steady-state optical extinction spectra of the LSPR region of IMO NCs with different Mo dopant concentrations. (c) Steady-state excitonic absorption (top panel) and variable–field MCD spectra (bottom panel) of IMO NCs collected at 5 K. (d) Magnetic field dependence of monochromatic excitonic MCD signals (black markers) at 3.93 eV from (a), along with its temperature dependence (blue markers). (e) Excitonic Zeeman splitting caused by a mixture of plasmon–induced splitting ($M_J = \pm 1$) and spin–induced Zeeman splitting ($M_J^{ground} = \{\pm 1/2\}$; $M_J^{excited} = \{\pm 1/2, \pm 3/2\}$). (Reprinted with permission from Yin et al.,[13] Copyright (2018) Springer Nature.) . . . . . 28

1.13 Schematic representation of MSM photodetectors with (a) planar devices geometry with interdigitated metal electrodes depicted as gray stripes on top of semiconductor photoactive layer. (b) Vertical device geometry consisting of a sandwich-like metal-semiconductor-metal heterostructure situated on top of a substrate. (Reprinted with permission from Shi et al.,[16] Copyright (2021) John Wiley and Sons.) . . . . . 31

1.14 (a) Schematic representation of the band diagram and working mechanism of a biased MSM photodetector. $E_V$, $E_C$, $E_F$, and $\phi_B$ are, respectively, the valence band, conduction band, and Fermi energy levels. (b) Cartoon depicting a MSM photodetector coupled with a waveguide, and (c) equivalent electric circuit of the photodetector device. (d) Plasmon-induced photocurrent enhancement mechanism displaying plasmon-induced hot carrier generation *via* coupling of surface plasmons at metal–semiconductor interface (substrate outcoupling). Plasmon energy release at the metal-superstrate (air) interface (superstrate outcoupling) leading to enhanced light extraction or redirecting energy toward the active region, is also depicted. (Reprinted with permission from Panchenko et al.,[17] Copyright (2018) John Wiley and Sons.) . . . . . 32

1.15 Schemes depicting mechanisms of plasmon-induced photocatalytic processes with schematic representation of the catalytic reaction (top panel), the potential energy surface of the molecular adsorbate (middle panel), and the electron energy distribution and transfer (bottom panel). (a) Schematic representation of indirect charge transfer (CT) mechanism, whereby energetic hot carriers are injected into the LUMO levels of molecular adsorbates, forming transient negative ions (TNIs). (b) Plasmon-induced interfacial charge transfer (PIICT). (c) Plasmon-induced resonant energy transfer (PIRET), *i.e.*, the resonant coupling between the plasmon and molecular adsorbate, inducing intramolecular electronic transitions therein. (d) Plasmon decay resulting in heating of the plasmonic NC and its surrounding. (e) Plasmonic NC acting like nanoantenna, thereby enhancing light-matter interactions at the nanoscale. (Reprinted with permission from Carlin et al.,[18] Copyright (2023) AIP Publishing.) . . . . . 34

2.1 Schematic representation of the experimental MCD setup. Broadband light emitted from a Xenon lamp (left cartoon) first enters a monochromator and a linear polarizer (box) to generate a linearly polarized monochromatic light beam. Passing through a photoelastic modulator, the linearly polarized beam is converted into circularly polarized light (CPL) with two helicities, *i.e.*, left and right circularly polarized light (LCP and RCP, respectively). Using focusing lens (blue ellipse, left), the LCP and RCP beams are focused on the entrance slit of the cryogenically-cooled superconducting electromagnet (middle box), whereby the direction of light propagation is parallel to the field vector of the homogeneous uniform magnetic field generated in the magneto-optical cryostat. The cryostat, placed at the center of the superconducting electromagnet, contains the sample space wherein the drop-cast NC thin films are immersed using a precision sample rod. Depending on the CPL absorptivity of the sample, absorption of RCP and LCP may occur to a different degree, which is defined as ellipticity ($\theta$) measured in millidegree units ($\theta$ = $A_{RCP}$—$A_{LCP}$). The transmitted RCP and LCP light beam is then passed through another lens (blue ellipse, right) and finally hits the detector (right). (Reprinted with permission from Yin et al.,[13] Copyright (2018) Springer Nature.) . . . . . 46

2.2 Schematic depiction of the origin of MCD signal intensities (top panels) and Zeeman splitting patterns (middle panels) of Faraday *A*-term (a), *B*-term (b), and *C*-term (c). Temperature (red markers) and magnetic field dependent MCD signals (blue markers) corresponding to plasmons (d) and localized paramagnetic carriers (e). Plasmons and free carriers show fundamentally different magneto-optical behavior as a function of external magnetic field strength and temperature: while plasmons show linear behavior (blue line) as a function magnetic field and temperature independence, localized carriers exhibit saturating magnetic field response (blue curve) fitted using Brillouin function and nonlinear temperature dependence following Curie-Weiss law. (a: Reprinted with permission from Han et al.,[19] Copyright (2020) John Wiley and Sons.) . . . . . 47

3.1 (a) Overview TEM image of $WO_{3-x}$ NCs. Inset: lattice-resolved TEM image of an individual nanorod, indicating its growth along the ⟨010⟩ direction. (b) XRD pattern of $WO_{3-x}$ NCs. Red trace is a simulated XRD pattern for bulk $WO_{2.72}$ (ICSD no. 24731). (c) Length and (b) width distribution histograms for $WO_{3-x}$ nanorods, determined from (a). . . . . 52

3.2 (a) FTIR and (b) photoluminescence emission spectra of the colloidal plasmonic $WO_{3-x}$ NCs. . . . . 53

3.3 (a) High-resolution W 4f XPS, and (b) O 1s XPS spectra of $WO_{3-x}$ NCs. Fitting and assignment of the deconvoluted peaks are shown in the graph. (c) Overview steady-state optical extinction spectrum (collected at 300 K) of the native colloidal $WO_{3-x}$ NCs dispersed in TCE (photograph displayed as inset), and (d) corresponding Tauc plot with estimated optical bandgap (Eg) of 3.75 eV. . . . . 54

3.4 Structural and optical characterization of colloidal native $WO_{3-x}$ NCs exposed to air for various time durations. (a) Band-gap-normalized (285 nm) steady-state optical extinction spectra of NCs exposed to air for 0-15 h (colored traces), demonstrating the decay of LSPR. Inset displays photographs of NC dispersions exposed to air for 0 h (left) and 15 h (right). (b) Time evolution of LSPR decay from (a) monitored at 1350 nm. (c) XRD pattern of NCs exposed to air for 0 h (blue trace) and 15 h (green trace). (Reference: ICSD no. 24731). (d) TEM micrographs of NCs exposed to air for 0 h (left) and 15 h (right). . . . . 55

3.5 (a) 5 K MCD spectra of $WO_{3-x}$ NCs collected at different magnetic field strengths, as indicated in the graph. Inset: magnified MCD spectra in the excitonic absorption range. (b) Magnetic field dependence of the MCD signal intensity from (a) at different wavelengths, as indicated in the graph. Brillouin and linear fits to the spectral intensities at 600 and 800 nm, respectively, are shown in the inset. . . . . 57

3.6 Low-temperature (5 K) steady-state UV–visible–NIR optical extinction spectrum of colloidal $WO_{3-x}$ NCs drop-cast on quartz MCD substrate. Deconvoluted bands are assigned to LSPR (red trace) and ligand-field transitions (LFT, green trace), respectively. . . . . 58

3.7 (a) Broad steady-state optical extinction band of colloidal $WO_{3-x}$ NCs. Black and red arrows indicate spectral positions of intraionic d-d transition (localized carriers) and LSPR (free carriers), respectively. (b) Schematic figure depicting magnetic field dependence for monochromatic MCD intensity of colloidal $WO_{3-x}$ NCs collected between 0–7 T at 5 K. Localized carriers (black trace) and free carriers (red trace) exhibit saturating or linear magneto-optical response, respectively. (c) Schematic figure representing the behavior of cyclotron free carriers (left panel) and localized carriers (right panel) in a nonzero magnetic field generating characteristic MCD spectral features, along with splitting mechanism and the corresponding Faraday MCD terms. . . . . 62

4.1 (a-c) XRD patterns of the (a) platelets, (b) iso-prisms, and (c) nanorods. Simulated XRD patterns of bulk $Cs_{0.33}WO_3$ (ICSD 253809) are shown as thin colored lines. (d-f) TEM micrographs of the (d) platelets, (e) iso-prisms, and (f) rods. Corresponding lattice-resolved TEM images of individual NCs along the prismatic plane are shown in the top insets, and white arrows indicate the NC dimension (length) along the <002> direction. Bottom insets illustrate the corresponding NC shapes. (g-i) Size distribution histograms corresponding to NC height (top panel) or NC width (bottom panel) for (g) platelets, (h) iso-prisms, and (i) rods. (j, k) Crystal structure of CWO NCs oriented along (j) basal and (k) prismatic planes. . . . . 67

4.2 High-resolution TEM micrographs of the prismatic planes of (a) platelets, (b) iso-prisms, and (c) rods presented as insets in Figure 1d-f. . . . . 68

4.3 TEM micrographs of CWO platelets (upper panel), iso-prisms (middle panel), and rods (bottom panel). Left panels: overview micrographs, middle panels: NCs oriented along basal planes, and right panels: NCs oriented along prismatic planes. . . . . 69

4.4 EDS spectra of CWO platelets (left), iso-prisms (middle), and rods (right). 69

4.5 Cartoon depicting the outer and inner shells of an iso-prism. Red arrows indicate the NC height (H) and width (W). The formula on the right was used to determine the volume of the hexagonal prism-shaped CWO NCs.[20] 70

4.6 (a) O 1s and (b) W 4f XPS spectra (thick black traces) of platelets (top), iso-prisms (middle), and rods (bottom). Shaded areas represent spectral contributions of various oxygen species (a), or deconvoluted $W^{6+}$ and $W^{5+}$ 4f spin-orbit doublets (b), as indicated in the graphs, and yellow traces are overall fits to the experimental data. . . . . 72

4.7 Volume-fraction-normalized O 1s XPS peak area ratio. . . . . 73

4.8 Optical extinction spectra of (a) colloidal suspensions of CWO NCs in TCE and (b) CWO NCs deposited on quartz substrates by drop casting from colloidal suspensions. Different traces correspond to specific NC shape (AR), as indicated in the graphs. Tauc plots for NCs having different ARs are shown in the inset of (a). . . . . 74

4.9 Variable-field 5 K MCD spectra of CWO NCs (left) and the corresponding magnetic field dependence of the integrated excitonic MCD intensities (right) for (a) platelets, (b) iso-prisms, and (c) rods. Insets in left panels show excitonic MCD band deconvolution, and the symbols in right panels correspond to deconvoluted components (designated by their peak maxima). The data in right panels are fit to linear or Brillouin function, as indicated. 77

4.10 (a) 7 T MCD spectra of CWO NCs sample from Figure S7, recorded at different temperatures, as indicated in the graph. (b) Temperature dependence of the integrated intensities of the spectra from (a). Inset: Integrated intensities of the MCD spectra as a function of $T^{-1}$. . . . . 78

4.11 (a) Optical absorption (top) and absorbance-normalized MCD (bottom) spectra of CWO platelets (pink traces), iso-prisms (green traces), and rods (blue traces). The spectra were collected at 6 T and 5K. (b) Molecular orbital diagram of a $(WO_6)^{6-}$ octahedral unit of CWO NCs (adapted from Yoshio et al.[21]) . . . . . 79

4.12 (a) Schematic representation of the exciton polarization mechanisms in CWO iso-prisms. (Top) exciton polarization induced by the angular momentum transfer from the cyclotron free electrons (dashed arrows) to the excitonic transition; (bottom) spin-induced excitonic Zeeman splitting caused by unpaired electrons localized on defect states (black dots). (b) Pictorial representation of the magnetic field dependence of the excitonic MCD signal intensity corresponding to the two exciton polarization mechanisms. (c) Illustration of the possible exchange interactions between $W^{5+}$ and neighboring $V_o$, responsible for the generation of high net spin state (S = 3/2). . 80

5.1 Structure of the IR metal-semiconductor-metal (MSM) photodetectors. (a) Semiconductor heterostructure layers grown by molecular beam epitaxy. The $In_{0.53}Ga_{0.47}As$ active region is grown between $In_{0.52}A_{l0.48}As$ barriers on an InP substrate. (b) Top view schematic of the interdigitated metal electrode geometry, where design parameters are electrode width (W $\sim$ 10 $\mu$m), spacing (S $\sim$ few $\mu$m), length (L $\sim$ 500 $\mu$m), and active area (A $\sim$ 500 $\mu$m $\times$ 540 $\mu$m) indicated by dashed red box. . . . . 86

5.2 Measurement setup for characterizing photodetector responsivity. (1) The broadband light source generates a beam that is collimated and then focused on the monochromator entrance slit; (2) wavelengths are selected by mechanical positioning of diffraction gratings; (3) the monochromator output is filtered and focused onto the wire-bonded MSM device; (4) a bias voltage is applied to the device and the photocurrent is measured using a current-voltage (I-V) amplifier. The output of the I-V amplifier is read out with a digital multimeter (DMM). Responsivity is determined from the DMM output and incident beam power measurements. . . . . 87

5.3 Structural and optical characterization of four plasmonic $WO_{3-x}$ NC samples. (a) Experimental X-ray diffractograms (blue traces) and reference XRD pattern (pink trace) of bulk $WO_{2.72}$ (ICSD No. 24731). (b) TEM micrographs of the NCs. (Inset: lattice-resolved TEM image of a NC). (c) Optical extinction spectra and (d) Raman spectra of the NCs. . . . . 89

5.4 Structural and optical characterization of four plasmonic $Cs_yWO_{3-x}$ NC samples. (a) Experimental X-ray diffractograms (blue traces) and reference XRD pattern (pink trace) of bulk hex-$Cs_{0.33}WO_3$ (ICSD No. 253809). (b) Optical extinction spectra and (c-e) TEM micrographs of the NCs. Insets: lattice-resolved TEM image of the prismatic (d) and basal plane (e) of a NC. 91

5.5 Optical extinction spectra of (a) colloidal and drop-cast plasmonic $WO_{3-x}$ and (b) $Cs_yWO_{3-x}$ NCs. . . . . 92

5.6 Beam profile (a) of the applied visible-NIR light source upon exiting the monochromator, and (b) its power spectrum over a wavelength range of 750-1800 nm using a 750 nm or 1400 nm filter to block higher order modes of diffracted light coming from monochromator. . . . . 93

5.7 Characterization of photodetector device performance as a function of bias voltage in dark (dashed line) and illumination (red traces). Dark current and photocurrent acquired at a wavelength of 1550 nm (176 $\mu$W mm$^{-2}$ incident power) for the as-fabricated InGaAs photodetectors A (a) and B (b). . . . 94

5.8 Pitting surface defects of an as-fabricated $In_{0.52}Al_{0.48}As/In_{0.53}Ga_{0.47}As$ on InP photodetector observed *via* a Nomarski microscopy scan (left), and a magnified view of pitting surface defects suspected to originate from native defects in the InP substrate. . . . . 95

5.9 Optical microscope images of (a) a bare MSM photodetector device before drop-casting NCs, and (b) after uniform deposition of CsWO NCs by drop-casting from diluted (150 g $L^{-1}$) solution. SEM micrographs of (c) device *A* with WO-1, and (d) device *B* CsWO-1 NCs deposited. . . . . 96

5.10 Photoresponsivity measured for (a) device *A* and (b) device *B* with (color trace) or without (black traces) NCs. Both devices exhibit enhancement in photoresponsivity in the presence of $WO_{3-x}$ (device *A*) and Cs:$WO_{3-x}$ NCs (device *B*). Photoresponsivity is determined by subtracting the dark current and normalizing the dark-current-corrected photocurrent with respect to the measured power spectrum of the broadband light source. . . . . 97

5.11 Plots of relative percent change in responsivity (RPD) as a function of wavelength obtained in the presence of drop-cast $WO_{3-x}$ (a) or Cs:$WO_{3-x}$ (b) NCs. The optical extinction spectrum of the different NC types (red traces) is plotted (in arbitrary units) on the right vertical axis in each plot. . . . . 98

5.12 External quantum efficiency (EQE) and detectivity of photodetector devices (a) *A* and (b) *B* obtained without (black traces) and by drop-casting $WO_{3-x}$ (a) or Cs:$WO_{3-x}$ (b) NCs. . . . . 99

6.1 (a) X-ray diffractogram of as-synthesized colloidal $WO_{3-x}$ NCs (ICSD no. 15254). Simulated XRD pattern for monoclinic $WO_{2.72}$ is shown with red trace. (b) Overview TEM micrograph of $WO_{3-x}$ NCs. Inset: Lattice-resolved TEM image of an individual $WO_{3-x}$ nanorod, indicating its growth along ⟨010⟩ direction with an interplanar lattice spacing of 3.95 Å. (c) Length and (d) width distribution histograms for $WO_{3-x}$ nanorods, determined from the TEM micrographs presented in (b). . . . . 105

6.2 (a) Overview UV-visible-NIR spectrum and (b) corresponding Tauc plot of the $WO_{3-x}$ NCs dispersed in TCE. Red arrow in (b) represents extrapolation of the onset of absorption to determine optical bandgap of the NCs ($E_g$=3.65 eV). . . . . 106

6.3 (a) Photograph of as-synthesized $WO_{3-x}$ NCs precipitated from toluene suspension using acetone. (b) Photograph demonstrating the poor dispersibility of as-synthesized $WO_{3-x}$ NCs (12 mg) in an aqueous Rh6G dye solution (5 mM). (c) Degradation of Rh6G dye by as-synthesized $WO_{3-x}$ NCs in dark at 20 °C. (d) Time-resolved dye degradation profile corresponding to the experiment shown in (c). . . . . 107

6.4 (a) FTIR spectra of the $WO_{3-x}$ NCs before ligand stripping (BLS, dark blue trace) and after ligand-stripped (ALS, light blue trace), and pure OLAC solvent (orange trace). The disappearance of characteristic -$CH_2$ stretching bands near 2855 and 2924 $cm^{-1}$ confirms successful removal of OLAC ligands from the NC surface. (b) XRD pattern of $WO_{3-x}$ NCs before ligand stripping (BLS, dark blue trace) and after ligand stripping (ALS, light blue trace), indicating retention of the crystalline structure of NCs following ligand removal. (ICSD no. 15254). (Asterisk denotes reflection peak from Si substrate). (c) UV-visible-NIR spectra of aqueous suspension of the ligand-stripped colloidal $WO_{3-x}$ NCs (light blue trace) and native $WO_{3-x}$ NCs dispersed in TCE (inset). (d) Tauc plots determined from (c) with the corresponding optical bandgap ($E_{og}$) of the NCs as indicating the arrows. . 108

6.5 Rh6G dye degradation by the ligand-stripped $WO_{3-x}$ NCs at 20°C in dark. (a) UV-visible absorption spectra of Rh6G aliquots collected at specific time intervals. Inset: photographs of the native Rh6G dye solution (5 mM) at 0 min (left), and after 120 min degradation (right). (b) Time-dependent degradation curve of Rh6G, and (c) its linearized form, illustrating the kinetics of dye degradation. (d) Rh6G dye degradation in the presence of various sacrificial agents: methanol (MeOH, hole scavenger), IPA (i-propanol, $OH^{\bullet}$ scavenger), $FeCl_3$ ($e^-$ scavenger), and AA (ascorbic acid, $O_2^{\bullet -}$ scavenger), highlighting the influence of reactive species on the degradation mechanism. Photothermal degradation percent was calculated from absorbance value at 526 nm at 120 min. . . . . 109

6.6 Photocatalytic degradation of Rh6G dye in the dark using the ligand-stripped colloidal $WO_{3-x}$ NCs. . . . . 110

6.7 Photocatalytic dye degradation by colloidal ligand-stripped $WO_{3-x}$ NCs in the dark at 20°C in the presence of various sacrificial agents (colored traces). Scavenged species are shown in brackets. . . . . 112

6.8 (a) X–ray diffractograms and (b–e) SEM micrographs of $WO_{3-x}$powder samples obtained by annealing the as-synthesized $WO_{3-x}$ NCs in air for 2 hours at different temperatures: (b) 350°C, (c) 400°C, (d) 600°C, and (e) 800°C, revealing a temperature-dependent morphological and size evolution of the NCs, as a result of the annealing. Black trace in (a) corresponds to XRD pattern of bulk $WO_{2.9}$ used as reference for the photothermal catalysis/adsorption measurements. (f) BET specific surface area of the NCs from the annealing series together with that of bulk $WO_{2.9}$. (g) Time-evolution of the Rh6G dye concentration change as a function of time for each sample in the annealing series. (Pink markers correspond to photodegradation profile of the ligand-stripped $WO_{3-x}$ NCs presented in Figure 6.5b). . . . . 113

6.9 (a-e) Steady-state optical extinction spectra of aliquots of Rh6G aqueous solution taken at specific time intervals for spectroscopically monitoring the adsorption-photothermal catalytic processes of $WO_{3-x}$ NCs annealed at 350°C (a), 400°C (b), 600°C (c), 800°C (d), and the commercial $WO_{2.9}$ (e). (f) Time evolution of adsorption/photothermal catalytic degradation of Rh6G for each sample in (a-e). . . . . 114

6.10 Plots of (a) PFO, (b) PSO, (c) linearized PSO, and (d) IPD kinetic models. 118

6.11 Adsorption isotherms and their corresponding linearized forms using Langmuir (a,b) and Freundlich (c,d) models, respectively, for $WO_{3-x}$ NCs annealed at 400°C for 2 hours. (Measurements were carried out at 20°C in dark). Fitting parameters can be seen in bottom right corner of each panel. 120

6.12 Linearized Dubinin–Radushkevich (D-R) isotherm model for $WO_{3-x}$ NCs annealed at 400°C for 2 hours. (Measurements were carried out at 20°C in dark). . . . . 122

6.13 ESI–MS spectra showing the molecular fragments of Rh6G degraded by the ligand-stripped $WO_{3-x}$ NCs (top panel), and $WO_{3-x}$ annealed at 400°C and (middle panel). ESI–MS spectrum of pure Rh6G dye (bottom panel) is shown as a reference. Insets show regions of the corresponding spectra between 100–250 $m/z$. . . . . 123

A.1 Steady-state photoluminescence emission spectrum (300 K) of as-synthesized $WO_{3-x}$ NCs dispersed in TCE. . . . . 159

A.2 (a) Variable-temperature excitonic MCD spectra collected at 7 T for the colloidal plasmonic $WO_{3-x}$ NCs presented in Chapter 3. (b) Integrated excitonic MCD intensity as a function of wavelength determined from (a). . 160

A.3 Normalized CD extinction spectra for colloidal $WO_{3-x}$ NC thin films. Spectra were collected at 5 K in the range of 0-7 T. . . . . 161

A.4 Saturation magnetization curve of $WO_{3-x}$ NCs. Experimental data were collected at 5 K in the range of 0-9 T and fitted with Brillouin function. . . 162

B.1 Optical extinction spectra of colloidal Cs:$WO_{3-x}$ nanoplatelets dispersed in TCE. . . . . 163

C.1 Example showing how the power spectrum and photocurrent data are processed to account for changes in power transmission through different diffraction gratings used in the monochromator. Two gratings are used over the range of wavelength values selected; the grating change occurs at 1500 nm. 164

C.2 The effect of successive drop-casts of $Cs_yWO_{3-x}$ NCs using a concentration of 135g/L. (a) Responsivity as a function of wavelength for successive drop-casts. (b) Relative percent difference in responsivity for successive drop-casts, measured at several bias voltages. The median (data points) and standard deviation (bars) of the relative percent difference are calculated over the full wavelength range shown in (a). . . . . 165

C.3 The effect of drop-cast concentration on the change in responsivity (RPD) for $Cs_yWO_{3-x}$ NCs. Samples were diluted in hexane. The RPD is measured over the full spectrum (900-1800 nm) and the median value plotted (bars indicate the standard deviation). . . . . 166

D.1 Plots showing the reusability of colloidal ligand-stripped $WO_{3-x}$ NC photocatalysts (12 mg). The measurements were performed in the dark at 20°C. 167

D.2 BET specific surface area measurements of the $WO_{3-x}$ NCs annealed at different temperatures for 2h. . . . . 168

D.3 X-ray diffractograms of $WO_{3-x}$ NCs annealed in air for 1-3 hours at 400°C (left panel), 500°C (middle panel), and 600°C (right panel). . . . . 169

# List of Tables


2.1 Sacrificial agents ("scavengers") and the corresponding scavenged particles/chemical species. . . . . 44

3.1 Table summarizing the spectral features seen in Figure 3.9. along with their assignment. . . . . 59

4.1 Geometric Parameters and Chemical Composition of As-Synthesized CWO NCs . . . . . 70

4.2 Calculated Parameters for As-synthesized CWO NCs Determined from TEM Images. . . . . 71

4.3 W 4f XPS Results for CWO NCs Presented in Figure 4.5. . . . . 72

4.4 O 1s XPS Results for CWO NCs Presented in Figure 4.5. . . . . 73

5.1 Summary of crystallographic and optical characterization of $WO_{3-x}$ NC samples. . . . . 90

5.2 Summary of crystallographic and optical characterization of $Cs_yWO_{3-x}$ NC samples. (Left and right columns of XRD correspond, respectively, to peak location (°) and broadening ($\beta$)). . . . . 92

5.3 Resistance values of as-fabricated MSM photodetector devices measured on a probe station with illumination under a white light source ($R_{light}$) or without illumination ($R_{dark}$) using bias voltage between -10 mV and +10 mV range. Optical power of ca. 18 $\mu$W mm$^{-2}$ was measured under illumination and ca. 32 nW mm$^{-2}$ in the dark. Device $A$ and $B$ were selected owing to their significant increase in conductivity under illumination, and possessing the same electrode geometry. Percentage change in resistance under illumination ($\Delta$R), and the mean resistance ($\mu$) and its standard deviation ($\sigma$) values for the array of 16 MSM detectors are also indicated. . . . . 93

6.1 Kinetic and fitting parameters extracted from Figure 6.10. . . . . 119

6.2 Summary of Isotherm Fitting Parameters Presented in Figure 6.11-12. . . . 122

D.1 BET specific surface area data of the $WO_{3-x}$ NCs annealed at different temperatures for 2h. . . . . 168

# List of Abbreviations

**AR=NC height/width** aspect ratio 5

**BET** Brunauer-Emmett-Teller 42

**ESI-MS** electrospray-ionization mass spectrometry 43

**FTIR** Fourier-transform infrared spectroscopy 42

**LCP and RCP, respectively** left and right circularly polarized light 20

**LFT** ligand-field transitions 49

**LSPR** localized surface plasmon resonance 1

**MCD** magnetic circular dichroism spectroscopy 64

**MIR** mid-infrared 1

**NCs** nanocrytals 1

**NFE** near-field enhancement 3

**NIR** near infrared 1

**PLE** photoluminescence emission 41

**Rh6G** Rhodamine 6G dye 38

**ROSs** reactive oxygen species 43

**XPS** X-ray photoelectron spectroscopy 41

# Chapter 1

## Introduction

Light is one of the most powerful tools for probing and controlling matter. Understanding how materials interact with electromagnetic radiation lies at the heart of countless scientific and technological advances. The optical behavior of materials is fundamentally governed by their complex dielectric function ($\epsilon(\omega)$), which describes how a material responds to an external electromagnetic field. Beyond the electronic band structure and crystal symmetry, the optical properties of nanostructures are primarily dictated by additional intrinsic effects such as quantum confinement, enhanced surface-to-volume ratios, chemical composition (doping), spatial distribution of dopants, and nanocrystal geometry (size and shape).[4] For instance, one of the earliest and most captivating examples of nanoscale light-matter interaction can be found in stained glasses or the ancient Roman Lycurgus cup from the 4th century A.D.[22] These objects famously display dichroic behavior, which is an anisotropic optical effect exhibited by nanosized metal particles embedded in glass, making these objects appear in different colors when light is reflected or transmitted. This remarkable optical phenomenon is nowadays understood to arise from localized surface plasmon resonance (LSPR) in metallic or colloidal doped plasmonic semiconductor nanocrytals (NCs),[23,24] giving rise to intense and tunable optical responses across the visible to near infrared (NIR) and mid-infrared (MIR) spectral regions.[25] Plasmonics, an emerging branch of nanophotonics exploring plasmon-based light–matter interactions at the nanoscale,[26] utilizes this size-dependent optical behavior to enable the design of materials with tunable optical properties, making nanomaterials especially attractive for diverse optoelectronic applications,[27,28] including (bio)chemical sensing,[29] optoelectronics,[30] quantum computing technologies,[31,32] visible–NIR–MIR photodetection,[33,34] photocatalysis,[35–37] and plasmon-enhanced spectroscopies.[38]

## 1.1 Physical Principles of Localized Surface Plasmon Resonances

Within the framework of classical electrodynamics, light is characterized by Maxwell's equations as a transverse oscillation of the electromagnetic field, whose propagation velocity is dictated by the refractive index of the surrounding medium.[39] When light of frequency $\omega$ is incident on a bulk metal, its oscillating electric field component ($\vec{E}$) is periodically and coherently displacing (polarizing) the free electron gas at the metal–dielectric interface, generating an oscillating free electron plasma[40] (Figure 1.1). From the electric polarization ($P$) inside the metal, the frequency-dependent dielectric constant ($\epsilon(\omega)$) can be obtained, according to equations 1.1–1.2:[41]

$$P = \frac{N_e e^2 E}{m^* \omega^2} \tag{1.1}$$

$$\epsilon(\omega) = 1 + \frac{P}{\epsilon_0 \vec{E}} = 1 - \frac{N_e e^2}{\epsilon_0 m^* \omega^2} \tag{1.2}$$

where $m^*$ is the electron effective mass, $N_e$ is the carrier density, $\epsilon_0$ is vacuum permittivity, and e is elementary charge, respectively. Under resonant conditions, the frequency of the incident light ($\omega$) matches the eigenfrequency of the resonant plasma ($\omega_p$) (equation 1.3), inducing a coherent quantized and propagating dipolar oscillation of the free charge carriers along the metal-dielectric interface (Figure 1.1a), known as surface plasmon resonance (SPR). Propagating waves involving surface plasmons are known as surface plasmon polaritons.[29,40] Importantly, however, when the size of the metal is reduced to subwavelength dimensions, the SPRs can no longer freely propagate along the metal-dielectric interface, but instead, the free electron oscillations become spatially confined within the nanoparticle volume (Figure 1.1b), leading to quantized localized surface plasmon resonances (LSPR).[29,42] Despite their quantized nature, both the propagating SPR and LSPR can be precisely modeled by the semi-classical Drude-Lorentz free electron theory (vide infra), which allows for expressing the resonant LSPR frequency ($\omega_{LSPR}$) as a function of $N_e$ and $m^*$, according to equations in 1.3 and 1.4:[22]

$$\omega_p = \sqrt{\frac{N_e e^2}{m^* \epsilon_0}} \tag{1.3}$$

$$\omega_{LSPR} = \sqrt{\frac{\omega_p^2}{1 + 2\epsilon_m} - \gamma^2} \tag{1.4}$$

where $\gamma$ is the carrier damping factor. Based on eq 1.4, the $\omega_p$ of the collectively oscillating free carriers within the plasmonic NC exhibit a nonlinear dependence on the free carrier density ($\omega_p \propto N_e$), as well as the optical parameters of the surrounding medium, such as solvent refractive index.[43] (For more information on LSPR parameters, see Section 1.1.1.3.). As a result of the spatial confinement of free carrier oscillations, the LSPR can lead to significant amplification of the electromagnetic field ($\vec{E}$) both within and around the NC to several orders of magnitude greater than the incident light ($\vec{E}_0$), leading to strong optical near-field enhancement (NFE) at the NC surface.[44]

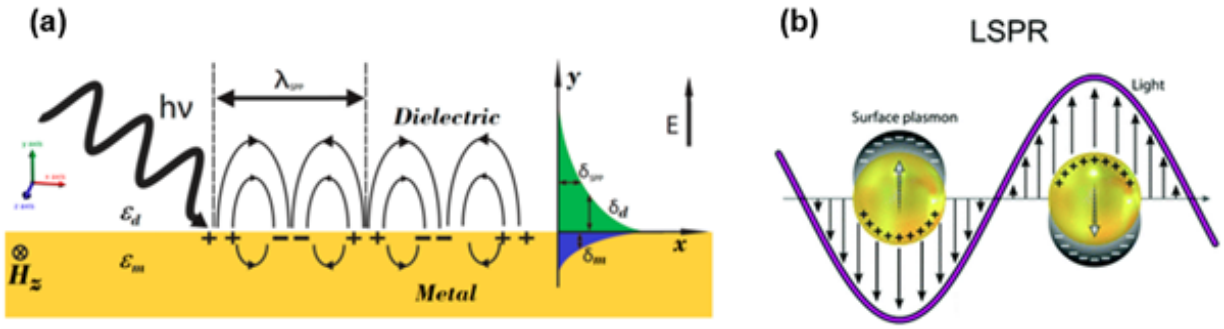



Figure 1.1: Schematic representation of (a) propagating surface plasmon polaritons along the metal-dielectric interface, and (b) dipolar localized surface plasmon resonance confined to a nanosized plasmonic particle. (a: Reprinted with permission from Aftab et al.,[1] Copyright (2023) Springer Nature. b: Reprinted with perission from Masson[2] Copyright (2020), Royal Society of Chemistry).

### 1.1.1 Optical Modelling of Plasmonic NCs

The optical response of conducting NCs, including their absorption and scattering characteristics, is fundamentally governed by the distribution of the electric field within and around the particle upon interaction with electromagnetic radiation, as described by Maxwell's equations.[29] In the simple case when the material possesses unit magnetic permeability ($\mu$), Maxwell's equations can be simplified to solve for the electric field inside the NC, based on eq 1.5:[4]

$$\nabla \times \nabla \times \vec{E} = -\mu_0 \frac{\partial D}{\partial t} \tag{1.5}$$

where $\vec{E}$ is the electric field vector, $\mu_0$ is the magnetic permeability of classical vacuum, and $D$ is the electric displacement field. From the NC point of view, the light-matter interaction can be decomposed into two components, specifically the incident and scattered electromagnetic fields ($\vec{E}_{in}$, and $\vec{E}_{sca}$, respectively), from which the total optical extinction can be obtained considering the total electric field inside ($\vec{E}_{in}$) in and outside ($\vec{E}_{in}$) of the NC upon interaction with light, based on equations 1.6–1.7:[4,40]

$$\vec{E}_{out}(x,y,z) = \vec{E_0}\hat{z} - [\frac{\epsilon_d - \epsilon_m}{\epsilon_d + 2\epsilon_m}]\alpha^3 E_0[\frac{\hat{z}}{r^3} - \frac{3z}{r^5}(x\hat{x} + y\hat{y} + z\hat{z})] \tag{1.6}$$

$$\vec{E}(x,y,z) = [\frac{3\epsilon_D}{\epsilon_D + 3\epsilon_D}]\vec{E_0}\hat{z} \tag{1.7}$$

Here, $\vec{E_0}$ is the magnitude of the electric field component of incident light ($\vec{E_{in}}$), {x, y, z} are spatial Euclidean coordinates relative to the NC center with their corresponding unit vectors, $\{\hat{x}, \hat{y}, \hat{z}\}$, respectively.

#### 1.1.1.1 Mie Scattering Theory

The physical description and mathematical modelling of LSPR can be dated back to the work of Gustav Mie in the early 20th century.[45] Mie developed an analytical solution using Maxwell's equations to describe the light-scattering properties of spherical Au nanoparticles with an isotropic dielectric constant ($\epsilon_d$) homogeneously dispersed in a uniform medium with dielectric constant ($\epsilon_m$).[29,46] Mie theory generally enables the calculation of absorption, scattering, and extinction cross-sections ($\sigma_{ext}$, $\sigma_{sca}$, and $\sigma_{abs}$, respectively) for NCs of subwavelength dimensions interacting with electromagnetic planewaves (quasistatic approximation). It demonstrates the size dependence of optical absorption and scattering of plasmonic NCs, based on equations 1.8-1.10:[4]

$$\sigma_{ext}(\omega) = 4\pi R^2 [K\sqrt{\epsilon_m}R] Im \frac{\epsilon_D(\omega) - \epsilon_m}{\epsilon_D(\omega) - 2\epsilon_m} \tag{1.8}$$

$$\sigma_{sca}(\omega) = 4\pi R^2 [K\sqrt{\epsilon_m}]^4 Im |\frac{\epsilon_D(\omega) - \epsilon_m}{\epsilon_D(\omega) - 2\epsilon_m}|^2 \tag{1.9}$$

$$\sigma_{abs} = \sigma_{ext} - \sigma_{sca} \tag{1.10}$$

where $k$ is the wavevector ($k = \omega/c$) of the incident electromagnetic plane wave, $R$ is the radius of the metal nanoparticle, and $\epsilon_D(\omega)$ is the frequency-dependent dielectric function dictating the fundamental optical properties of the nanostructure. The dielectric function is complex valued ($\epsilon_D(\omega) = \epsilon_1(\omega) + i\epsilon_2(\omega)$), so whether it is real ($i\epsilon_2(\omega) = 0$) or complex with a positive or negative real component ($\epsilon_1(\omega) > 0$ or $\epsilon_1(\omega) < 0$, respectively) will determine the type of optical responses of the NC.[26,40] Based on equation (1.5–1.6.), if the dielectric function is positive and real valued, the NC exclusively exhibits optical scattering and no absorption. However, for a complex dielectric function with a positive real component (*i.e.*, $\epsilon_D(\omega) = \epsilon_1(\omega) + i\epsilon_2(\omega)$, such that $\epsilon_1(\omega) > 0$), the optical response of the NC involves Rayleigh (inelastic) scattering. Of particular importance is the case when the dielectric function is complex number with a negative real part ($\epsilon_1(\omega) < 0$).[26,40] In this case, whereby the NC is expected to exhibit maximum optical extinction when $\epsilon_1(\omega) = -2\epsilon_m$, which is satisfied under resonant photon absorption generating LSPR. Importantly, the dielectric function with negative real part ($\epsilon_1(\omega) < 0$) is generally an indicator of materials possessing high free carrier density, which is a necessary factor for sustaining LSPR.[3]

#### 1.1.1.2 Gans Theory

Although Mie's theory accurately describes optical extinction of metallic nanostructures, it is strictly limited to spherical nanoparticle geometry. However, in the early 1900s, Richard Gans developed an analytical model to extend and generalize Mie's scattering theory to non-spherical nanostructures of arbitrary aspect ratio (AR=NC height/width).[47] Based on Gans theory, the absorption cross-section ($\sigma_{abs}$) for a prolate spheroid can be obtained by equation 1.11:[29]

$$\sigma_{abs} = \frac{\omega}{3c}\epsilon_m^{3/2} V \sum_j \frac{(1/P_j^2)\epsilon_2}{\{\epsilon_1 + [1 - P_j/P_j]\epsilon_m\}^2 + \epsilon_2^2} \tag{1.11}$$

where $P_j$ includes depolarization factors ($PA, PB, PC$) for each axis of the NC (with $A > B = C$ for a non-spherical NC) summed over in three dimensions ($j$). As the shape of the NC changes, each depolarization factor leads to an anisotropic alteration of both the real ($\epsilon_1$) and imaginary ($\epsilon_2$) parts of the dielectric function, resulting in the generation of multiple LSPR modes along different axes of the NCs, such as transverse ($x - y$ plane) or longitudinal (along $z$-axis) LSPR modes.

#### 1.1.1.3 Drude-Lorentz Free Electron Model

Although Mie–Gans theory provides an good model of the interaction between electromagnetic waves and metallic nanoparticles based on macroscopic boundary conditions, it relies on a dielectric function introduced independently to characterize the material's optical response.[48,49] Importantly, while LSPR is most commonly observed in coinage metal nanoparticles such as Au, Ag, and Cu, similar plasmonic effects can also occur in degenerately-doped compound semiconductor NCs (e.g., Cs:$WO_{3-x}$, Al:ZnO, Sn:$In_2O_3$) possessing sufficiently high free carrier densities (typically on the order of $10^{19}$–$10^{22}$ $cm^{-1}$)[3,4,11] (Figure 1.2). In this context, the semi-classical Drude–Lorentz model can be regarded as a complementary model to Mie–Gans theory, in which the frequency-dependent permittivity is explicitly associated with underlying charge carrier dynamics. In the Drude–Lorentz model, free carriers are treated as classical mobile charges harmonically oscillating around the lattice ions of a solid, driven by the electric vector component ($\vec{E}$) of an oscillating electromagnetic field, which induces a periodic displacement ($\vec{D}$) of the carriers, according to equation 1.12:[10,50,51]

$$\vec{D} = \epsilon_0 \epsilon_o pt - \frac{N_e e^2 \vec{E}}{m^*(\omega^2 + i\gamma\omega)} \tag{1.12}$$

In the eq. 1.12, where $\epsilon_{opt} = \epsilon_\infty \approx n^2$ ($n$ is the refractive index) is the dielectric constant measured in the optically transparent spectral region of the given plasmonic semiconductor NC. The Drude–Lorentz model relates $\vec{D}$ to the dielectric function $\epsilon_D(\omega)$ *via* equation 1.13:

$$\epsilon_D(\omega) = \epsilon_\infty(1 - \frac{\omega_p^2}{\omega^2 + i\gamma\omega}) \tag{1.13}$$

where $\omega_p$ is the plasma frequency. Importantly, combining equations 1.12 and 1.13, one can find the square root relationship between $\omega_p$ and $N_e$, according to equation 1.14:

$$\omega_p = (\frac{N_e^2}{\epsilon_0 \epsilon_\infty m^*})^{1/2} \tag{1.14}$$

Owing to the collective response of free carriers and the direct dependence of LSPR absorption on the number of free carriers in plasmonic semiconductor NCs, the Drude–Lorentz model predicts an approximately linear relationship between the absorption coefficient ($\alpha$) and $N_e$ (equation 1.15):[50]

$$\alpha = \frac{\epsilon_\infty \omega_p^2}{nc\omega^2\tau} = \frac{N_e^2}{\epsilon_0 nc\tau m^*} \tag{1.15}$$

where $c$ and $\tau$ are the speed of light and damping time, respectively. From these parameters, the Drude–Lorentz model predicts that degenerately-doped semiconductor NCs (with $N_e \sim 10^{19}$–$10^{22}$ carriers/cm$^3$) exhibit LSPR absorption in the visible–far infrared (FIR) spectral region[3] (Figure 1.2). Importantly, in plasmonic nanostructures, intrinsic scattering processes can reduce the LSPR intensity, leading to optical losses and simultaneously broadening of LSPR spectral bands, characterized by damping constant ($\tau$), as demonstrated in equation 1.16:[4]

$$\gamma = \sum \gamma_i = \gamma_{e-e} + \gamma_{e-ph} + \gamma_{e-ion} + \gamma_s + \gamma_{ib} \tag{1.16}$$

where $\gamma_{e-e}$, $\gamma_{e-ph}$, $\gamma_{e-ion}$, $\gamma_s$, $\gamma_{ib}$ correspond, respectively, to the electron-electron, electron-phonon, electron-ionized impurity, surface, and interband scattering processes.

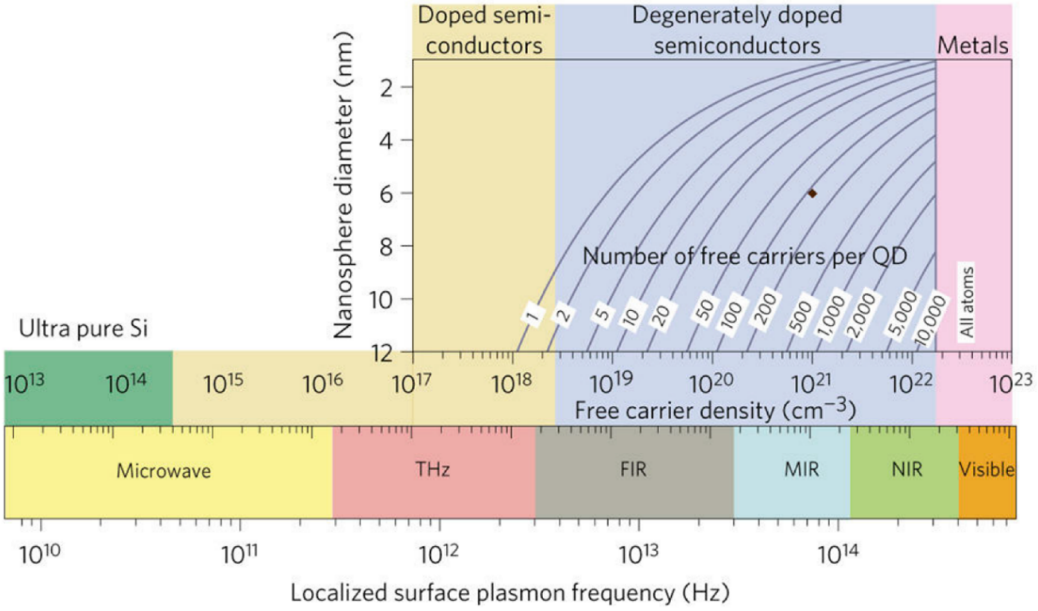



Figure 1.2: Free carrier density and LSPR frequency range for plasmonic materials. (Reprinted with permission from Luther et al.,[3] Copyright (2011) Springer Nature.)

## 1.2 Plasmonic Compound Semiconductor NCs

In the past several years, plasmonic compound semiconductor NCs (such as Sn:$In_2O_3$, Cs:$WO_{3-x}$, Al:ZnO, $WO_{3-x}$, $TiO_{2-x}$, etc.) have attracted considerable attention in the plasmonics community, owing to their widely-tunable free carrier densities ($\sim 10^{18–21}$ carrier/$cm^{-3}$),[3] allowing for the modulation of LSPR energy across the visible–NIR–MIR spectral region.[4,11] While coinage metal NCs possess high free carrier densities ($\sim 10^{21–22}$ carrier/$cm^{-3}$) giving rise to narrow LSPR bands in the visible region,[22] plasmonic semiconductor NCs require intrinsic or extrinsic doping mechanisms to generate the sufficient number of free carriers for sustaining LSPR in the visible–NIR–MIR spectral region (Figure 1.2). Unlike metals, for which carrier properties are largely fixed, plasmonic compound semiconductor NCs offer a unique degree of LSPR tunability *via* compositional (doping) design.[4,11,24,52] This allows for modulation not only of carrier density ($N_e$) and carrier type (n- or p-type), but also of parameters such as carrier mobility,[53] trapping or activation,[54,55] and scattering.[56] For instance, in metal oxide NCs, dopants and/or ionized oxygen vacancies introduce charge scattering centers that play a central role in limiting carrier mobility and thus enhancing carrier damping.[57] This, in turn, results in broad, asymmetric LSPR absorption bands, which deviate from the narrow, symmetric features typically observed in plasmonic metal nanostructures, affecting key plasmonic descriptors, such as the resonance frequency ($\omega_p$), LSPR spectral line width ($\Gamma$), and the overall LSPR quality factor ($Q = \omega_p/\Gamma$).[58,59] Importantly, such impurity-driven effects must be taken into account when analyzing LSPR behavior in these materials, which can often be controlled *via* static (structural)[60–62] or dynamic (external stimuli-driven)[63,64] modulation, as discussed later for doped plasmonic semiconductor metal oxide NCs. This tunability, while advantageous, also necessitates careful interpretation of spectroscopic data, particularly in systems where multiple electronic transitions or complex defect landscapes may obscure the LSPR response (as will be presented and further discussed in Chapter 3).

Interestingly, the LSPR phenomenon has been observed not only in n-type but also in p-type compound semiconductor nanocrystals (NCs), such as binary copper chalcogenides ($Cu_2X$, X={S, Se, Te}).[4,65–67] In contrast to n-type systems, wherein LSPR arises from the oscillation of conduction-band electrons, p-type copper chalcogenide NCs exhibit LSPR due to the collective oscillations of free holes in the valence band, which serve as the majority carriers. The p-type conductivity in substoichiometric copper chalcogenides originates from positively charged copper vacancies, the formation of which under ambient conditions is thermodynamically favored relative to elemental copper ($Cu^0$) due to their higher chemical potential.[67,68] Similarly to metal oxides, copper chalcogenide NCs also support free carrier concentrations in the range of $\sim 10^{18} - 10^{21}$ $cm^{-3}$ enabling visible–NIR–MIR LSPR absorption (Figure 1.3), which can be modulated *via* the extent of copper deficiency and/or

NC morphology or size. For instance, colloidally-synthesized pseudospherical $Cu_{2-x}S$ NCs have exhibited a size-dependent redshift in NIR LSPR, accompanied by a reduced Q-factor, which has been attributed to enhanced surface scattering of charge carriers with decreasing NC size. The same study further revealed that the initially non-plasmonic (stoichiometric) $Cu_2S$ NCs could acquire LSPR response through post-synthetic oxidation, which increased copper deficiency (and thus hole concentration) over time.[3] Conversely, in originally plasmonic (non-stoichiometric) $Cu_{2-x}S$ ($x = 0.9$) NCs, LSPR was achieved by reducing copper vacancies by using Cu(I) salts.[69] In another case, Ce(IV)-mediated oxidation of $Cu_{2-x}Se$ NCs induced a substantial increase in copper deficiency, resulting in a blueshift of the LSPR along with enhanced intensity and Q-factor. Beyond such post-synthetic strategies, compositional tuning has also emerged as a robust method for modulating LSPR in copper chalcogenides. For example, substitutional doping of $Cu_{2-x}S$ NCs with Se or Te (forming $Cu_{2-x}S_ySe_{1-y}$ or $Cu_{2-x}S_yTe_{1-y}$) has led to increased LSPR energy and improved Q-factors.[70] This was attributed to a combination of higher copper vacancy populations and a reduced effective mass of free carriers introduced by Se/Te dopants. Similarly, in indium-doped copper sulfide NCs ($Cu_xIn_yS_2$, with $0.88 \leq x \leq 1.01$, and $0.95 \leq y \leq 0.91$), systematic variations of the Cu:In precursor ratio initially produced a pronounced LSPR redshift, which eventually disappeared at higher In doping levels ($y = 0.6$), corresponding to a critical drop in carrier concentration due to suppressed copper vacancy formation.[71]

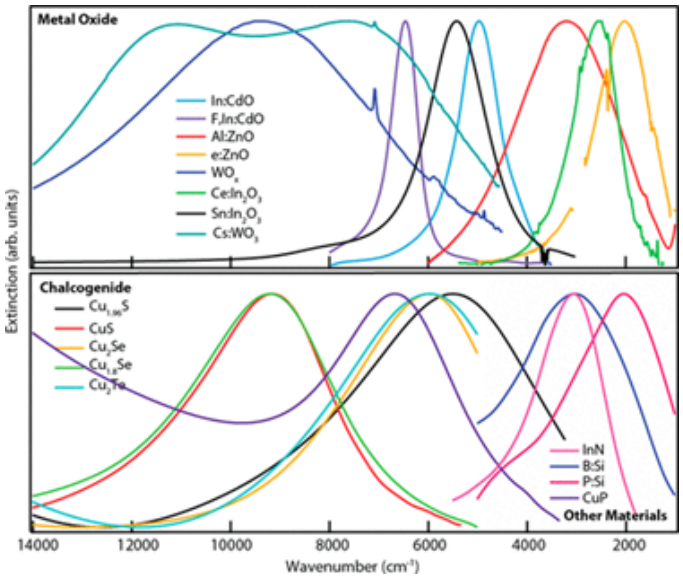



Figure 1.3: LSPR absorption of various n- and p-type semiconductor NCs. (Reprinted with permission from Agrawal et al.,[4] Copyright (2018) American Chemical Society.)

### 1.2.1 Generating LSPR in Plasmonic Semiconductor Metal Oxide NCs

#### 1.2.1.1 Non-Stoichiometry

Despite their wide electronic bandgaps ($E_g \sim 2.5$–$3.5$ eV), several n-type binary metal oxide (e.g., $WO_3$, $MoO_3$, $TiO_2$, $In_2O_3$, $SbO_2$) NCs exhibit appreciable optical absorption in the visible–NIR region, giving rise to their characteristic coloration.[11] In these so-called transparent conducting oxide (TCO) NCs,[72] optical absorption is governed by their native defect chemistry, predominantly oxygen vacancies.[4,73–75] Driven by thermodynamic processes, the presence of oxygen vacancies introduces deviations from ideal stoichiometry thereby producing oxygen-deficient non-stoichiometric phases (e.g., $WO_{3-x}$, $MoO_{3-x}$, $TiO_{2-x}$, etc.), and also leads to a disrupted charge balance in the material (*i.e.*, $O_{Lattice} \rightarrow V_o + 2e^- + 1/2O_2$).[4,10] In order to restore overall charge neutrality, the material compensates by either altering the oxidation states of nearby lattice ions (e.g., $M_M^{z+} + ne^- \rightarrow M_M^{(z-n)+}$) or by forming additional donor defects.[41] In general, oxygen vacancy concentration in TCO NCs can be modulated *via* adjusting oxygen partial pressure during synthesis or by performing post-synthesis annealing in air.[76]

One of the most intriguing and technologically relevant TCO materials, non-stoichiometric tungsten suboxides ($WO_y$) have for long been known to possess various levels of oxygen-deficiency ($2.625 < y < 2.92$), exhibiting a wide variety of thermodynamically stable crystal structures and morphologies, known as Magnéli phases.[77,78] The formation of Magnéli phases in oxygen-deficient $WO_{3-x}$ reflects the ordering of a high density of oxygen vacancies into crystallographic shear planes. As these vacancy-derived structures grow and begin to connect between neighboring NCs, a percolation threshold can be reached where continuous pathways for electron transport emerge. This transition enables greater carrier delocalization and stronger plasmonic coupling within the NC network.[5,79,80] With the aid of first principles calculations, Migas et al.[5] investigated the stoichiometry–electronic structure relationship of several of the Magnéli phases of tungsten oxide, including $W_{32}O_{84}$, $W_3O_8$, $W_{18}O_{48}$, $W_{17}O_{47}$, $W_5O_{14}$, $W_{20}O_{58}$, and $W_{25}O_{73}$ (Figure 1.4a), predicting their metallic conductivity with free carrier densities ranging between $1.62 \times 10^{22}$–$2.90 \times 10^{21}$ cm$^{-3}$, respectively. Interestingly, these calculations also demonstrated how the oxygen vacancy formation at specific lattice sites impacts the Fermi level positions, free carrier densities, and carrier localization in these various Magnéli phases. For the $W_{18}O_{48}$ ($WO_{2.72}$) nanowires the oxygen vacancy formation at the $1h$ or $2n$ Wyckoff positions (*i.e.*, symmetry-equivalent atomic positions) causes negligible deviations in bandgap energy and overall electronic band structure. On the other hand, the removal of an oxygen atom from the $2m$ position leads to a significant reduction in bandgap energy (Figure 1.4 c–e), albeit leaving the band

dispersion near the energy gap region and the Fermi level almost invariant, similar to vacancy formation at the $2n$ position (Figure 1.4d). These observations were rationalized by the impact of site-specific oxygen vacancy formation on the extent of distortion of [$WO_6$] octahedra.

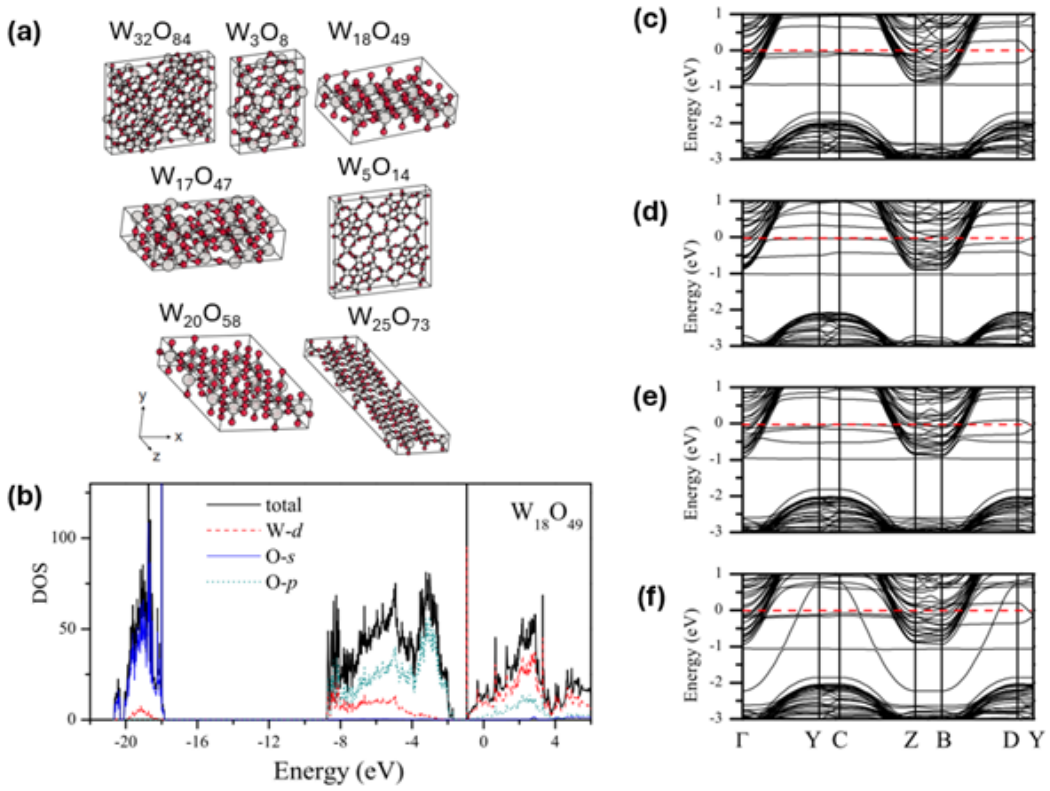



Figure 1.4: (a) Crystallographic unit cell of various Magnéli phases of tungsten oxide. (b) Total and projected density of states (DOS) of $W_{18}O_{49}$, showing the orbital composition of valence and conduction bands. (c–f) Electronic band structures of $W_{18}O_{49}$ nanowires (c) with no oxygen vacancy, (d) with one oxygen vacancy in the $1h$ Wyckoff position, (e) with oxygen vacancy in the $2n$ position, and (f) in the $2m$ position. (Red dashed line corresponds to Fermi level). (Adapted with permission from Migas et al.,[5] Copyright (2010) AIP Publishing.)

In their seminal paper, Manthiram and Alivisatos et al.[76] presented the colloidal synthesis of high-quality, uniformly shaped, monoclinic $WO_{3-x}$ nanorods, using a hot-injection of tungsten(V) ethoxide into a solvent mixture of oleic acid and trioctylamine at 315°C under inert atmosphere. The authors observed a broad optical absorption band extending

from the visible to NIR–MIR region, which, based on the linearity of peak wavelength shift as a function of solvent refractive index ($\sim$ 280 nm/refractive index unit) and peak fitting results (Mie–Gans theory), they assigned to LSPR absorption. Annealing the same NCs in air at elevated temperatures for different time urations (175°C, 0-6 min) resulted in an approximately threefold reduction in LSPR peak intensity and a ca. 150 nm red-shift in LSPR band position, suggesting a concurrent decrease in free carrier density and level of oxygen deficiency. Using tungsten(V) ethoxide-based colloidal hot injection synthesis, Prusty et al.[81] have demonstrated that the reaction temperature plays a critical role in *in–situ* modulating oxygen vacancy concentration and thus free carrier density in ultrathin ($\sim$ 1 nm) $WO_{3-x}$ nanoplatelets without any post-synthesis treatments. Using optical absorption spectroscopy and X-ray diffractometry, the authors also demonstrated the crucial role of long-chain aliphatic hydrocarbons and amines in the formation of colloidal $WO_{3-x}$ nanoplatelets. Davis Jr et al.[82] further investigated and reported a detailed study on the colloidal synthesis mechanism and modulation of shape anisotropic monoclinic plasmonic $WO_{3-x}$ NCs. Lee et al.[83] developed surface-ligand-controlled approach for enhancement of free carrier density in plasmonic $WO_{3-x}$ nanoplatelets synthesized via hot injection of tungsten(V) ethoxide. Using tetradecylphosphonic acid (TDPA) coordinating ligands, the authors reported that the binding of tridentate phosphate headgroup ($PO_3$–) of TDPA prevents the formation of shallow surface trap states, facilitating the transfer of oxygen vacancy-related electrons into the conduction band of the NCs. Beyond the monoclinic phase, Nayak et al.[84] also presented the selective colloidal synthesis of hexagonal $WO_{3-x}$ NCs, using thermal decomposition of $W(CO)_6$ at elevated temperatures. Using dried oleylamine solvent, the authors reported the selective formation of the monoclinic and hexagonal $WO_{3-x}$ phases, exhibiting distinct electronic, optical, and electrochemical properties.

#### 1.2.1.2 Interstitial Doping

Modulation of free carrier density in semiconductor NCs can also be achieved *via* intentional doping, which involves the incorporation of a foreign doping element into the interstitial sites of the NC host lattice. Owing to their relatively open crystal structure, certain metal oxides (such as, $WO_3$ or $MoO_3$) allow for interstitial doping of smaller (usually metal) ions (Figure 1.5a),[4,85] which generally leads to a substantial increase in free carrier density. Among these materials, tungsten oxides interstitially doped with alkali metal ions (*i.e.*, $M_yWO_{3-x}$, M={Li, Na, K, Cs, Rb}; with $0 \leq y \leq 0.33$), called alkali tungsten bronzes, have been the subject of numerous studies investigating their crystal and electronic structure, metallic conductivity, and optical and magnetic properties.[86–89] In particular, oxygen-deficient hexagonal cesium-doped tungsten oxide ($Cs_yWO_{3-x}$) NCs have gained significant attention in the nanophotonics research community owing to their

highly tunable LSPR resonances across the entire visible–NIR–MIR spectral region enabling a wide range of technological applications such as electrochromic smart windows, photocatalysis, and sensing.[90,91] Using density functional theory (DFT) calculation, Lee et al.[92] investigated the interstitial ion intercalation chemistry and fundamental optoelectronic properties of (hexagonal) $h$–Na:$WO_3$ and $h$-K:$WO_3$. They predicted that the introduction of $K^+$ ion into the hexagonal voids (B-site) of the host lattice is thermodynamically more favorable than that of $Na^+$, due to a larger electrostatic screening effect between the lattice O atoms by electron charge depletion effect along the M–M channel. In their DFT studies, Yang et al.[93] investigated the electronic structure of various mono-doped and co-doped alkali tungsten bronzes (*i.e.*, $A_zM_yWO_3$; {A,M}=alkali ion) and theoretically predicted a generally higher thermodynamic stability of the co-doped systems compared to the mono-doped ones. Additionally, the authors also predicted a significant shift of the Fermi level into the conduction band as a result of (co)doping, leading to metallic conductivity and enhanced optical absorption in the visible–NIR region, demonstrating the excellent applicability of these materials as NIR smart windows. Mattox et al.[94] reported the first colloidal synthesis protocol for interstitial $Cs^+$ doping of tungsten oxide NCs, using fixed amounts of metal chloride precursors and a mixture of oleic acid and oleylamine in specific molar ratios. With this, the authors obtained plasmonic hex-Cs:$WO_{3-x}$ nanoplatelets, pseudo-spheres, and cubes, exhibiting tunable dual-band LSPR resonances across the visible–NIR region. In their seminal work, Kim et al.[7] established a protocol for the synthetic modulation of aspect ratio (AR=NC height/width) of colloidal plasmonic hex–Cs:$WO_{3-x}$ NCs, yielding high-quality, shape and size-selective hex-Cs:$WO_{3-x}$ nanoplatelets (AR$\sim$0.3), iso-prisms (AR$\sim$1), and nanorods (AR$\sim$1.7). Using steady-state optical extinction spectroscopy and COMSOL simulations, the authors also investigated the origin of the AR-dependent LSPR band-splitting observed in the visible–NIR region. In hex-Cs:$WO_{3-x}$ NCs, the dual-band dipolar LSPR resonances (Figure 1.5b) have been assigned to arise from longitudinal ($LSPR_{\parallel}$) and transverse ($LSPR_{\perp}$) plasmon modes,[89] as a result of the different effective carrier mass ($m^*$), high-frequency permittivity ($\epsilon$) and damping factor ($\gamma$) along the prismatic (c-axis) and basal (a- and b-axis) planes of the NCs. Surprisingly, while the nanoplatelets (low AR) exhibited a large LSPR band splitting in the visible-NIR region, as expected, the dual-band LSPR absorption spectrum was also observed for iso-prisms (low AR). In the nanorods (high AR), the two LSPR modes were found to overlap, indicating that the spectral position of the LSPR absorption band for hex-Cs:$WO_3$ NCs is a result of the strong interplay between the shape and crystalline anisotropy.[7]

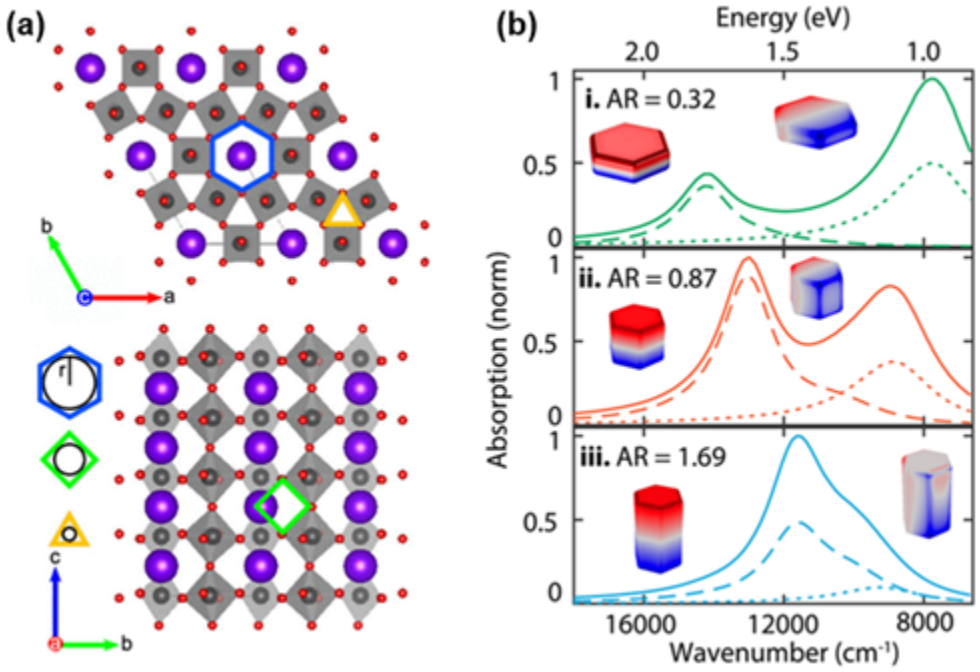



Figure 1.5: (a) Schematic representation of the basal plane (top panel) and prismatic plane (bottom panel) of *hex*-Cs:$WO_{3-x}$ NCs with hexagonal (blue), tetragonal (green), and trigonal (yellow) interstitial voids, respectively. Oxygen, cesium, and tungsten atoms are depicted as red, purple, and gray spheres, respectively. (b) AR-dependent LSPR band-splitting in *hex*-Cs:$WO_{3-x}$ nano-platelets (top panel), iso-prisms (middle panel), and rods (bottom panel). (a: Reprinted with permission from Zydlewsky et al.,[6] Copyright (2022) American Chemical Society. b: Reprinted with permission from Kim et al.,[7] Copyright (2016) American Chemical Society.)

Using spectroscopic ellipsometry and optical absorption spectroscopy, Machida et al.[8] reported a detailed study on the electronic structure of a series of alkali- and oxygen deficient $Cs_yWO_{3-x}$ NCs, presenting precise spectral deconvolution of the visible–NIR absorption bands into two anisotropic plasmon ($LSPR_{\parallel}$ and $LSPR_{\perp}$) and one polaron peaks (Figure 1.6a). Using DFT calculations, Yoshio and Adachi et al.[95] computationally reproduced the experimental dielectric function of alkali and oxygen deficient tungsten bronze NCs, suggesting the two-fold origin of the free carriers. On one hand, the electrons associated with charge compensation of $Cs^+$ dopants that occupy the W $d_{yz}$ and $d_{zx}$ orbitals (Figure 1.6c) become fully delocalized along the prismatic plane. On the other hand, electrons originating from oxygen vacancies are partially localized on the W $d_{xy}$ and $d_{x^2-y^2}$ orbitals (Figure 1.6b and d) which lie near the conduction band edge and are associated

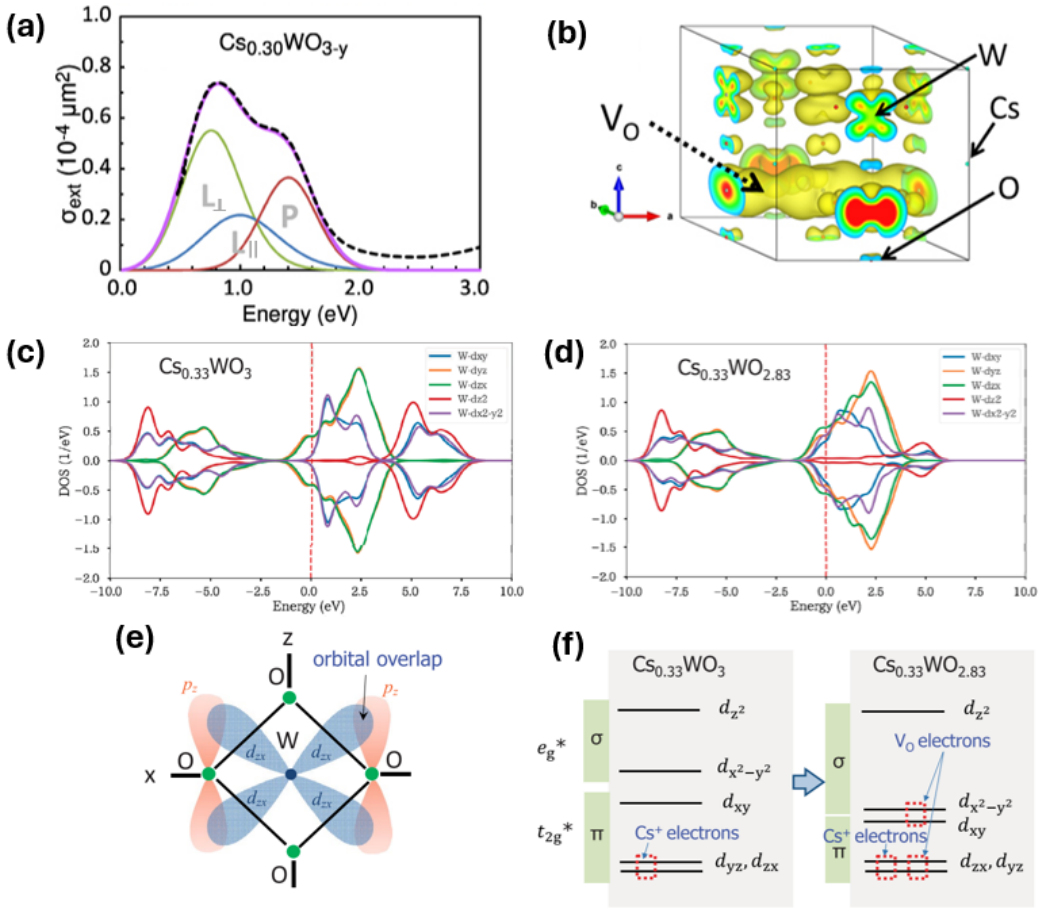



Figure 1.6: (a) Deconvolution of optical extinction spectrum of oxygen-deficient $Cs_{0.30}WO_{3-x}$ NCs exhibiting plasmonic band-splitting in the visible–NIR region with $LSPR_{\perp}$ and $LSPR_{\parallel}$ modes and polaronic (P) contributions. (b) Electron density distribution in the unit cell of $Cs_{0.30}WO_{2.67}$ NCs. (c) Total DOS of stoichiometric $Cs_{0.30}WO_3$ and (d) oxygen-deficient $Cs_{0.30}WO_{2.83}$ NCs. Red dashed line indicates Fermi level. (e) Scheme depicting the hybridization of W–d and O–p orbitals projected onto the $x$–$z$ plane in a $[WO_6]$ octahedron. (f) Molecular orbital diagrams of $Cs_{0.30}WO_3$ (left panel) and oxygen-deficient $Cs_{0.30}WO_{2.83}$ (right panel) NCs showing the W–d orbitals accommodating the $V_o$- and $Cs^+$-donated electrons. (a: Adapted with permission from Machida et al.,[8] Copyright (2019) AIP Publishing. c-f: Repreinted with permission from Machida et al.,[9] Copyright (2024) Springer Nature.)

with the basal plane. Using first principles DFT calculations, Machida and Adachi et al.[9] further elucidated the electronic structure of K, Rb, and Cs monodoped, oxygen-deficient alkali tungsten bronze NCs, revealing that W $d_{xy}$ and $d_{x^2-y^2}$ orbitals are strongly hybridized with O-p orbitals (Figure 1.6e), constructing $t_{2g}^*$ and $e_g^*$ states that form $\pi$ and $\sigma$ bonds (Figure 1.6f), respectively, in the [$WO_6$] octahedral building blocks.

#### 1.2.1.3 Aliovalent Doping

Aliovalent doping (*i.e.*, the substitutional incorporation of foreign heterovalent ions into the NC host lattice)[4] is another major chemical doping method developed for metal oxides in order to tune their free carrier density. Depending on the dopant valence state and energetic proximity of the dopant orbitals relative to the host lattice bands, aliovalent doping generally allows for introducing significant amount of additional free electrons into the conduction band (degenerate doping), leading to a corresponding upward shift of the Fermi level and widening of the optical bandgap ($E_{og}$) (Burstein–Moss shift) (Figure 1.7a) and a corresponding blue shifting of LSPR (Figure 1.7b).[11] Important to note, however, that although extrinsic doping of pure (undoped) metal oxide NCs initially increases the free electron concentration, further dopant incorporation beyond a critical level may lead to significant alterations to the electronic band structure and non-negligible electrostatic interactions between dopant ions and free carriers in the NCs.[96,97] For instance, the electric charge ($Z$) or orbital energy of the dopant can significantly influence the carrier damping and trapping *via* ionized impurity scattering ($\propto Z^2$), which reduces the overall mobility of the free electrons, and thus the LSPR intensity and Q-factor.[57] For instance, IMO or Ce:$In_2O_3$ NCs have been reported to show much narrower LSPR band width ($\Gamma$), and thus high Q-factor compared to that observed for Sn:$In_2O_3$ (ITO), Ti:$In_2O_3$ (TTO), or Sb:$In_2O_3$ (ATO) NCs. This was rationalized by the weaker hybridization between the dopant (Mo, Ce) valence orbitals and the CBM (In 5s, O 2p).[54,75,98] Furthermore, different dopant-concentration-dependent carrier effective mass, resulting in a more pronounced electrostatic screening of the free carriers from the ionized impurity scattering. In a separate study, Bhachu et al.[98] reported that in Mo:$In_2O_3$ (IMO) NCs, molybdenum is present predominantly as $Mo^{4+}$ ($4d^2$) (rather than $Mo^{6+}$ ($4d^0$)) possessing two strongly localized $t_{2g}$ up-spin states below and one $t_{2g}$ down-spin states above the CBM. This leads to an increased hybridization between dopant orbitals and CBM states and thus an enhanced carrier scattering. Schimpf et al.[99] also investigated the carrier scattering effects in photodoped ZnO and Al:ZnO NCs and reported a significantly greater enhancement of electron scattering and thus reduced LSPR energy and Q-factor in Al:ZnO NCs compared to photodoped ZnO NCs.[100] They attributed this observation to the strong electrostatic interaction between $Al^{3+}$ ion and free electrons in the CB.[101] Interestingly, aliovalent doping of the same lattice with different ions can also impact the density and mobility of free

carriers, hence influencing the LSPR band shape and energy. Such an effect was reported in CdO NCs doped with gallium (GCO), indium (ICO), aluminum (ACO), or tin (ICO) NCs, wherein the $In^{3+}$ doping caused a significant bathochromic shift of LSPR compared to $Sn^{4+}$ doping, and only a negligible LSPR peak shift was observed when doping with $Ga^{3+}$ or $Al^{3+}$ (Figure 1.7c).[12] Beyond the dopant charge ($Z$), the mobility and scattering of free carriers also correlate to the dopant ionic radius ($r$). For instance, Dy:CdO NCs have been reported to exhibit a milder lattice distortion compared to vacancy-doped CdO NCs due to the large difference in ionic radii between dysprosium and oxygen, resulting in a stronger LSPR response in Dy:CdO.[102]

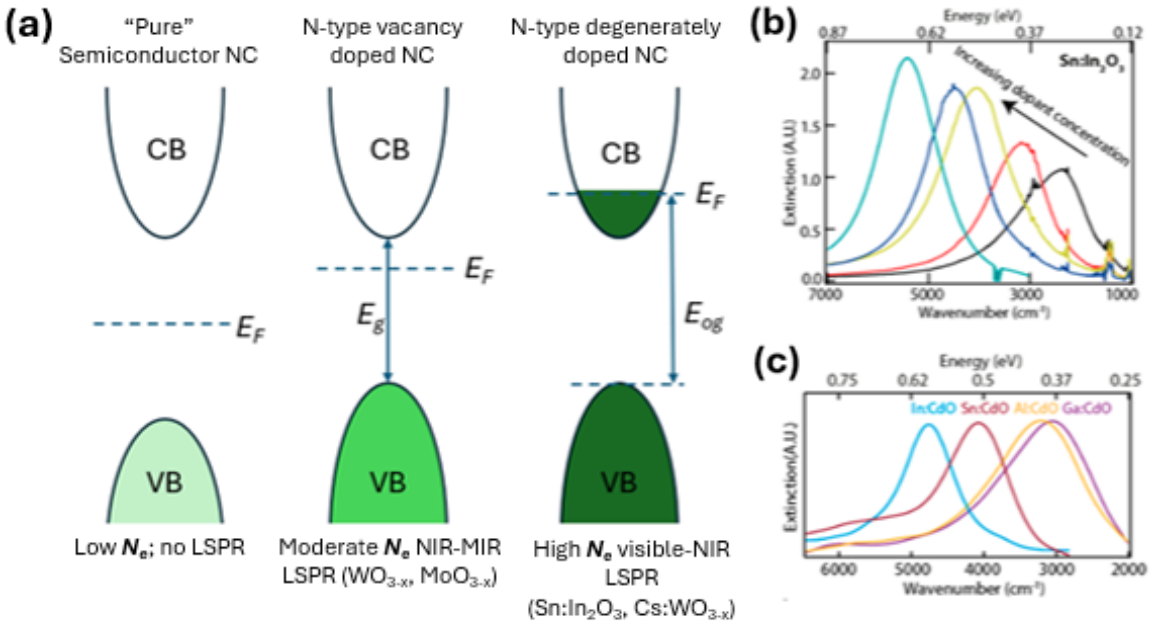



Figure 1.7: (a) Schematic representation of the CB filling (and Burstein-Moss shift) of degenerately-doped semiconductor NCs. (b) Modulation of free carrier density and thus LSPR energy of $Sn:In_2O_3$ NCs. (c) Impact of various aliovalent dopant ions ($In^{3+}$, $Sn^{4+}$, $Al^{3+}$, and $Ga^{3+}$) on the LSPR energy of CdO NCs. (a: Adapted with permission from,[10] Copyright (2023) Elsevier. b: Reprinted with permission from Agrawal et al.,[11] Copyright (2017) Annual Reviews. c: Reprinted with permission from Diroll et al.,[12] Copyirght (2014) American Chemical Society.)

Interestingly, the free carrier density, carrier mobility, and LSPR factors can be further enhanced via aliovalent co-doping, *i.e.*, the incorporation of multiple different heterovalent

ions into the NCs lattice. Xingchen et al.[103] reported a significant enhancement in carrier mobility and carrier density (ca. 20%) achieved via co-doping colloidal In:CdO NCs with $F^-$ ion, resulting in blue shift of LSPR and an increase in the Q-factor. Meanwhile, in $In_2O_3$ NCs co-doped with $Sn^{4+}$ and $F^-$ ion (F:ITO), the $F^-$ ion was found to occupy oxygen sites in the lattice ($F_O^\bullet$), resulting in a decrease in $V_O^{\bullet\bullet}$, but an increase in free carrier concentrations due to the negative charge of $F^-$.[104] Since the ionized impurity scattering quadratically scales with dopant ionic charge ($\propto Z^2$), the $F_O^\bullet$ defects are expected to lead to weaker carrier scattering compared to ionized oxygen vacancies ($V_O^{\bullet\bullet}$, resulting in reduced carrier damping ($\Gamma$) and enhanced LSPR Q-factor. It is important to note, however, that doping plasmonic semiconductor NCs with open–subshell dopant ions (e.g., $Mo^{5+}$, $Mn^{3+}$, $Fe^{3+}$, or $Cr^{3+}$) may not necessarily increase the free carrier density, but instead lead to changes in the magnetic properties (*via* the introduction of paramagnetic d electrons into the lattice) in addition to the plasmonic behavior of the NCs.[105]

### 1.2.2 Static Modulation of LSPR in Plasmonic Semiconductor Metal Oxide NCs

#### 1.2.2.1 Impact of Spatial Distribution of Dopants in NCs

Beyond the influence of dopant incorporation alone (*vide supra*), the spatial distribution of dopants within doped plasmonic semiconductor metal oxide NCs also plays a critical role in modulating the host lattice–free carrier interactions, and thus the LSPR properties. For instance, using a slow precursor injection method, Lounis et al.[73,106] precisely controlled the radial distribution of $Sn^{4+}$ dopants in ITO NCs with homogeneous or surface-rich $Sn^{4+}$ dopant profiles. Interestingly, in the case of homogeneous $Sn^{4+}$ distribution, ITO NCs exhibited a strongly asymmetric LSPR line shape, attributed to strong frequency-dependent carrier scattering. However, in the surface-rich case, a more symmetric LSPR line shape was observed due to negligible carrier scattering. These results suggest that $Sn^{4+}$ dopants distributed near the NC surface (surface-rich doping) can still effectively donate electrons to the conduction band while remaining spatially separated from the primary free conduction pathways within the bulk of NCs, resulting in reduced ionized impurity scattering and LSPR damping. This study was further extended by Crockett et al.[107] and Jansons et al.[108] who have conducted a systematic investigation into the influence of radial $Sn^{4+}$ dopant distribution on the LSPR properties of spherical core/shell $In_2O_3$–ITO or core/shell ITO-$In_2O_3$ NCs. By employing a slow-growth synthesis approach, they selectively confined $Sn^{4+}$ dopants either to the shell (core/shell $In_2O_3$-ITO) or core (core/shell ITO–$In_2O_3$) region of the NCs. In the case of core/shell $In_2O_3$-ITO NCs, the presence of dopants near the NC surface initially led to a blueshift of LSPR due to increased carrier density and carrier

activation. Whereas in the case of core/shell ITO–$In_2O_3$ NCs, after an initial blueshift attributed to the passivation of surface trap states reducing $Sn^{4+}$ dopant activation, a continuous redshift of LSPR was observed owing to the decrease of Ne as a function of $In_2O_3$ shell thickness. In both core/shell configurations, reduced LSPR damping was observed compared to homogeneously doped structures, indicating spatial segregation of $Sn^{4+}$ dopant either to the core or shell of the NCs to be a viable route for minimizing carrier scattering and thus improve NFE.

In addition to dopant concentration and spatial distribution, surface-related electronic effects introduce further complexity in shaping the optical behavior of doped metal oxide NCs.[109,110] prominent example is the formation of a near-surface zone with suppressed free carrier density, called a surface depletion layer. This region emerges due to Fermi level pinning by surface states, commonly induced by adsorbed species such as hydroxyl groups or organic ligands, leading to band bending that drives charge carriers away from the surface toward the NC core. As a result, a portion of the NC becomes effectively non-conductive, reducing the free carrier population available to sustain LSPR absorption and thereby influencing the $\omega_p$, LSPR intensity and linewidth. Since the degree of band bending, and thus the width of depletion layer, is strongly influenced by dopant concentration and spatial distribution, plasmonic NCs exhibiting such depletion can be conceptually described as core–shell structures with a conductive core and a plasmonically inactive shell, wherein the resulting spatial inhomogeneity weakens electromagnetic coupling, leading to a redshifted LSPR and reduced sensitivity to changes in the surrounding dielectric environment.

#### 1.2.2.2 Impact of Nanocrystal Geometry

Owing to the critical influence of NC size and shape on the surface states and defect chemistry of plasmonic compound semiconductor NCs, static modulation of free carrier density and thus LSPR properties of plasmonic metal oxide NCs can also be achieved via precise control of NC geometry. Beyond hex-Cs:$WO_{3-x}$ NCs exhibiting shape- and crystalline anisotropy and tunable dual-band LSPR depending on NC aspect ratio[7] (see Section 1.2.1.2.), other plasmonic semiconductor NC systems also exhibit morphology-controlled LSPR.[111–114] For instance, in two separate studies Cho et al.[115] investigated the electronic structure and LSPR absorption of FITO NCs. They found that $Sn^{4+}$ and $F^-$ co-doping, on one hand, increases free carrier density as expected, furthermore, it also stabilizes the (100) facets of $In_2O_3$, leading to cube morphology of the NCs. Interestingly, FITO nanocubes exhibit dipolar multiband LSPR in the visible–NIR region, associated to charge accumulation at the corners, edges, and faces of the nanocubes. Finite element method simulations and experimental studies suggested a particularly strong NFE and high sensitivity to changes dielectric environment for the corner modes, which was attributed to the non-uniformity of depletion layer most strongly impacting the corners and faces of the

FITO nanocubes. Agrawal et al.[116] observed size- and shape-dependent LSPR and NFE in faceted cube-octahedral ICO NCs. Similarly to FITO, ICO cube-octahedral NCs also exhibited multi-band LSPR resonances in the visible-NIR region attributed to the corner, face, and edge modes, providing a robust framework for controlling and engineering optical functionality in semiconductor metal oxide NCs.

## 1.3 Magneto-Optical Properties of Plasmonic Semiconductor NCs

### 1.3.1 Magnetic Circular Dichroism Spectroscopy of LSPR

Modulating LSPR with external stimuli provides a direct and powerful way to control optical properties of plasmonic semiconductor NCs, making it essential for applications in sensing, photonics, and nanotechnology. Interestingly, since localized surface plasmons are generated by resonant photon absorption, not only the frequency but the polarization of the coherently oscillating free carriers can also be manipulated in plasmonic nanostructures.[19,117] For instance, when a localized surface plasmon is resonantly excited by left and right circularly polarized light (LCP and RCP, respectively), the free carriers of charge $q$ experience an electric Lorentz force ($\vec{F_E}$) imparted by the electric vector component of the incident electromagnetic field, giving rise to the carriers' cyclotron oscillatory motion in opposite directions (Figure 1.9a).[117] As a result, two degenerate cyclotron plasmonic modes of opposite helicity (LCP ($\sigma^-$); and RCP ($\sigma^+$), respectively) and equal resonant frequencies ($\omega_0$) are generated. However, in the presence of a homogeneous, uniform, and nonzero external magnetic field ($\vec{B} \neq 0$) applied parallel to the direction of light propagation (called Faraday configuration), an additional magnetic Lorentz force ($\vec{F_B}$) acting on the cyclotron free carriers arises, lifting the degeneracy of the cyclotron magneto-plasmonic modes generated,[118] based on eq 1.17:

$$\vec{F_{net}} = \vec{F_E} + \vec{F_B} = m^*(\frac{d\vec{v}}{dt}) + \gamma m^* \vec{v} = q(\vec{E} + (\vec{v} \times \vec{B})) \tag{1.17}$$

where $\vec{B}$ is the external magnetic field strength; $q$, $\vec{V}$, and $m^*$, respectively, are the charge ($q = -|e|$ for conduction band electrons ($e^-_{CB}$), and $q = +|e|$ for valance band holes $h^+_{VB}$)), velocity, and effective mass of the carriers, and $\gamma$ is the damping factor, respectively. Based on the relative orientation of $\vec{F_e}$ with respect to the $\vec{F_B}$ induced in $\vec{B} \neq 0$, the angular frequency of the non-degenerate cyclotron magneto-plasmonic modes will shift ($\omega_B^{\pm}$) relative to the that of the zero-field cyclotron oscillations ($\omega_0$) (Figure 1.9b), as in eq 1.18 below:

$$\omega_B^{\pm} = \omega_0 \pm \frac{qB}{2m^*} = \omega_0 \pm \frac{\omega_c}{2} \tag{1.18}$$

where $\omega_c = qB/m^*$ is the classical cyclotron frequency of charge carriers, respectively. The magnetic-field-induced (so-called normal Zeeman) splitting of the cyclotron magneto-plasmonic modes is a linear function of the applied magnetic field strength and can be detected using magnetic circular dichroism (MCD) spectroscopy, which measures the differential absorption of LCP and RCP light (*i.e.*, $\Delta A = A_{LCP} - A_{RCP}$) in an external magnetic field, Importantly, since the cyclotron magneto-plasmonic modes are selective for either LCP ($\sigma^-$) or RCP ($\sigma^+$) light, their resulting MCD signal will have a derivative shape in angular frequency space,[117,118] as depicted in Figure 1.9b.

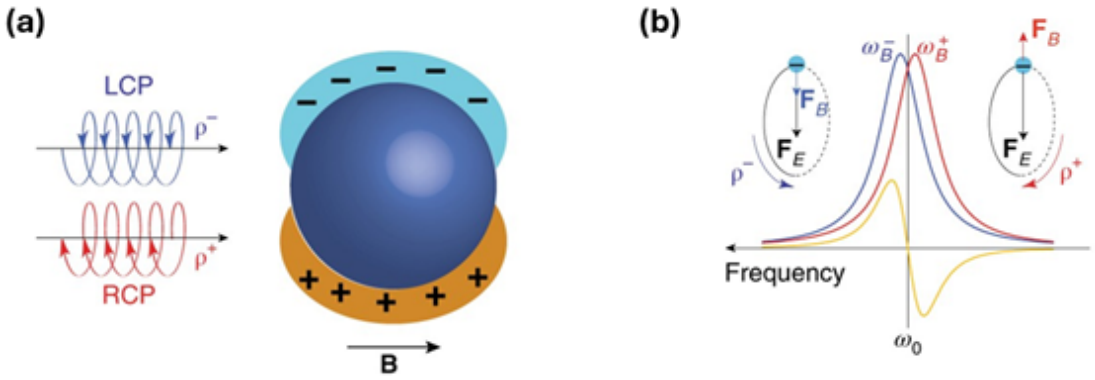



Figure 1.8: (a) Cartoon depicting the cyclotron free carrier oscillations generated by the sequential absorption of LCP (blue spiral arrows) and RCP light (red spiral arrows) propagating parallel to a nonzero, homogeneous, uniform external magnetic field ($\vec{B} \neq 0$). (b) Schematic representation of the derivative-shape MCD spectral response arising from cyclotron free carriers in $\vec{B} \neq 0$. (Reprinted with permission from Yin et al.,[13] Copyright (2018) Springer Nature.)

In their seminal work, Hartstein et al.[14] conducted variable-field MCD spectroscopy measurements and first reported phenomenological observations of characteristic LSPR magneto-optical responses of plasmonic colloidal n-type ZnO, n-type Sn:$In_2O_3$ (ITO), and p-type $Cu_{2-x}Se$ NCs, as model systems for plasmonic nanostructures. Shown in Figure 1.9, the authors observed full derivative-shape MCD signal for the $Cu_{2-x}Se$ NCs (green trace), meanwhile for ITO (orange trace) and ZnO (blue trace) NCs only the onset of MCD signal was recorded due to detector limitations in the visible–NIR region. Owing to the opposite

sign of the majority charge carriers in n-ITO and n-ZnO ($e^-_{CB}$) compared to in p-$Cu_{2-x}Se$ NCs ($h^+_{VB}$), the leading edge of the plasmonic MCD signals appeared with opposite signs, as explained by eq 1.17 (*vide supra*). Owing to their metallic nature, plasmonic Au (red traces) and Ag (gray traces) NCs also exhibit derivative-shape MCD signals with a leading negative edge albeit at higher energies in the visible region relative to those of ZnO, ITO or $Cu_{2-x}Se$ NCs due to their intrinsically higher carrier densities ($N_e^{(Au,Ag)} \sim 10^{22}$ carrier/cm$^3$ and $N_e^{(ITO,ZnO,Cu_{2-x}Se)} \sim 10^{20-21}$ carrier/cm$^3$).

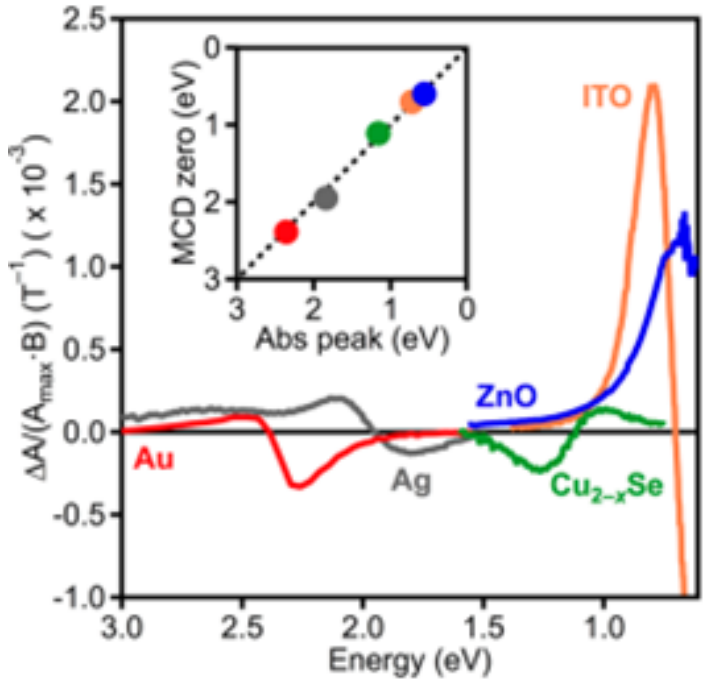



Figure 1.9: Normalized variable-field MCD spectra of the LSPR region of n-ZnO (d=3.1 nm), n-ITO (d=5.5 nm), p-$Cu_{2-x}Se$ (d=16.9 nm), Au (d=12.8 nm), and Ag (d=50 nm) NCs. Inset: MCD crossover energies plotted as a function of absorption peak energies. (Reprinted with permission from Hartstein et al.,[14] Copyright (2017) American Chemical Society.)

#### 1.3.1.1 Intrinsic Plasmon-Exciton Interactions

As presented in the previous section, magneto-plasmonic modes in semiconductor NCs constitute quantized collective free carrier excitations whose frequency dispersion and signal polarization are directly governed by magnetic-field-induced lifting of the mode degeneracy. The ability to modulate the orientation and magnitude of the angular momentum of cyclotron free carrier oscillations *via* circularly polarized light or external magnetic fields provides a compelling framework for investigating the influence of cyclotron magneto-plasmon modes, as a collective electronic degree of freedom, on excitonic states in plasmonic semiconductor NCs. Intrinsic plasmon–exciton interactions in semiconductor NCs originates from the coexistence, mutual perturbation and coupling of two fundamentally different and energetically non-resonant electronic excitations confined within the same nanostructure (hence the "intrinsic" nature). Namely, these are the (*i*) collective intraband LSPR oscillations of free carriers, and (*ii*) the exciton (*i.e.*, Coulombically-bound electron–hole pair) as interband (band-to-band) transition. In their seminal work, Yin et al.[13] presented the first experimental evidence for intrinsic plasmon-exciton coupling interactions in degenerately doped plasmonic compound semiconductor NCs, using variable-field and variable-temperature MCD spectroscopy and colloidal 10% Sn:$In_2O_3$ NCs, as model system for the plasmonic semiconductor nanostructure. Shown in Figure 1.10a, they observed negatively polarized variable-field MCD bands (bottom panel), the peak minima of which perfectly coincided with the inflection point (∼4.2 eV) of the interband absorption region (∼3.8–6.1 eV) (top panel), thus evidencing the excitonic origin of these MCD signals. Importantly, for the ITO NCs no optical absorption signal attributed to LSPR was detected in the spectral vicinity of the excitonic region, thus excluding the possibility of the spectral overlap and hence the resonant nature of plasmon–exciton coupling interactions. Notably, the monochromatic excitonic MCD peak intensities exhibited a linear dependence on the external magnetic field strength ($B$) (Figure 1.10b), and complete temperature independent nature (Figure 1.10c). Importantly, in the absence of LSPR resonances such as in stoichiometric $In_2O_3$ NCs (Figure 1.10a middle panel), no excitonic MCD signal was detected even at the highest magnetic fields (B = 7 T). For instance, in degenerately doped plasmonic ITO NCs wherein the conduction band is highly populated by free electrons, the cyclotron free electrons near the Fermi level can transfer their angular momentum to the exciton (obeying the corresponding conservation law), thus leading to cyclotron free carrier-induced Zeeman splitting of the NC excited states ($M_j = \pm 1$ in Figure 1.10d).

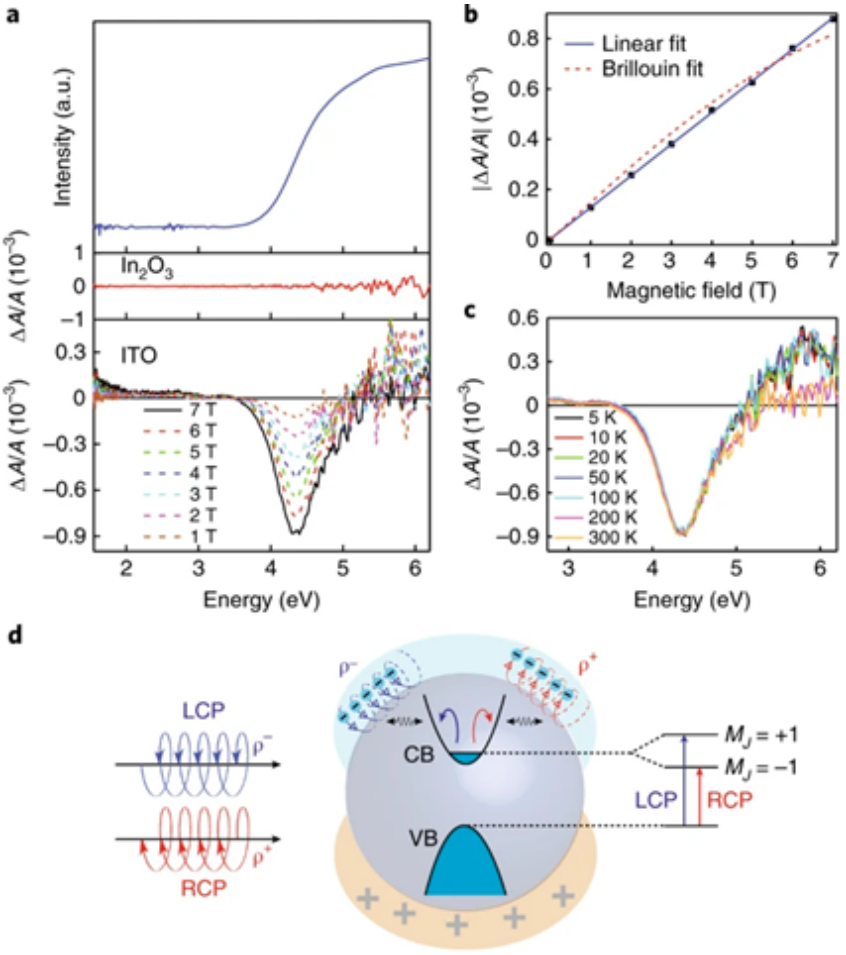



Figure 1.10: (a) Excitonic absorption spectrum (300 K, 0 T) of plasmonic 10% Sn:$In_2O_3$ NCs (blue trace, top panel) with corresponding variable-field MCD spectra collected between 1–7 T range at 5 K (bottom panel); and MCD spectrum of plasmonic $In_2O_3$ NCs collected at 300 K, 7 T (middle panel). (b) Plot of monochromatic excitonic MCD peak intensities (from (a)) as a function of magnetic field strength. Solid line (blue trace) and dashed curve (red trace) correspond to linear and Brillouin fitting, respectively. (c) Variable-temperature MCD spectra of 10% Sn:$In_2O_3$ NCs, showing the temperature independent nature of plasmon-induced excitonic MCD signals. (d) Schematic depiction of the cyclotron free carrier-induced excitonic Zeeman splitting mechanism, with $M_j = \pm 1$ excited states. (Reprinted with permission from Yin et al.,[13] Copyright (2018) Springer Nature.)

To explain these phenomenological observations, in their separate paper Yin et al.[15] modeled the magneto-plasmonic modes as classical cyclotron oscillations of free charge carriers possessing a total orbital angular momentum ($L_z$) and cyclotron radius ($\sigma_{cyclo}$), the magnitudes of which depend on the magnetic field strength ($B$), as quantified in eqn 1.19 and eqn 1.20, respectively. In fact, $L_z$ consists of the ($i$) cyclotron angular momentum component ($L_z^{cyclo}$) of the classical orbit formed by the free carrier oscillations, and the ($ii$) canonical ($L_z^{can}$) and ($iii$) diamagnetic ($L_z^{dia}$) components associated with the electron rotation relative to the center of mass of the wavefunction, according to eqs. 1.19-1.21:

$$L_z = L_z^{cyclo} + L_z^{can} + L_z^{dia} = \frac{2}{\omega_c} E_{rot} + (sign(B)(2n + |l| + 1)\hbar) \tag{1.19}$$

$$L_z^{cyclo} = m^* \omega_c \sigma_{cyclo}^2 \tag{1.20}$$

$$\sigma_{cyclo} = \frac{m^* \nu_F}{|q|B} \tag{1.21}$$

where $E_{rot}$ is the rotational kinetic energy of free charge carriers, $n$ is the number of radial nodes in the electronic wavefunction, $l$ is the canonical orbital angular momentum quantum number, and $\nu_F$ is the Fermi velocity of carriers. Because of their opposite electric charges, the direction of cyclotron oscillation associated with the free electrons and holes are oriented antiparallel under the same magnetic field orientation, which causes the sign reversal of the LSPR MCD signal (*vide supra*). Importantly, for plasmonic semiconductor NCs possessing sufficiently high carrier densities the excitonic MCD signal follows the same behavior as the LSPR MCD signal, indicating the interrelated nature of the two phenomena.

Although the underlying mechanism of intrinsic cyclotron free carrier-induced excitonic Zeeman splitting has remained the subject of ongoing investigation, theoretical models suggest the possibility of involvement of chiral optical phonons (*i.e.*, quantized lattice vibrations) as mediator of the plasmon–exciton angular momentum transfer process.[13,14] Nonethless, by utilizing the quantized orbital angular momentum of free-carrier oscillations as a controllable quantum degree of freedom, the emerging field of plasmontronics establishes a novel platform for next-generation quantum information and optoelectronic technologies with coherence, tunability, and controllable helicity.[41]

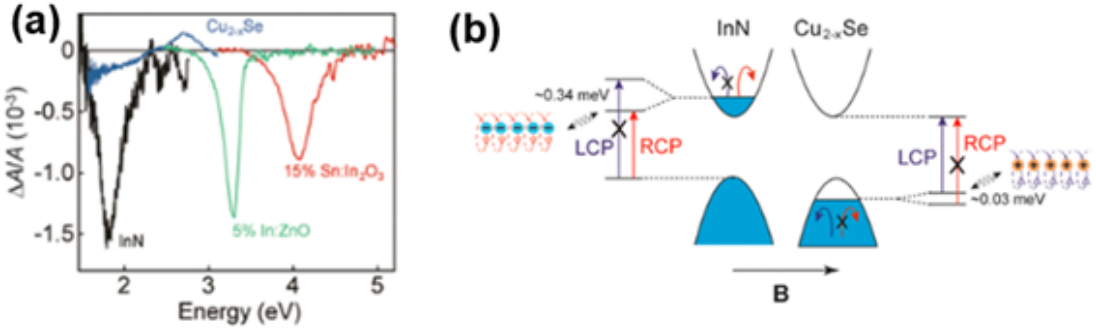



Figure 1.11: (a) Excitonic MCD bands of colloidal n-type plasmonic InN, 5% Sn:$In_2O_3$, 15% Sn:ZnO, and p-type $Cu_{2-x}Se$ NCs. Under the same magnetic field orientation, the excitonic MCD signals are oppositely polarized for p and n-type plasmonic semiconductor NCs depending on the charge of the majority charge carrier (*i.e.*, $q_e = -|e|$, and $q_h = +|e|$). (b) Schematic representation of the cyclotron free carrier-induced excitonic Zeeman splitting in n-type (left) and p-type (right) plasmonic semiconductor NCs. (Reprinted with permission from Yin et al.,[15] Copyright (2022) American Chemical Society.)

#### 1.3.1.2 Magnetic Circular Dichroism and Excitonic Interactions of Localized Charge Carriers

In contrast to degenerately doped plasmonic semiconductor NCs, the LSPR absorption in non-stoichiometric plasmonic binary metal oxide (e.g., $WO_{3-x}$, $MoO_{3-x}$, $TiO_{2-x}$, etc.) originates from charge compensating electrons generated by the presence of oxygen vacancies (see Section 1.2.1.1.).[73] These electrons, however, can become partially localized on the d–orbitals of neighboring metal ion centers (e.g., Mo/W) or donor-defects (e.g., oxygen vacancies), generating localized paramagnetic ground electronic states ($W^{5+}$, $Mo^{5+}$, $Ti^{3+}$: $d^1$).[4,11] The localized carriers, in turn, introduce a distinct type of magnetic exchange interaction that fundamentally differs from that presented for the collective free carrier oscillations (*vide supra*).[119] Importantly, the spin orientation of localized carriers is sensitive to the external magnetic field, exhibiting Curie-type paramagnetic behavior. In an external magnetic field, the localized carriers in the ground state undergo spin-induced (anomalous) Zeeman splitting, thus introducing a manifold of ($M_J$) states, which interact with the NC excited states via spin exchange interactions. The variable-field magneto-optical response attributed to spin-induced excitonic Zeeman splitting was observed in shape-uniform plasmonic colloidal IMO (0.3% $Mo^{5+}$) NCs (Figure 1.12a).[13] Shown in Figure 1.12c, the inflection point of the steady-state optical absorption band assigned to the interband transition in IMO NCs perfectly coincides with the MCD bands detected, indi-

cating the excitonic nature of these transitions. However, unlike in ITO NCs (Figure 1.10a), IMO NCs exhibit a more complex excitonic MCD band structure ($\sim$ 3.1–4.9 eV range) composed of derivative-shape signals (Figure 1.12c bottom panel) instead of complete band polarization. (Importantly, similarly to IMO, other diluted magnetic semiconductor NCs such as $\{W^{5+}$, $Co^{2+}$, $Ni^{2+}\}$:$In_2O_3$,[120] or $Mn^{2+}$:CdSe NCs also exhibit derivative-shape excitnonic MCD signals due to the magnetic interactions between localized spin and exciton.[121]) Notably, the monochromatic excitonic MCD peak intensity recorded at 3.9 eV of IMO NCs exhibit a purely linear magnetic field dependence (Figure 1.12d) yet Curie-Weiss type temperature dependent behavior characteristic to localized paramagnetic electrons. This magneto-optical behavior and MCD spectral response is a manifestation of the coexistence of the plasmon–induced and spin-induced (anomalous) Zeeman splitting of the NCs band edge states (at $\vec{B} \neq 0$): specifically, ($i$) the conduction band free electrons undergoing cyclotron oscillations transfer their angular momentum to the exciton, leading to plasmon–induced Zeeman splitting of the NC excited states (Figure 1.12e $M_J = \pm 1$), and ($ii$) the paramagnetic electrons localized on $Mo^{5+}$ ($d^1$) ions cause the spin-induced Zeeman splitting of both the ground and excited band edge states of the NCs (Figure 1.12e $M_J = \{\pm 1/2, \pm 3/2\}$), thus creating a ground and excited state manifold with several allowed transitions (with selection rule: $\Delta M_J = n | n \in \mathbb{N}$).

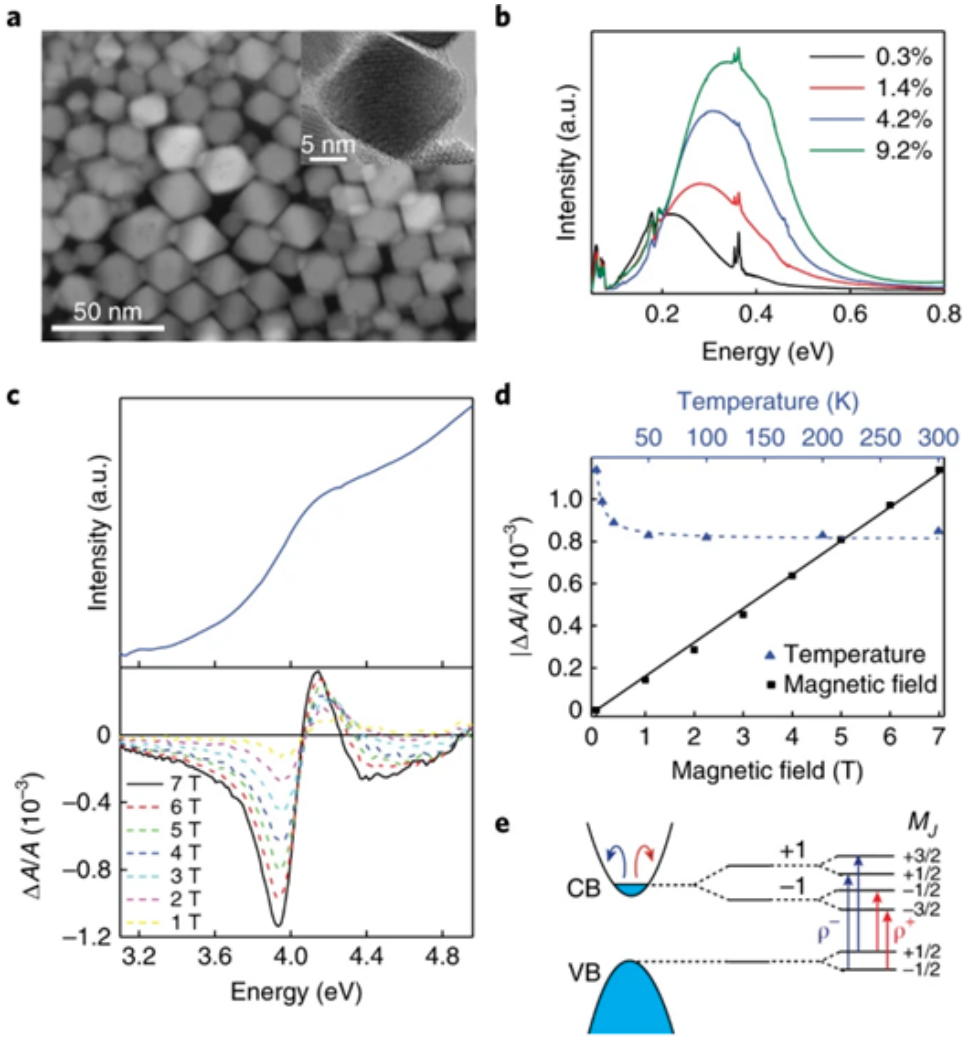



Figure 1.12: (a) Scanning electron micrograph of colloidal IMO NCs (inset: lattice resolved TEM micrograph). (b) Steady-state optical extinction spectra of the LSPR region of IMO NCs with different Mo dopant concentrations. (c) Steady-state excitonic absorption (top panel) and variable–field MCD spectra (bottom panel) of IMO NCs collected at 5 K. (d) Magnetic field dependence of monochromatic excitonic MCD signals (black markers) at 3.93 eV from (a), along with its temperature dependence (blue markers). (e) Excitonic Zeeman splitting caused by a mixture of plasmon–induced splitting ($M_J = \pm 1$) and spin–induced Zeeman splitting ($M_J^{ground} = \{\pm 1/2\}$; $M_J^{excited} = \{\pm 1/2, \pm 3/2\}$). (Reprinted with permission from Yin et al.,[13] Copyright (2018) Springer Nature.)

## 1.4 Photonic Applications of Plasmonic Semiconductor Metal Oxide NCs

### 1.4.1 Semiconductor-Based Photodetectors

Over the past few decades, there has been an increasing demand for photodetection technologies capable of sensing light across a wide spectral range, motivated by applications such as optical communication, optoelectronics,[122] quantum computing,[32,123] spectroscopy,[124] environmental monitoring,[125] and thermal and bio-imaging.[126] In particular, semiconductor-based NIR-MIR photodetector devices have attracted significant technological attention,[127–129] as these wavelengths carry critical information related to molecular vibrations, thermal radiation, and low-energy electronic transitions, utilized in some form by these aforementioned applications.

The general operation principle of photodetector devices involves three sequential processes, namely the (*i*) photoexcitation and generation of hot carriers by incident electromagnetic radiation, (*ii*) the separation of photogenerated charge carriers, and (*iii*) transportation and conversion of separated charge carriers into electrical signal output.[130] Upon illuminating a semiconductor ($h\nu \geq E_g$), the photogenerated free electrons and holes can move in opposite directions under the influence of an electric field, either externally applied or inherently present within the device material. Depending on the origin of the electric field responsible for the charge carrier separation, photodetector devices can be classified into photoconductive or photovoltaic devices.[131] In photoconductive devices, a semiconductor layer is equipped with two ohmic contacts (generally metal–semiconductor heterointerfaces), and the electric field necessary for charge carrier transport and collection is established by a small external bias applied across the contacts. In contrast, photovoltaic devices rely on built-in electric fields (*i.e.*, space charge region) at the junctions (generally semiconductor-semiconductor heterointerfaces) to achieve carrier separation, eliminating or reducing the need for an applied external bias. This latter category includes conventional p-n junction photodiodes, p-i-n structures where an intrinsic insulating layer enhances absorption and carrier collection, and Schottky-based devices, including both Schottky barrier and metal–semiconductor–metal photodetectors.[132]

#### 1.4.1.1 Structure and Operation Principle of Conventional MSM Photodetectors

Metal-semiconductor-metal (MSM) photodetectors are a prominent class of optoelectronic devices that utilize a semiconductor (S) layer integrated between two metal (M)

contacts, forming back-to-back Schottky junctions at the heterointerfaces.[16] The internal electric fields established at these junctions enable efficient separation and collection of photogenerated charge carriers, often requiring only a small reverse and forward bias ($V_b$) at the two metal–semiconductor interfaces for operation. In conventional MSM photodetectors, the semiconductor component (generally intrinsic semiconductor with low electrical conductivity and capacitive charging, and high chemical purity) constitutes the primary photoactive medium, absorbing incident radiation near the reverse-biased interface. Upon illumination, the photogenerated charge carriers are collected at the metal electrodes forming the forward-bias Schottky junction interface.[132]

The practical realization and optimization of MSM photodetector devices is fundamentally enabled by advanced semiconductor fabrication techniques, most notably molecular beam epitaxy and photolithography. Molecular beam epitaxy (MBE) provides one of the most powerful platforms for the growth of high-quality semiconductor heterostructures with precise control over layer composition and thickness.[133,134] In parallel, photolithography enables the precise engineering of spatial configuration (*i.e.*, "patterning") of metallic contacts and photoactive surface regions. The combination of MBE and photolithography allow for the fabrication of diverse MSM device geometries, such as planar or vertical structures (Figure 1.13), wherein the spatial orientation and arrangement of electrodes relative to the semiconductor absorption region can be tailored to modulate electronic band structure, carrier transport pathways, and thus optical properties of the individual layers of the MSM heterostructures.[16] In the planar device geometry (Figure 1.13a), the metal contacts are generally arranged as interdigitated (i.e., comb-like parallel strips) on the surface of the top semiconductor surface, enabling direct exposure of the active layer to incident light and facilitating efficient photocarrier generation. Whereas the vertical device geometry (Figure 1.13b) is a sandwich-like heterostructure consisting of a semiconductor layer positioned between top and bottom metal electrodes, whereby the upper metal electrode is typically fabricated with reduced thickness or sufficient optical transparency to allow NIR-MIR light penetration into the photoactive region.[135]

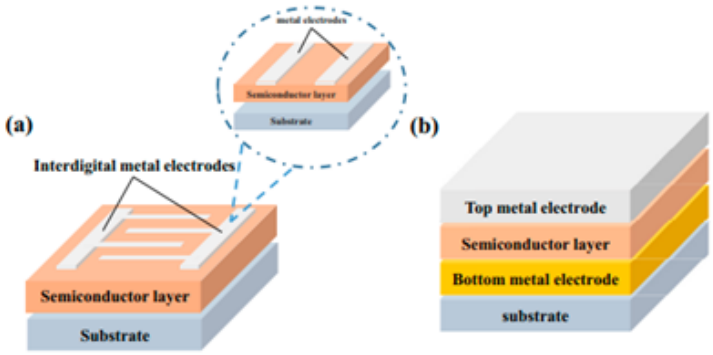



Figure 1.13: Schematic representation of MSM photodetectors with (a) planar devices geometry with interdigitated metal electrodes depicted as gray stripes on top of semiconductor photoactive layer. (b) Vertical device geometry consisting of a sandwich-like metal-semiconductor-metal heterostructure situated on top of a substrate. (Reprinted with permission from Shi et al.,[16] Copyright (2021) John Wiley and Sons.)

One of the most widely used material platforms for MSM-based NIR-MIR photodetection are heterostructures consisting of III-V ternary alloys epitaxially grown on wide bandgap semiconductors.[136] A common example is n-InGaAs/InP heterostructure,[137] wherein the narrow and direct bandgap of InGaAs ($E_g =\sim 0.57$ eV) enables efficient photon absorption across the NIR spectral region ($\sim 900-1700$ nm), while its lattice compatibility with wide bandgap InP ($E_g = 1.47$ eV) allows for the growth of high-quality (low defect density) epitaxial InGaAs layers. Despite its manufacturing simplicity, a major drawback of InGaAs/InP heterostructures lies in the relatively low Schottky barrier ($\phi_B^{InGaAs/InP)} \approx 0.2$ eV),[138] which results in a nonnegligible dark current even under low applied biases. To overcome this limitation, various barrier enhancement strategies have been developed, including the epitaxial growth of a thin, undoped, lattice-matched InAlAs layer on InGaAs, using organo-metallic chemical vapor deposition (OMCVD) or MBE methods,[139,140] resulting in sufficient increase of Schottky barrier at the heterointerfaces ($\Delta\phi_{InAlAs/InGaAs} =\sim 0.8$ eV) and thus minimization of dark current.[136]

#### 1.4.1.2 Plasmon-Enhanced NIR-MIR Photodetectors

Integrating plasmonic nanostructures into the active regions of photodetectors provides a powerful pathway to enhancing NIR–MIR light detection beyond the limits of conventional photodetectors (*vide supra*). One of the primary mechanisms underlying photoresponse improvement in plasmonic photodetectors involves the plasmon-induced near-field enhancement effect. This is because at resonant optical excitations, plasmonic nanostruc-

tures act as optical antennas (resonators) that concentrate and confine incident light into nanoscale volumes, resulting in local electromagnetic field densities around the nanostructure that are orders of magnitude higher than the incident field, the energy of which can facilitate enhanced free carrier generation. Importantly, numerous optoelectronic applications require not only enhanced detection of optical signals but also the targeted transport of photons between specific parts within the photodevice. In this context, plasmonic waveguides and gratings serve as efficient photon channels and couplers, respectively, utilizing surface plasmon polaritons (*i.e.*, propagating charge carrier oscillations along non-confined metal–dielectric interfaces) as quantized mediators of optical energy.

Importantly, upon resonant photon absorption, plasmons can undergo non-radiative decay *via* Landau damping ($\sim$ 100 fs), generating hot carriers. Since hot carriers populate energy levels above the Fermi level of the plasmonic nanostructure, they can be injected into the adjacent semiconductor when their kinetic energy is higher than Schottky barrier ($\phi_B$) and the tangential momentum continuity conditions are satisfied. Therefore, under applied bias the hot-carrier-induced enhancement of photocurrent can be determined from the increase in electrical current under illumination relative to the dark state.

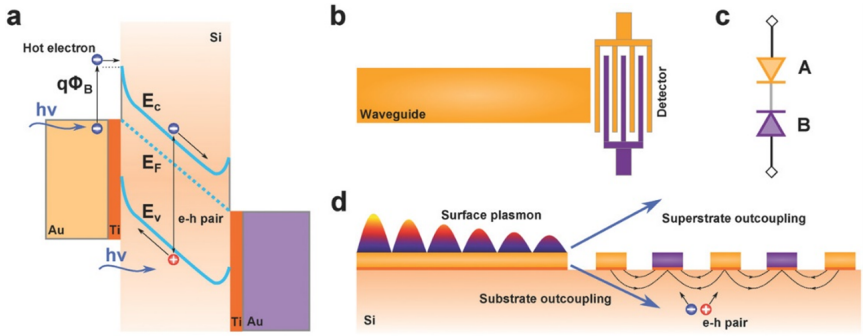



Figure 1.14: (a) Schematic representation of the band diagram and working mechanism of a biased MSM photodetector. $E_V$, $E_C$, $E_F$, and $\phi_B$ are, respectively, the valence band, conduction band, and Fermi energy levels. (b) Cartoon depicting a MSM photodetector coupled with a waveguide, and (c) equivalent electric circuit of the photodetector device. (d) Plasmon-induced photocurrent enhancement mechanism displaying plasmon-induced hot carrier generation *via* coupling of surface plasmons at metal–semiconductor interface (substrate outcoupling). Plasmon energy release at the metal-superstrate (air) interface (superstrate outcoupling) leading to enhanced light extraction or redirecting energy toward the active region, is also depicted. (Reprinted with permission from Panchenko et al.,[17] Copyright (2018) John Wiley and Sons.)

### 1.4.2 Plasmonic Photocatalysis Using Metal Oxide NCs

Plasmonic photocatalysis is classified as a heterogeneous catalytic process because the active catalytic system consists of a solid-state materials that mediates chemical reactions occurring at interfaces with molecular reactants. In conventional plasmonic photocatalytic systems, plasmonic nanostructures (generally coinage metal NCs) are integrated with wide-bandgap semiconductors (usually TCO NCs, such as $TiO_2$, ZnO, etc.) forming a hetero-nanostructure,[141–143] while the reactants are present in a separate gas or liquid phase. However, over the past few decades, single-phase plasmonic photocatalysts[144–146] in which the plasmonic and catalytic functionalities are intrinsically integrated within a single material, have received significant attention in the nanophotonics community due, in part, to their reduced structural and electronic complexity, enabling more direct interpretation of plasmon-induced photophysical effects. Beyond enhanced light absorption, single-phase plasmonic nanostructures can introduce additional and fundamentally distinct mechanisms that contribute to photocatalytic activity, including electromagnetic NFE,[147,148] plasmonic photothermal heating,[149] injection of energetic hot carriers,[150,151] and various resonant or non-resonant energy transfer processes.[152,153] The interplay between these plasmonic effects and traditional (excitonic) semiconductor photocatalytic processes gives rise to various complex charge-transfer dynamics at the plasmonic nanostructure–adsorbate interfaces occurring within ultrafast (femto-picosecond) timescales,[154–157] which directly govern reaction selectivity and efficiency. For instance, within approximately 10-100 fs after resonant photon absorption, the LSPR may decay non-radiatively, generating hot electrons (holes) with energies well above (below) the Fermi level.[158] Although carrier recombination is highly probabilistic due to spatial confinement,[159] these energetic hot carriers can migrate to the surface of the plasmonic nanostructure and thereby (indirectly) transfer into the unoccupied electronic levels (e.g., LUMO) of the molecular adsorbates (Figure 1.16a).[18,160–162] Interestingly, owing to the resonant nature of the plasmons and molecular electronic levels, LSPR decay can also lead to direct excitation of energetic hot electrons into the LUMO level of molecular adsorbates, giving rise to the so-called plasmon-induced interfacial charge transfer (PIICT) processes (Figure 1.16b).[163,164] Oscillating electric field associated with the plasmon and the transition dipole of the molecular adsorbate (acceptor species) can, even in the absence of direct electrical contact, undergo resonant coupling (*i.e.*, plasmon-induced resonant energy transfer, PIRET),[165,166] leading to the formation of an exciton within the acceptor species (Figure 1.16c). However, at longer timescales (nano-picoseconds), plasmons undergo thermalization *via* carrier-carrier and carrier-phonon coupling processes, leading to a temperature increase of the plasmonic nanostructure and its surrounding, called plasmonic photothermal effect (Figure 1.16d).[167] Finally, owing to their enhanced electric near field, the plasmonic nanostructures can also act like an optical an-

tenna,[168] enhancing various optical and/or electronic processes such interband transitions and interfacial charge transfer, leading to enhanced photocatalytic activity.

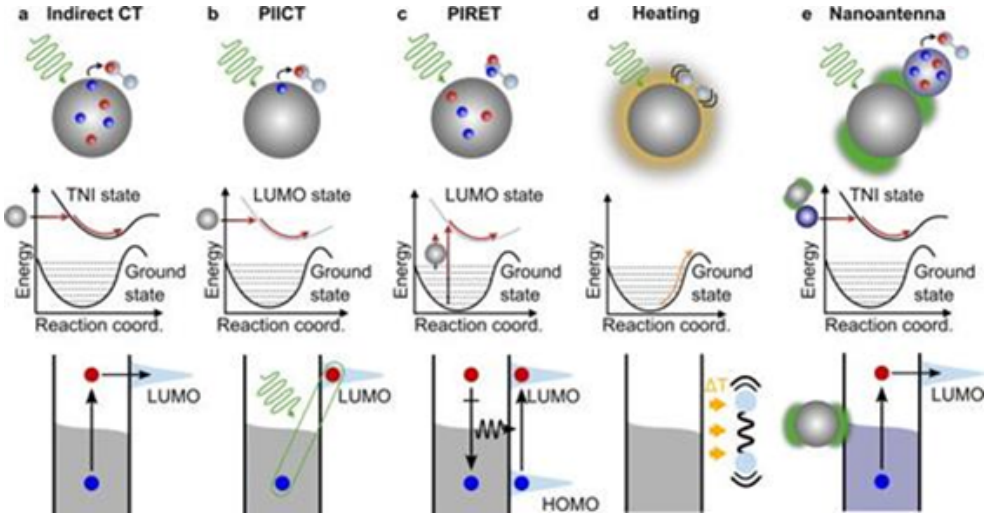



Figure 1.15: Schemes depicting mechanisms of plasmon-induced photocatalytic processes with schematic representation of the catalytic reaction (top panel), the potential energy surface of the molecular adsorbate (middle panel), and the electron energy distribution and transfer (bottom panel). (a) Schematic representation of indirect charge transfer (CT) mechanism, whereby energetic hot carriers are injected into the LUMO levels of molecular adsorbates, forming transient negative ions (TNIs). (b) Plasmon-induced interfacial charge transfer (PIICT). (c) Plasmon-induced resonant energy transfer (PIRET), *i.e.*, the resonant coupling between the plasmon and molecular adsorbate, inducing intramolecular electronic transitions therein. (d) Plasmon decay resulting in heating of the plasmonic NC and its surrounding. (e) Plasmonic NC acting like nanoantenna, thereby enhancing light-matter interactions at the nanoscale. (Reprinted with permission from Carlin et al.,[18] Copyright (2023) AIP Publishing.)

In the literature, several studies report on the enhanced photocatalytic activity of single-phase plasmonic metal oxide NCs. For instance, Xi et al.[169] investigated the formation of methane produced by the photocatalytic reduction of $CO_2$ (0.029 $mgl^{-1}g^{-1}h^{-1}$), using sub-stoichiometric $W_{18}O_{49}$ NCs as plasmonic model system. In order to modulate the level of non-stoichiometry, the authors implemented a $H_2O_2$-based post-synthetic oxidation of the NCs for 3 hours and demonstrated a significant reduction or complete disappearance of photocatalytic activity, as a result of the decreased free carrier density and thus LSPR. Yan et al.[170] reported a significant improvement ($\sim$ 0.2–15% quantum yield) in NIR-driven

photocatalytic water oxidation by $WO_{3-x}$ nanosheets post-synthetically annealed in $H_2$-atmosphere at elevated temperatures (747°C for 6 hours), demonstrating the presence of oxygen vacancies play a crucial role in plasmonic photocatalysis. Using UPS spectroscopy, Paik et al.[171] have shown that the CB minimum in non-stoichiometric $WO_{3-x}$ nanowires is more negative than the standard hydrogen reduction potential and it lays also at at higher energies compared to the CB minimum in oxidized ($NOBF_4$-treated) $WO_{3-y}$ ($y < x$) NCs. The authors reported an appreciable plasmonic photocatalytic $H_2$ evolution ($\sim$ 460 $\mu$mol $h^{-1}$ $g^{-1}$) for colloidal $WO_{3-x}$ nanowires containing 1% photo-deposited Pt on the surface as a co-catalyst, using a solution mixture of methanol and water (50/50 vol%) and visible light illumination. Tang et al.[172] synthesized plasmonic $WO_{3-x}$ nanosheets using elemental tungsten powder and isopropanol-based solvothermal method and investigated their photocatalytic activity under visible light illumination ($\lambda > 470$ nm), using methyl orange as a model compound. Using various radical sacrificial agents (scavengers), the authors demonstrated that hot holes with sufficiently high energy could be injected directly either into the adsorbed methyl orange molecules or generate $OH^{\bullet}$ radical by oxidizing water. Similar to holes, energetic hot electrons can also be directly injected into water (thus reducing it to form superoxide ($O_2^{\bullet -}$) radicals) or methyl orange, both of which ultimately leads to the degradation of the dye. Shi et al.[173] have investigated the impact of post-synthesis annealing in reducing (10% $H_2/N_2$) or inert (100% $N_2$) atmospheres at elevated temperatures (400–600°C) on the photocatalytic $H_2$ evolution of non-stoichiometric $WO_{3-x}$ nanosheets. While the NC annealed in $N_2$ were photocatalytically inactive, appreciable photocatalytic activity (60.4 $\mu$mol $h^{-1}$ $g^{-1}$) was reported for the $WO_{3-x}$ NCs annealed in reducing atmosphere for 3 hours at 500°C. Based on these observations, the authors concluded that oxygen vacancies can promote the adsorption and activation of $N_2$ molecules., Furthermore, they can also enhance the migration efficiency of photogenerated charge carriers in the NCs, thus leading to increased photocatalytic activity.

Besides $WO_{3-x}$, non-stoichiometric $MoO_{3-x}$ NCs have also been reported to exhibit significant photocatalytic activity under NIR light illumination. For instance, Cheng et al.[174] reported a detailed study on the non-aqueous synthesis of plasmonic non-stoichiometric $MoO_{3-x}$ nanosheets of approximately 200 $nm^{-1}$ $\mu$m thickness. The synthesis product exhibited a deep blue color, characteristic to non-stoichiometric $MoO_{3-x}$ NCs, which was attributed to plasmonic absorption with optical absorption maximum at $\sim$ 680 nm. Using $NH_3BH_3$ solution as model system for chemical hydrogen storage material, the authors then investigated the photocatalytic $H_2$ evolution reaction of $MoO_{3-x}$ nanosheets under visible light illumination. Notably, a nearly 4 times greater photocatalytic activity ($\sim$ 5.7 mol% $min^{-1}$) was observed for the non-stoichiometric $MoO_{3-x}$ nanosheets compared to bulk stoichiometric $MoO_3$, demonstrating the critical role of the catalyst's free carrier density and surface-to-volume ratio in plasmonic photocatalysis.[146] Using solvothermal method, Yin

et al.[175] synthesized molybdenum–tungsten oxide $Mo_xW_{1-x}O_{3-y}$ NCs, exhibiting strong LSPR absorption in the visible-NIR region and observed that compositional tuning of the NCs directly translates into an approximately 1.2 fold improvement in photocatalytic $H_2$ evolution rate under visible ($\lambda > 420$ nm) irradiation compared to in dark conditions, by promoting more efficient light harvesting and charge carrier excitation.

## 1.5 Motivation and Scope of this Thesis

The main motivation of the research discussed in this thesis is to investigate the correlation between electronic structure and inherent magneto-optical properties of doped plasmonic semiconductor metal oxide NCs and explore the potential nanophotonic and industrial applications thereof.

**Chapter 2** introduces the experimental methodologies implemented in this work. In **Chapter 3**, using colloidally–synthesized nonstoichiometric plasmonic $WO_{3-x}$ nanorods as a model system, I demonstrate the uncertainty of using conventional optical absorption spectroscopy to identify the plasmonic nature or extract plasmonic parameters of complex semiconductor metal oxide NCs that contain free charge carriers, based on the energy, shape, and intensity of the optical absorption bands. Using variable-field and variable-temperature MCD spectroscopy, a technique capable of disentangling carrier behavior (carrier localization/delocalization) and various fundamental electronic transitions, the origin of the visible–NIR optical absorption bands formerly erroneously attributed only to high-energy plasmons in $WO_{3-x}$ was successfully elucidated.

In **Chapter 4**, I investigate the correlation between NC morphology and intrinsic plasmon–exciton exchange interactions in colloidal plasmonic hexagonal Cs:$WO_{3-x}$ NCs of different aspect-ratios, wherein the visible–NIR LSPR absorption originates from charge-compensating electrons generated in the presence of oxygen vacancies and/or Cs-derived free carriers. Using variable-field and variable-temperature MCD spectroscopy, I demonstrate how the modulation of NC aspect ratio, as a simple geometric parameter, allows for manipulation of the origin and nature of carrier–exciton interactions, and thus the excitonic Zeeman splitting pattern in degenerately-doped plasmonic semiconductor metal oxide NCs, providing promising opportunities for new investigations of these materials in spintronics and related quantum technologies.

In **Chapter 5**, I investigate the enhanced performance of InGaAs planar MSM photodetectors operating in the NIR spectral region, using drop-cast colloidal $WO_{3-x}$ and

Cs:$WO_{3-x}$ NCs as a photoactive component. Through several optoelectronic measurements, I present the enhancements devices' response by up to a factor $\sim 2.5$, broadly consistent with the plasmonic absorption spectra of the NCs. The results reported in this chapter indicate that suitably prepared conductive metal oxide NCs are a promising family of materials for NIR plasmonic applications.

In **Chapter 6**, I present a comprehensive approach to decouple adsorption effects from true photocatalytic activity observed in colloidal plasmonic $WO_{3-x}$ NCs, as a model system for metal oxide-based plasmonic photocatalysts. Through systematic photocatalysis and adsorption experiments, I show that dye adsorption can significantly contribute to apparent degradation in photocatalytic studies, potentially leading to overestimation of photocatalytic efficiency if not properly accounted for. To modulate the native oxygen vacancy concentration and thereby tune their LSPR intensity, the as-synthesized $WO_{3-x}$ NCs were post-synthetically annealed in air at various temperatures. This controlled modulation lays the foundation for a systematic study of how LSPR activity correlates with both dye adsorption behavior and photocatalytic performance. A significant portion of this chapter is devoted to exploring the role of surface chemistry in colloidal, as well as annealed $WO_{3-x}$ powder samples. As-synthesized colloidal plasmonic NCs are typically stabilized with long-chain insulating organic ligands, which impede dye adsorption and hinder catalytic interactions at the NC surface. I demonstrate that complete removal of these ligands leads to more accessible and catalytically active surfaces, not only improving dye adsorption but also significantly enhancing the photocatalytic degradation rate and apparent rate constant. The ongoing research presented in this chapter aims to isolate and quantify the individual contributions of adsorption and photocatalysis. This work provides a framework for more accurate evaluation of plasmonic photocatalysts and underlines the importance of controlling vacancy concentration and surface chemistry in optimizing photocatalytic performance.

# Chapter 2

## Experimental Section

## 2.1 Nanocrystal Syntheses

### 2.1.1 Materials

Oleylamine (OLAM, technical grade 70 %), oleic acid (OLAC, technical grade 90 %), isopropanol (IPA, HPLC grade ≥99.9%), ethanol (EtOH, HPLC grade ≥99.9 %), methanol (MetOH, HPLC grade ≥99.9 %), toluene (HPLC grade, ≥99.8 %), anhydrous toluene (HPLC grade ≥99.8 %), anhydrous N,N-dimethylformamide (DMF, HPLC grade ≥99.8 %), acetone (HPLC grade, ≥99.9%), hexane (≥98.5 %), tetrachloroethylene (TCE, ≥99.5 %), iron(III) chloride ($FeCl_3$; 95%), nitrosonium tetrafluoroborate ($NOBF_4$; 95 %), acetonitrile (ACN; HPLC grade ≥99.9 %), and tungsten(IV) chloride ($WCl_4$; 95 %) were all purchased from Sigma-Aldrich. Powder cesium chloride (CsCl; 99.9 %), and Rhodamine 6G dye (Rh6G) were obtained from Strem Chemicals Inc.; and Exciton Corp. Chemical Inc, respectively. All chemicals were used as received, and handled adhering to the protocols specified in material-specific safety data sheets (MSDSs).

### 2.1.2 Synthesis of Colloidal $WO_{3-x}$ NCs

Oxygen-deficient tungsten oxide ($WO_{3-x}$) nanorods were synthesized via thermal decomposition of $W(CO)_6$ following a modified procedure for the synthesis of tungsten nanoparticles by Sahoo et al.[176] A mixture of OLAC and OLAM in 3.2:1 volumetric ratio was injected into a round-bottom flask and degassed for approximately 30 min under continuous stirring. The flask was then purged using a gentle flow of nitrogen and heated to 300 °C at 0.5 °C/s. When the reaction temperature reached 100 °C, 1.056 g of $W(CO)_6$ was quickly added to the flask whereupon the reaction mixture turned yellow-brownish.

As the temperature approached 300 °C, the color gradually changed to greenish and finally to deep blue, indicating the formation of sub-stoichiometric tungsten oxide NCs.[76] After 1 h at 300°C, the reaction mixture was allowed to naturally cool down to room temperature. The as-synthesized NCs were transferred to test tubes with a small amount of toluene and washed three times using a mixture of acetone/EtOH = 1:1 (V/V). The washed product was sonicated and centrifuged at 3000 rpm for approximately 5 min to separate the NCs from the native slurry and to remove any organic residue. A portion of the purified sample was dispersed in hexane or TCE for optical measurements, while the remaining part was transferred with acetone on a watch glass, dried overnight, and saved in a powder form.

### 2.1.3 Ligand Stripping of As-synthesized Colloidal $WO_{3-x}$ NCs

In order to remove the OLAC coordinating ligands from the surface of the as-synthesized $WO_{3-x}$ NCs, a $NOBF_4$-based ligand stripping procedure was implemented following the protocol reported by Jeong et al. with some minor modifications. Briefly, approximately 2 mL of the concentrated dispersion of as-synthesized $WO_{3-x}$ NCs (∼200 mg) was precipitated in an argon-filled glovebox and redispersed in 5 mL of anhydrous hexane contained in a 20 mL scintillation vial (for the synthesis and precipitation of $WO_{3-x}$ NCs see *Experimental Section 2.1.2.*). In a separate scintillation vial inside the glovebox, 120 mg of $NOBF_4$ was weighed and dispersed in 2 mL of anhydrous DMF, which was then united with the vial containing the hexane dispersion of $WO_{3-x}$ NCs. The resultant initially heterogeneous mixture, consisting of a hexane dispersion as the upper phase and a $NOBF_4$-DMF solution as the lower phase, was homogenized by vigorous stirring for 5 minutes.[177] Upon settling, a gradual color change in the lower phase was observed, indicating the transfer of ligand-stripped $WO_{3-x}$ NCs from the nonpolar hexane phase into the polar DMF phase. After decanting the upper phase, the DMF dispersion was centrifuged at 5000 rpm for 10 min, and the NC pellet was then redispersed and washed twice with a 5 mL DMF—toluene mixture (1:2 V/V) and precipitated with 2 mL of hexane. The as-obtained product was finally dispersed in 1 mL of DMF and stored under $N_2$ until further use.

### 2.1.4 Post-Synthesis Annealing of As-Synthesized $WO_{3-x}$ NCs

To control the concentration of oxygen vacancies, post-synthetic annealing of the as-synthesized colloidal $WO_{3-x}$ NCs was performed. First, the native NCs were first precipitated following the procedure described in Section 2.1.2., then approximately 1 g of the precipitated NCs was placed into porcelain crucibles and annealed in ambient air at specific temperatures ranging from 350-800°C, using a Thermo Scientific Lindberg/Blue M Mini-Mite 1100°C laboratory tube furnace.

### 2.1.5 Synthesis of Colloidal Cs:$WO_{3-x}$ NCs

For the assessment of the effect of aspect ratio on the magneto-optical properties of hex-Cs:$WO_{3-x}$ NCs, we adopted previously reported colloidal synthesis protocols using standard Schlenk line techniques with some minor modifications.[7,94,178] Briefly, $WCl_4$ (66 mg) and CsCl (20 mg) powder precursors were placed in a round-bottom flask, to which a mixture of degassed OLAM and OLAC in specific OLAM:OLAC molar ratios (platelets: 1.00:52.8; iso-prisms: 1.00:3.67; rods: 1.00:2.07) was injected. The reaction mixtures were first degassed at 120 °C for 30 min, then heated to 300 °C at 0.5 °C/sec and kept at that temperature for 120 min under a gentle flow of $N_2$ gas. The reaction was quenched by rapidly cooling the flask to room temperature, and the products were transferred into centrifuge tubes using ∼5 mL of toluene. To flocculate the NCs, 5.5 mL of acetone (anti-solvent) was injected into each tube assisted by vortex mixing. The samples were then centrifuged at room temperature at ca. 7800 rpm for 5 min to isolate the NCs from the dispersion medium. The obtained NC pellets were redispersed in 4 mL of toluene, and 1 mL of acetone was added into the centrifuge tubes to flocculate the nanocrystals. In order to retain the coordinating ligands of the NCs during the washing step, 20 $\mu$L of OLAC and OLAM were added to samples followed by a gentle vortex mixing for 5 min. After repeating this purification cycle two more times, the NCs were redispersed in 5 mL of toluene. Finally, for optical measurements, 1 mL of a toluene dispersion was once again flocculated with acetone following the above procedure, and redispersed in 4.5 mL of TCE. All the samples were stored under $N_2$ atmosphere until further use. We confirmed high reproducibility of the structure, morphology, and extinction spectra of the NCs prepared with a given OLAM:OLAC molar ratio under described synthesis conditions (as presented in Chapter 4).

## 2.2 Characterization

### 2.2.1 X-Ray Diffraction

The crystallinity and phase purity of the samples were investigated by X-ray diffractometry (XRD) using a Malvern Panalytical-Aeris Diffractometer equipped with a Cu K$\alpha$1 radiation source ($\lambda$ = 1.54056 Å) and a vertical goniometer (radius 145 mm). Nanocrystals were drop-cast onto optical microscope glass slides. The XRD measurements were conducted under ambient conditions at 1.20°/min or 2.00°/min scanning speed between 20—75° range. For referencing the XRD patterns, the Inorganic Crystal Structure Database (ICSD) was used.

### 2.2.2 Transmission Electron Microscopy

Transmission electron microscopy (TEM) and energy dispersive X-ray spectroscopy (EDS) measurements were conducted to investigate the morphology (and size distribution) and the elemental composition of NCs, respectively, using a JEOL-2010F microscope operating at 200 kV. Aliquots ($\sim$20 $\mu$L) of original toluene dispersions of NCs were diluted in hexane (1:50 vol.), and ca. 10 $\mu$L of such a suspension was drop-cast on copper grids with lacey Formvar/carbon support films. The TEM micrographs were analyzed using ImageJ software.

### 2.2.3 Scanning Electron Microscopy

To investigate the morphology and surface characteristics of the $WO_{3-x}$ powder samples, scanning electron microscopy (SEM) was performed under vacuum using a FEI Quanta Feg 250 SEM microscope operating with accelerating voltages of 15 kV. Before imaging, powder specimens were deposited onto aluminum sample holders using conductive carbon adhesive tape.

### 2.2.4 UV-visible-NIR Absorption Spectroscopy

The optical extinction spectra of the colloidal or thin-film NC samples were collected with a Varian Cary 5000 UV-visible-NIR spectrophotometer. For the optical measurements of the colloidal NC samples, diluted TCE dispersions were loaded into a quartz cuvette of 1 cm path length. For measurements of the NC thin films, NCs were deposited on a 1 cm $\times$ 1 cm custom-cut strain-free quartz substrate and allowed to naturally dry at room temperature under inert $N_2$ atmosphere.

### 2.2.5 Photoluminescence Emission Spectroscopy

To investigate the optical emission properties of colloidal $WO_{3-x}$ NCs, steady-state photoluminescence emission (PLE) spectroscopy measurements were performed at room temperature, using 290 nm excitation. The NCs were suspended in TCE, 2.5 ml of which was then injected into standard (1 cm $\times$ 1 cm) four-clear-sided quartz cuvettes for PL measurements.

### 2.2.6 X-Ray Photoelectron Spectroscopy

The NC surface composition and the tungsten electronic structure were studied by X-ray photoelectron spectroscopy (XPS) using a Thermo-VG Scientific ESCALab 250 microprobe equipped with a monochromatic Al K$\alpha$1 radiation source ($\lambda$ = 8.340150 Å) and

a charge neutralizer. For the calibration of the W 4f and O 1s XPS spectra, adventitious C 1s core level XPS signal (binding energy of 284.8 eV) was used as a reference. All XPS spectra were background corrected using Touggard (for O 1s XPS) or Shirley model (for W 4f XPS), and the different spectral components were fitted and analyzed using CasaXPS software.

### 2.2.7 Raman Spectroscopy

Raman spectroscopy measurements were conducted using a Renishaw (Chicago, IL) Raman Microscope System equipped with an Olympus MD Plan 50×/0.75 objective lens and a spectrograph including a 1200 I/mm grating and an entrance slit of 100 $\mu$m. Powder or drop-cast NC thin film samples were excited using a 785 nm SLM CW laser (Integrated Optics, Vilnius, Lithuania) with a power of 35 mW. All Raman spectra were collected using a single-scan acquisition mode with 30 s acquisition time. To reduce fluorescent background, Raman spectra were collected 15 min post laser irradiation. Spectral calibration was performed against the most intense peak of (520.7 $cm^{-1}$) a silicon standard.

### 2.2.8 Fourier-Transform Infrared Spectroscopy

Fourier-transform infrared spectroscopy (FTIR) measurements were conducted on the TCE colloidal dispersion of NCs or NC thin films using a FTIR Bruker Tensor 37 spectrophotometer.

### 2.2.9 Specific Surface Area Measurements

The specific surface area of the powder $WO_{3-x}$ samples annealed at different temperatures was determined *via* $N_2$ physisorption using the Brunauer-Emmett-Teller (BET) method. Before measurement, approximately 0.1500 g of dried sample was thoroughly degassed under vacuum at 80°C for 2 h to eliminate any adsorbed moisture and impurities. The adsorption–desorption isotherms were then recorded at 77 K (the boiling point of liquid $N_2$) using a Micromeritics Gemini VII 2390a surface area analyzer.

Adsorbate uptake data were plotted as $\frac{p/p_0}{n(1-p/p_0)}$ versus $p/p_0$ to create a linear BET plot in the relative pressure range of approximately 0.05-0.30. The specific surface area ($S_{BET}$) can be determined, using equation 2.1:

$$S_{BET} = \frac{n_m N_A \sigma}{m} \tag{2.1}$$

where $N_A$ is Avogradro's number, $\sigma$ is the molecular cross-sectional area of $N_2$ (typically $\sim$0.162 $mm^2$), and $m$ is the sample mass.

### 2.2.10 Adsorption and Photocatalytic Measurements

The adsorption and photocatalytic experiments were conducted at controlled temperatures and optical conditions inside a custom-made photocatalysis fume hood with reflective walls designed to block any external stray light. To maintain precise temperatures between 1 and 40°C, a 50 mL aqueous solution of 5 ppm Rh6G dye was added to a 100 mL jacketed beaker connected to a circulating water bath (Cole-Parmer Polystat 6L). The solution temperature was continuously monitored using a digital-analog thermometer immersed in the beaker. To minimize solvent evaporation and prevent deviations in concentration during the experiments, the beaker was sealed with parafilm and covered with a watch glass. After reaching thermal equilibrium, specific amounts (5-15 mg) of $WO_{3-x}$ annealed powder samples or colloidal NCs drop-cast on optical microscope glass slides were added into the beaker and vigorously stirred. Each adsorption or photocatalytic measurement was performed for a total duration of 2 hours. To spectroscopically monitor the temporal progression of Rh6G adsorption or degradation (plasmonic photocatalysis), aliquots of 1.5 mL were taken from the beaker and centrifuged at 7000 rpm for 5 minutes. Finally, the optical extinction spectra of the supernatant were recorded in a dark room using UV-visible-NIR transparent quartz cuvettes (1 cm pathlength; Aireka Scientific Co., Ltd) with the Cary 5000 UV-visible-NIR spectrophotometer. Following the optical measurements, the collected supernatants were transferred to 10 mL scintillation vials and stored at 4°C in a laboratory refrigerator for further analysis. Various sacrificial agents were employed in the photocatalytic experimental setup to qualitatively investigate the degradation mechanism of Rh6G dye, and the role of different photocatalytically generated radicals. In order to assess dye degradation during adsorption or photocatalytic processes, electrospray-ionization mass spectrometry (ESI-MS) measurements were performed, using a Thermo Scientific LTQ-XL Linear Ion Trap instrument. For each measurement, samples were purified by centrifugation (7000 rpm for 30 min) and syringe filtering (0.2 $\mu$m pore size). The resulting solutions were diluted in 50:50 MilliQ:MeOH with 1% formic acid.

#### 2.2.10.1 Photocatalysis Using Sacrificial Agents

In this work, various sacrificial agents were employed within the photocatalytic experimental setup to qualitatively investigate the degradation mechanism of Rh6G dye. By selectively introducing chemical species that act as "scavengers" for photogenerated holes, electrons, or other reactive oxygen species (ROSs) as reaction intermediates, such as hydroxyl radicals ($OH^{\bullet}$) or superoxide radical ion ($O_2^{\bullet -}$) (Table 2.1), the recombination rate of electron-hole pairs and/or redox reactions of ROSs were systematically controlled.

Table 2.1: Sacrificial agents ("scavengers") and the corresponding scavenged particles/chemical species.

| Sacrificial Agent | Scavenged species |
|---|---|
| Methanol (MeOH) | hole ($h^+$) |
| Isopropanol (IPA) | $OH^{\bullet}$ |
| $FeCl_3$ | $e^-$ |
| Ascorbic Acid (AA) | $O_2^{\bullet -}$ |

#### 2.2.10.2 Recyclability Measurements

To evaluate the stability and reusability of the $WO_{3-x}$ as a photocatalyst or adsorbents, recyclability tests were conducted through three consecutive photocatalytic degradation or adsorption cycles, respectively, using Rh6G dye under identical experimental conditions, as specified below.

***Adsorber recycling***. After each adsorption cycle, the adsorber (12 mg) was recovered by centrifugation at 7000 rpm for 10 minutes at room temperature, followed by washing it three times with a mixture of deionized water and EtOH in 1:1 volumetric ratio to remove residual reactants or byproducts. Subsequently, the washed adsorber was first dried in ambient conditions at 60°C, then annealed in air at 200 °C to remove any molecular species that remain adsorbed. As-purified adsorbers were then reused in the subsequent cycle.

***Photocatalyst recycling***. 12 mg of the ligand-stripped $WO_{3-x}$ NCs were deposited on a standard optical microscope glass slide and dried under an inert atmosphere in a glovebox. After each photocatalysis cycle, the glass slide containing the NCs was removed from the Rh6G dye solution (50 mL, 5 ppm) and thoroughly washed three times with deionized water under inert atmosphere, applying care to minimize NC loss during the recovery process. Subsequently, the glass slide was allowed to naturally dry in a glovebox.

For both the adsorber and photocatalyst recycling, gravimetric analysis was implemented after each washing cycle to quantify the NC loss during purification process. All recyclability measurements were spectroscopically monitored across three successive cycles using optical extinction spectroscopy (vide infra). To further investigate the $WO_{3-x}$ sample durability during recycling tests, XRD measurements were employed to assess potential

degradation or phase transformation over multiple cycles.

### 2.2.11 Magnetic Circular Dichroism (MCD) Spectroscopy

In MCD spectroscopy, a chromophore is probed by measuring the difference between the absorption of left and right circularly polarized light (CPL) in an external magnetic field applied parallel to the light propagation direction (called Faraday configuration). The MCD intensity of an allowed transition from a ground state $|A\rangle$ to an excited state $|J\rangle$ (obeying $\Delta M_J = \pm 1$ selection rule) is defined as:[117]

$$\frac{\Delta A}{E} = \frac{2N_0\pi^3\alpha^2 Cl \log e}{250hcn}\mu_B B[A_1(|\frac{\delta f(E)}{\delta E}) + (B_0 + \frac{C_0}{kT})f(E)] \tag{2.2}$$

where ΔA is the differential absorption between left and right CPL, $E$ is the energy of CPL ($E = h\nu$), $\alpha$ is the electric permeability, $N_0$ is the Avogadro's number, $C$ is the concentration of the absorbing species, $l$ is the optical path length, $n$ is the refractive index of the optical medium, $\mu_B$ is the Bohr magneton, and $B$ is the applied magnetic field. The $A_1$, $B_0$, and $C_0$ are called MCD (Faraday) $A$, $B$, and $C$ terms, respectively, *f(E)* is the spectral line shape function, and $\delta f(E)/\delta E$ is its first derivative. Schematic representation of Faraday terms $A$ and $C$ is shown in Figure 2.2. The $A$ term (Figure 2.2a) is associated with the Zeeman splitting of the excited state, leading to absorption transitions for the right and left CPL that are slightly shifted in energy relative to each other. This shift results in a derivative-like MCD spectral line shape (Figure 2.2). Faraday $A$ term is generally temperature-independent and linearly dependent on magnetic field strength (Figure 2.2d).

In contrast to the $A$ term, the $C$ term involves Zeeman splitting of the degenerate ground states (Figure 2.2c) present in paramagnetic species. At high external magnetic field and low temperatures, the higher-energy ground state becomes increasingly depopulated. Hence, the $C$-term MCD signal intensity saturates as a function of $B$, and it follows Curie-type temperature dependence (Figure 2.2e).[117,179]

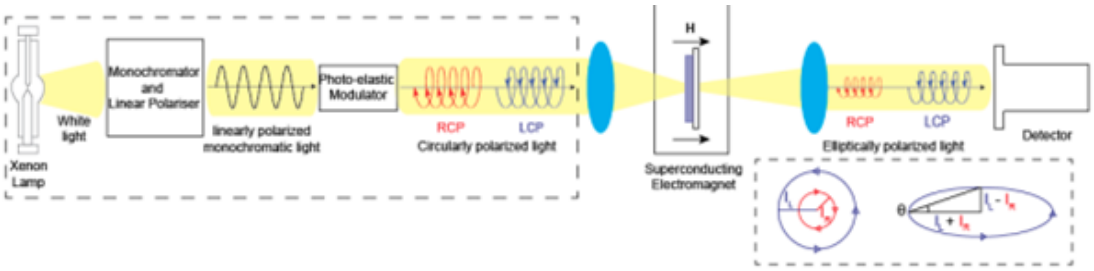



Figure 2.1: Schematic representation of the experimental MCD setup. Broadband light emitted from a Xenon lamp (left cartoon) first enters a monochromator and a linear polarizer (box) to generate a linearly polarized monochromatic light beam. Passing through a photoelastic modulator, the linearly polarized beam is converted into circularly polarized light (CPL) with two helicities, *i.e.*, left and right circularly polarized light (LCP and RCP, respectively). Using focusing lens (blue ellipse, left), the LCP and RCP beams are focused on the entrance slit of the cryogenically-cooled superconducting electromagnet (middle box), whereby the direction of light propagation is parallel to the field vector of the homogeneous uniform magnetic field generated in the magneto-optical cryostat. The cryostat, placed at the center of the superconducting electromagnet, contains the sample space wherein the drop-cast NC thin films are immersed using a precision sample rod. Depending on the CPL absorptivity of the sample, absorption of RCP and LCP may occur to a different degree, which is defined as ellipticity ($\theta$) measured in millidegree units ($\theta$ = $A_{RCP}$—$A_{LCP}$). The transmitted RCP and LCP light beam is then passed through another lens (blue ellipse, right) and finally hits the detector (right). (Reprinted with permission from Yin et al.,[13] Copyright (2018) Springer Nature.)

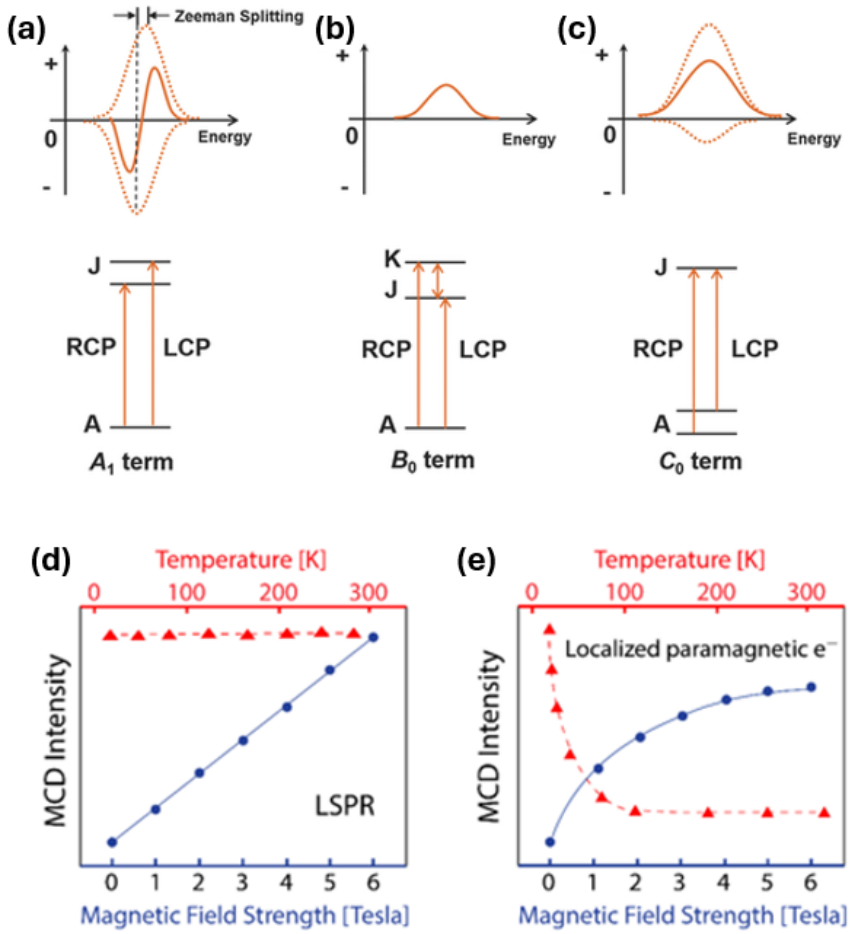



Figure 2.2: Schematic depiction of the origin of MCD signal intensities (top panels) and Zeeman splitting patterns (middle panels) of Faraday $A$-term (a), $B$-term (b), and $C$-term (c). Temperature (red markers) and magnetic field dependent MCD signals (blue markers) corresponding to plasmons (d) and localized paramagnetic carriers (e). Plasmons and free carriers show fundamentally different magneto-optical behavior as a function of external magnetic field strength and temperature: while plasmons show linear behavior (blue line) as a function magnetic field and temperature independence, localized carriers exhibit saturating magnetic field response (blue curve) fitted using Brillouin function and nonlinear temperature dependence following Curie-Weiss law. (a: Reprinted with permission from Han et al.,[19] Copyright (2020) John Wiley and Sons.)

# Chapter 3

## Revisiting Plasmonic Properties of Complex Semiconductor Nanocrystals Using Magnetic Circular Dichroism Spectroscopy: A Cautionary Tale

In this chapter, I re-examine the magneto-optical properties of complex semiconductor NCs that have recently been reported to have unique and promising plasmonic properties. In particular, I focus on MCD spectroscopy of non-stoichiometric plasmonic $WO_{3-x}$ NCs, as model system. I present that the MCD spectra of $WO_{3-x}$ NCs follow a linear dependence of intensity on the magnetic field at low-photon energies ($\lambda$ >800 nm) and saturation behavior at higher photon energies ($\lambda$ <600 nm), clearly confirming that this spectrum has two different contributions (LSPR and ligand-field transitions of $W^{5+}$ ions). I demonstrate that caution must be exercised when assigning the absorption spectra of complex semiconductor NCs, particularly those containing transition-metal ions, to LSPR.

## Overview

Plasmonic semiconductor nanocrystals (NCs) have emerged as an attractive alternative to noble metal nanoparticles. They typically exhibit LSPR in the infrared range, which can be tuned by controlling the type and concentration of charge carriers. Compositionally and electronically complex semiconductor NCs have attracted significant attention due to their reported plasmonic properties, such as bipolar behavior (off-stoichiometric spinel-type gallium iron oxide or GFO), wide tunability (copper iron chalcogenide or $Cu_xFe_yS_{2-z}Se_z$), and extremely broad LSPR (oxygen-deficient $WO_{3-x}$). However, the origin of these unusual properties remains unclear. Here, we comparatively investigate the plasmonic properties of these semiconductor NC materials using magnetic circular dichroism (MCD) spectroscopy,

owing to the highly specific response of LSPR to the magnetic field and light polarization. In all systems, we find indisputable evidence that the LSPR absorption bands have been mischaracterized. The MCD signal corresponding to the absorption spectrum of $WO_{3-x}$ NCs shows Brillouin function dependence on the magnetic field at high photon energies (attributed to d—d ligand-field transitions (LFT) of $W^{5+}$) and linear dependence in the near-infrared range (attributed to LSPR), indicating that the broad absorption spectrum of $WO_{3-x}$ NCs is only partly associated with LSPR. The results of this work help resolve notable discrepancies in the literature, underline the challenges in assigning absorption bands of complex semiconductor NCs to LSPR, and demonstrate that MCD spectroscopy is an invaluable tool for characterization of these materials.

## 3.1 Introduction

In recent years, there has been a surge in the investigation of new plasmonic materials in reduced dimensions.[180,181] Among emerging materials that exhibit localized surface plasmon resonance (LSPR), degenerately doped semiconductor nano-crystals (NCs) have attracted particular attention.[4] The focus on this class of materials stems from the possibility to control charge carrier type and concentration (and therefore LSPR) in them[182] and to exploit a potential correlation between different functional properties.[13,41] Various applications of plasmonic semiconductor nanostructures have been proposed or demonstrated, including those in sensors,[183] surface-enhanced spectroscopies,[184] photovoltaics,[185] and photocatalysis.[186,187] While LSPR in semiconductor NCs is typically manifested as a broad-band absorption in the near-to-mid infrared spectral region,[4] many applications require large tunability of the plasmon resonance and would significantly benefit from the visible-light LSPR absorption which is more characteristic for metal nanoparticles owing to their inherently high carrier density. Among the most intriguing possibilities associated with high-energy plasmon absorption is the resonant coupling between plasmons and excitons. The prospects of such applications have stimulated the search for plasmonic semiconductor materials that can be obtained in the nanocrystalline form and allow for different means of tuning LSPR and achieving high-energy plasmon absorption.

Although most reports on tuning LSPR have focused on aliovalently doped transparent metal oxide NCs,[54,56,103,188,189] a number of studies have recently reported high-energy tunable LSPR in NCs made of complex semiconductor materials, including oxygen-deficient $WO_{3-x}$ and $MoO_{3-x}$,[76,190] or metallic $ReO_3$,[191,192] NCs. For instance, high-energy LSPR in $WO_{3-x}$ NCs, spanning the visible and NIR spectral range, has been implied to result from a high concentration of conduction band electrons originating from the presence of oxygen vacancies.[76] On the other hand, $ReO_3$ has a metallic character, which has been associated with a partial d-orbital occupancy of Re(VI) ($d^1$ system).[193] Given the metallic

character of $ReO_3$, the absorption band with a maximum at ca. 500-600 nm for colloidal $ReO_3$ NCs has been assigned to LSPR.[191,192]

Despite the remarkable scientific and technological opportunities potentially provided by high-energy plasmon resonance in semiconductor nanostructures, there have been some notable discrepancies associated with the assignment of the LSPR absorption bands. This is particularly related to the energy, intensity, and shapes of the absorption bands assigned to LSPR. Most notably, the spectral positions and/or intensities of the NIR or visible spectral bands are often inconsistent with the carrier density achievable in semiconductor materials based on the Drude model of the free electron gas.[194–196] The problem is compounded by the fact that interband or intra-ionic transitions are also possible throughout the NIR and visible spectral regions in complex semiconductors, particularly those containing transition-metal elements. These facts imply that the assignment of broad high-energy bands in the visible-NIR absorption spectra of complex semiconductor NCs to LSPR is often lacking strong evidence and that rigorous quantitative treatment of the spectral bands potentially associated with LSPR is necessary even for semiconductor NCs that contain, or are expected to contain, a relatively high concentration of free charge carriers. While absorption spectroscopy is routinely used to investigate LSPR in colloidal NCs, it lacks the specificity to unambiguously distinguish plasmon resonance from other possible transitions resulting in broad structureless absorption bands, notwithstanding possible evidence of the presence of free charge carriers. A reliable way of associating an absorption band with LSPR is to perform absorption measurements in the presence of an external force to which LSPR has a specific response. Magnetic circular dichroism (MCD) spectroscopy involves measuring the difference in the absorption of left and right circularly polarized light when an external magnetic field is applied parallel to the light propagation direction.[117] Since free charge carriers are sensitive to both electric and magnetic fields, MCD spectroscopy represents a unique method capable of identifying the plasmon resonances.[118] When LSPR is excited by circularly polarized light, two cyclotron plasmonic modes are generated, corresponding to left and right circular polarization. These two modes involve cyclotron motion of charge carriers in the opposite directions and are degenerate in the absence of an external magnetic field. However, application of an external magnetic field leads to an additional Lorentz force, such that the overall force ($\vec{F}$) acting on free carriers can be described classically as:

$$F = m \cdot (\frac{d\vec{v}}{dt}) + \gamma m \cdot \vec{v} = q\vec{E} + q(\vec{v} \times \vec{B}) \tag{3.1}$$

where $B$ is the external magnetic field; $q$, $m^*$, and $\vec{v}$, respectively, are the charge ($q = -|e|$ for the electrons and $q = +|e|$ for the holes), effective mass, and velocity of the carriers,

respectively; and $\gamma$ is the damping factor. The frequencies of the magnetoplasmonic modes selectively excited by circularly polarized light having the opposite polarization ($\omega_B\pm$) are given by:

$$\omega_B^{\pm} = \omega_0 \pm \frac{\omega_c}{2} \tag{3.2}$$

where $\omega_0$ is the LSPR band frequency at $B = 0$, and $\omega_c$ is the frequency of the cyclotron oscillations of free carriers about the magnetic field axis, defined as $\omega_c = qB/m^*$. The shift of the magnetoplasmonic modes relative to $\omega_0$ is given by $\Delta\omega_0 =\mid \omega_B - \omega_0 \mid = g(\omega_0)B$, where $g(\omega_0) = q/2m^*$ . As a result, the LSPR MCD spectrum exhibits a derivative-shaped signal that is linearly dependent on the magnetic field and independent of temperature.[118] On the other hand, MCD spectroscopy is also sensitive to electron spin states of the absorbing species, which is particularly important for interrogating the absorption spectra of complex metal oxides containing transition-metal ions that often exhibit intra-ionic or charge-transfer transitions in the visible-to-NIR regime.[197–201]

## 3.2 Results and Discussion

### 3.2.1 Structural and Optical Characterization

Oxygen-deficient tungsten (VI) oxide can adopt different crystal structures depending on the specific W/O ratio. The colloidal $WO_{3-x}$ NCs synthesized according to the procedure described in the Experimental Section have a rod-like morphology, as evident from the TEM image in Figure 3.1a. These nanorods are single-crystalline (Figure 3.1a, inset) and have a mean length of 37 ± 14 nm and a mean thickness of 5.2 ± 1.5 nm (Figure 3.1c,d). The measured lattice fringe separation determined from the high-resolution TEM image in the inset of Figure 3.1a is ca. 3.8 Å, which is in good agreement with the lattice spacing along the ⟨010⟩ direction in the monoclinic $W_{18}O_{49}$ ($WO_{2.72}$). The XRD pattern of the obtained NCs (black trace in Figure 3.1b) is dominated by two peaks at 23.4 and 48.1°, which can be assigned to the (010) and (020) planes, respectively, of the monoclinic $WO_{2.72}$, based on its agreement with the XRD pattern of bulk $WO_{2.72}$ (red trace in Figure 3.1b). These two peaks are sharper and more pronounced relative to other reflections, corroborating an oriented growth of the nanorods along ⟨010⟩ direction.

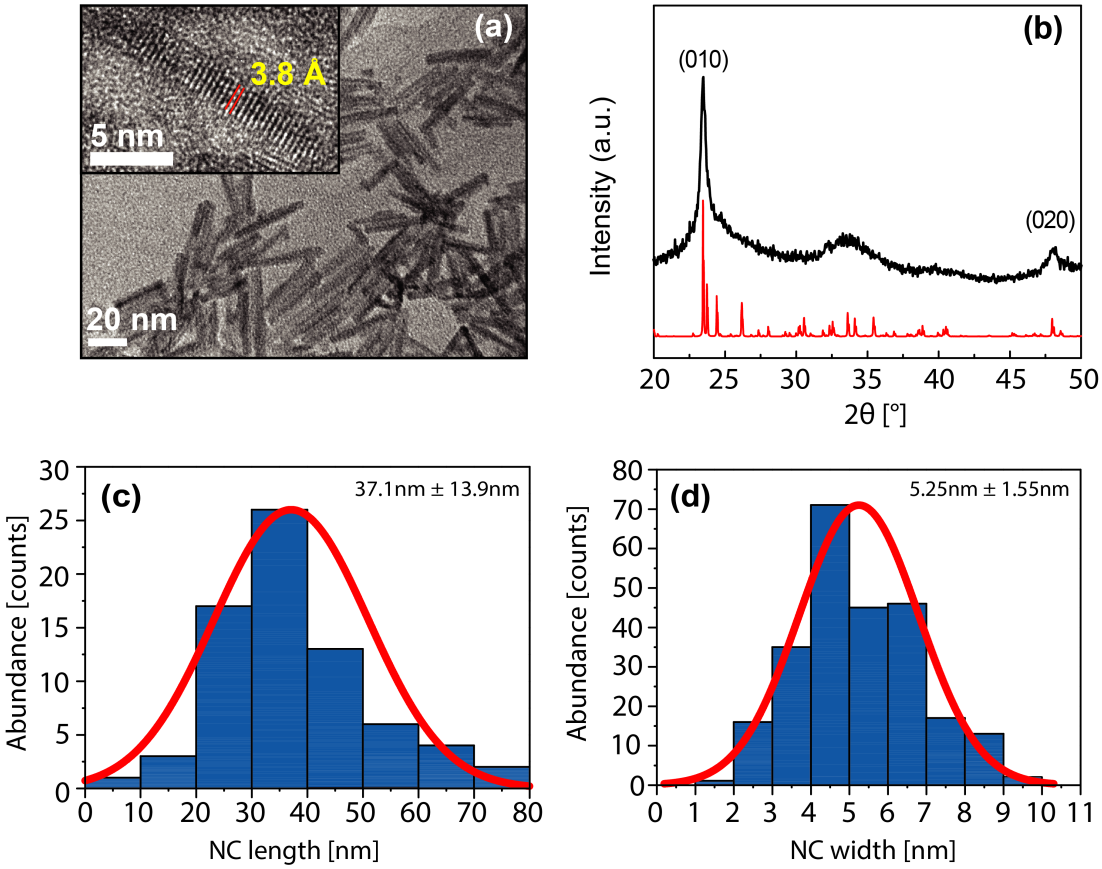



Figure 3.1: (a) Overview TEM image of $WO_{3-x}$ NCs. Inset: lattice-resolved TEM image of an individual nanorod, indicating its growth along the ⟨010⟩ direction. (b) XRD pattern of $WO_{3-x}$ NCs. Red trace is a simulated XRD pattern for bulk $WO_{2.72}$ (ICSD no. 24731). (c) Length and (b) width distribution histograms for $WO_{3-x}$ nanorods, determined from (a).

To investigate the surface chemistry of the NCs, Fourier-transform infrared (FTIR) spectroscopy measurements were performed. In Figure 3.2a, two intense bands are observed near 2855 $cm^{-}1$ and 2924 $cm^{-}1$ originating, respectively, from the symmetric and asymmetric methylene (-$CH_2$) stretching modes of oleic acid (OLAC) capping ligand. The bands appearing at lower energies near 1680 and 1480 $cm^{-}1$ can be attributed, respectively, to the terminal carbonyl (-C=O) stretching mode and the asymmetric and symmetric carboxyl (-COO-) stretching modes, the presence of which indicates the coordination of OLAC ligands to surface W atoms via the carboxylate head group. To investigate the optical

emission properties of $WO_{3-x}$ NCs, steady-state photoluminescence emission (PLE) spectroscopy measurements were performed, using 290 nm optical excitation. Shown in Figure 3.2b, the PLE spectrum of the NCs consists of a broad and asymmetric band ranging between 380-650 nm with a peak maximum near 385 nm. Based on the low-temperature PL studies reported by Cho et al.,[202] the broad PLE spectrum of $WO_{3-x}$ NCs originates from a mixture of interband excitonic recombination (at 400 nm) and CB electron-deep defect state recombination (at ∼475 nm).

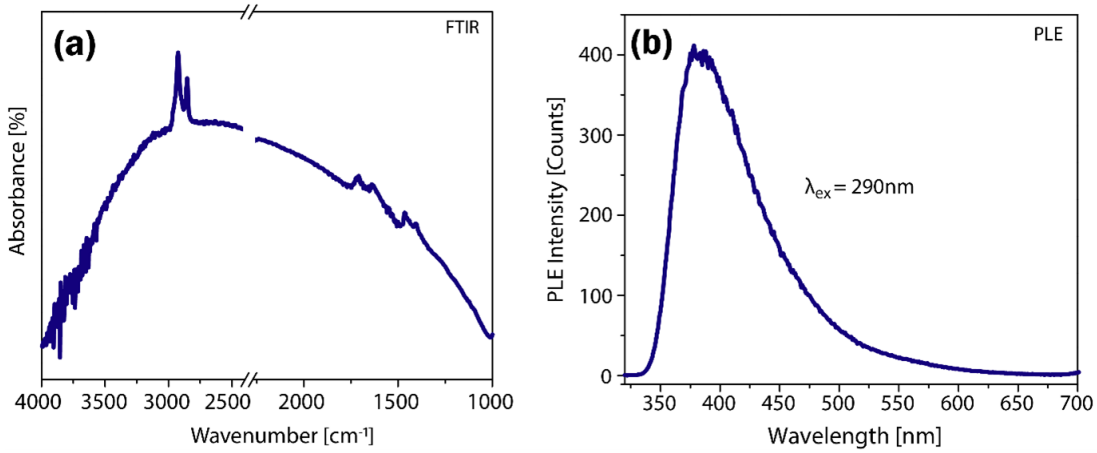



Figure 3.2: (a) FTIR and (b) photoluminescence emission spectra of the colloidal plasmonic $WO_{3-x}$ NCs.

The electronic structure of the tungsten sites in $WO_{3-x}$ NCs was investigated by XPS. Figure 3.3a shows the W 4f XPS spectrum of the sample from Figure 3.1a. The two relatively broad peaks with the maxima at ca. 35.5 and 37.6 eV are attributed to $^4f_{7/2}$ and $^4f_{5/2}$ spin-orbit doublet transitions, respectively.[203] The asymmetry and broadening of these peaks suggest the presence of tungsten in multiple oxidation states. The deconvolution of the XPS peaks reveals that $W^{5+}$ coexists with $W^{6+}$ as the dominant oxidation state in $WO_{3-x}$ NCs.[203,204] The relative amount of $W^{5+}$, determined by integrating the deconvoluted XPS peaks, is ca. 6%. A relatively large fraction of tungsten sites reduced from $W^{6+}$ to $W^{5+}$ is associated with the formation of oxygen vacancies, which act as electron donors in metal oxide NCs. O 1s XPS measurements were performed to quantitatively assess the native oxygen defect concentration in the NCs. Shown in Figure 3.3b, the O 1s XPS spectrum consists of one prominent peak near 530.2 eV accompanied by a shoulder near 531.9 eV, which can be assigned, respectively, to lattice oxygen and oxygen-related defects.

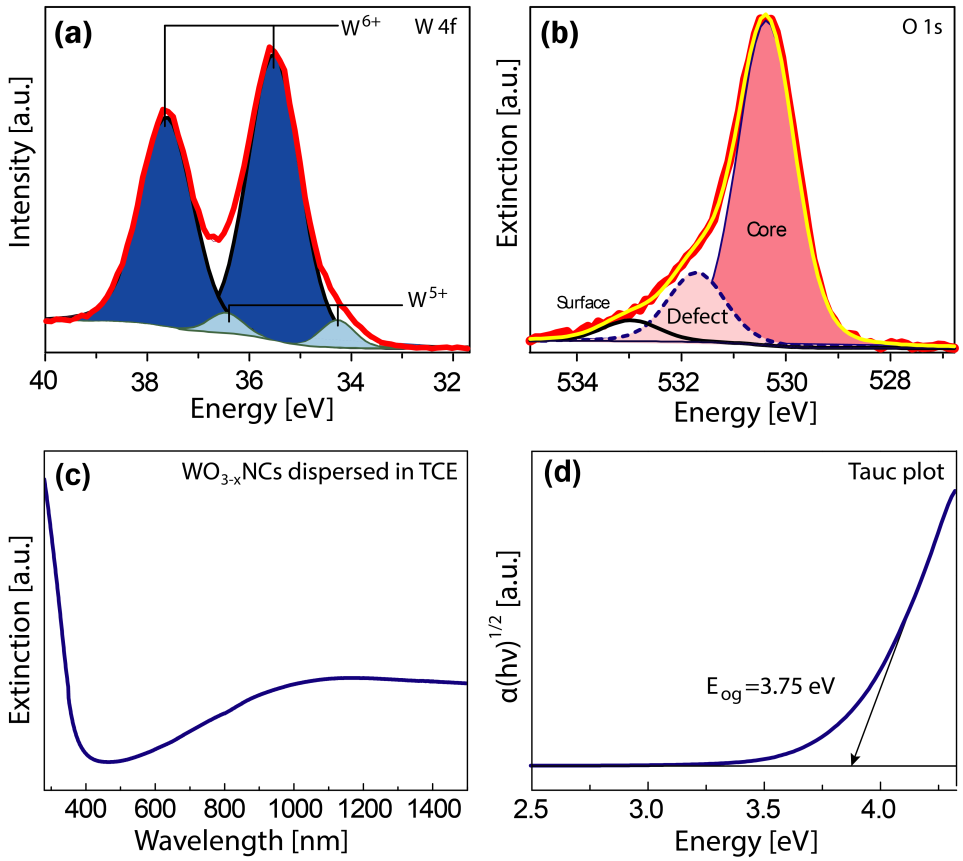



Figure 3.3: (a) High-resolution W 4f XPS, and (b) O 1s XPS spectra of $WO_{3-x}$ NCs. Fitting and assignment of the deconvoluted peaks are shown in the graph. (c) Overview steady-state optical extinction spectrum (collected at 300 K) of the native colloidal $WO_{3-x}$ NCs dispersed in TCE (photograph displayed as inset), and (d) corresponding Tauc plot with estimated optical bandgap (Eg) of 3.75 eV.

A weak secondary shoulder appearing at higher binding energies near 533 eV can be attributed to oxygen-containing coordinating ligands and surface contaminants on NC surface. The steady-state optical extinction spectrum of the $WO_{3-x}$ NCs is shown in Figure 3.3c. The broad absorption band throughout the visible and NIR has been attributed to LSPR enabled by the presence of oxygen-vacancy-induced free conduction band electrons. The sharp increase in UV absorption is attributed to the inter-band transitions.[76,205] In order to experimentally determine the optical bandgap of the colloidal $WO_{3-x}$ NCs, the

steady-state optical extinction spectrum from Figure 3.3c was converted to Tauc plot (Figure 3.3d), which suggested a direct bandgap of 3.75 eV for the NCs. To assess the air sensitivity of LSPR, the as-synthesized $WO_{3-x}$ NCs were exposed to air for different durations at room temperature.

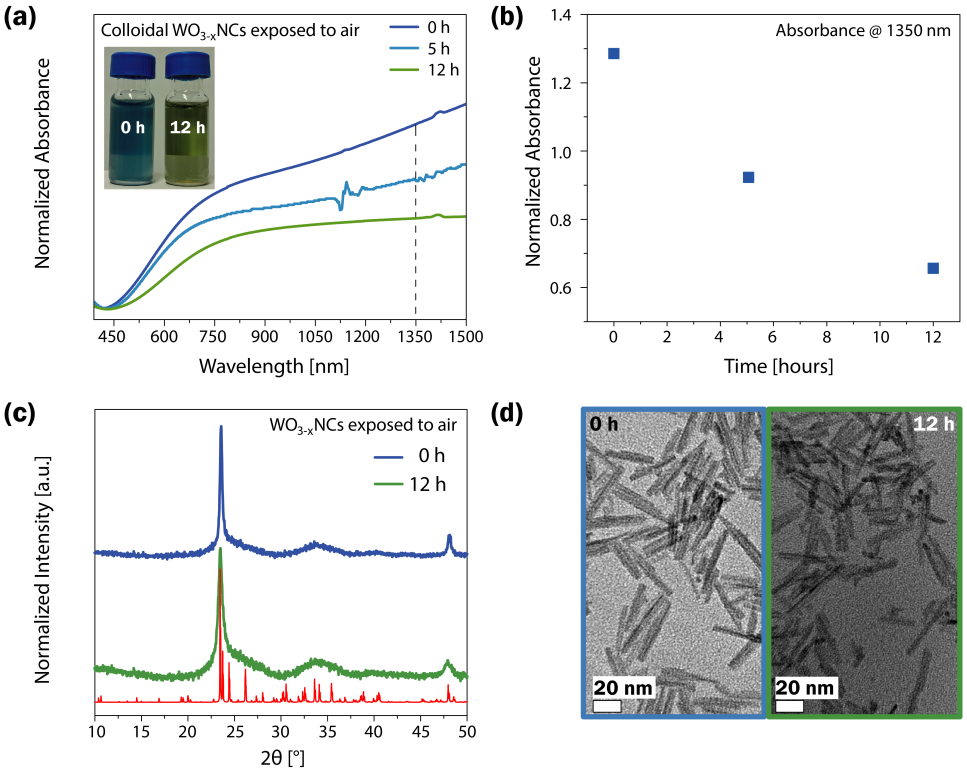



Figure 3.4: Structural and optical characterization of colloidal native $WO_{3-x}$ NCs exposed to air for various time durations. (a) Band-gap-normalized (285 nm) steady-state optical extinction spectra of NCs exposed to air for 0-15 h (colored traces), demonstrating the decay of LSPR. Inset displays photographs of NC dispersions exposed to air for 0 h (left) and 15 h (right). (b) Time evolution of LSPR decay from (a) monitored at 1350 nm. (c) XRD pattern of NCs exposed to air for 0 h (blue trace) and 15 h (green trace). (Reference: ICSD no. 24731). (d) TEM micrographs of NCs exposed to air for 0 h (left) and 15 h (right).

As can be seen in Figure 3.4a, the as-synthesized NCs (dark blue trace) exhibited a broad and intense absorption band starting at 450 nm and extending into the visible-NIR region with a shoulder appearing near 750 nm. While the spectral feature in the visible region

showed negligible deviation, the NIR absorption bands beyond 850 nm (light blue and green traces) exhibited a significant red shift and an exponential decrease in intensity as a function of time (Figure 3.4b). This observation can be clearly attributed to the decrease of free carrier density ($N_e$) in the NCs. Interestingly, $WO_{3-x}$ NCs exposed to air for 15 h showed no alterations in crystal structure (Figure 3.4c) and morphology (Figure 3.4d) compared to the as-synthesized NCs.

### 3.2.2 Magneto-Optical Properties of Colloidal $WO_{3-x}$ NCs

5 K MCD spectra of $WO_{3-x}$ NCs collected at different magnetic fields are shown in Figure 3.5a. While our spectropolarimeter does not allow us to carry out the measurements in a broad NIR range, the recorded MCD spectrum is consistent with the absorption spectrum in Figure 3.3c. We observed an increased MCD signal intensity in the visible range starting at ca. 400 nm, which has a positive sign and a shoulder at ca. 600 nm. A much narrower MCD peak centered at ca. 330 nm coincides with the band gap absorption (inset in Figure 3.5a). An increase in the magnetic field strength leads to an increase in the MCD intensity for both visible and NIR features. The MCD intensities are plotted against the magnetic field strength for different wavelengths in the visible-NIR range, which is the focus of this work, in Figure 3.5b. Surprisingly, there is an appreciable deviation in the field dependence, particularly at lower magnetic field strengths (1-5 T), for different wavelengths between 600 and 800 nm (Figure 3.5b). The MCD intensities at shorter wavelengths show a clear saturation trend with increasing magnetic field strength. At longer wavelengths, saturation gradually decreases, forming a larger spread between data points with increasing magnetic field strength. These results indicate that the absorption spectrum of $W_{3-x}$ NCs does not have a single origin (*i.e.*, only LSPR). The field-induced saturation of the MCD signal at 600 nm (the distinct shoulder observed in the MCD spectrum) is in excellent agreement with the Brillouin function characteristic for the spin state S = 1/2 (inset in Figure 3.5b, black line). Based on its magnetic field dependence and the agreement with the reported ligand-field spectroscopic investigations, we attribute the majority of the visible absorption, including the shoulder at 600 nm, to the d-d ligand field (LFT) transitions of $W^{5+}$ ($d^1$ system, S = 1/2).[206,207] On the other hand, the MCD signal at 800 nm largely has a linear dependence on the magnetic field (inset in Figure 3.5b, red line), which is characteristic for the plasmon resonance.[14,118] We, therefore, conclude that the room temperature absorption spectrum of $WO_{3-x}$ NCs in the visible range is only partly due to LSPR, contrary to the general assignment in the literature.[76,204,208]

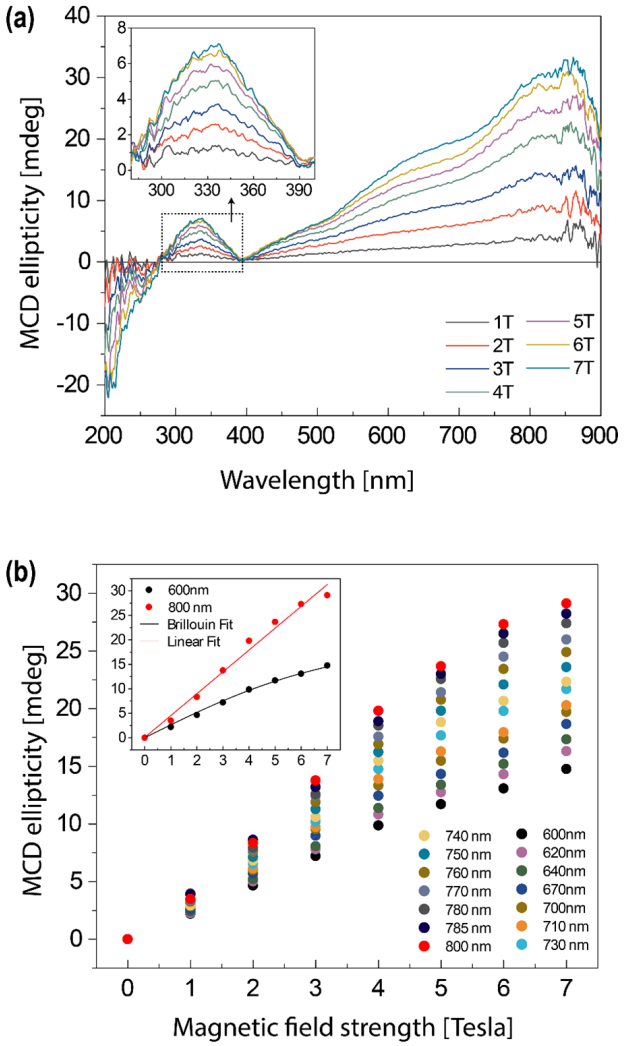



Figure 3.5: (a) 5 K MCD spectra of $WO_{3-x}$ NCs collected at different magnetic field strengths, as indicated in the graph. Inset: magnified MCD spectra in the excitonic absorption range. (b) Magnetic field dependence of the MCD signal intensity from (a) at different wavelengths, as indicated in the graph. Brillouin and linear fits to the spectral intensities at 600 and 800 nm, respectively, are shown in the inset.

The LSPR spectrum lies deeper in the NIR, which is also in agreement with the achievable carrier density in this material. Importantly, the spectroscopic transitions that may coexist with the LSPR in complex semiconductor NCs are often not readily distinguished in room-temperature absorption spectra, underscoring the effectiveness of MCD spectroscopy

for reliable identification of plasmon resonance. Excitonic MCD intensity also follows the linear dependence on the magnetic field owing to the transfer of the angular momentum from the plasmon-related free electrons in cyclotron motion to the excited states.[15,55,119,209]

### 3.2.3 Revisiting Optical Extinction Spectrum and Free Carrier Density of Colloidal $WO_{3-x}$ NCs

The variable-field MCD spectra presented in Figure 3.5 enabled the correct analysis of the optical extinction spectrum and determination of free carrier density of the $WO_{3-x}$ NCs. As can be seen in Figure 3.6, the low-temperature optical extinction spectrum of the NCs was deconvoluted into a LFT-band in the visible and LSPR band in the NIR region.

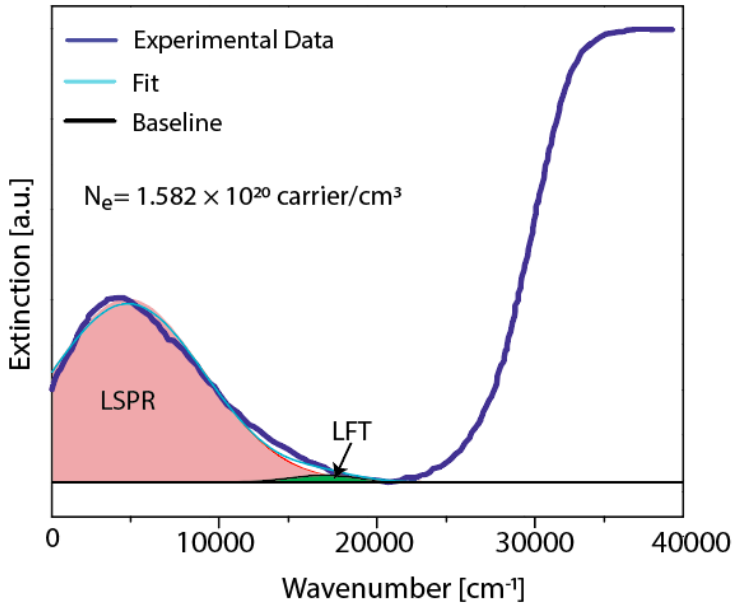



Figure 3.6: Low-temperature (5 K) steady-state UV–visible–NIR optical extinction spectrum of colloidal $WO_{3-x}$ NCs drop-cast on quartz MCD substrate. Deconvoluted bands are assigned to LSPR (red trace) and ligand-field transitions (LFT, green trace), respectively.

Table 3.1: Table summarizing the spectral features seen in Figure 3.9. along with their assignment.

| Carrier type/ Quasiparticle | Spectral Feature/ Transition | Spectral Position ($cm^{-1}$) | FWHM ($cm^{-1}$) |
|---|---|---|---|
| Free | LSPR | 4813.706 | 11510.52 ($\gamma$) |
| Localized | LFT ($W^{5+}$, d-d) | 17241 | 5000 |
| Exciton | Interband | 25487.12 | — |

*$\gamma$ value correspond to LSPR damping factor.*

To determine the free carrier density of the NCs, the analysis reported by Prusty et al.,[81] and Davis Jr. et al.[82] were adapted. According to Mie-Gans scattering theory, the polarizability ($\alpha_j$) of an oblate spheroid particle with axes $a = b > c$ (c corresponding to the rotational z-axis) is defined in equation 3.3:

$$\alpha = 3\epsilon_0 V \frac{\epsilon_j - \epsilon_m}{3\epsilon_m + 3L_j(\epsilon_j - \epsilon_m)} \tag{3.3}$$

$j = \{1, 2, 3\}$, $V$ is volume of spheroid, and $L_j$ are depolarizability factors for spheroid particles. Considering z as rotational axis, the geometrical factors are expressed in equation 3.4:

$$L_z = \frac{1}{e^2}(1 - \frac{\sqrt{1-e^2}}{e} arcsin(e)) \tag{3.4}$$

where $L_x + L_y + L_z = 1$ ($L_x = L_y$ are the in-plane depolarizability factors), and $e$ is eccentricity, defined as:

$$e^2 = \frac{a^2 - c^2}{a^2} \tag{3.5}$$

Based on Drude-Lorentz model (*vide infra*), for LSPR to occur the denominator of equation 3.3 must vanish, that is:

$$3\epsilon_m + 3L_j(\epsilon_{r,j} - \epsilon_m) = 0 \tag{3.6}$$

which enables the algebraic determination of the real part of $\epsilon_j$ (*i.e.*, $\epsilon_{r,j}$, as follows:

$$\epsilon_{r,j} = -\frac{(1 - L_j)}{L_j}\epsilon_m \tag{3.7}$$

Based on the Drude model, $\epsilon_r$ can be expressed as a function of frequency of light ($\omega$), according to equation 3.8:

$$\epsilon_r = \epsilon_\alpha - \frac{\omega_p^2}{\omega^2 + \gamma^2} \tag{3.8}$$

where $\epsilon_\alpha$= 4.5 was used as high frequency dielectric constant of tungsten oxide; $\omega_p$ is the bulk plasma frequency and $\gamma$ is the bulk collision frequency. Using equations 3.7 and 3.8, the $\omega_{LPSR}$ can be quantified, as:

$$\omega_{LSPR}^2 = \frac{\omega_p^2}{\epsilon_{alpha} + \kappa\epsilon_m} - \gamma \tag{3.9}$$

where $\kappa$ is shape factor and defined as:

$$\kappa = \frac{1 - L_j}{L_j} \tag{3.10}$$

For any plasmonic material, the bulk plasma frequency $\omega_p$ directly relates to the free carrier density $N_e$ as follows:

$$\omega_p^2 = \frac{N_e e^2}{\epsilon_0 m_e} \tag{3.11}$$

where $m_e$ and $m_0$ are the effective mass and rest mass, respectively, of an electron ($m_e$ = $1.2m_0$ for colloidal plasmonic non-stoichiometric $WO_{3-x}$ nanorods).

Using eqs. 3.9 and 3.11, $N_e$ in colloidal plasmonic non-stoichiometric $WO_{3-x}$ nanorods can be qunatified, as follows:

Based on Figure 3.6, $\omega_{LSPR}$ and FWHM in $WO_{3-x}$ NCs is:

$$\omega_{LSPR} = 1.44 \times 10^{14} Hz \implies \omega_{LSPR}^2 = 2.08 \times 10^{28} Hz^2$$

$$FWHM(=\gamma) = 3.45 \times 10^{14} Hz \implies \gamma^2 = 1.19 \times 10^{29} Hz^2$$

**Charge carrier (electron) parameters**:

$\epsilon = 8.85419 \times 10^{-12}$ F/m
$m_e = 1.2 \times m_0 \approx 1.09308 \times 10^{-30}$ kg
$|e| \approx 1.60218 \times 10^{-19}$ C

From which the $\omega_p$ of $WO_{3-x}$ NCs can be quantified as:

$$\omega_p = 6.47848 \times 10^{14} Hz \implies \omega_p^2 = 4.19708 \times 10^{29} Hz^2$$

From which, $N_e$ in $WO_{3-x}$ NCs is:

$N_e = 1.5824 \times 10^{26}$ carrier/m$^3$ $\approx$ $1.5824 \times 10^{20}$ **carrier/cm$^{-3}$**

The calculated free electron density ($\sim 1.582 \times 10^{20}$ cm$^{-3}$) above is generally consistent with values required to support LSPR in doped plasmonic metal oxides such as $WO_{3-x}$, $MoO_{3-x}$, $TiO_{2-x}$ NCs. At this carrier density, $\omega_{LSPR}$ is sufficiently high to generate strong plasmonic absorption features spanning the visible-NIR region. At higher energies in the visible region (∼400-600 nm), however, intraionic (d-d) ligand-field and polaronic transitions arising from $W^{+5}$ centers significantly contribute to the optical response. These transitions spectrally overlap with the LSPR tail appearing in the late visible (>750 nm) and NIR regions (Figure 3.6 and Figure 3.7a), resulting in broad optical extinction bands. Such interplay between plasmonic and localized electronic excitations underlies the pronounced broadband optical behavior characteristic of these highly doped metal oxide systems.

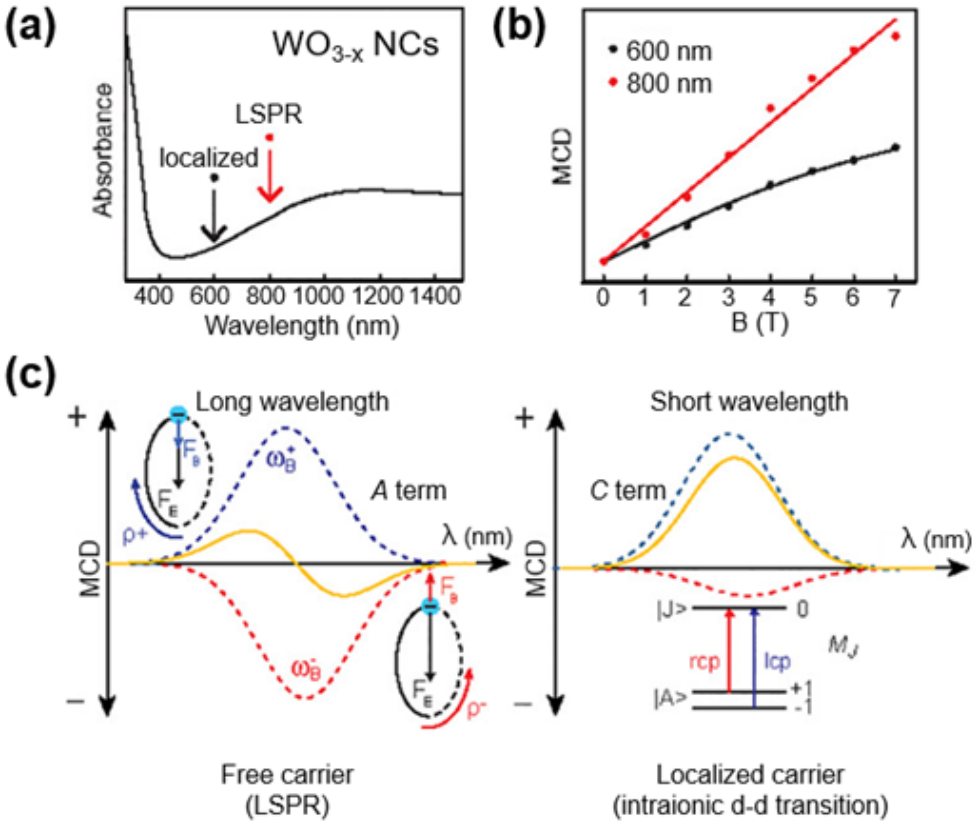



Figure 3.7: (a) Broad steady-state optical extinction band of colloidal $WO_{3-x}$ NCs. Black and red arrows indicate spectral positions of intraionic d-d transition (localized carriers) and LSPR (free carriers), respectively. (b) Schematic figure depicting magnetic field dependence for monochromatic MCD intensity of colloidal $WO_{3-x}$ NCs collected between 0–7 T at 5 K. Localized carriers (black trace) and free carriers (red trace) exhibit saturating or linear magneto-optical response, respectively. (c) Schematic figure representing the behavior of cyclotron free carriers (left panel) and localized carriers (right panel) in a nonzero magnetic field generating characteristic MCD spectral features, along with splitting mechanism and the corresponding Faraday MCD terms.

# Chapter 4

## Aspect-Ratio-Controlled Excitonic Zeeman Effects in Alkali Tungsten Bronze Nanocrystals Revealed by Magnetic Circular Dichroism Spectroscopy

In this chapter of my thesis, I present the aspect-ratio-controlled modulation of the the magnetic- field-induced exciton polarization in plasmonic hex-Cs:$WO_{3-x}$ NCs. Variable-field MCD spectra reveal a transition from excitonic Zeeman splitting driven by localized electrons in platelets (low AR nanostructures) to exciton polarization dominated by free-carrier cyclotron effects in rods (high AR nanostructures). The observed trends arise from electron localization differences between the basal plane (a–b) and prismatic (c) plane of the NCs. I present how paramagnetic electrons localized on oxygen vacancies in the basal plane ($V_{o,a}$) lead to spin-induced Zeeman splitting of the excitonic states, while the alkali-derived free carriers itinerant along the prismatic plane enable cyclotron-induced exciton polarization.

## Overview

Plasmonic nanostructures are characterized by a quantized collective oscillation of free charge carriers induced by resonant photon absorption. Charge carriers in plasmonic nanostructures can interact with other quasiparticles, including excitons, phonons, or magnons, under specific conditions, resulting in the emergence of unique quantum phenomena. Here we investigated the effect of geometry of substoichiometric plasmonic Cs:$WO_{3-x}$ NCs on the interactions between free electrons and excitons. By adjusting the colloidal synthesis conditions, we controlled the NC aspect ratio (height/width) and thereby the location, concentration, and spatial distribution of charge carriers and their interaction with the

exciton in prism-shaped Cs:$WO_{3-x}$ NCs. Using magnetic circular dichroism spectroscopy (MCD), we demonstrate the modulation of the magnetic-field-induced excitonic Zeeman effects in these nanocrystals as a function of their aspect ratio, enabled by the cooperative effect of strong electron localization on oxygen vacancies at the basal plane and the delocalization of Cs-derived electrons along the prismatic plane. The results of this work show that modulation of the carrier-exciton interactions in degenerately doped semiconductor NCs can be achieved by manipulation of their aspect ratio, as a simple geometric parameter, providing a potential for applications of these materials for research in nanophotonics, optoelectronics, and correlated quantum materials.

## 4.1 Introduction

Collective oscillations of free charge carriers driven by resonant photon absorption in nanostructures exhibiting subwavelength spatial confinement, called localized surface plasmon resonance (LSPR), has been at the forefront of research in nanophotonics over the past few decades.[210] In particular, plasmonic semiconductor metal oxide NCs have attracted ever-increasing attention in recent years owing to their highly controllable free charge carrier densities ranging from $10^{18}$ to $10^{22}$ $cm^{-3}$,[4,23] which, in contrast to noble-metal NCs, can be modulated by different doping strategies,[11,52] including aliovalent,[54,58,103,115,211,212] electrochemical,[63] vacancy,,[73,75,81] or photon-induced doping.[213,214] Based on the semiclassical Drude model of metallic conductivity, modulation of carrier density enables tuning of the LSPR absorption from the NIR to MIR range,[3,23,73,75] rendering plasmonic metal oxide NCs excellent candidates for a wide range of nanophotonic applications, including NIR-MIR photodetection,[215,216] electrochromic smart windows,[217–220] photocatalysis,[146,172] sensing,[221,222] and surface-enhanced Raman[222] or infrared spectroscopies.[124,184]

Interestingly, certain plasmonic semiconductor NCs may possess anisotropic morphologies (e.g., $WO_{3-x}$ rods,[76] $Cu_{2-x}Te$ platelets,[223] In-doped CdO (In:CdO) cuboctahedra,[224] and $Cu_{2-x}S$ disks[225]), resulting in shape-dependent LSPR spectra. For instance, hexagonal cesium-doped tungsten oxide (hex-Cs:$WO_3$ or CWO) nanoprisms have been reported to exhibit dual-band dipolar LSPR in the visible and NIR regions assigned to longitudinal ($LSPR_{\parallel}$) and transverse ($LSPR_{\perp}$) plasmon modes, owing to the difference in the effective carrier mass (m*), high-frequency permittivity ($\epsilon_{\infty}$), and damping factor ($\gamma$) along the prismatic (c-axis) and basal (a- and b-axis) planes.[7,20,89,178] Recently, experimental and computational studies have revealed a strong correlation between LSPR band splitting and NC aspect ratio (AR = height/width), demonstrating morphology-dependent tunability of the LSPR energy for colloidal hex-Cs:$WO_3$ NCs. Surprisingly, while the low aspect-ratio platelets (AR $\approx$ 0.3) exhibit a large splitting of the LSPR band, as expected, with $LSPR_{\perp}$ and $LSPR_{\parallel}$ centered at ca. 0.8 and 1.75 eV, respectively, a dual-band LSPR

absorption spectrum has also been observed for iso-prisms having AR $\approx$ 1, with a significant bathochromic shift of the $LSPR_{\parallel}$ (ca. 0.38 eV) and a much smaller hypsochromic shift of $LSPR_{\perp}$ (*ca.* -0.16 eV). For AR $\approx$ 1.8 (nanorods), the two LSPR modes overlap (both peak at *ca.* 1 eV), indicating that the spectral position of the LSPR absorption band for hex-Cs:$WO_3$ NCs is a result of the strong interplay between the shape and crystalline anisotropy.,[7,178] Importantly, different studies on the electronic structure of oxygen-deficient hex-Cs:$WO_{3-x}$ NCs have suggested the 2-fold origin of the free carriers. On one hand, the electrons associated with charge compensation of $Cs^+$ dopants that occupy the W $d_{yz}$ and $d_{zx}$ orbitals become fully delocalized along the prismatic plane.[21] On the other hand, electrons originating from oxygen vacancies are partially localized on the W $d_{xy}$ and $d_{x^2-y^2}$ orbitals, which lie near the conduction band edge and are associated with the basal plane.[8,9,95,226]

Since the localized surface plasmon is generated by resonant photon absorption, the polarization of the coherently oscillating free carriers can also be manipulated in plasmonic nanostructures.[19,117] For instance, when a localized surface plasmon is resonantly excited by left and right circularly polarized light (LCP and RCP, respectively), the free carriers undergo cyclotron motion in opposite directions, leading to the formation of two degenerate cyclotron plasmonic modes of opposite helicity. In the presence of a homogeneous and uniform external magnetic field applied parallel to the direction of light propagation, an additional magnetic Lorentz force ($\vec{F_L}$) acts on the cyclotron free carriers (eq 4.1), lifting the degeneracy of cyclotron magneto-plasmonic modes.[118]

$$\vec{F_L} = m^* \cdot (d\vec{v}/d\vec{t}) + \gamma m^* \cdot \vec{v} = q(\vec{E} + (\vec{v} \times \vec{B})) \tag{4.1}$$

In eq 4.1, $\vec{B}$ is the external magnetic field strength; q, $\vec{v}$, $m^*$, respectively, are the charge ($q = -|e|$ for the electrons, and $q = +|e|$ for the holes), velocity, and effective mass of the carriers; and $\gamma$ is the damping factor. The magnetic-field-induced splitting of the cyclotron plasmonic modes is a linear function of the applied magnetic field strength and can be detected using magnetic circular dichroism (MCD) spectroscopy, which measures the differential absorption of LCP and RCP light in an external magnetic field.[118] Importantly, in degenerately doped n-type semiconductor NCs (e.g., Sn:$In_2O_3$, Al:ZnO, etc.), wherein the conduction band is highly populated by free electrons, the circular motion of free carriers near the Fermi level can transfer their angular momentum to the exciton, leading to the net polarization of the conduction band states.[13,55,119] However, in nonstoichiometric plasmonic metal oxide NCs (e.g., $WO_{3-x}$, $MoO_{3-x}$, etc.), the LSPR originates from the electrons generated *via* charge compensation caused by the presence of oxygen vacancies as native defects. These electrons can become partially localized near the donor-defects (e.g., oxygen vacancies) generating paramagnetic states ($W^{5+}$, $Mo^{5+}/d^1$), which, in turn,

leads to spin-induced splitting of the NC band states.[13,119,179] The type and relative concentration of the free and localized carriers and the spatial distribution of the donor-defect states within the plasmonic NCs cooperatively affect the exciton splitting mechanism and carrier polarization.[119,179,227] Given the observed anisotropies of the LSPR, the exciton polarization can also be influenced by the NC shape and size, which is a much less explored phenomenon.[209,228]

In the present work, we investigated the aspect-ratio-controlled modulation of the magnetic-field-induced exciton polarization in plasmonic Cs:$WO_{3-x}$ NCs, as a model system for the shape and crystalline anisotropy of the plasmonic properties of semiconductor NCs. For the platelets (low-AR nanostructures), we observed a strong saturation of the excitonic MCD signal with increasing magnetic field strength, arising from the presence of highly localized unpaired electrons. On the other hand, for the iso-prisms (mediumAR anostructures) and rods (high-AR nanostructures), we observed a combination of saturation and linear dependence, and fully linear dependence, respectively, of the excitonic MCD signal on the magnetic field strength. These differences are attributed to the interplay of the spin- and plasmoninduced polarization of the excitonic states, which is determined by the effect of NC faceting on the carrier localization. The results of this study demonstrate that manipulation of the aspect ratio of degenerately doped semiconductor NCs can allow for unique control of their excitonic magneto-optical properties, providing promising opportunities for further fundamental investigations and potential applications of this phenomenon in quantum technologies.

## 4.2 Results and Discussion

### 4.2.1 Structural and Optical Characterization of Cs:$WO_{3-x}$ NCs

The family of interstitially doped transition metal oxides of the general formula $A_yMO_{3-x}$ (A: {alkali metal}; M: {W, V, Ti, Nb, or Mo}), called bronzes may adapt various crystal structures depending primarily on the radius of dopant ion intercalated and the extent of non-stoichiometry. For instance, doping with smaller alkali ions (e.g., $Li^+$ or $Na^+$) generate perovskite tungsten bronzes, while the presence of larger alkali ($K^+$, $Rb^+$, $Cs^+$) or complex (e.g., $NH_4^+$) ions at interstitial lattice sites leads to the formation of hexagonal tungsten bronzes.[86,88] In the present study, we synthesized three different samples of Cs:$WO_{3-x}$ (henceforth CWO) colloidal NCs using specific molar ratios of OLAM and OLAC as parameters to control the AR (see the Materials and Methods section). As shown in Figure 4.1a-c, significant peak broadening is observed in measured XRD patterns for all samples (thick lines) relative to the simulated pattern of bulk hexagonal $Cs_{3-x0.33}WO_3$ reference ($P6_3/mcm$, thin lines), providing qualitative confirmation of the nanocrystalline nature of

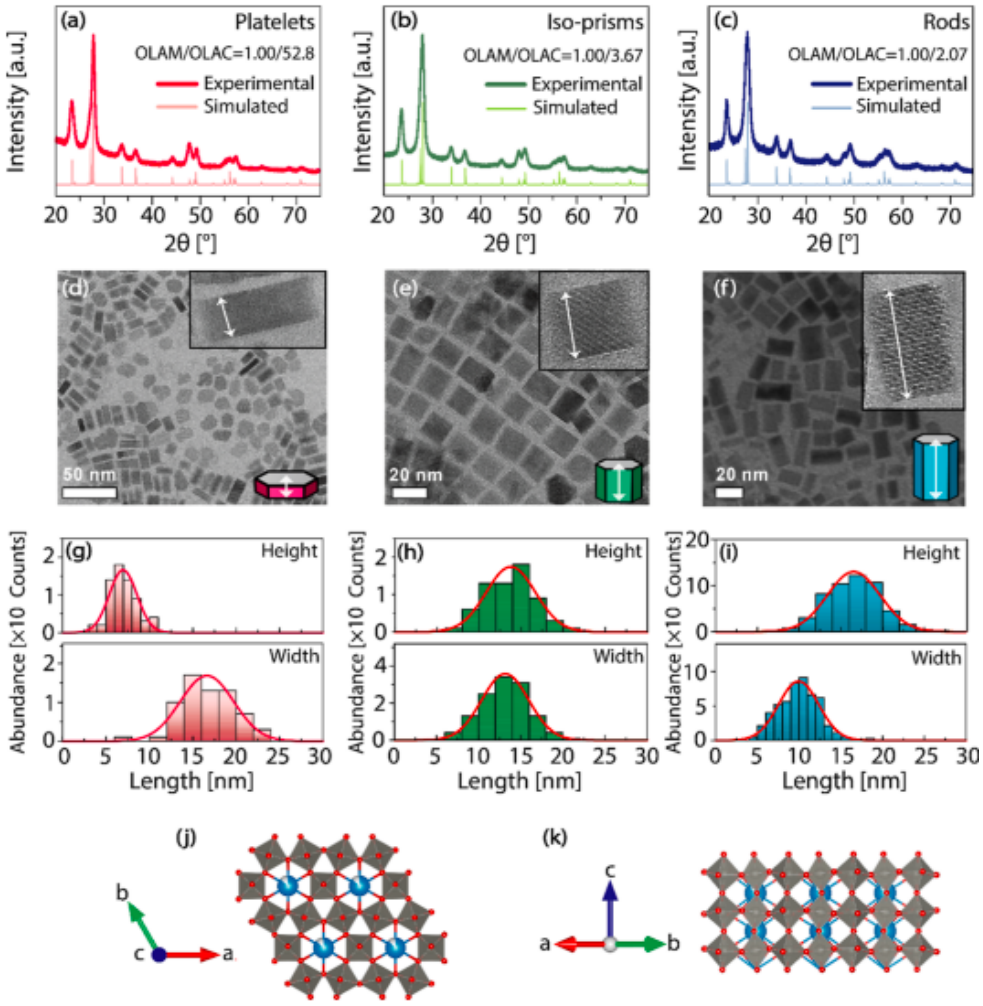



Figure 4.1: (a-c) XRD patterns of the (a) platelets, (b) iso-prisms, and (c) nanorods. Simulated XRD patterns of bulk $Cs_{0.33}WO_3$ (ICSD 253809) are shown as thin colored lines. (d-f) TEM micrographs of the (d) platelets, (e) iso-prisms, and (f) rods. Corresponding lattice-resolved TEM images of individual NCs along the prismatic plane are shown in the top insets, and white arrows indicate the NC dimension (length) along the <002> direction. Bottom insets illustrate the corresponding NC shapes. (g-i) Size distribution histograms corresponding to NC height (top panel) or NC width (bottom panel) for (g) platelets, (h) iso-prisms, and (i) rods. (j, k) Crystal structure of CWO NCs oriented along (j) basal and (k) prismatic planes.

each sample. The $P6_3/mcm$ phase was chosen as a reference XRD pattern since no *(h0l)/l* = odd reflections were present in the experimental diffractograms and because the alkali content Cs/W $\geq$ 0.25 was determined by EDS measurements (Table 4.1, and Figure 4.4).[229] The excellent match between the peak positions in the experimental and reference XRD patterns attests to the formation of hexagonal-phase CWO NCs. The absence of any reflections attributed to secondary crystal phases indicates that all three samples possess a high phase purity. Two most intense peaks near 23° and 28° can be assigned to the (002) prismatic and (200) basal planes, respectively.

The TEM micrographs presented in Figure 4.1d-f reveal shape-uniformity and the single-crystalline nature of the samples corresponding to XRD patterns in Figure 1. The OLAM/ OLAC molar ratios of 1.00:52.8, 1.00:3.67, and 1.00:2.07 correspond to the formation of platelets (Figure 4.1d), iso-prisms (Figure 4.1e), and nanorods (Figure 4.1f), respectively, proving the successful control of AR via the implemented synthesis method (see Materials and Methods). High-resolution TEM images (top right insets) display the height of the prismatic plane of the corresponding single nanostructures along the < 002 > growth direction (white arrows). In the high-resolution TEM images, we observed a slight decrease in the lattice spacing along the < 002 > direction as a function of AR (Figure 4.2).

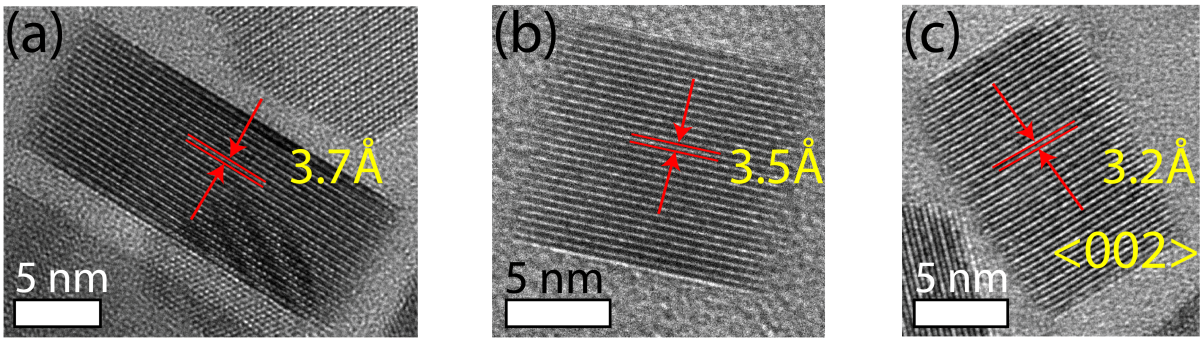



Figure 4.2: High-resolution TEM micrographs of the prismatic planes of (a) platelets, (b) iso-prisms, and (c) rods presented as insets in Figure 1d-f.

The size distribution histograms (Figure 4.1g-i) of the NC height (top panels) and width (bottom panels) were determined using a large number of NCs (Figure 4.3), and the obtained values are given in Table 4.1 (additional calculations can be found in Table 4.2). By taking the arithmetic ratio of the mean height (H) and width (W) values obtained from the histograms, the mean AR was found to be 0.4, 1.0, and 1.7 for the platelets, iso-prisms, and rods, respectively (Table 1). Apart from a small decrease (∼6 nm) in the lateral (basal

plane) and a more appreciable increase (∼12 nm) in the axial (prismatic plane) dimension of the NCs, a narrow size distribution was observed for both H and W as the AR increases. From this observation, one can infer that H plays the main role in the variation of AR, which is also related to the changes in the NC volume and the surface-to-volume ratio, as the most critical variable for the native defect concentration in NC systems.

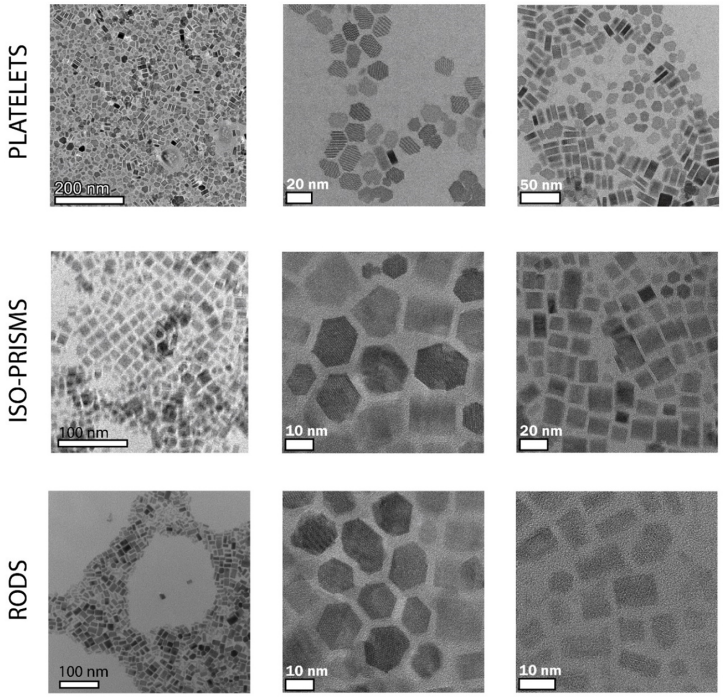



Figure 4.3: TEM micrographs of CWO platelets (upper panel), iso-prisms (middle panel), and rods (bottom panel). Left panels: overview micrographs, middle panels: NCs oriented along basal planes, and right panels: NCs oriented along prismatic planes.

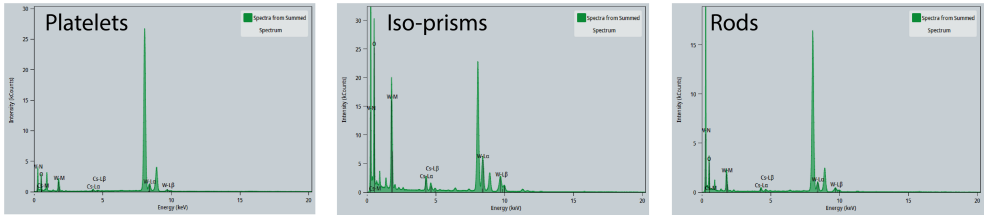



Figure 4.4: EDS spectra of CWO platelets (left), iso-prisms (middle), and rods (right).

Table 4.1: Geometric Parameters and Chemical Composition of As-Synthesized CWO NCs

| sample | height (H) [nm] | width (W) [nm] | mean AR (AR = H/W) | O 1s peak area ratio[a] | $W^{5+}/W^{6+}$ [%][a] | Cs/W [at %][a] |
|---|---|---|---|---|---|---|
| platelets | 7.0 (±1.6) | 16.6 (±3.1) | 0.4 | 5.18 | 15.9 | 0.25 |
| iso-prisms | 13.8 (±2.9) | 13.2 (±2.8) | 1.0 | 1.78 | 14.7 | 0.29 |
| rods | 16.6 (±3.2) | 9.9 (±2.4) | 1.7 | 0.46 | 15.4 | 0.27 |

In metal oxides, the native defects are predominantly oxygen-related (e.g., oxygen vacancies, surface hydroxyl groups, or under-coordinated surface oxygen sites). These native defects have recently been reported to strongly correlate to the electronic properties of metal oxide NCs, depending on their concentration, location, and interaction within a NC.[109,228] To quantitatively assess the native defect concentration as well as the elemental surface composition, we performed W 4f and O 1s XPS measurements for each CWO NC sample. Oxygen 1s XPS spectra (Figures 4.6a) collected for the platelets iso-prisms (middle), and rods (bottom) consist of two prominent peaks with the maxima near 532.3 eV (light shaded area) and 531.8 eV (dark shaded area), which can be assigned to the oxygen-related defects and lattice oxygen, respectively. The low-intensity signals at higher binding energies near 533.8 eV can be attributed to oxygen-containing ligands on NC surfaces and organic surface contaminants.[230] To quantitatively assess the correlation between the AR and the native defect concentration, we determined the ratios of the oxygen defect to lattice oxygen peak areas and normalized them to the NC volume fractions assuming 2 nm penetration depth of X-ray photons (Figure 4.5 and Table 4.2). A decreasing trend in the volume-fraction-normalized O 1s XPS peak ratio with increasing AR was observed (Figure 4.7), whereby the platelets possess the highest concentration of oxygen defects (84%), relative to the iso-prisms (64%) and rods (31%). This trend in the oxygen defect concentration is in excellent agreement with that found for other plasmonic metal oxide NC systems.[228]

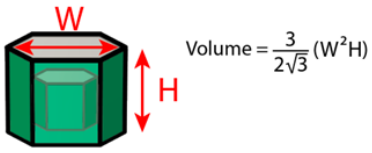



Figure 4.5: Cartoon depicting the outer and inner shells of an iso-prism. Red arrows indicate the NC height (H) and width (W). The formula on the right was used to determine the volume of the hexagonal prism-shaped CWO NCs.[20]

Table 4.2: Calculated Parameters for As-synthesized CWO NCs Determined from TEM Images.

| Sample | Height (H) [nm] | Width (W) [nm] | Mean AR (AR=H/W) | Outer Vol. [$nm^3$] | Inner Vol. [$nm^3$] | Volume Fraction[a] |
|---|---|---|---|---|---|---|
| **Platelets** | 7.0 (±1.6) | 16.6 (±3.1) | 0.4 | 1663.33 | 917.47 | 0.55 |
| **Iso-prisms** | 13.8 (±2. 9) | 13.2 (±2. 8) | 1.0 | 2082.37 | 1281.88 | 0.62 |
| **Rods** | 16.6 (±3.2) | 9.9 (±2.4) | 1.7 | 1408.99 | 789.11 | 0.56 |

[a] *To determine the volume fraction, the height and width of the nanocrystals were taken from the TEM image analysis (outer shell), both of which were reduced by 2 nm (inner shell) as the mean penetration depth of the X-ray probe.*

To investigate the surface composition and tungsten speciation in each sample of the AR series, W 4f XPS measurements were performed and the obtained spectra are shown in Figure 4.6b. For the platelets (top), iso-prisms (middle), and rods (bottom), two intense peaks are observed at ca. 35 and 38 eV, accompanied by a shoulder near 33.5 eV. Based on the spectral intensity, band shape, and binding energies of the observed features, the spectra (thick black traces) were deconvoluted into the $^4f_{5/2}$ and $^4f_{7/2}$ spin-orbit doublets of the $W^{6+}$ ion at higher binding energies (dark shaded area), and the $W^{5+}$ ion at lower binding energies (light shaded area).[230–232] Unlike the O 1s spectra in Figure 4.6a, W 4f spectra for the three samples are qualitatively similar, indicating a similar speciation of tungsten ions.

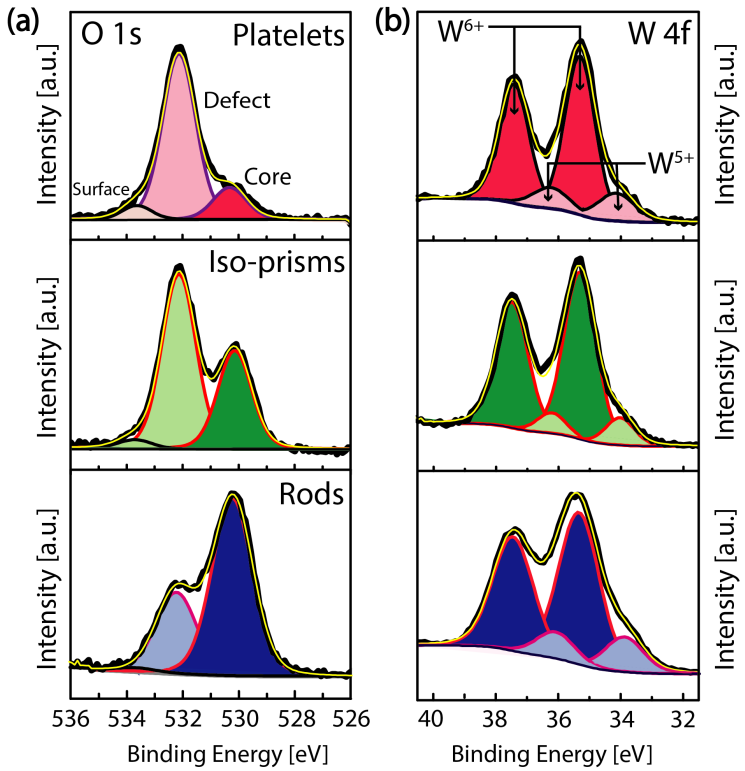



Figure 4.6: (a) O 1s and (b) W 4f XPS spectra (thick black traces) of platelets (top), iso-prisms (middle), and rods (bottom). Shaded areas represent spectral contributions of various oxygen species (a), or deconvoluted $W^{6+}$ and $W^{5+}$ 4f spin-orbit doublets (b), as indicated in the graphs, and yellow traces are overall fits to the experimental data.

Table 4.3: W 4f XPS Results for CWO NCs Presented in Figure 4.5.

| **Sample** | **$W^{5+}$ $4f_{5/2}$ Area** | **$W^{5+}$ 4f $_{7/2}$ Area** | **$W^{6+}$ 4f $_{5/2}$ Area** | **$W^{6+}$ 4f $_{7/2}$ Area** | **$W^{5+}/W^{6+}$ (%)** | **Vol. Frac. Norm. (%)** |
|---|---|---|---|---|---|---|
| **Platelets** | 554.83 | 738.06 | 3496.661 | 4651.46 | 15.9 | 28.9 |
| **Iso-prisms** | 1973.37 | 2625.19 | 13467.15 | 17914.28 | 14.7 | 23.7 |
| **Rods** | 5428.04 | 7220.71 | 35338.09 | 47005.91 | 15.4 | 27.5 |

Table 4.4: O 1s XPS Results for CWO NCs Presented in Figure 4.5.

| Sample | Carbonation (C-O) | $W^{5+}$-O ($V_o$) | $W^{6+}$-O (Core) | $V_o$/Core ratio | $V_o$/Core Vol. Frac. Norm. |
|---|---|---|---|---|---|
| **Platelets** | 2273.28 | 30677.48 | 5921.80 | 5.18 | 9.42 |
| **Iso-prisms** | 2047.97 | 39376.83 | 22168.49 | 1.78 | 2.86 |
| **Rods** | 1650.15 | 34627.78 | 75667.76 | 0.46 | 0.82 |

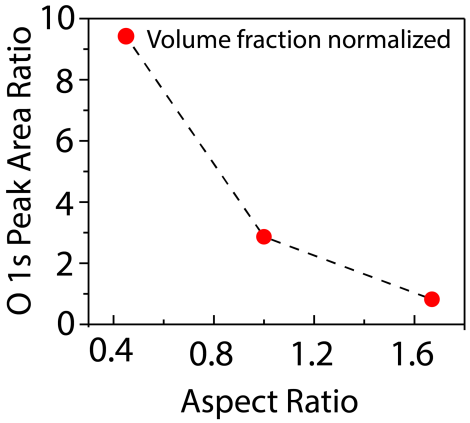



Figure 4.7: Volume-fraction-normalized O 1s XPS peak area ratio.

Taking into account the probe depth of the XPS measurements, the spectral analysis (Figure 4.6, and Tables 4.3 and 4.4) revealed negligible variations in the volume-normalized $W^{5+}/W^{6+}$ ratio across all of the samples in the AR series. Specifically, the $W^{5+}/W^{6+}$ molar ratio is estimated to be ~16% for the platelets and ~15% for both the iso-prisms and rods. This result is of particular importance since in nonstoichiometric tungsten(VI) oxides ($WO_{3-x}$), $W^{5+}$ ions are known to originate from the reduction of $W^{6+}$ ions by ionized oxygen vacancies in the host lattice ($Vo^{\bullet\bullet}$ or $Vo^{\bullet}$). Hence, the negligible deviations in the $W^{5+}/W^{6+}$ ratio would suggest a similar concentration of oxygen vacancies in the NCs regardless of the AR, which is at odds with the oxygen XPS spectra. These findings raise important questions about the origin of the defect formation in CWO NCs and their effect on the magneto-optical properties of NCs having different AR.

To address these questions, first we investigated the electronic structure of the CWO NCs by using steady-state optical absorption spectroscopy (Figure 4.8a). Two distinct regions are identified in UV-vis-NIR absorption spectra in Figure 3a for the platelets (pink trace), iso-prisms (green trace), and rods (blue trace). A feature at the high-energy side

with a strong onset at ∼3 eV and monotonously extending into the UV region is assigned to the excitonic (interband) transition. The optical band gaps are similar for all NCs, and they were determined using the Tauc plots to be ca. 3.97 eV (Figure 4.8a, inset). In the low-energy range, a broad band is observed for all three NC samples, which originates partly from the LSPR absorption in the NIR and partly from the polaronic absorption and/or $W^{5+}$ intraionic d-d transitions in the visible (vide supra).[8,9,95,179,233] For the iso-prism (green trace) or rod samples (blue trace), only one absorption peak appears near 0.9 eV whose bandwidth is slightly broader for the iso-prisms (1.1 eV) compared to the rods (0.73 eV) due to the somewhat larger separation of the polaronic and longitudinal/transverse LSPR modes. For the platelets (pink trace), a clear splitting of the NIR band is observed, with the appearance of two distinct peaks near 1.3 and 0.7 eV, ascribed to the mixture of polaron and longitudinal LSPR absorption at higher and the transverse LSPR absorption at lower energies. Absorption spectra of the CWO thin films prepared by drop-casting colloidal NCs on quartz substrates are shown in Figure 4.8b. Despite a slight divergence caused by differences in the film thickness, all NC samples exhibit extinction profiles in the UV-visible region similar to those of the colloidal NC dispersions in Figure 4.8a.

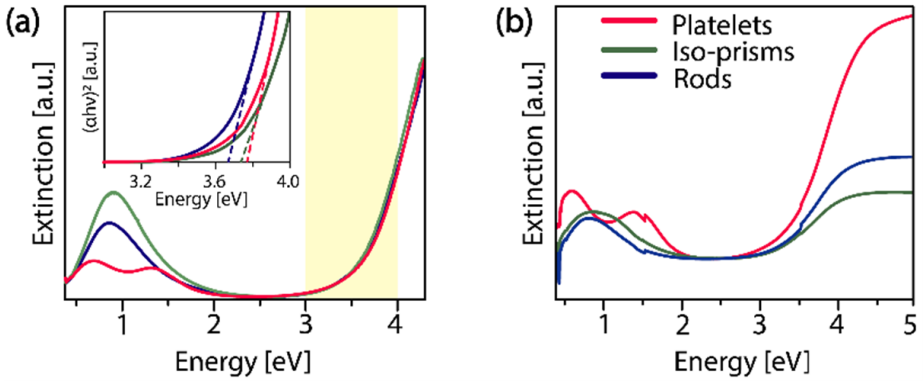



Figure 4.8: Optical extinction spectra of (a) colloidal suspensions of CWO NCs in TCE and (b) CWO NCs deposited on quartz substrates by drop casting from colloidal suspensions. Different traces correspond to specific NC shape (AR), as indicated in the graphs. Tauc plots for NCs having different ARs are shown in the inset of (a).

### 4.2.2 Magneto-optical properties of Cs:$WO_{3-x}$ NCs

To investigate the effect of AR on the magneto-optical properties of CWO NCs, we performed MCD measurements on samples in Figure 4.8b. Figure 4.9 (left panels) compares the normalized 6 T, 5 K MCD spectra of the platelets (4.9a), isoprisms (4.9b), and rods

(4.9c). In the UV region (3.5-5.0 eV) each sample exhibits an intense positive band that coincides with the corresponding band edge absorption (see Figure 4.11a). Notably, for the nanoplatelet sample, an intense shoulder at ca. 4.4 eV is observed on the high-energy side of the excitonic MCD band (Figure 4.9a, left panel). Although much weaker and slightly red-shifted, this shoulder is also present in the spectra of iso-prisms and rods (left panels in Figure 4.9b,c, respectively). Based on their spectral position, we assign these shoulders to interband transitions between the valence band and high-erenergy excited states in the conduction band of CWO NCs, analogous to the ligand-to-metal charge transfer (LMCT) transition in $[(WO)_6]^6$ complex (Figure 4.11b).[21,209] Meanwhile, on the low-energy side of the excitonic MCD band, a negative asymmetric signal with a minimum near 3.0 eV appears for each sample. This feature merges with the blue tail of the low-energy band. The assignment of this spectral feature to intraionic (d-d) ligand-field transitions can be ruled out because those usually appear at lower energies in the visible region (∼1.0-2.5 eV) for octahedrally coordinated $d^1$ transition metal ions ($V^{4+}$, $Ti^{3+}$, or $W^{5+}$).[234,235] This energy range, however, generally overlaps with interionic charge transfer ($O \rightarrow W^{5+}$) transition.[209]

Notably, the excitonic MCD signals (Figure 4.9a left panels) show singular polarization (*i.e.*, no derivative shape) for all CWO NC samples in the AR series. This is because in degenerately doped semiconductor NCs (such as CWO or Sn:$In_2O_3$ (ITO) NCs) in an external magnetic field the cyclotron motion of free charge carriers generates an angular momentum that is imparted to the excitonic states, inducing their selective polarization.[13] Importantly, cyclotron carrier-induced exciton polarization, and thus the sign and magnitude of the excitonic MCD signal, strongly depends on various factors related to intrinsic carrier properties (e.g., carrier type, concentration, scattering, delocalization, and effective mass) as well as the size and electronic band structure of the NC host lattice.[15,119,209] For instance, while the excitonic MCD band for CWO NCs is positively signed (Figure 4.9a left panels), typical n-type semiconductor NCs, including ITO, InN, and Sb:$SnO_2$ (ATO) NCs, have been observed to exhibit negatively signed excitonic MCD signals.[13,15,55,119,179,209] It has been proposed that this difference may be due to the different character of the conduction band, in analogy to diluted magnetic semiconductors (DMSs);[236] whereas the conduction band of CWO is composed predominantly of symmetry-sensitive W d orbitals, the conduction band of typical plasmonic semiconductor NCs is dominated by symmetry-invariant metal cation (In, Sn, Zn etc.) s orbitals.[15] In order to further investigate the magneto-optical behavior of CWO NCs having different aspect ratios, we performed variable-field MCD measurements (0-6 T, 5 K) for each NC sample in the UV-visible region (spectra shown in different colors in Figure 4.9, left panels). Among all of the aforementioned spectral features, the most prominent changes are observed within the excitonic region (∼3.2-5.0 eV). The intensity of the excitonic MCD signal increases with magnetic field strength for all samples, although at a different rate for the platelets compared to the iso-prisms, or

rods. While the excitonic MCD spectra for platelets begin to converge with increasing magnetic field strength, the increase in MCD intensity for iso-prisms or rods appears to be nearly or completely linear.

Based on the observed band shapes of the MCD spectra in the present study (see also Figure 4.11a for direct comparison), together with those reported for octahedral $d^1$ complexes, we deconvoluted the MCD bands of CWO NCs into two (for platelets) or three (for iso-prisms and rods) components, as shown in the insets of Figure 4.9a-c.[237] To quantitatively assess the field dependences of the excitonic transitions in different CWO nanostructures, we plotted the integrated intensities of the deconvoluted MCD peaks as a function of magnetic field strength (Figure 4.9, right panels), which show remarkable trends across the AR series. Specifically, while the data points corresponding to deconvoluted bands peaking at 3.70 and 4.29 eV for the platelets strongly saturate (red symbols), those at 3.53 and 3.79 eV for rods exhibit purely linear behavior (blue symbols). Interestingly, the coexistence of a saturating (3.53 eV) and linear (3.78 eV) trend was observed for the iso-prism sample (green symbols), thus forming an intermediate state between the platelets and rods with regards to the magneto-optical properties. Due to low spectral intensity, the magnetic field dependence of high-energy components at 4.12 and 4.07 eV for the iso-prisms and rods, respectively, was not further analyzed. These results are indicative of two interlinked phenomena: on one hand, the 2-fold magneto-optical behavior of the exciton manifesting in saturating or linear trends as a function of magnetic field strength and, on the other hand, the ability to modulate these trends using aspect ratio for CWO NCs. While the linear field dependence is characteristic of free carrier-induced MCD signal ($A$-term), the saturating excitonic MCD intensities indicate localized-carrier—exciton exchange interaction ($C$-term).44,47,48,50 $C$-term MCD typically assumes paramagnetism in the ground state, and the excitonic MCD intensity ($I_{MCD}$), therefore, saturates with the magnetic field ($B$) according to the Brillouin function in equation 4.2:

$$I_{MCD} = \frac{1}{2} N g_S \mu_B [(2S+1)\frac{g_S \mu_B}{2k_B T} - coth(\frac{g_S \mu_B}{2k_B T})] \tag{4.2}$$

where $N$ is the number density of paramagnetic centers and $S$ is their effective spin state, T is temperature, $\mu_B$ is Bohr magneton, $k_B$ is Boltzmann constant, and $g$ is Landé g-factor. Using a $g$ value of 1.663 (as the principal g-tensor element experimentally determined for electrons localized in the basal plane of triclinic sodium tungsten bronzes) and a net spin state ($S$) of 3/2, an excellent Brillouin function fit to the excitonic MCD intensity was achieved for platelets (black lines in the right panel of Figure 4.9a).[238] Variable-temperature MCD spectra of platelet-like NCs are also consistent with $C$-term behavior (Figures 4.10).

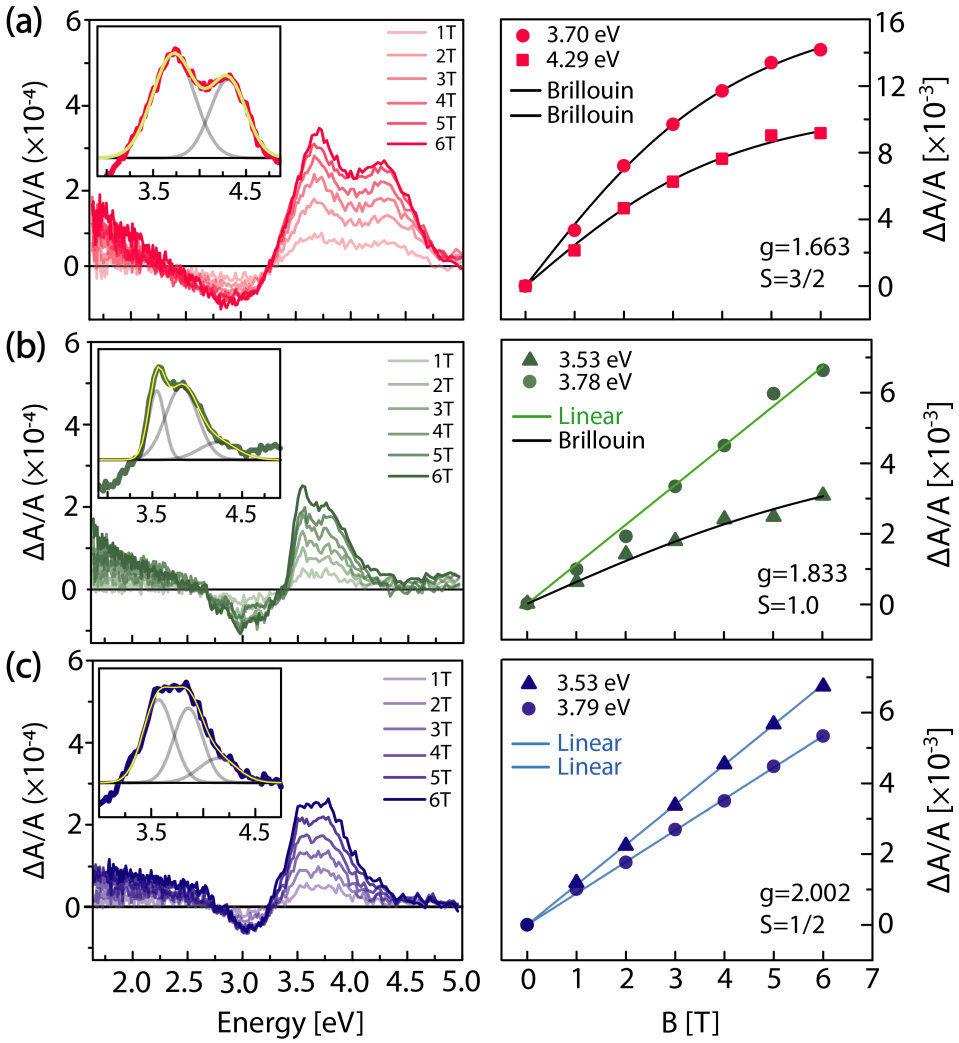



Figure 4.9: Variable-field 5 K MCD spectra of CWO NCs (left) and the corresponding magnetic field dependence of the integrated excitonic MCD intensities (right) for (a) platelets, (b) iso-prisms, and (c) rods. Insets in left panels show excitonic MCD band deconvolution, and the symbols in right panels correspond to deconvoluted components (designated by their peak maxima). The data in right panels are fit to linear or Brillouin function, as indicated.

Reconciling the electronic structure with NC geometry, namely, the relation between oxygen deficiency ($V_o$ content), carrier localization, and AR of CWO NCs, could enable

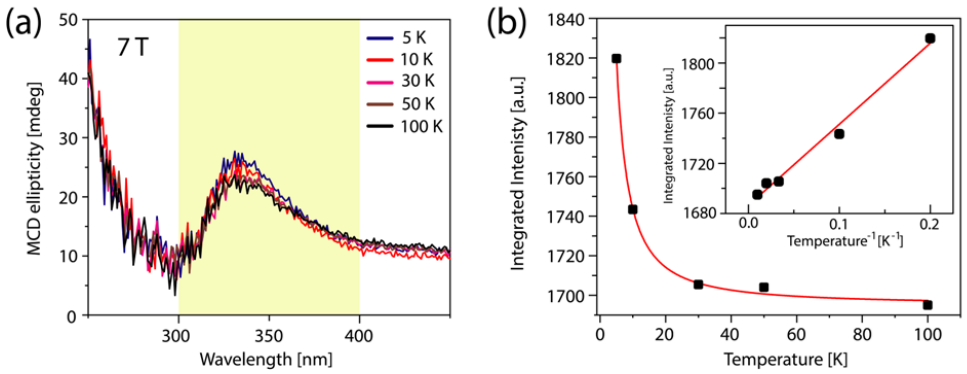



Figure 4.10: (a) 7 T MCD spectra of CWO NCs sample from Figure S7, recorded at different temperatures, as indicated in the graph. (b) Temperature dependence of the integrated intensities of the spectra from (a). Inset: Integrated intensities of the MCD spectra as a function of $T^{-1}$.

understanding of the magneto-optical properties presented in this study. In a number of studies, Yoshio and Adachi[8,9,95] provided elaborate analysis on the charge density distribution and optical excitation of free and localized carriers in a series of nonstoichiometric hex-$Cs_yWO_{3-x}$ ($0.163 \leq y \leq 0.33$; $0 \leq x \leq 0.33$) samples using ab initio density functional theory calculations and spectroscopic ellipsometry. Based on the electronic structure of the $[WO_6]^{6-}$ unit cluster, as a building block of hex-$WO_{3-x}$ (Figure 4.11b), the lowest-energy unoccupied electronic states accessible for dopant electrons lie in the $t_{2g}^*$ antibonding $\pi$-state, which are composed of W $d_{yz}$, $d_{zx}$, and $d_{xy}$ orbitals hybridized with axial (z) or equatorial (xy) p orbitals (Figure 1.6e). The W $d_{x^2-y^2}$ and $d_{xy}$ orbitals, on the other hand, are hybridized with equatorial oxygens to form $\sigma$ antibonding $e_g^*$ states at higher energies (Figure 1.6f).[9,21] Furthermore, electronic band structure and partial density of states (PDOS) calculations for alkali tungsten bronzes have revealed that the alkali-derived electrons populate W $d_{yz}$ and $d_{zx}$ states (Figure 1.6c-d) and exhibit free carrier behavior along the prismatic ($LSPR_{\parallel}$) and, to some extent, basal ($LSPR_{\perp}$) plane (Figure 4.12a, top). On the other hand, excess electrons on oxygen vacancies in the basal plane along the a-axis ($V_{o,a}$) are highly localized and generally do not contribute to the LSPR (Figure 4.12a, bottom).[8] The difference in the excitonic MCD signal intensity due to electron (de)-localization is illustrated in Figure 4.12b. Consequently, for the platelets, the $V_o$-derived carriers are mostly localized in the a-b plane within a small NC volume fraction (Figure 4.5), owing to the small thickness (*i.e.*, prismatic plane) of NCs, consistent with high (∼83.8%) oxygen deficiency observed in the O 1s XPS spectrum (Figure 4.6a, top panel). Although

some of the $V_o$-derived carriers may be delocalized, and therefore contribute to plasmonic absorption (mostly $LSPR_\perp$) together with the completely free Cs-derived carriers under resonance conditions, the overall carrier—exciton interaction in platelets under external magnetic fields appears to be predominantly due to localized electron spin (anomalous Zeeman effect), as evident from the strongly saturating excitonic MCD response. The high concentration of oxygen vacancies generating localized carriers (Figure 4.6a and 4.7) leads to a strong clustering and ordering of the paramagnetic spin states in the platelets, explaining the high net spin state (S = 3/2).

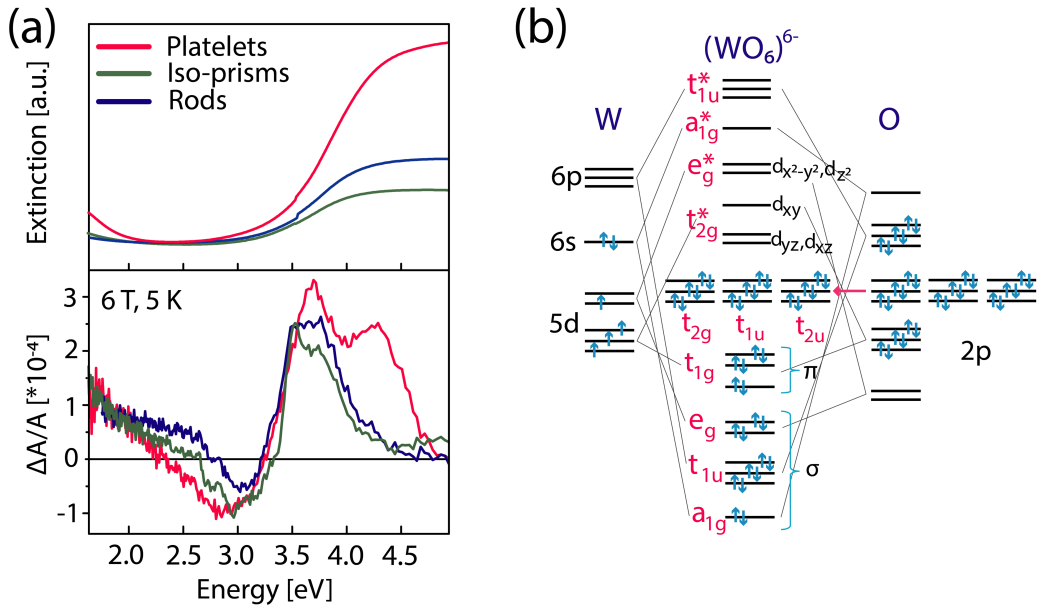



Figure 4.11: (a) Optical absorption (top) and absorbance-normalized MCD (bottom) spectra of CWO platelets (pink traces), iso-prisms (green traces), and rods (blue traces). The spectra were collected at 6 T and 5K. (b) Molecular orbital diagram of a $(WO_6)^{6-}$ octahedral unit of CWO NCs (adapted from Yoshio et al.[21])

A possible mechanism of such ordering, involving $W^{5+}$ and neighboring $V_o$, is illustrated in Figure 4.12c. Other configurations involving unpaired electrons on $W^{5+}$ or oxygen vacancies are also plausible. Based on XPS data from Figure 4.6, as AR increases from 0.4 to 1, the extent of oxygen deficiency drops significantly, inducing a nearly 3.5-fold decrease in $V_o$-derived carrier concentration (Figure 4.7) for the iso-prisms compared to platelets. This change in $V_o$ density leads to a reduced saturation of the excitonic MCD intensity (Figure 4.9b right panel). From the Brillouin fitting, the values of the apparent

spin state and the g-factor corresponding to the MCD intensity at 3.5 eV are reduced to 1.0 and 1.833, respectively. Although the contribution of spin-induced splitting in iso-prisms is a consequence of non-negligible concentration of localized carriers, increase in NC volume associated with elongated prismatic planes leads to Cs-derived free electrons, and a mixed contribution of spin-induced and free-carrier-induced exciton polarization mechanisms. For the rods, excitonic MCD intensity shows purely linear field dependence on the magnetic field (Figure 4.9c right panel), indicating a dominant contribution of free carriers, associated with the prismatic plane ($LSPR_{\parallel}$), to exciton polarization.

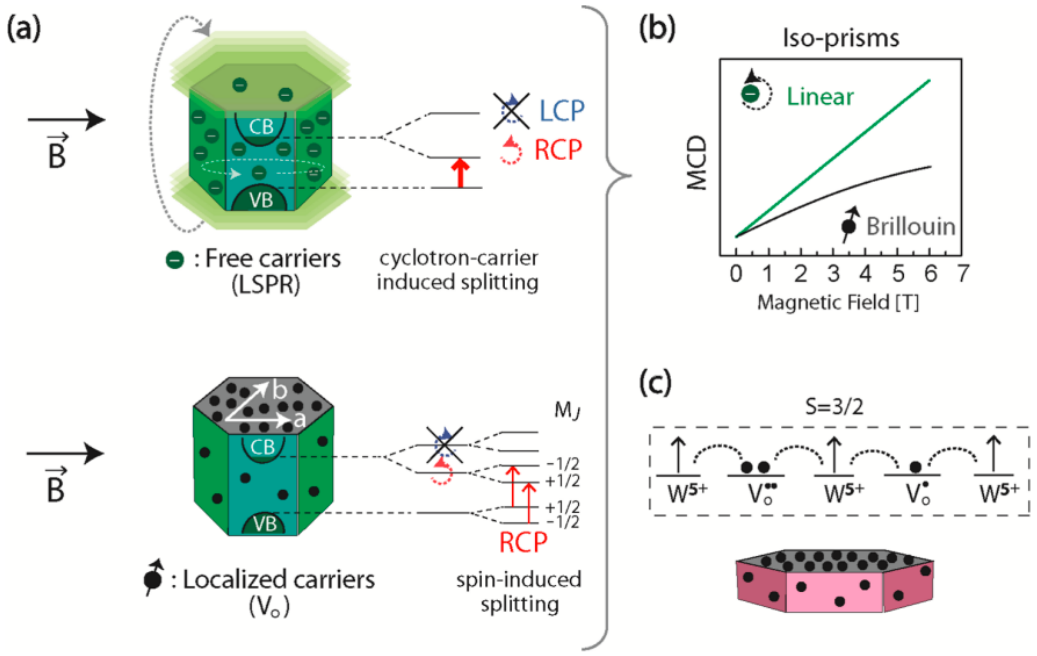



Figure 4.12: (a) Schematic representation of the exciton polarization mechanisms in CWO iso-prisms. (Top) exciton polarization induced by the angular momentum transfer from the cyclotron free electrons (dashed arrows) to the excitonic transition; (bottom) spin-induced excitonic Zeeman splitting caused by unpaired electrons localized on defect states (black dots). (b) Pictorial representation of the magnetic field dependence of the excitonic MCD signal intensity corresponding to the two exciton polarization mechanisms. (c) Illustration of the possible exchange interactions between $W^{5+}$ and neighboring $V_o$, responsible for the generation of high net spin state (S = 3/2).

Figure 4.12 shows a schematic representation of the two exciton polarization mechanisms in a CWO iso-prism. The free electrons undergoing a cyclotron trajectory in a

homogeneous external magnetic field transfer their angular momentum to the exciton, leading to net exciton polarization (vide supra). Concurrently, the carriers strongly localized on oxygen vacancy sites form paramagnetic states, leading to the spin-induced Zeeman splitting of the band edge states in an external magnetic field (Figure 4.12b). The coexistence of the two polarization mechanisms in CWO NCs leads to the linear or saturating excitonic MCD signals. The excitonic magneto-optical response trends depend on the extent of carrier localization as well as the concentration of localized and delocalized carriers within the NCs, which is ultimately related to AR.

## 4.3 Conclusions

In summary, we investigated the effect of the aspect ratio of substoichiometric hexagonal cesium-doped tungsten oxide (alkali tungsten bronze) NCs on their magneto-optical properties in the excitonic spectral range. Specifically, we performed low-temperature variable-field MCD measurements on nanometer-sized platelets (AR = 0.4), iso-prisms (AR = 1.0), and rods (AR = 1.7), exhibiting LSPR in the visible-NIR range. The LSPR in these materials originates from chargecompensating electrons generated in the presence of oxygen vacancies and Cs-derived free carriers. For the platelets, excitonic MCD signal intensity saturates with increasing magnetic field, indicating an excitonic Zeeman splitting induced by highly localized unpaired electrons. For the isoprisms, we observed a combination of saturation and linear dependence of the excitonic MCD intensity on the magnetic field, suggesting the coexistence of spin-induced excitonic Zeeman splitting and cyclotron-free-carrier-induced exciton polarization. The nanorods show a purely linear dependence of the excitonic MCD intensity on the magnetic field due to the dominant effect of the angular momentum from the cyclotron electrons. The observed trend is attributed to the difference in carrier localization on the basal and prismatic planes of hexagonal alkali tungsten bronze NCs. The excess electrons in the basal plane are largely localized on oxygen vacancies along the a-axis, resulting in anomalous Zeeman splitting, while those in the prismatic planes (mostly derived from the alkali metal dopants) are free, resulting in exciton polarization induced by free electrons in cyclotron motion. Modulation of the aspect ratio therefore allows for manipulation of the nature of carrier—exciton interactions and thus the exciton splitting pattern. The results of this work demonstrate that simple geometric parameters, such as the aspect ratio, of degenerately doped semiconductor NCs allow for manipulation of their exciton polarization and magneto-optical properties, providing promising opportunities for investigations and potential applications of these materials in spintronics and related quantum technologies.

# Chapter 5

## Enhancement of Photoresponse for InGaAs Infrared Photodetectors Using Plasmonic $WO_{3-x}$/Cs:$WO_{3-x}$ Nanocrystals

In this Chapter of my thesis, plasmonic non-stoichiometric $WO_{3-x}$ and Cs:$WO_{3-x}$ NCs are used as photoactive materials in epitaxially-grown planar InGaAs MSM photodetectors operating in the NIR spectral region. After characterizing the optoelectronic properties (such as dark and photocurrent current) of the fabricated devices, NCs were drop-cast on the active region of the devices. In the presence of the NCs, clear enhancements of photoresponsivity by up to a factor $\sim$2.5 was measured, broadly consistent with the plasmonic absorption spectra of the NCs. The study presented in this Chapter indicates that suitably prepared TCO NCs are a promising family of materials for NIR plasmonic applications.

## Overview

Semiconductor metal oxide nanostructures have been promising candidates for the development of novel photodetector devices owing to their widely tunable LSPR across the visible to NIR spectral region, besides their environmental benignity, and relatively low cost of production. Currently, the most widely explored and implemented technological platforms for improving the performance of NIR photodetection beyond that of the well-established III-V semiconductor p-i-n (PIN) junctions include the in-situ epitaxially-grown low-bandgap inorganic nanowire arrays, 2D nanostructures, or various hybrid organic-inorganic hetero-nanostructures as photoactive materials. However, the controlled growth of such photoactive nanostructures of high-quality has been imposing numerous technological challenges particularly in the large-scale and cost-effective production, and thus commercialization of most semiconductor-based optoelectronic devices. In this work, we

investigate a cost-effective approach for the enhancement of photoresponsivity in a planar metal-semiconductor-metal (MSM) NIR photodetector using colloidally-synthesized shape and size-uniform substoichiometric plasmonic $WO_{3-x}$ NCs and hexagonal Cs:$WO_{3-x}$ nanoprisms as NIR photoactive materials. We report a nearly three-fold enhancement of the optical-to-electric conversion efficiency in the fabricated photodetectors via the application of drop-cast colloidal suspensions of plasmonic $WO_{3-x}$ or Cs:$WO_{3-x}$ NCs. The results of this work demonstrate the potential for a scalable and cost-effective approach for improving NIR photodetector device performance using synthetically tailored plasmonic metal oxide NCs as photoactive materials.

## 5.1 Introduction

Light detection in the near-infrared (NIR) and infrared (IR) wavelength ranges has numerous applications in fields such as biomedical imaging and sensing, thermal imaging, and telecommunications.[131,239–242] Initially, mesoscopic-scale inorganic semiconducting materials were the primary candidates for developing faster, smaller, and more sensitive detectors. However, recent efforts have shifted towards engineering inorganic, organic, and hybrid inorganic/organic semiconducting nanostructures to significantly enhance performance, reduce device size, and create flexible form factor devices for industrial applications.[242–244] Promising approaches include designing III-V semiconductor nanowires, in situ-grown metal/semiconductor nanoparticles, and utilizing chemical vapor deposition or exfoliation techniques to produce 2D inorganic graphene/perovskite structures for optoelectronic devices.[243,245,246]

During the past few decades, interest in the physics and applications of IR photodetectors with a tunable band gap for telecommunication wavelengths ($\sim$1.2–1.7 $\mu$m) has grown, especially those based on III-V semiconductors such as InGaAs.[247,248] Several InGaAs photodetector designs are commonly studied, such as PN or PIN junctions, avalanche, and metal-semiconductor-metal (MSM) photodetectors.[248] MSM detectors are desirable for telecommunication applications due to their fast response times and ease of fabrication and integration with other electronics.[136,249–253]

A standard MSM photodetector consists of interdigitated metallic electrodes deposited on an active layer, such as InGaAs, forming two Schottky junctions in series. A finger electrode design is often chosen for simplicity of the device, both in terms of fabrication and characterization. MSM detectors can suffer from large dark currents due to relatively low Schottky barriers, however, this can be mitigated by introducing a lattice-matched InAlAs top layer to increase the barrier height. Performance improvements have been achieved through band gap tuning *via* $In_xGa_{1-x}As$ alloy concentration, Schottky barrier enhance-

ment, and superlattice structures.[248,251,254] In this paper, we explore the use of plasmonic semiconductor NCs to enhance the optical-to electrical conversion efficiency of InGaAs MSM photodetectors, as measured by responsivity in the wavelength range of 1-1.7 $\mu$m.

Plasmonics primarily focuses on the generation, propagation, and detection of plasmonic waves, which are collective electronic excitations resulting from the interaction between an electromagnetic (EM) field and a metal/dielectric interface.[255–257] When EM waves interact with a metallic surface, a coherent charge density oscillation coupled to the EM field arises, known as a surface plasmon. Strong nanoscale confinement leads to localized surface plasmon resonances (LSPRs), characterized by discrete optical absorption bands and electric fields orders of magnitude larger than those associated with free space EM waves. Given their nanoscale dimensions, integration of plasmonic nanostructures with micro- and nanoelectronic devices is possible, and holds the potential to enhance device performance or realize novel functionalities.

Conductors with sub-wavelength dimensions support LSPRs, whose resonance frequencies depend on the geometry and free carrier density of the nanostructure, as well as its orientation with respect to the polarization of the EM field. Depending on the material, LSPRs can span from the ultraviolet to the far-IR. Upon illumination, nanoscale regions of strong EM field enhancement, referred to as hot-spots, are generated at the surface of the structure. Plasmonics have been widely used to enhance the performance of photodetector and photovoltaic devices.[128,258–263] The enhanced EM field surrounding nanostructures can be harnessed in optoelectronic devices by generating LSPRs to improve responsivity across a broad range of frequencies. LSPR mechanisms that contribute to enhanced responsivity include: (1) increased concentration of the incident EM field and extended optical path length within the semiconductor, thereby enhancing photon absorption, and (2) plasmonic energy transfer from the nanostructure to the semiconductor through direct electron transfer.[264] Because of these broadband optical properties, plasmonic nanostructures have found use in a variety of applications including catalysis, medicine, surface chemistry, solar cells and sensing.[255–257,265–271]

Typically, Au and Ag nanoparticles (NPs) exhibit strong LSPRs and are used as plasmonic materials in the visible[272] or UV[273–275] spectral ranges. An emerging area of interest focuses on identifying high performance plasmonic materials compatible with other frequency ranges of interest, from NIR to terahertz.[216,276–278] Fundamentally, the physics of LSPR does not change in the IR compared to the visible region, but the material requirements are dramatically different. The optical resonances in Au and Ag can be tuned to a degree by changing the size and shape of nanostructures, but the charge carrier densities ($\sim 10^{22}$ cm$^{-3}$) that primarily determine the plasmonic frequency response are fixed. NIR applications require materials with lower carrier concentrations compared to metals, such as degenerately doped or non-stoichiometric semiconductors.[3,188,279,280] There have been

several reports on the use of materials such as transition metal oxides,[54,281] nitrides[282] and doped semiconductors[283] for IR plasmonic photodetectors.

Two candidate materials for IR plasmonics are $WO_{3-x}$[216] and $Cs_yWO_{3-x}$[278] NCs. Compared to commonly used plasmonic Au/Ag nanostructures exhibiting LSPR in the UV-visible region, both $WO_{3-x}$ and $Cs_yWO_{3-x}$ possess visible-NIR LSPR due to their lower carrier densities, in the range of $10^{18}$-$10^{22}$ $cm^{-3}$. These materials are known to have optical absorption in the NIR, but their effectiveness as plasmonic materials for enhancement of responsivity in a photodetector has not yet been thoroughly investigated; only one recent study has investigated photodetector enhancement in the visible light range using $WO_{3-x}$ nanowire arrays.[216] The carrier densities of these materials can also be tuned *via* the chemical synthesis procedure (e.g. extrinsic doping). However, a potential challenge when using $WO_{3-x}$ and $Cs_yWO_{3-x}$ NCs, despite being environmentally benign, is their rate of oxidation in air. Oxidation degrades the carrier concentration over time or with exposure to higher temperatures, which may lead to changes in crystal structure by reducing the oxygen vacancy concentration, and thus the carrier density.

## 5.2 Experimental Section

### 5.2.1 Photodetector Device Fabrication

The MSM photodetector devices (Figure 5.1a) were fabricated using a 2 cm × 2 cm semi-insulating, double-side, polished InP(001) as substrate. The substrate was first heat treated (∼520°C for ca. 10 min) in order to remove any surface adsorbates, then a three-layered heterostructure consisting of InAlAs/InGaAs/InAlAs of specific film thicknesses (Figure 5.1a) was grown on the cleaned surface at 470 °C ± 10 °C (2.5 Å/s growth rate) using molecular beam epitaxy (MBE). Next, the photosensitive integrated surface electrode patterns were created on top of the heterostructure. For this, a 2 cm × 2 cm chip of the wafer was first cleaned by sonication in acetone and isopropanol for 2 min, then a bilayer of positive photoresists (∼1.3 µm thick) consisting of polydimethylglutarimide (PMGI) polymer and Shipley 1813 were homogeneously deposited on top of the wafer by spin-casting at 5000 RPM for 60 seconds. In order to solidify the spin-coated photoresist layer, the wafer was first heat treated at 120°C for 90 s, followed by the creation of the integrated surface electrode patterns and bond pads (Figure 5.1b) by optical photolithography using Heidelberg instruments MLA 150 maskless aligner system. Any residue at surfaces exposed was removed by applying a plasma ash for 20 min. The wafer then underwent a 1 min etching treatment in HF to remove surface oxides, and subsequently a Ti/Au (20/80 nm) surface top layer was created by electron beam evaporation. Finally, aliquots of the colloidal toluene dispersions of $WO_{3-x}$ or Cs:$WO_{3-x}$ NCs were first diluted with hexane yielding a

concentration of 100 g $L^{-1}$ and 152 g $L^{-1}$, respectively, 0.5 $\mu$L of which were then separately drop-cast onto the active areas of photodetectors and dried with $N_2$ gas.

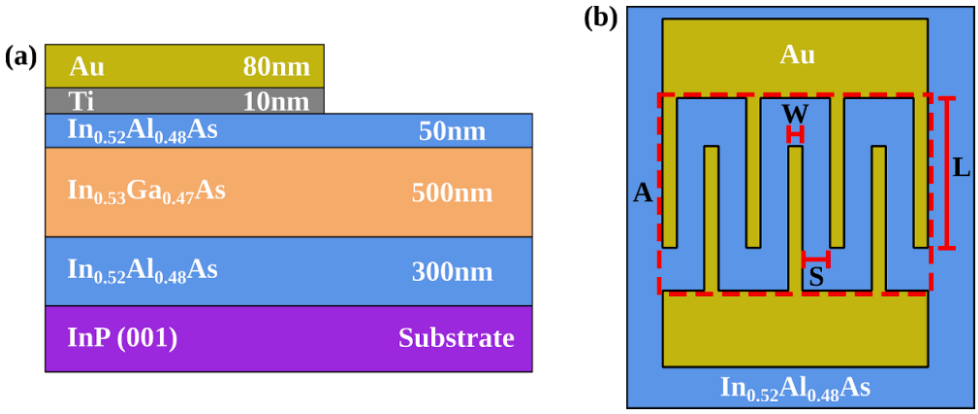



Figure 5.1: Structure of the IR metal-semiconductor-metal (MSM) photodetectors. (a) Semiconductor heterostructure layers grown by molecular beam epitaxy. The $In_{0.53}Ga_{0.47}As$ active region is grown between $In_{0.52}A_{l0.48}As$ barriers on an InP substrate. (b) Top view schematic of the interdigitated metal electrode geometry, where design parameters are electrode width (W $\sim$ 10 $\mu$m), spacing (S $\sim$ few $\mu$m), length (L $\sim$ 500 $\mu$m), and active area (A $\sim$ 500 $\mu$m $\times$ 540 $\mu$m) indicated by dashed red box.

### 5.2.2 Photocurrent Measurement Setup

The photodetector device performance was characterized by the NIR photoresponse detected via measuring the generated photocurrent as a function of bias voltage and incident wavelength of the UV-visible-NIR light source, using a custom-made optical setup schematically depicted in Figure 5.2. Broadband UV-visible-NIR light beam (240-2400 nm) was generated by a Thorlabs SLS402 Mercury-Xenon short-arc lamp, collimated and focused into the entrance slit (2 mm aperture size) of a Sciencetech monochromator using a Thorlabs LA4464-f = 60.0 mm UV fused plano-convex uncoated lens. The monochromator is equipped with three Blaze gratings (100-700 nm; 700-1500 nm; 1500-3500 nm) resting on rotatable stations to enable proper positioning with respect to the incident beam. The diffracted beam for a selected wavelength exits at a 2 mm slit then passes through a FEL1400 or FEL0750 long-pass filters to remove higher-order diffracted wavelength modes. Subsequently, the output monochromatic beam is focused using a Thorlabs LA5370-f = 40.0 nm planoconvex $CaF_2$ uncoated lens positioned before a post-mounted iris diaphragm and finally projected onto the sample focal plane.

The photodetector devices are attached on a printed circuit board and wire-bonded to Au-plated pins connected to an external circuit *via* a custom socket. To ensure alignment and positioning with respect to the beam of selected wavelengths, the photodetector device is mounted on a lateral (XY) translation stage using Thorlabs single-axis PT1 and PT series components. The bias voltage is supplied to the source/drain electrodes of the photodetector using a Keithly 230 programmable voltage source. The photocurrent generated is received by a DL instruments 1212 current–voltage amplifier, wherefrom the output signal is fed into an Agilent 34401A digital multimeter.

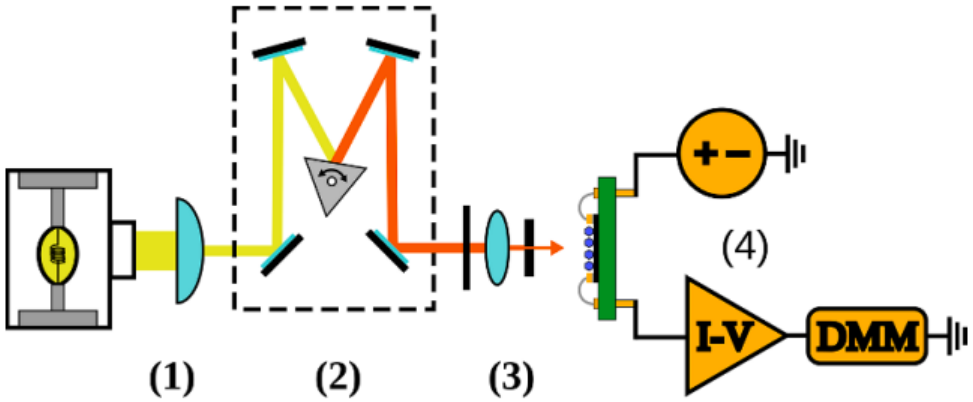



Figure 5.2: Measurement setup for characterizing photodetector responsivity. (1) The broadband light source generates a beam that is collimated and then focused on the monochromator entrance slit; (2) wavelengths are selected by mechanical positioning of diffraction gratings; (3) the monochromator output is filtered and focused onto the wire-bonded MSM device; (4) a bias voltage is applied to the device and the photocurrent is measured using a current-voltage (I-V) amplifier. The output of the I-V amplifier is read out with a digital multimeter (DMM). Responsivity is determined from the DMM output and incident beam power measurements.

### 5.2.3 Photoresponsivity Measurements

To ensure stable operating temperature and stability of the output optical spectrum, the Mercury-Xenon UV-visible-NIR lamp is turned on for 1 hour prior to each photoresponsivity measurement. After reaching optimal operating conditions, the setup is covered with an opaque blackout fabric to block ambient light, then the power spectrum of the broadband light source is acquired using a Thorlabs 700-1800 nm, 50 nW-40 mW Ge photodiode power sensor over a wavelength range of 750-1400 nm using 5 nm data intervals. The

power sensor is positioned in the focal plane behind the post-mounted iris diaphragm, and the FEL0750 filter (or FEL1400 filter for the 1400-1800 nm wavelength region) is placed in between the monochromator and LA5370 focusing lens. After obtaining the power spectrum, the power sensor is removed, and a chosen photodetector device is then positioned in the beam path using the XY translation stage to maximize photocurrent detection at the 550 nm reference wavelength. For data correction, the photodetector dark current is also recorded over a bias voltage ranging between -1 V to +1 V with the irises closed. Finally, the spectral responsivity of the device is acquired by measuring the photocurrent as a function of bias voltage across the same wavelength values as the power spectrum.

## 5.3 Results

Non-stoichiometric binary tungsten suboxides ($WO_y$) can adapt various crystal structures (known as Magnéli phases) depending on the level of oxygen deficiency ($2.625 < y < 2.92$).[5] In this study, we colloidally synthesized and characterized several batches of $WO_{3-x}$ NCs (labelled as WO-1-4) to account for synthetic reproducibility, as crucial parameter for any device fabrication. All the $WO_{3-x}$ NC samples obtained exhibited monoclinic crystal structure (*P 1 2/m 1*), as evidenced by the excellent match between the experimental X-ray diffractogram of NCs (Figure 5.3a blue traces) and the simulated XRD pattern (Figure 5.3a pink trace) of bulk monoclinic $WO_{2.72}$. Besides a broad peak centering at approximately 33° originating from (-144) planes, the two dominant peaks appearing near 23° and 48° can be assigned to (010) and (020) planes, respectively, suggesting the oriented growth of the NCs along the $< 010 >$ direction. In the TEM micrographs (Figure 5.3b), this observation was confirmed by the presence of elongated NCs (nanorods) with mean length of approximately 32.1 nm ± 7.8 nm and a diameter of 4.3 nm ± 1.4 nm. High-resolution (HR) TEM of a $WO_{3-x}$ nanorod with a mean lattice spacing of 3.7 Å along the $< 010 >$ growth direction (red arrows) is shown as inset of Figure 5.3b (first panel). In the optical extinction spectra (Figure 5.3c) of $WO_{3-x}$ NCs dispersed in TCE, two distinct regions can be observed. The intense UV absorption with an onset starting near 450 nm can be assigned to excitonic (interband) transition, while the broad optical absorption band starting near 450 nm and extending into the NIR region originates partly from intraionic (d-d) ligand-field transitions at higher energies (near the early onset in the visible region) and LSPR absorption associated with the collective free carrier oscillations in $WO_{3-x}$ NCs.[179] Importantly, apart from a slight fluctuation at lower energies, the optical extinction spectra of the colloidal (Figure 5.3c black trace) and drop-cast (blue trace) samples are virtually identical across the entire UV-visible-NIR region, which is a crucial factor for photodetection purposes. The electronic structure of $WO_{3-x}$ NCs was further

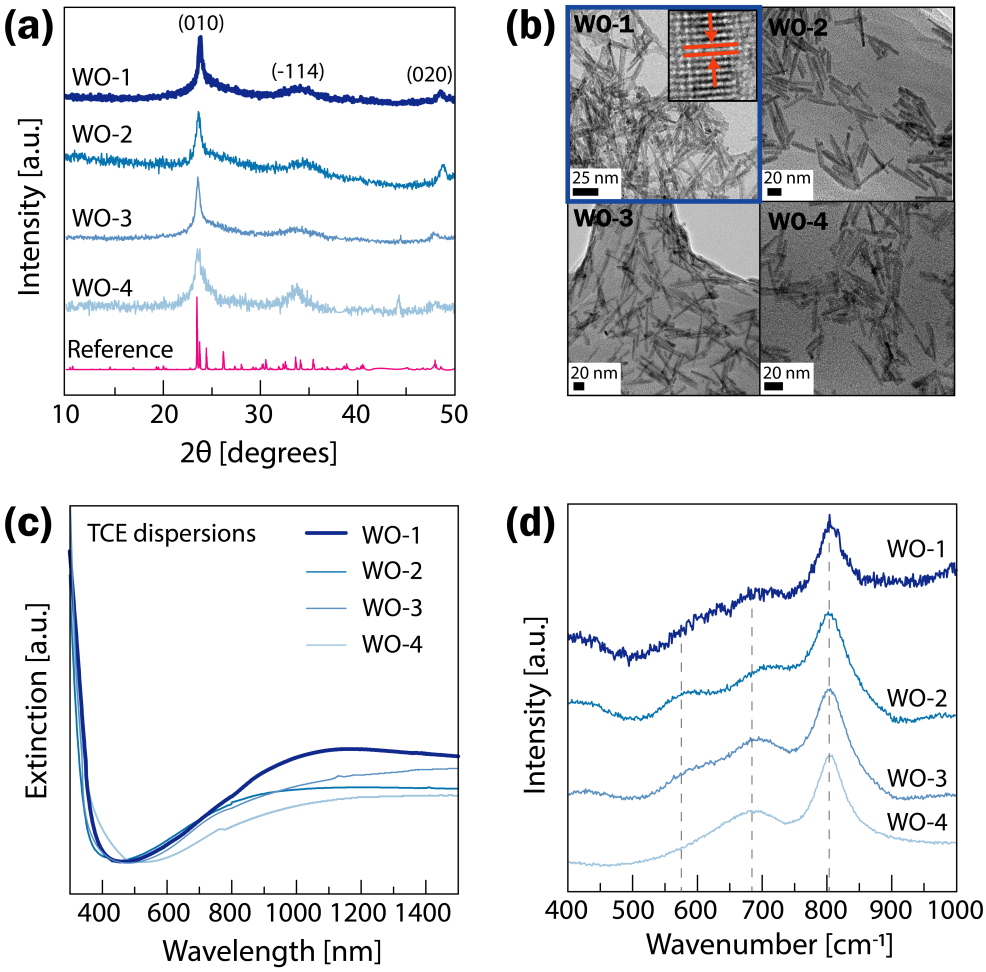



Figure 5.3: Structural and optical characterization of four plasmonic $WO_{3-x}$ NC samples. (a) Experimental X-ray diffractograms (blue traces) and reference XRD pattern (pink trace) of bulk $WO_{2.72}$ (ICSD No. 24731). (b) TEM micrographs of the NCs. (Inset: lattice-resolved TEM image of a NC). (c) Optical extinction spectra and (d) Raman spectra of the NCs.

characterized using Raman spectroscopy (for experimental parameters, see Section 2.2.7). As can be seen in Figure 5.3d, the Raman spectrum consists of two peaks near 690 and 805 $cm^{-1}$, which can be assigned to the out-of-plane wagging ($\gamma$)(O-W-O) and ($\nu$)(O-W-O) stretching modes of the $WO_6$ octahedra.[284–286] For samples WO-1-3, the peak at 690 $cm^{-1}$ is accompanied by a shoulder centering near ~580 $cm^{-1}$ can be attributed to weak

$\delta$(O-W-O) bending modes (weakened O–lattice bonds), which arises in oxygen-deficient $WO_{3-x}$ NCs as a result of alterations in O/W atomic ratio.[287] The electronic structure and tungsten speciation was investigated using X-ray photoelectron spectroscopy (XPS). The W 4f XPS spectrum (Chapter 3, Figure 3.3a), suggested approximately 6% of $W^{+5}$ in the $WO_{3-x}$ NCs.[179] For the photodetector device characterization, only one sample from the $WO_{3-x}$ NC batches was selected and used (labelled as WO-1); all the photoresponsivity results discussed later in the text correspond to measurements using WO-1 sample.

Table 5.1: Summary of crystallographic and optical characterization of $WO_{3-x}$ NC samples.

| **Sample** | **UV-NIR** | **XRD** | | **XRD** | | **TEM** | |
|---|---|---|---|---|---|---|---|
| | Max [nm] | Location (010); broadening | | Location (020); broadening | | NC Length; Width [nm] | |
| **WO-1** | 1126 | 23.4 | 0.5 | 48.3 | 0.8 | 37 (±14) | 5.2±(1.5) |
| **WO-2** | 1098 | 23.8 | 0.5 | 48.3 | 0.6 | 31 (±17) | 5.4±(2.0) |
| **WO-3** | 1153 | 23.7 | 0.7 | 48.1 | 1.3 | 47 (±11) | 4.2±(1.1) |
| **WO-4** | 1210 | 23.8 | 0.8 | 48.1 | - | 30 (±20) | 5.6±(1.8) |

When tungsten oxide is doped with metal ions, a family of non-stoichiometric compounds of the general formula $M_yWO_3$ (M is usually an alkali metal ion) is formed, called tungsten bronzes.[86] Unlike extrinsically undoped $WO_3$, the crystal structure as well as the electronic and optical properties of tungsten bronzes can be significantly modulated by the radius and electric charge of the dopant intercalated.[288,289] Similarly to the $WO_{3-x}$ samples, we also synthesized several batches of $Cs_yWO_{3-x}$ NCs (labelled as CsWO-1-4) using the colloidal synthesis protocol described in Chapter 2.1.3. Based on the XRD patterns (Figure 5.4a green trace), $Cs_yWO_{3-x}$ NCs crystallized in hexagonal phase and possess high phase purity, as suggested by the excellent match between the experimental data (green traces) and the simulated XRD pattern of bulk hexagonal $Cs_{0.29}WO_3$ (black trace). The two most intense peaks appearing near 23.3° and 27.7° can be assigned to the (002) prismatic and (200) basal planes, respectively. Beside the XRD peak broadening, the nanocrystalline nature of the samples is also confirmed by low-resolution TEM micrographs (Figure 5.4c-d) revealing a rod-like shape for the as-synthesized $Cs_yWO_{3-x}$ NCs with a mean length and width of approximately 17.8 nm and 10.4 nm (aspect ratio 1.6), respectively. The insets in Figure 5.4 display lattice-resolved TEM images of a prismatic (d) and basal plane (e) of a $Cs_yWO_{3-x}$ nanoprism along the $< 002 >$ growth direction. Similarly to the $WO_{3-x}$ NCs, the optical extinction spectra of $Cs_yWO_{3-x}$ NCs (Figure 5.4b) also exhibit a broad

visible-NIR band between ca. 480-3000 nm originating from a mixture of polaronic and intraionic ligand-field transtitions at higher energies (visible region) and LSPR absorption at lower energies (visible-NIR).[179,290] As discussed in earlier chapters (Chapter IV), CsWO NCs possess $LSPR_{\parallel}$ and $LSPR_{\perp}$ modes, with tunability of $LSPR_{\parallel}$ by NC AR. Given the AR value of ∼1.6 for the CsWO NCs presently used, the two LSPR modes overlap resulting in the broadened visible-NIR band shown in Figure 5.4b (Figure 1.5b). The intense UV absorption before 500 nm can be assigned to interband transitions attributed to the semiconducting nature of $Cs_yWO_{3-x}$ NCs. The crystallographic and optical characterization of the $WO_{3-x}$ and $Cs_yWO_{3-x}$ NCs samples are summarized in Table 5.1-5.2. For the photodetector device characterization, only one sample from the CsWO NC batches was selected (labelled as CsWO-1) and investigated for the photoresponsivity measurements, as discussed later in the text.

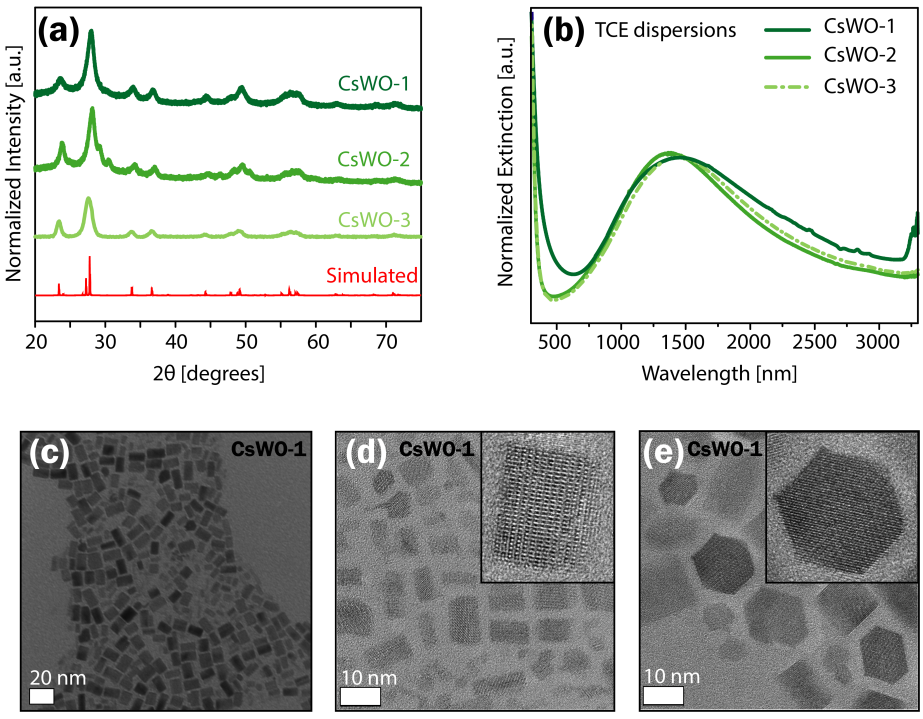



Figure 5.4: Structural and optical characterization of four plasmonic $Cs_yWO_{3-x}$ NC samples. (a) Experimental X-ray diffractograms (blue traces) and reference XRD pattern (pink trace) of bulk hex-$Cs_{0.33}WO_3$ (ICSD No. 253809). (b) Optical extinction spectra and (c-e) TEM micrographs of the NCs. Insets: lattice-resolved TEM image of the prismatic (d) and basal plane (e) of a NC.

Table 5.2: Summary of crystallographic and optical characterization of $Cs_yWO_{3-x}$ NC samples. (Left and right columns of XRD correspond, respectively, to peak location (°) and broadening ($\beta$)).

| Sample name | AR (H/W) | UV-NIR Max[nm] | XRD °(002) | $\beta$ | XRD °(200) | $\beta$ | XRD °(112) | $\beta$ | XRD °(202) | $\beta$ |
|---|---|---|---|---|---|---|---|---|---|---|
| **CsWO-1** | 1.6 | 1442 | 23.4 | 0.8 | 27.7 | 1.3 | 33.8 | 0.8 | 36.7 | 0.9 |
| **CsWO-2** | 1.5 | 1363 | 23.6 | 0.8 | 28.0 | 1.4 | 34.2 | 0.9 | 37.0 | 0.8 |
| **CsWO-3** | 1.6 | 1449 | 23.8 | 0.8 | 28.1 | 1.3 | 33.9 | 1.0 | 36.9 | 0.9 |

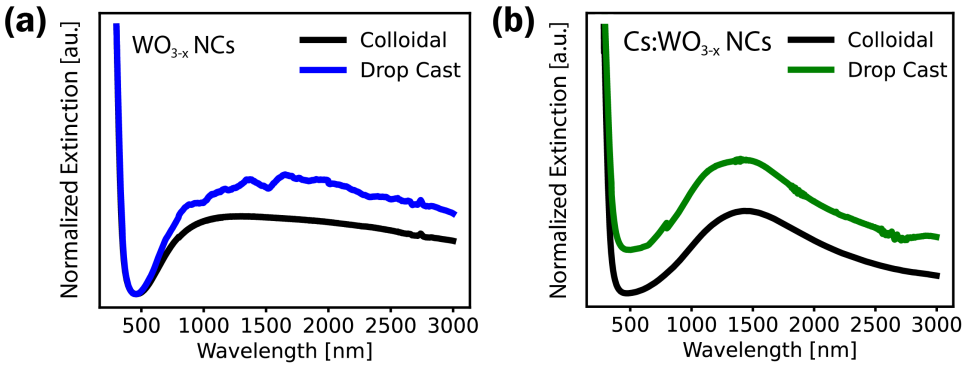



Figure 5.5: Optical extinction spectra of (a) colloidal and drop-cast plasmonic $WO_{3-x}$ and (b) $Cs_yWO_{3-x}$ NCs.

### 5.3.1 Photodetector Characterization

First, the beam profile and power spectrum of the Xenon-Halogen visible-NIR light source (Figure 5.6) were recorded and optimized. Then, photoresponsivity measurements were carried out by probing the electrical resistances ($\mu$) of an array of 16 MSM photodetector devices under white light illumination ($R_{light}$) or in the dark ($R_{dark}$), using an Agilent E5262A probe station.

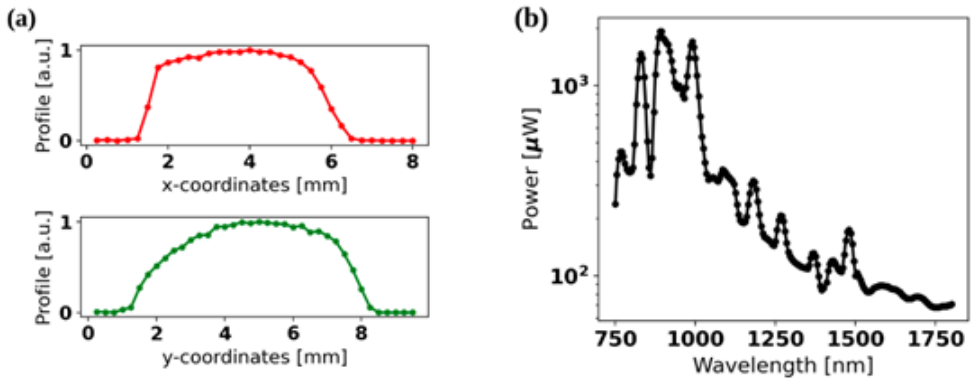



Figure 5.6: Beam profile (a) of the applied visible-NIR light source upon exiting the monochromator, and (b) its power spectrum over a wavelength range of 750-1800 nm using a 750 nm or 1400 nm filter to block higher order modes of diffracted light coming from monochromator.

Table 5.3 summarizes the mean resistance values obtained for the entire MSM array (1st row of the table) applying bias voltages between -10 mV and +10 mV. In the MSM array, two devices were found to exhibit significant increase in conductivity under illumination. Interestingly, they also had the same electrode geometry (with an active area of 500 $\mu$m $\times$ 540 $\mu$m) and finger configuration (with finger length, width and spacing of 500 $\mu$m, 10 $\mu$m, and 3 $\mu$m, respectively). These devices were labelled as $A$ and $B$ and selected for further measurements in the present study.

Table 5.3: Resistance values of as-fabricated MSM photodetector devices measured on a probe station with illumination under a white light source ($R_{light}$) or without illumination ($R_{dark}$) using bias voltage between -10 mV and +10 mV range. Optical power of ca. 18 $\mu$W mm$^{-2}$ was measured under illumination and ca. 32 nW mm$^{-2}$ in the dark. Device $A$ and $B$ were selected owing to their significant increase in conductivity under illumination, and possessing the same electrode geometry. Percentage change in resistance under illumination ($\Delta$R), and the mean resistance ($\mu$) and its standard deviation ($\sigma$) values for the array of 16 MSM detectors are also indicated.

| **Device** | **$R_{dark}$ [MΩ]** | **$R_{light}$ [MΩ]** | **ΔR [%]** |
|---|---|---|---|
| **Entire array** ($\mu \pm \sigma$) | 4.24 ± 2.44 | 0.144 ± 0.0950 | –96.6 |
| **A** | 0.200 | 0.0183 | –90.8 |
| **B** | 4.550 | 0.1810 | –96.0 |

Photoresponsivity measurements for devices $A$ and $B$ were carried out by monitoring photocurrent versus bias voltage at 1550 nm, using the optical setup described above (Figure 5.2). For both devices, we observed dark current (Figure 5.7), with a magnitude significantly greater compared to similar InGaAs MSM photodetectors reported in the literature,[136,251] even with the InAlAs barrier layer present.

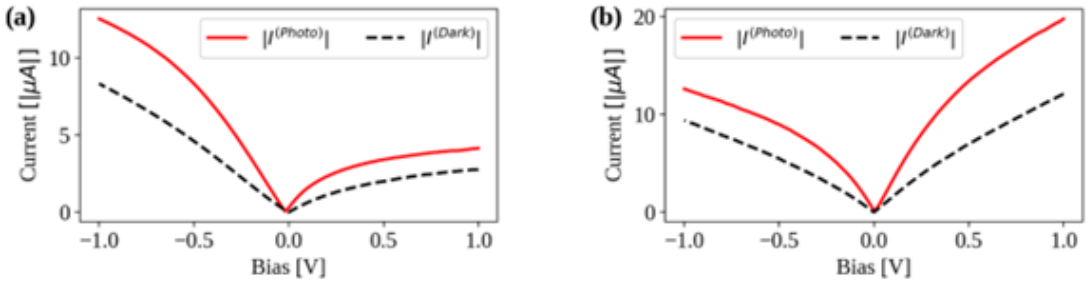



Figure 5.7: Characterization of photodetector device performance as a function of bias voltage in dark (dashed line) and illumination (red traces). Dark current and photocurrent acquired at a wavelength of 1550 nm (176 $\mu$W mm$^{-2}$ incident power) for the as-fabricated InGaAs photodetectors A (a) and B (b).

We attributed the observed increase in dark current to pitting surface defects (Figure 5.8) in the InAlAs/InGaAs wafer material with estimated defect density of $\sim 10^6$ cm$^{-2}$. Such defects (assumably native to the InP substrate) can lead to surface regions of lowered Schottky barrier, thus generating low-resistance pathways between the surface metal electrodes and InGaAs active layer.[291,292] Based on the work of Bhattacharya et al.,[293] we used a double Schottky barrier model to calculate the dark current ($J(V)$) in the devices, according to equation 5.1:

$$J(V) = \frac{2J_s(\phi_1)J_s(\phi_2)sinh(\frac{\beta}{2n})}{J_s(\phi_1)exp(\frac{\beta}{2n}) + J_s(\phi_2)exp\frac{-\beta V}{2n}} \tag{5.1}$$

where $\phi_1$ and $\phi_2$ are Schottky barriers for either contact, $n$ is the ideality factor (assumed to be same for both contacts), $J_s(\phi_1/2)$ are the thermionic saturation current densities for either contact, and $\beta = 1/(k_BT)$. Using this model, we estimated an average Schottky barrier height of $< \phi_A > \approx 0.53$ eV and $\phi_B > \approx 0.50$ eV between the MSM contacts in devices $A$ and $B$, respectively, which are also consistent with earlier theoretical predictions ($\phi_{theoretical} \approx 0.7$ eV).[251,292]

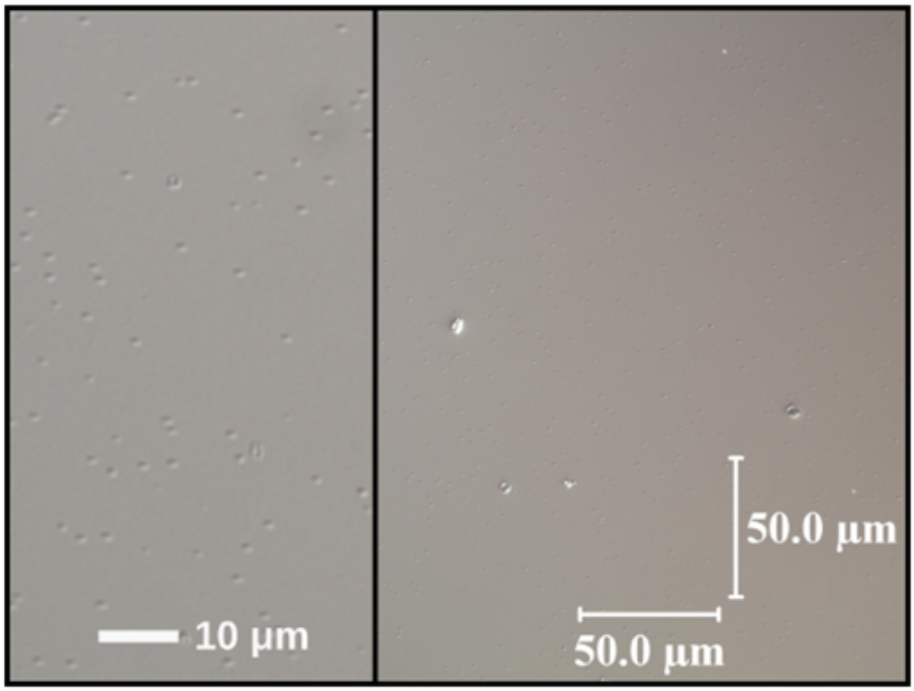



Figure 5.8: Pitting surface defects of an as-fabricated $In_{0.52}Al_{0.48}As/In_{0.53}Ga_{0.47}As$ on InP photodetector observed *via* a Nomarski microscopy scan (left), and a magnified view of pitting surface defects suspected to originate from native defects in the InP substrate.

### 5.3.2 Photodetector Device Performance

Spectral responsivity, defined as the ratio of the dark-current-corrected output photocurrent to the incident optical power, measures the optical-to-electrical conversion efficiency of optoelectronic devices. To probe the enhancement of spectral responsivity of the bare (NC free) photodetectors $A$ and $B$, first the dark current, photocurrent, and power spectrum of the broadband visible-NIR light source were measured using a fixed bias voltage (-1 V). Subsequently, 0.5 $\mu$L of the dilute WO-1 (100 g/L) or CsWO–1 (152 g/L) NC samples were separately drop-cast onto the interdigitated finger electrode region (photoactive area) of device $A$ (WO-1) and $B$ (CsWO-1), respectively. Figure 5.9 below shows an optical microscope image, respectively, of a device before (a) and after drop-casting NCs, and SEM micrographs of (c) device $A$ with CsWO-1, and (b) device $B$ with WO-1 NCs deposited. Due to the significant variability in the quantity and uniformity of NC deposition (Figure 5.9c,d), drop-casting of NCs and photoresponsivity measurements were repeated several times using the protocol described above.

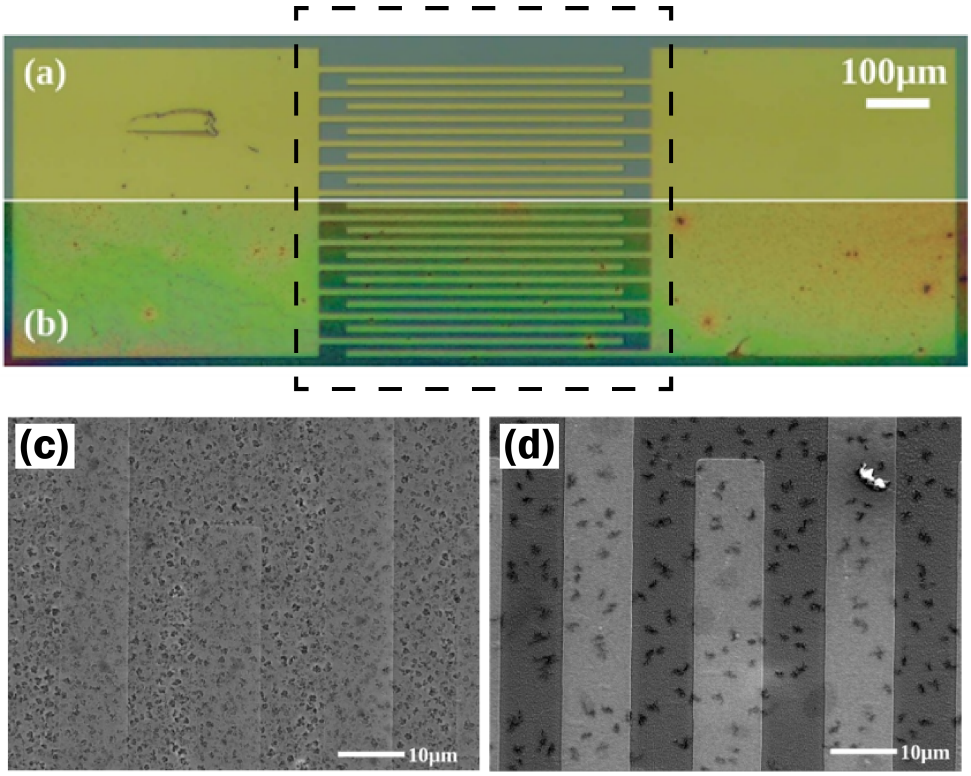



Figure 5.9: Optical microscope images of (a) a bare MSM photodetector device before drop-casting NCs, and (b) after uniform deposition of CsWO NCs by drop-casting from diluted (150 g $L^{-1}$) solution. SEM micrographs of (c) device *A* with WO-1, and (d) device *B* CsWO-1 NCs deposited.

Figure 5.10 below shows the photoresponsivity measurement results obtained for devices *A* and *B* with (colored traces) and without NCs (black traces) present, respectively. Prior to depositing the NCs, both devices exhibit a wavelength-dependent photoresponsivity characteristic of MSM photodetectors with InGaAs active layer (Figure 5.10 black traces).[294,295] In the presence of NCs, both devices show significant photoenhancement in the visible-NIR spectral region. Importantly, the nonnegligible fluctuations in the observed responsivity (Figure 5.10 colored traces) are reproducible and do not arise from measurement noise (uncertainty due to noise was found to be smaller than the plot line width). These fluctuations may originate from wave interference due to the electrode geometry or the sharp spectral features in the broadband light source that are not fully removed by the normalization protocol implemented. Using the observed responsivity values, we obtained the wavelength-dependent specific detectivity ($D^*(\lambda, f_0)$) for both devices, using equation

5.2:

$$D^*(\lambda, f_0) = \frac{\sqrt{A}R(\lambda)}{S(f_0)} \tag{5.2}$$

where $A$ is the electrode contact area, $R(\lambda)$ is the wavelength-dependent responsivity, $S(f_0)$ is the current noise spectral density at an operating frequency $f_0$. At 1 Hz operating frequencies, devices $A$ and $B$ possessed virtually identical peak detectivities of $D^*_A \approx D^*_B \sim 10^6$ cm Hz$^{1/2}$, whereas at 1 MHz, $A$ and $B$ showed order of magnitude difference with values of $D^*_A \sim 10^7$ cm Hz$^{1/2}$ and $D^*_B \sim 10^8$ cm Hz$^{1/2}$, respectively. The detectivities above 1 MHz, are relevant for applications in telecommunication,[136] are comparable to other NIR photodetectors that typically range between $D^*_A \sim 10^8 - 10^{14}$ cm Hz$^{1/2}$.[246,263,296] These results demonstrate that increased photoresponsivity can be achieved in InGaAs MSM photodetectors with the deposition of plasmonic $WO_{3-x}$ or Cs:$WO_{3-x}$ NCs onto the active layer of the photodetectors.

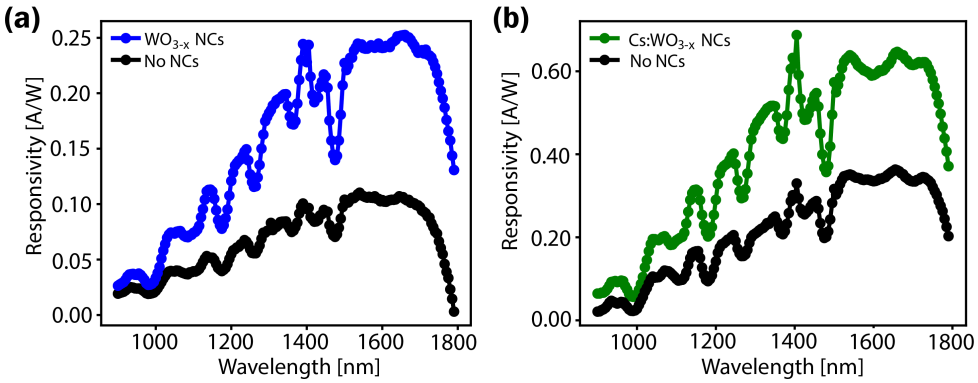



Figure 5.10: Photoresponsivity measured for (a) device $A$ and (b) device $B$ with (color trace) or without (black traces) NCs. Both devices exhibit enhancement in photoresponsivity in the presence of $WO_{3-x}$ (device $A$) and Cs:$WO_{3-x}$ NCs (device $B$). Photoresponsivity is determined by subtracting the dark current and normalizing the dark-current-corrected photocurrent with respect to the measured power spectrum of the broadband light source.

To assess the device performance, we assessed the relative enhancement of photoresponsivity as a function of wavelength and compared it with the optical extinction of the drop-cast NCs. For this, we used the relative percent difference (RPD), expressed in equation 5.3:

$$RPD(\lambda) = \frac{R_{NC}(\lambda) - R_0(\lambda)}{R_0(\lambda)} \times 100\% \tag{5.3}$$

where $\lambda$ is wavelength, $R_{NC}(\lambda)$ and $R_0(\lambda)$ are the photoresponsivities with and without NCs, respectively. Figure 5.11 shows the RPD versus wavelength plots in the wavelength range of 1000-1700 nm for devices $A$ (a) and $B$ (b) with the optical extinction spectrum of drop-cast NCs (red traces) from Figure 5.5 overlaid. Apart from some deviations likely arising from aggregation effects and nonuniform film thickness, the $RPD(\lambda)$ spectra for both devices show a good overall agreement with the corresponding optical extinction spectrum of drop-cast NCs. RPD for devices $A$ ($WO_{3-x}$) and $B$ (Cs:$WO_{3-x}$) was found to be within 60%–150% and 58%–125%, respectively, indicating a significant overall enhancement in photoresponsivity.

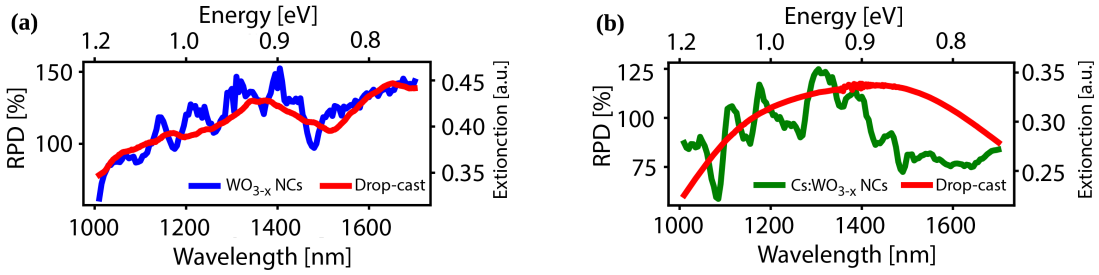



Figure 5.11: Plots of relative percent change in responsivity (RPD) as a function of wavelength obtained in the presence of drop-cast $WO_{3-x}$ (a) or Cs:$WO_{3-x}$ (b) NCs. The optical extinction spectrum of the different NC types (red traces) is plotted (in arbitrary units) on the right vertical axis in each plot.

To further examine the observed enhancement in photoresponsivity, we also assessed the external quantum efficiency (EQE) of the devices. EQE quantifies the ability of optoelectronic devices to convert incident photons to electric charges collected in the electrodes as a function of wavelength, as follows:[16]

$$EQE(\lambda) = \frac{R(\lambda)hc}{q_e\lambda} \times 100\% \tag{5.4}$$

where $h$ and $c$ are Plank's constant and speed of light, respectively. Shown in Figure WWW below, the EQE was measured for both devices with (colored traces) and without the corresponding NCs present (black traces). Using the data presented in Figure 5.12,

the highest EQE for both devices was found in the wavelength range of 1400–1600 nm. At 1400 nm, the EQE of device $A$ increases from ∼7% to 20%, while device $B$ exhibits an increase from ∼25% to 60%, indicating an approximately 2-3-fold increase in the number of photogenerated charge carriers in the presence of plasmonic $WO_{3-x}$ ($A$) or Cs:$WO_{3-x}$ ($B$) NCs. Before the addition of NCs, the EQE values were found to be comparable to other NIR photodetectors and are enhanced by the addition of NCs.[297]

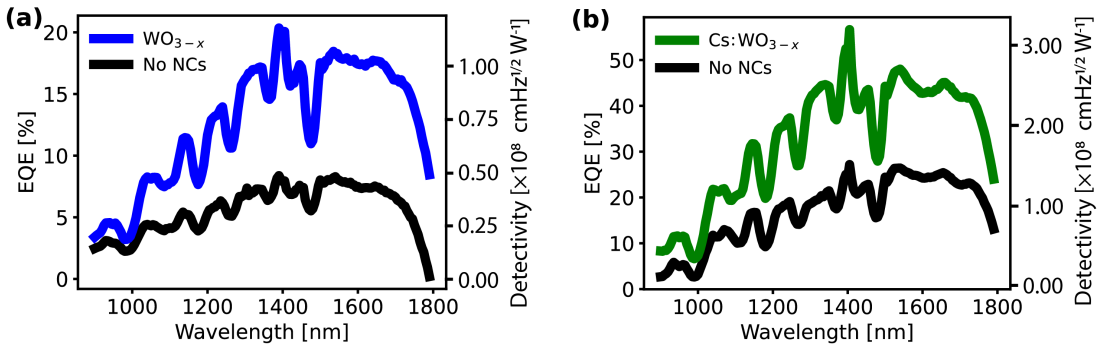



Figure 5.12: External quantum efficiency (EQE) and detectivity of photodetector devices (a) $A$ and (b) $B$ obtained without (black traces) and by drop-casting $WO_{3-x}$ (a) or Cs:$WO_{3-x}$ (b) NCs.

## 5.4 Discussion

In recent years, several different mechanisms have been proposed for the enhancement of photoresponse in MSM optoelectronic devices using plasmonic nanostructures as photoactive components. According to one of proposed mechanisms, upon resonant (visible-NIR) photon absorption, the LSPR modes generated in the plasmonic NCs lead to enhanced electric fields in the InGaAs surface layer of the MSM photodetector *via* electromagnetic near-field enhancement (NFE),[7,178] facilitating the generation of charge carriers at a higher rate.[298] Another possible mechanism, called plasmon-induced hot electron injection (HEI), involves the injection of photogenerated charge carriers from the plasmonic NCs into the conduction band of surrounding bulk InGaAs semiconductor (given a low enough Schottky barrier), generating a photocurrent under an applied bias.[263,299,300] Finally, the third possible mechanism states that the NC thin films can act as an anti-reflective coating on the surface of MSM photodetector, leading to enhanced photon scattering and thus enhancement in photoresponsivity.[264,301,302]

Although the data presented in this work does not serve as evidence nor can it disentangle the above mechanisms, a recent study has demonstrated that plasmon-induced HEI can play a significant role in enhancing photoresponsivity in similar nanostructure-based photodetectors.[263,297] In a recent study,[216] plasmonic $WO_{3-x}$ NCs were used as active material for visible-NIR photodetection, and the authors assigned the observed photoresponse to the HEI-driven plasmonic photoenhancement mechanism. A careful way of testing whether HEI is the dominant mechanism for the photoenhancement observed in our devices, the relation between material properties and the generation and injection of energetic hot carriers needs to be explored. For instance, with the deposition of a thin, wide-bandgap insulating layer between the plasmonic NCs (photoactive area) and the InGaAs/InAlAs surface, suppression of hot carrier injection can be achieved. The influence of hot carrier injection on photoresponsivity could then be investigated by varying the doping concentration (LSPR energy) in the NCs, where higher doping concentration would be expected to increase the rate of hot carrier injection, thus yielding a stronger increase in photoresponsivity. The magnitude and distribution of the plasmon-generated electromagnetic field (plasmonic NFE) can be modulated by the NC morphology (plasmonic hot spots), which is a primary parameter for their packing behavior on the detector surface.[7] Hence, the optimization of NC morphology and the correlation thereof with photoenhancement measurements is imperative, for which finite-difference time domain (FTDT) computer simulations could be used.[7,178]

Finally, stronger plasmonic NFE around the NCs can also facilitate the generation of electron–hole pairs at a higher rate in the insulating InGaAs/InAlAs layer. Since the magnitude of the electric field ($|\vec{E}|$) strongly depends on the distance ($r$) around the plasmonic NCs ($|\vec{E}| \propto 1/r^2$), enhancement in photoresponsivity can also be tuned by modulating the thickness of the InGaAs/InAlAs insulating layer.[298]

## 5.5 Conclusions

In this chapter, colloidally synthesized shape and size-uniform substoichiometric plasmonic $WO_{3-x}$ and Cs:$WO_{3-x}$ NCs were demonstrated to exhibit an enhancement of visible–NIR photoresponsivity in easy-to-fabricate MSM photodetectors by depositing them on the active area of the devices. The results of this work show the potential of both non-stoichiometric and doped transition metal oxide plasmonic NCs for visible-NIR optoelectronic applications requiring, such as high-speed optical fiber or telecommunication. Furthermore, the ease of NC deposition by drop-casting was also demonstrated to be convenient for rapid prototyping of modified MSM detectors; however, this needs further optimization to achieve consistency for industrial scaling and application.

# Chapter 6

## Decoupling Molecular Surface Adsorption and Plasmonic Photocatalysis on $WO_{3-x}$ Nanocrystals – A Spectroscopic Investigation

This chapter investigates the plasmonic photocatalytic activity of colloidally-synthesized substoichiometric $WO_{3-x}$ NCs using Rhodamine 6G dye as a model system. The primary goal is to understand how surface chemistry and the concentration of native defect (oxygen vacancy) influence photocatalytic performance. I demonstrate that the removal of the oleic acid ligand shell from the surface of the colloidal NCs significantly enhances their photocatalytic activity by increasing the accessibility of catalytically active sites. In addition, this chapter explores the effect of the concentration of the native oxygen vacancy on photocatalytic efficiency, which is systematically varied *via* post-synthesis annealing in air. Annealing induces sintering of the NCs, resulting in the formation of larger domains with a reduced surface-to-volume ratio. Consequently, adsorption processes occurring concurrently with photocatalysis become increasingly significant and must be carefully considered. The work presented in this chapter specifically aims to study the contribution of adsorption process to the overall photocatalytic activity, providing a clearer understanding of how surface properties and morphological changes influence the observed behavior of $WO_{3-x}$ NCs.

## Overview

Developing new sustainable catalysts capable of harnessing a wide range of the solar radiation spectrum is necessary to optimize sustainable photocatalytic technologies. Plasmonic photocatalysts, such as substoichiometric plasmonic metal oxides ($MO_{y-\delta}$), are among the most promising photoactive materials owing to their strong optical absorp-

tion spanning the ultraviolet to the infrared region, covering a significant portion of the solar spectrum. As well, these materials present a more sustainable solution than their precious-metal counterparts due to their low cost, low toxicity and tunable optical properties, which can be tailored by varying the vacancy concentrations using synthetic and post-synthetic treatments. Substoichiometric metal oxides exhibit coupled adsorptive and catalytic properties, due to the photothermal effects arising from their near-to-mid-infrared plasmon resonances. Therefore, both components need to be accounted for to accurately assess the overall effects and to determine pathways to isolate individual components or optimize their synergistic effects for specific applications. Here, we investigate the coexistence of adsorption and photothermal catalysis for Rhodamine 6G dye as model compound using substoichometric plasmonic $WO_{3-x}$ NCs as the adsorber and photocatalyst. Using a combination of steady-state electronic adsorption spectroscopy, surface area analysis, and electrospray ionization mass spectrometry, we examine the coupling between the adsorption and photothermal catalytic activity. The results of this work show that the contribution from adsorption processes can be modulated via post-synthetic annealing, facilitating analysis of adsorption parameters, while retaining coupling with the photocatalysis.

## 6.1 Introduction

Photocatalysis has attracted considerable attention as a central component of various sustainable technology solutions.[303] Notably, it allows for a direct conversion of solar radiation into chemical fuel *via* water splitting[304–308] or wastewater treatment by degradation of organic pollutants.[172,307,309] Realizing the full potential of these processes requires the design of environmentally benign high surface-area photocatalysts with optical absorption broadly tunable throughout the visible to NIR–MIR spectral regions.

Over the past two decades, plasmonic nanomaterials have emerged as promising candidates for solar-driven technologies, increasingly competing with conventional semiconductor-based photocatalysts[310] that rely on spatially separated electron-hole pairs generated through interband (excitonic) transitions upon ultraviolet (UV) light absorption. Historically, nanostructures made of noble metals such as gold (Au) and silver (Ag) have been the focus of plasmonics research due to their well-established and facile synthetic protocols, which allow for size and shape tunability, and high free carrier densities ($\sim 10^{23}$ carrier/cm$^3$), enabling LSPR in the visible region.[311–313] These resonances originate from the collective oscillation of free charge carriers at the surface of NCs induced by absorption of electromagnetic radiation, thereby significantly improving the energy harvesting efficiency in the visible spectrum and enabling a wide array of photonic processes, including photocatalysis, photodetection, and optical sensing.[36,314] However, the reliance on noble metals for green solar energy technologies comes with significant limitations, including high materials

cost,[315] restricted spectral tunability of LSPR (by NC size and shape) to the visible spectral range,[316,317] and potential susceptibility to degradation processes such as sulfidation and/or oxidation (particularly for Ag NCs).[318] The emergence of plasmonic compound semiconductor nanostructures, particularly binary sub-stoichiometric transparent conducting oxides (TCOs) such as $WO_{3-x}$, $MoO_{3-x}$, and $TiO_{2-x}$, has addressed many of the aforementioned challenges. For instance, in contrast to plasmonic coinage metal NCs, free carrier densities in binary TCO NCs ($\sim 10^{20}$–$10^{22}$ $cm^{-3}$) can be finely tuned *via* synthesis or post-synthesis modulation of oxygen vacancy concentration, enabling broad tunability of LSPR frequencies across the visible–NIR–MIR regions and opening new possibilities for photocatalytic and optoelectronic applications.[4,76,81,83,319] The existence of NIR-MIR LSPR frequencies facilitates these materials to exhibit photothermal catalysis where catalytic behaviour can be exhibited in the absence of light due to the thermal radiation under room temperature conditions. The coexistence of band edge (excitonic) photocatalytic activity in the UV-visible region of the spectrum in conjunction with NIR–MIR LSPR based photothermal catalysis is ideal for optimizing the use of solar radiation for chemical transformations, making materials that exhibit these properties promising as eco-friendly photocatalysts for environmental remediation.[146]

Among TCOs, sub-stoichiometric tungsten oxide ($WO_{3-x}$) has become one of the most promising plasmonic semiconductor photocatalysts.[320] Compared to other wide-band-gap semiconductors such as $TiO_2$ (Eg $\approx$ 3.2 eV), its narrower optical band gap of approximately 2.4-2.8 eV enables enhanced solar absorption.[319,321] Importantly, a wide range of stoichiometries can be realized in $WO_{3-x}$ ($0 < x < 0.72$), leading to a variety of crystallographic phases (Magnéli phases) exhibiting LSPR in the visible–NIR region.[5,77,322] In addition to its favorable optical properties, $WO_{3-x}$ is chemically robust, non-toxic,[323,324] and readily synthesized at scale,[325] positioning it as a viable alternative to noble metals and complex heterostructures in photocatalytic technologies. Nanostructured $WO_{3-x}$ exhibits superior photocatalytic efficiency compared to bulk, which results from a combination of greater specific surface area and LSPR-derived photocatalytic activity.[171] Low-dimensional tungsten oxide phases may also exhibit a strong propensity for surface adsorption of various organic moieties, which can influence the mechanism of photocatalytic degradation of organic pollutants. This interplay complicates interpretation of the obtained photocatalytic data, hindering rational optimization of $WO_{3-x}$-based photocatalytic systems.

Although different studies have separately examined the adsorption behavior[326,327] and plasmon-driven photocatalytic activity[82,171,172,175] of tungsten oxide, comprehensive understanding of the relationship between these phenomena and the strategy to selectively modulate their effect are still lacking. As an example, Hkiri et al.[327] have investigated adsorption of methylene blue on $WO_3$ nanoflakes and showed that adsorption kinetics can be described by a pseudo-second-order model. Based on intra-particle diffusion analysis they

proposed a two-stage mechanism involving surface adsorption and intraparticle diffusion. The adsorption kinetics of other organic dyes on $WO_3$ has been further studied by Arteage-Jimenéz et al.,[328] demonstrating the dominant contribution of electrostatic interactions to the adsorption process. On the other hand, the photocatalytic activity of $WO_3$ originates from the excitonic transition in the visible-to-UV region, which can be tailored based on the $WO_3$ size and morphology [11]. In sub-stoichiometric $WO_{3-x}$, catalytic activity can also be associated with LSPR in the visible-to-NIR range, leading to plasmonic photocatalysis. Paik et al.[171] and Tang et al.[172] demonstrated LSPR-based photocatalysis for hydrogen generation and degradation of methyl orange, driven by hot carrier generation in these materials. While there is strong evidence of photodegradation with these materials, the correlation between the adsorption and NIR photocatalytic effects arising from LSPR in $WO_{3-x}$ (and other plasmonic metal oxide systems) remains unclear. Addressing this gap is essential to tailor $WO_{3-x}$ nanomaterials toward specific applications, such as efficient wastewater treatment, where balancing adsorption and photocatalysis is critical.

In this work, we systematically investigated the relationship between adsorption and plasmon-induced catalytic activities of ligand-stripped $WO_{3-x}$ NCs modified by controlled annealing at different temperatures, using Rhodamine 6G (Rh6G) dye as a representative analyte. We demonstrated that plasmon-induced degradation of adsorbed Rh6G molecules in dark is a dominant process for as-synthesized NCs. Upon low-temperature annealing of the NCs the photocatalytic activity strongly subsides but the adsorption capacity dramatically increases, owing to the change in the NC surface structure. The electrospray ionization mass spectrometry (ESI–MS) measurements confirmed these findings and allowed us to identify key products of plasmon-induced degradation. The results of this work allow for detailed exploration and independent optimization of the adsorption and photocatalytic properties of $WO_{3-x}$ NCs for a range of different applications through controlling surface-to-volume ratio, oxygen vacancy levels, and surface structure.

## 6.2 Results and Discussion

### 6.2.1 Structural and Optical Characterization

To investigate the structure, morphology, and optical properties of as-synthesized $WO_{3-x}$ NCs, we conducted XRD, TEM, and UV–visible–NIR optical extinction spectroscopy measurements, respectively. In the XRD pattern obtained for a typical NC thin film deposited on a glass substrate (Figure 6.1a, blue trace), three dominant peaks at 24.9°, 34.8°, and 48.5° can be assigned to the (010), (-114), and (020) planes of the monoclinic $WO_{2.72}$, respectively, based on the match with the simulated XRD pattern of bulk $WO_{2.72}$ (red trace in Figure 6.1a). Non-negligible peak broadening observed in the experimental XRD

pattern can be attributed to the nanocrystalline nature of the sample. Among the three aforementioned peaks, those corresponding to the (010) and (020) planes are sharper and somewhat more pronounced relative to other reflections, suggesting an oriented growth of the NCs along the ⟨010⟩ direction. The oriented growth is corroborated by TEM imaging (Figure 6.1b), which reveals the presence of rod-like NCs with a mean length of 43.4 ± 7.5 nm (Figure 6.1c) and a mean width of 5.2 ± 1.4 nm (Figure 6.1d). The measured lattice fringe separation determined from the high-resolution TEM image (inset in Figure 6.1b) is

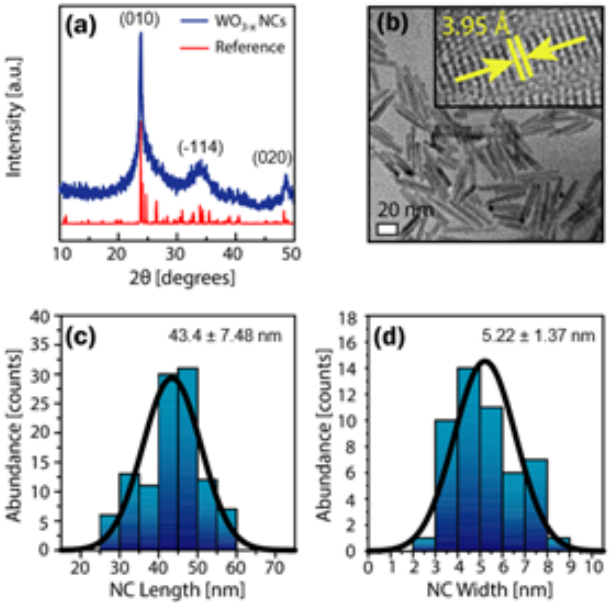



Figure 6.1: (a) X-ray diffractogram of as-synthesized colloidal $WO_{3-x}$ NCs (ICSD no. 15254). Simulated XRD pattern for monoclinic $WO_{2.72}$ is shown with red trace. (b) Overview TEM micrograph of $WO_{3-x}$ NCs. Inset: Lattice-resolved TEM image of an individual $WO_{3-x}$ nanorod, indicating its growth along ⟨010⟩ direction with an interplanar lattice spacing of 3.95 Å. (c) Length and (d) width distribution histograms for $WO_{3-x}$ nanorods, determined from the TEM micrographs presented in (b).

ca. 3.95 Å, which is in good agreement with the lattice spacing along the ⟨010⟩ direction in the monoclinic $W_{18}O_{49}$ ($WO_{2.72}$).[179]

Optical extinction spectrum of the as-synthesized $WO_{3-x}$ NCs dispersed in TCE is shown in Figure 6.2a. The broad absorption feature starting near 500 nm and extending into the NIR region can be assigned to a mixture of intraionic ligand-field (d-d) transitions at the high-energy side (visible region) and LSPR at lower energies (NIR region).[179] The intense UV absorption with the onset at ca. 420 nm can be attributed to the excitonic

(interband) transition of the $WO_{3-x}$ NCs. Using the Tauc plot in Figure 2b, the optical bandgap of the NCs was determined to be ~3.65 eV, which is in excellent agreement with band gap values reported in literature for colloidal $WO_{3-x}$ NCs.[179]

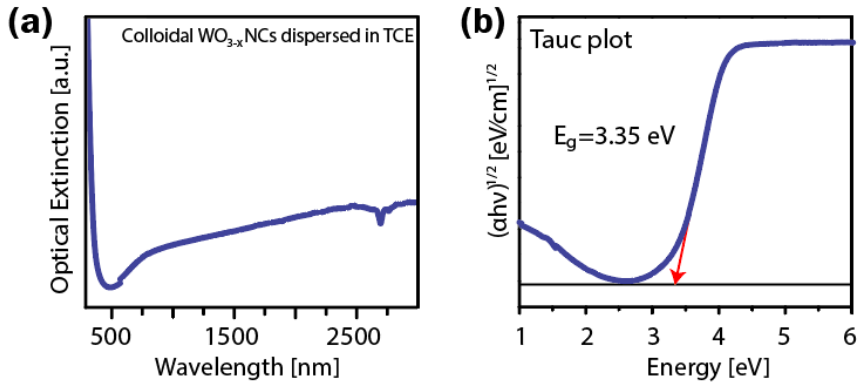



Figure 6.2: (a) Overview UV-visible-NIR spectrum and (b) corresponding Tauc plot of the $WO_{3-x}$ NCs dispersed in TCE. Red arrow in (b) represents extrapolation of the onset of absorption to determine optical bandgap of the NCs ($E_g$=3.65 eV).

### 6.2.2 Investigation of Photocatalytic Activity of $WO_{3-x}$ NCs

To investigate plasmon-induced photocatalytic activity of $WO_{3-x}$ NCs, 12 mg of ligand-stripped NCs precipitated from the concentrated toluene dispersion (shown in Figure 6.3a) were added into 50 mL aqueous solution of Rh6G dye (5 ppm) at room temperature under vigorous stirring in dark (Figure 6.3b). To monitor the Rh6G dye degradation over time, aliquots of 1.5 mL were taken every 20 min. These aliquotes were centrifuged at 7000 rpm to separate the catalyst from the dye solution. Subsequently, optical absorption spectrum of each aliquot was recorded (colored traces in Figure 6.3c). The absorbance of each subsequent aliquot exhibits a gradual decrease relative to the initial Rh6G dye solution containing no $WO_{3-x}$ NCs (0 min). According to Lambert–Beer law, the relative change in dye concentration ($C/C_0$) is equal to the relative change in optical absorbance ($A/A_0$), where $C_0$ and $A_0$ are the initial concentration and absorbance of the starting Rh6G dye solution (at 0 min), respectively. We assessed the time evolution of the Rh6G dye degradation by plotting the normalized optical absorbance maxima of each aliquot (at 526 nm) as a function of time, resulting in the exponential trend shown in Figure 6.3d. Interestingly, the as-synthesized $WO_{3-x}$ NCs exhibited a rather low degradation efficiency, as evidenced by the small reduction in absorbance between successive aliquots, as well as the overall time (ca. 520 min) necessary for the degradation of only ~88 % of

the initial amount of Rh6G dye (Figure 6.3c). We hypothesize that this low degradation efficiency arises from the strongly bound OLAC coordinating ligands on the colloidal NC surfaces which hinder the accessibility of the catalytically active surface sites to Rh6G dye molecules.[329–331] To prove this hypothesis, we first implemented $NOBF_4$-based ligand stripping of the native $WO_{3-x}$ NCs to remove the OLAC coordinating ligands (see Section 2.1.3),[171,177] and subsequently assessed the photocatalytic activity of the ligand-free NCs.

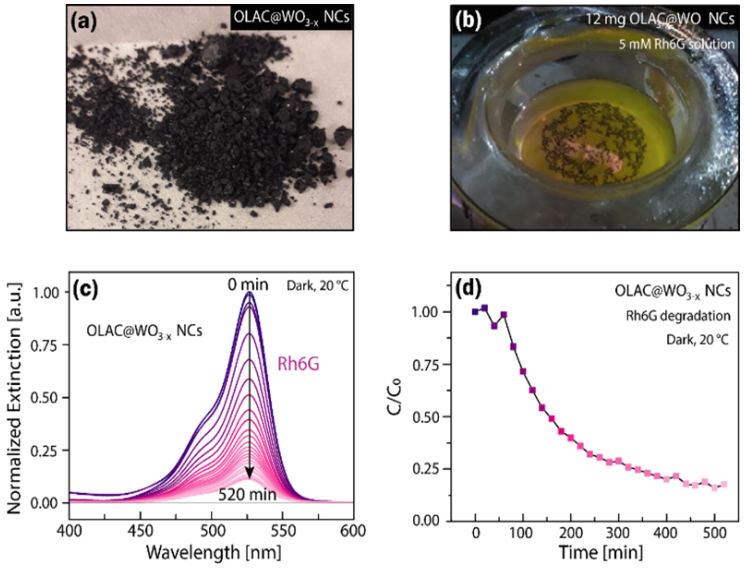



Figure 6.3: (a) Photograph of as-synthesized $WO_{3-x}$ NCs precipitated from toluene suspension using acetone. (b) Photograph demonstrating the poor dispersibility of as-synthesized $WO_{3-x}$ NCs (12 mg) in an aqueous Rh6G dye solution (5 mM). (c) Degradation of Rh6G dye by as-synthesized $WO_{3-x}$ NCs in dark at 20 °C. (d) Time-resolved dye degradation profile corresponding to the experiment shown in (c).

Figure 6.4a compares the normalized FTIR spectra obtained for the $WO_{3-x}$ NCs before ligand stripping (BLS, dark blue trace) and after ligand stripping (ALS, light blue trace). FTIR spectrum of OLAC is also shown for comparison (orange trace). For as-synthesized $WO_{3-x}$ NCs (dark blue trace), two intense bands are observed near 2855 $cm^{-1}$ and 2924 $cm^{-1}$ originating, respectively, from the symmetric and asymmetric methylene (-$CH_2$) stretching modes of OLAC capping ligand. For the pure OLAC, another intense band appears at ca. 1710 $cm^{-1}$ which can be assigned to the terminal carbonyl (-C=O) stretching mode.[332,333] Interestingly, the feature almost completely vanishes for as-synthesized OLAC-capped $WO_{3-x}$ NCs. The carbonyl stretching mode is accompanied by two

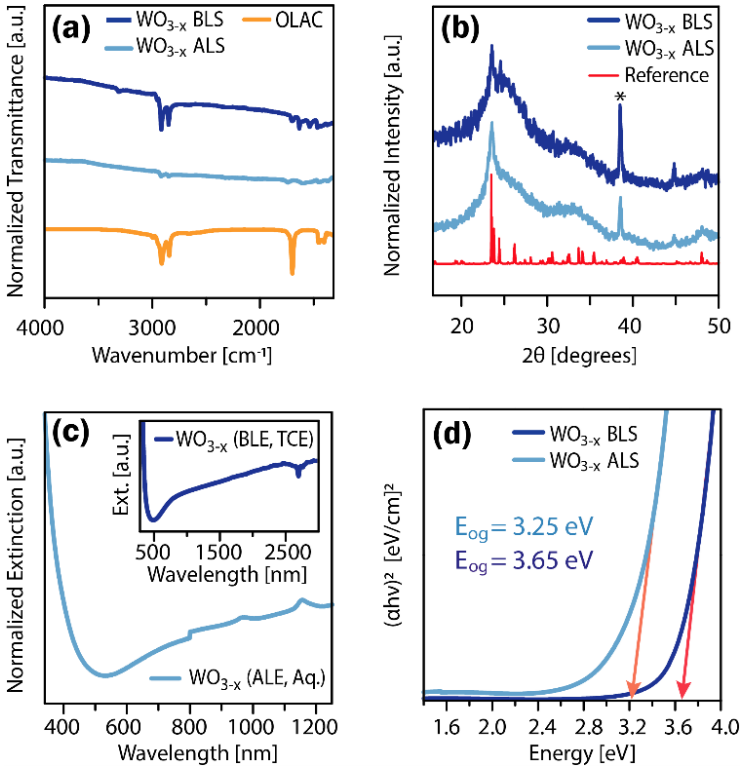



Figure 6.4: (a) FTIR spectra of the $WO_{3-x}$ NCs before ligand stripping (BLS, dark blue trace) and after ligand-stripped (ALS, light blue trace), and pure OLAC solvent (orange trace). The disappearance of characteristic -$CH_2$ stretching bands near 2855 and 2924 $cm^{-1}$ confirms successful removal of OLAC ligands from the NC surface. (b) XRD pattern of $WO_{3-x}$ NCs before ligand stripping (BLS, dark blue trace) and after ligand stripping (ALS, light blue trace), indicating retention of the crystalline structure of NCs following ligand removal. (ICSD no. 15254). (Asterisk denotes reflection peak from Si substrate). (c) UV-visible-NIR spectra of aqueous suspension of the ligand-stripped colloidal $WO_{3-x}$ NCs (light blue trace) and native $WO_{3-x}$ NCs dispersed in TCE (inset). (d) Tauc plots determined from (c) with the corresponding optical bandgap ($E_{og}$) of the NCs as indicating the arrows.

additional weak bands near 1598 $cm^{-1}$ and 1544 $cm^{-1}$, originating, respectively, from the asymmetric and symmetric -COO- stretching modes, the presence of which indicates the coordination of OLAC ligands to surface W atoms *via* the carboxylate head group. Notably, the FTIR spectrum of the ligand-stripped $WO_{3-x}$ NCs exhibits negligible intensities of all OLAC-characteristic bands, confirming the successful removal of OLAC ligands from

the NC surface. To assess if the implemented post-synthesis ligand stripping causes any crystallographic change, we performed XRD measurements before and after ligand removal. As evidenced from Figure 6.4b, XRD patterns obtained for the native (dark blue trace) and ligand-stripped (light blue trace) $WO_{3-x}$ NCs are almost identical and match the simulated XRD pattern of bulk monoclinic $WO_{2.72}$ (red trace). Figure 6.4c shows an optical extinction spectrum of the ligand-stripped NCs. This spectrum is qualitatively in excellent agreement with that of as-synthesized $WO_{3-x}$ NCs throughout the UV-visible-NIR region (inset in Figure 6.4c).

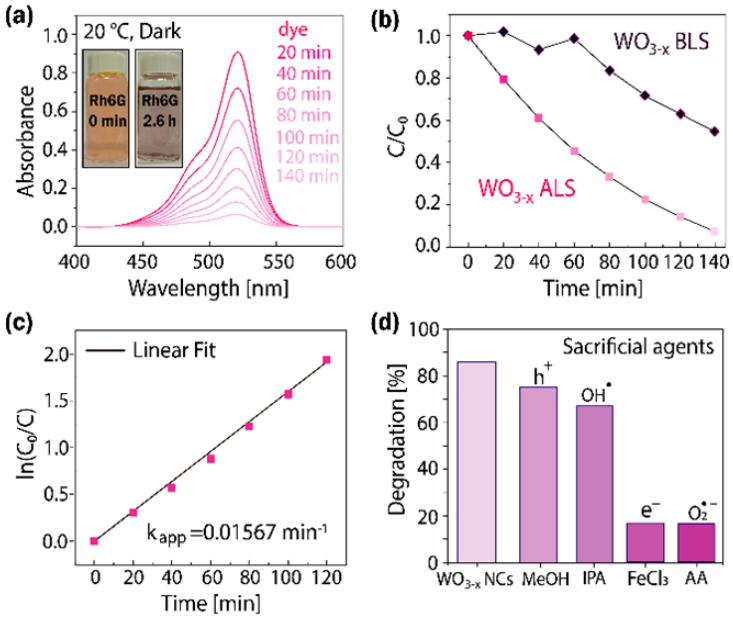



Figure 6.5: Rh6G dye degradation by the ligand-stripped $WO_{3-x}$ NCs at 20°C in dark. (a) UV-visible absorption spectra of Rh6G aliquots collected at specific time intervals. Inset: photographs of the native Rh6G dye solution (5 mM) at 0 min (left), and after 120 min degradation (right). (b) Time-dependent degradation curve of Rh6G, and (c) its linearized form, illustrating the kinetics of dye degradation. (d) Rh6G dye degradation in the presence of various sacrificial agents: methanol (MeOH, hole scavenger), IPA (i-propanol, $OH^{\bullet}$ scavenger), $FeCl_3$ ($e^-$ scavenger), and AA (ascorbic acid, $O_2^{\bullet -}$ scavenger), highlighting the influence of reactive species on the degradation mechanism. Photothermal degradation percent was calculated from absorbance value at 526 nm at 120 min.

Although the spectral features for as-synthesized and ligand-stripped NCs are virtually identical in the visible-to-NIR region (LSPR and ligaad-field transitions), there is a small

difference in the onset of the excitonic absorption in the UV regions. This was confirmed by the Tauc plots (Figure 6.4d), indicating a red shift of the optical band gap of the ligand-stripped (light blue trace) relative to as-synthesized NCs (dark blue trace). This reduction in the optical band gap ($\Delta E_{og} \sim 0.51eV$), also known as inverse Burstein-Moss shift, can be attributed to the depopulation of conduction band states in the ligand-stripped NCs as a result of the strong oxidizing power of $NOBF_4$. Importantly, the implemented ligand stripping did not induce significant change of the plasmonic properties of NCs.

We then investigated how ligand stripping of $WO_{3-x}$ NCs impacts their photocatalytic activity compared to the as-synthesized NCs. For this investigation, ligand-stripped NCs (12 mg) were drop-cast on a glass slide, which was then immersed in 50 mL (5 mM) aqueous solution of Rh6G in dark at room temperature. Aliquots of 1.5 mL were taken at equal time intervals, and their optical absorption spectra were recorded (Figure 5a). Remarkably, nearly complete dye degradation was achieved after ca. 140 min. Figure 6.5b compares the normalized rate of degradation of Rh6G facilitated by as-synthesized (black symbols) and ligand stripped (pink symbols) $WO_{3-x}$ NCs. Applying ligand-stripped NCs, nearly 3.3 times increase in the rate of degradation was realized compared to that achieved using as-synthesized NCs (Figure 6.5b), proving the detrimental impact of OLAC coordinating ligand on the photocatalytic activity. Dye degradation experiments with the ligand-stripped NCs were also carried out at various temperatures (Figure 6.6).

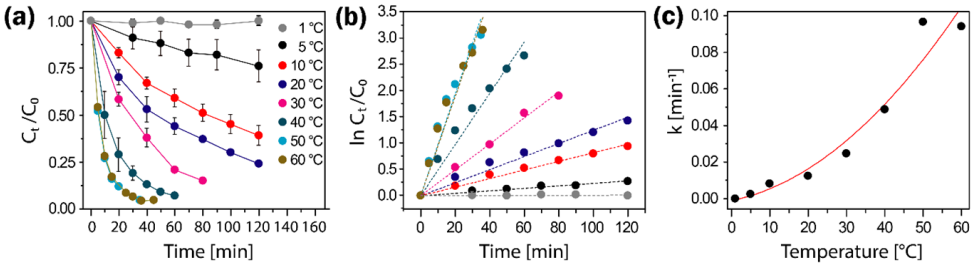



Figure 6.6: Photocatalytic degradation of Rh6G dye in the dark using the ligand-stripped colloidal $WO_{3-x}$ NCs.

Using Langmuir-Hinshelwood kinetic model, which is applicable to heterogeneous reactions proceeding sequentially *via* monomolecular adsorption, reaction, and subsequent desorption of chemical species, we estimated an apparent rate constant for Rh6G degradation ($k_a$) of ~0.0157 $min^{-1}$. (For further information on the Langmuir-Hinschelwood kinetic model, see Section 6.2.4). This $k_a$ value is notably higher (0.00196 $min^{-1}$) than that observed for similar plasmonic semiconductor metal oxide photocatalysts.[319] To gain qualitative insight into the plasmon-induced photocatalytic degradation processes, we used

different sacrificial agents to assess the impact and role of various redox species on overall catalytic efficiency (Figure 6.7). Sacrificial agents (or scavengers) are organic or inorganic compounds that can interfere in-situ with highly reactive redox species such as $OH^{\bullet}$ and $O_2^{\bullet-}$ radicals, $h^+$, or $e^-$, produced during heterogeneous photocatalytic processes,[334] according to equations 6.1-6.4:[335]

$$Photoexcitation : MO_y \xrightarrow{h\nu} MO_y e^-_{CB} + MO_y h^+_{VB} \tag{6.1}$$

$$Carrier\ recombination : MO_y e^-_{CB} + MO_y h^+_{hB} \rightarrow MO_y + heat \tag{6.2}$$

$$ROS\ generation : MO_y h^+_{hB} + H_2O \rightarrow MO_y + OH^{\bullet} + H^+ \tag{6.3}$$

$$Pollutant\ degradation : OH^{\bullet} + P \rightarrow Y \tag{6.4}$$

where $P$ and $Y$ are the organic pollutant and its degradation product, respectively. Figure 5d shows the relative decrease in percentage of the photothermal catalytic Rh6G dye degradation in the presence of isopropanol (IPA, $OH^{\bullet}$ scavenger), methanol (MeOH, $h^+$ scavenger), ascorbic acid (AA, $O_2^{\bullet-}$ scavenger), and $FeCl_3$ ($e^-$ scavenger), as sacrificial agents. All the sacrificial agents used in this study decreased the IR photocatalytic activity of the ligand-stripped $WO_{3-x}$ NCs, proving their active role in the dye degradation process. In particular, the most intense ($\sim$12 fold) decrease in the catalytic activity of the NCs was found in the presence of $FeCl_3$ and AA, indicating the significant role of electrons and $O_2^{\bullet-}$ radicals, respectively, in the dye degradation. This is because oxygen-deficient $WO_{3-x}$ NCs possesses n-type semiconducting behavior, whereby free conduction band (CB) electrons are readily consumed for the reduction of oxidizing agents ($FeCl_3$) as well as molecular oxygen adsorbed on the NC surface to form $O_2^{\bullet-}$ radicals ($e^-(CB) + O_2 \rightarrow O_2^{\bullet-}$). Meanwhile, the IR (i.e., thermal) photocatalytic activity of the plasmonic $WO_{3-x}$ NCs is only slightly inhibited in the presence of MeOH and IPA as $h^+$ and $OH^{\bullet}$ scavengers, respectively. In n-type semiconductor metal oxide NCs (e.g., $WO_{3-x}$, $TiO_{2-x}$, ZnO, $MoO_{3-x}$, etc.), $h^+$'s are intrinsically much less abundant than electrons. Due to their high redox activity, the residual photogenerated holes can either directly oxidize dye molecules adsorbed on the NC surface, or they can produce reactive oxygen species, such $OH^{\bullet}$ radicals, which subsequently facilitate dye oxidation.

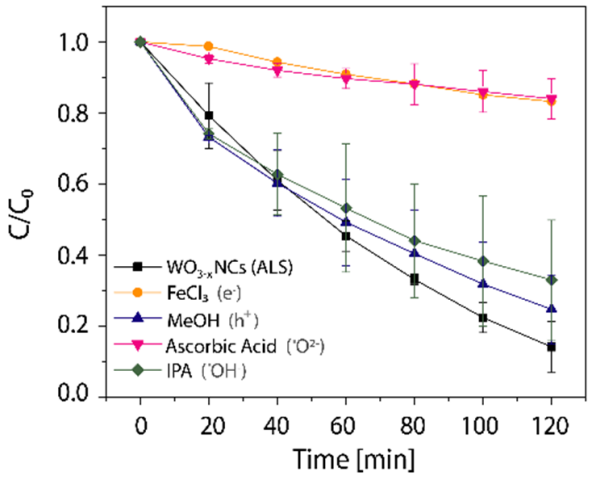



Figure 6.7: Photocatalytic dye degradation by colloidal ligand-stripped $WO_{3-x}$ NCs in the dark at 20°C in the presence of various sacrificial agents (colored traces). Scavenged species are shown in brackets.

### 6.2.3 Investigating the Correlation between Adsorption and Photocatalytic Activity

To control the level of oxygen deficiency, as-synthesized colloidal $WO_{3-x}$ NCs were annealed in air at different temperatures for 2 hours. Figure 6a presents XRD patterns of $WO_{3-x}$ NCs annealed at various temperatures between 350 and 800°C. As shown in Figure 6.1a, X-ray diffractograms of colloidally synthesized $WO_{3-x}$ NCs have broad peaks at ca. 24.9°, 34.8°, and 48.5° corresponding, respectively, to the (010), (-114), and (020) planes of the bulk monoclinic $WO_{2.72}$ phase (shown also as dark blue trace in Figure 6.8a for comparison). As annealing temperature increases (≥350°C), NCs undergo a change in the crystal structure accompanied by an increase in the primary NC size, as evidenced by the emergence of new diffraction peaks between ca. 25° and 60° and a gradual decrease in peak broadening. This is because annealing $WO_{3-x}$ (or other oxygen deficient metal oxide) NCs in air allows for oxygen incorporation into the crystal lattice, thus leading to the change in NC phase, as well as an increase in grain size due to enhanced NC aggregation and coalescence.[336] It is important to note that oxygen incorporation into the crystal structure as a result of high-temperature annealing of the NCs also leads to changes in their free carrier density, thus altering the LSPR properties. The increase in the grain size is further corroborated by the SEM micrographs shown in Figure 6b-e, providing visual

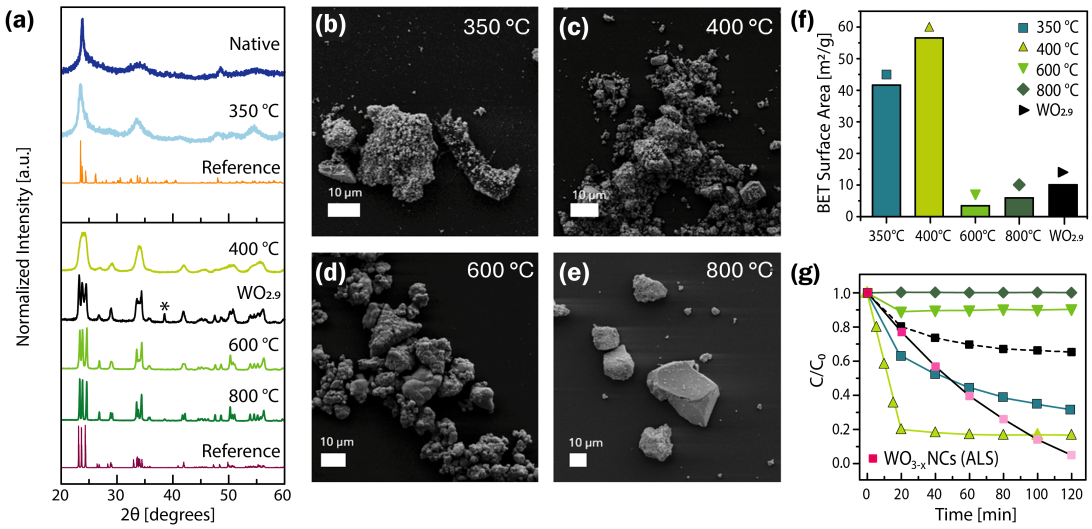



Figure 6.8: (a) X–ray diffractograms and (b–e) SEM micrographs of $WO_{3-x}$powder samples obtained by annealing the as-synthesized $WO_{3-x}$ NCs in air for 2 hours at different temperatures: (b) 350°C, (c) 400°C, (d) 600°C, and (e) 800°C, revealing a temperature-dependent morphological and size evolution of the NCs, as a result of the annealing. Black trace in (a) corresponds to XRD pattern of bulk $WO_{2.9}$ used as reference for the photothermal catalysis/adsorption measurements. (f) BET specific surface area of the NCs from the annealing series together with that of bulk $WO_{2.9}$. (g) Time-evolution of the Rh6G dye concentration change as a function of time for each sample in the annealing series. (Pink markers correspond to photodegradation profile of the ligand-stripped $WO_{3-x}$ NCs presented in Figure 6.5b).

representation of the temperature-induced NC sintering. To estimate the specific surface area (as one of the important parameters characterizing adsorption efficiency and capacity), BET measurements were conducted on each sample in the annealing series, the results of which are shown in Figure 6.8f (and Figure D2 in Appendix). Interestingly, the largest surface area was measured for NCs annealed at 400°C (56.6 $m^2/g$). In comparison, nearly two-, four-, and eight-times smaller values were found for the NCs annealed at 350°C, 800°C, and 600°C, respectively (Figure 6.8f), suggesting no systematic trend between annealing temperature and surface area of the NCs.

We then sought to investigate the correlation between adsorption and thermal photocatalytic activity of the annealed sample series in the dark at room temperature using Rh6G

dye as a model system. To quantify the kinetics of the adsorption/catalytic degradation processes, aliquots of 1.5 mL were taken from the 50 mL aqueous Rh6G dye solution (5 ppm) at specific time intervals. These aliquotes were centrifuged and their optical extinction spectra measured, following the same procedure as for the as-synthesized $WO_{3-x}$ NCs. (For further information, see Section 2.2.10) Figure 6.8g presents the time-evolution of the Rh6G dye concentration change as a function of time (colored symbols) monitored over 2 hours for each sample in the series (Figure 6.9). All samples except for the NCs annealed at 800°C exhibit non-zero adsorption affinity for the Rh6G dye, which varies markedly for different annealing temperatures, reflecting distinct surface chemistries and adsorption site densities induced by the post-synthesis thermal treatments. Interestingly, the concentration profiles for the NCs annealed at 350°C (blue squares) and bulk $WO_{2.9}$ (black squares) follow an exponential-like decay, indicating a gradual adsorption of Rh6G and the resulting in the removal of approximately 30% (6.3 mg· $g^{-1}$) and 50% (10.5 mg· $g^{-1}$) of the initial amount of dye, respectively (Figure 6.8g, 6.9f). Notably, however, the NCs annealed

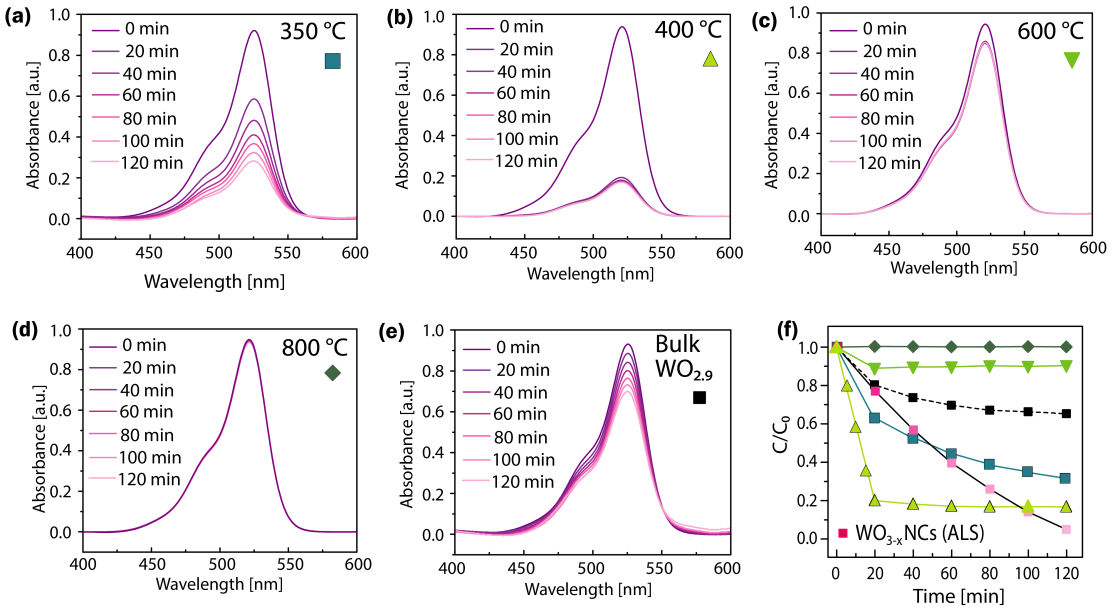



Figure 6.9: (a-e) Steady-state optical extinction spectra of aliquots of Rh6G aqueous solution taken at specific time intervals for spectroscopically monitoring the adsorption-photothermal catalytic processes of $WO_{3-x}$ NCs annealed at 350°C (a), 400°C (b), 600°C (c), 800°C (d), and the commercial $WO_{2.9}$ (e). (f) Time evolution of adsorption/photothermal catalytic degradation of Rh6G for each sample in (a-e).

at 400°C (yellow-green triangles) and 600°C (light-green triangles) show a pronounced initial decline during the first 20 min, corresponding to roughly 80% (16.8 mg· $g^{-1}$) and 10% (2.1 mg· $g^{-1}$) adsorbate uptake, respectively, after which the system reaches a quasi-steady state, indicating a rapid occupation of the available adsorption sites. Based on the adsorption profile and kinetic measurements presented in Figure 6.8g (and Figure 6.10), we hypothesized that the pronounced surface interactions observed for $WO_{3-x}$ NCs annealed at 400°C, may also involve chemisorption of dye.

### 6.2.4 Adsorption and Kinetic Studies

Accurately describing how solutes interact with solid surfaces in liquid media is fundamental to advancing our understanding of adsorption processes, particularly in applications involving pollutant removal and water purification. To assess and quantify the time evolution and kinetics of dye adsorption processes, the following balance equations presented in equation 6.5-6.17 can be used.[327,337–339] Equation 6.5 quantifies the amount of dye adsorbed at time $t$, as follows:

$$q_t = \frac{(C_0 - C_t) \times V}{W} \tag{6.5}$$

where $q_t$ $(mg/g)$ is the adsorbed amount of dye at time t per unit mass of adsorber (NCs), $C_t$ (mol/l) and $C_0$ are the equilibrium (final) and initial concentration and of dye solution of volume $V$ $(l)$, respectively, and $W$ $(g)$ is the dry mass of adsorber ($WO_{3-x}$ NCs). At each time interval, the percentage value of dye removed can be quantified (equation 6.6).

$$Adsorption\ \% = \frac{(C_0 - C_t)}{C_0} \times 100 \tag{6.6}$$

After the adsorption system has reached adsorption–desorption equilibrium (at $t_\infty$), the equilibrium quantity of adsorbate per unit mass of adsorber ($q_e$, mg/g) can be determined, as expressed in equation 6.7:

$$q_e = \frac{(C_0 - C_{t,\infty}) \times V}{W} \tag{6.7}$$

To investigate the kinetic aspect of the adsorption processes, we used the pseudo-first-order (PFO), pseudo-second-order (PSO), and intra-particle diffusion (IPD) models. For PFO and PSO kinetics, Langmuir's adsorption kinetic model provides theoretical basis,

which assumes reversibility of adsorption–desorption processes between solute (A) and an adsorption site (B) on the adsorbent surface, as expressed in equation 6.8:

$$A + B \underset{}{\overset{k_a, k_d}{\rightleftharpoons}} AB \tag{6.8}$$

where $k_a$ and $k_d$ are adsorption and desorption rate constants, respectively. With the formation of AB complexes, a fraction of the adsorbate surface sites becomes gradually occupied over time ($\theta_t$) (eventually fully covered by a monomolecular layer of adsorbate ($\theta_e$)), according to equation 6.9:

$$\theta_t = \frac{q_t}{q_{max}} = \frac{C_0 - C_t}{q_{max} W} \tag{6.9}$$

where $q_{max}$ (mg/g) theoretical maximum (monolayer) adsorption capacity. Owing to the proportionality between $\theta_t$ and $q_t$, the following relation can be expressed:

$$\frac{d\theta_t}{dt} = \frac{dq_t}{dt} = k_1[q_e - q_t] + k_2[q_e - q_t]^2 \tag{6.10}$$

$$where:\ k_1 = [k_a^2(C_0 - q_{max}W)^2 + 2k_a k_d(C_0 + q_{max}W) + k_d^2]^{1/2} \tag{6.11}$$

$$and:\ k_2 = k_a q_{max} W \tag{6.12}$$

where $k_1$ ($min^{-1}$, eq 6.11) and $k_2$ ($mg{\cdot}g^{-1}min^{-1}$, eq 6.12) are first order and second order rate constants, respectively. In fact, one can see from eq 6.10 that the Langmuir kinetic model can describe both first and second order physisorption processes. With the assumption of $q_e \ll k_1/k_2$, equation 6.10 can be simplified to Lagergren's PFO kinetic equation,[340,341] as in equation 6.13:

$$\frac{dq_t}{dt} = k_1[q_e - q_t] \tag{6.13}$$

Applying boundary conditions ($q_t = 0$ at $t = 0$; and $q_t = q_t$ at t=t) on equation 6.13 results in equation 6.14,

$$q_t = q_e(1 - e^{-k_1 t}) \tag{6.14}$$

which can then be linearized, according to equation 6.15:

$$ln(q_e - q_t) = ln(q_e) - \frac{k_1 t}{2.303} \tag{6.15}$$

In contrast to PFO, pseudo-second-order (PSO) kinetic model can generally be applied to adsorption processes, wherein the rate-limiting step is governed by strong physisorption or chemisorption processes. Since the condition of $q_e \ll k_1/k_2$ (that is, $k_1 \ll k_2\ (\theta_e - \theta_t)$ no longer holds for PSO kinetics (unlike for the PFO kinetic model), equation 6.15 can be simplified to equation 6.16, as follows:[337]

$$q_t = \frac{q_e^2 k_2 t}{1 + q_e k_2 t} \tag{6.16}$$

with its commonly used linearized form presented by Ho and McKay et al.[342] (equation 6.17):

$$\frac{t}{q_t} = \frac{t}{q_e} + \frac{1}{k_2 q_e^2} \tag{6.17}$$

In Figure 6.8, I present a series of $WO_{3-x}$ NC samples annealed at different temperatures, among which, in particular, NCs annealed at 350°C or 400°C exhibit a substantial specific surface area (Figure 6.8f) and porosity (Figure 6.8b,c). These structural features, together with the surface chemistry of the NCs, result in substantial adsorption of Rh6G dye, which may potentially influence the mass transfer step and diffusion processes of the dye within the porous network of the adsorbate. To account for these effects, the intraparticle diffusion (IPD) kinetic model is invoked, which involves and allows for assessing three main mass transfer processes: (*i*) the external diffusion (*i.e.*, diffusion of adsorbate in the solution–adsorber interface towards adsorber surface), (*ii*) internal/intraparticle diffusion (*i.e.*, mass transfer of adsorbate inside the pores of adsorbent, and (*iii*) the actual adsorption of solute onto adsorber surface sites.[343] For an adsorber containing nanoparticles of radius r allowing for an intrinsic diffusivity ($D$) of the solute, the initial rate of IPD kinetics can be expressed as:

$$q_t = k_p t^{1/2} + C \tag{6.18}$$

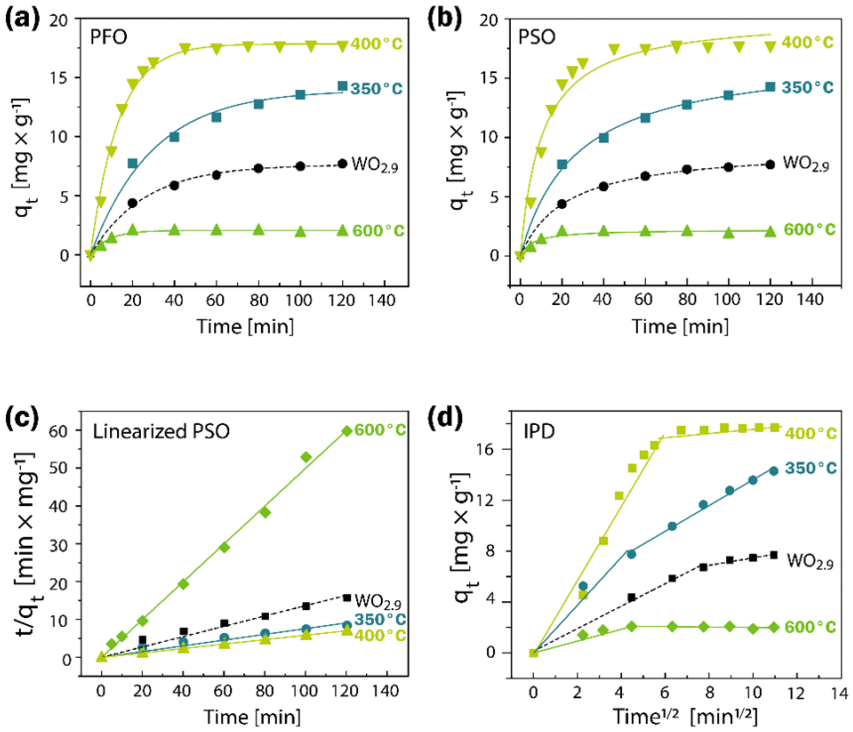



Figure 6.10: Plots of (a) PFO, (b) PSO, (c) linearized PSO, and (d) IPD kinetic models.

where $k_{IPD}$ ($mg \cdot g^{-1} \cdot min^{-1/2}$) is IPD rate constant and C (mg/g) is constant. According to Weber and Morris's empirical theory,[344] the $q_t$ vs $t^{1/2}$ plot yields a straight line for adsorption processes (with slopes yielding $k_p$), wherein the IPD is the rate controlling step.[345] As can be seen in Figure 6.10d, the IPD kinetic fittings for each NC sample in the annealing series resulted in multiple linear segments, which, in fact, can be attributed to different diffusion (mass transfer) steps occurring at different time scales.

Table 6.1: Kinetic and fitting parameters extracted from Figure 6.10.

| Kinetic models | | | |
|---|---|---|---|
| **PFO** | | | |
| Sample | $q_e$ [mg/g] | $k_1$ [$min^{-1}$] | $R^2$ |
| WO-350 | 13.946 | 0.034 | 0.9871 |
| WO-400 | 17.844 | 0.075 | 0.9934 |
| WO-600 | 2.055 | 0.116 | 0.9731 |
| $WO_{2.9}$ | 7.619 | 0.039 | 0.9964 |
| **PSO** | | | |
| | $q_e$ [mg/g] | $k_2$ [$g \cdot mg^{-1} \cdot min^{-1}$] | $R^2$ |
| WO-350 | 17.110 | 0.002 | 0.9967 |
| WO-400 | 20.290 | 0.005 | 0.9650 |
| WO-600 | 2.232 | 0.075 | 0.9294 |
| $WO_{2.9}$ | 0.916 | 0.005 | 0.9995 |
| **IPD** | | | |
| | **Step I** | | **Step II** |
| | $k_{IPD}$ [$mg \cdot g^{-1} \cdot min^{-1/2}$] | $R^2$ | $k_{IPD}$ [$mg \cdot g^{-1} \cdot min^{-1/2}$] | $R^2$ |
| WO-350 | 1.838 | 0.9801 | 1.012 | 0.9898 |
| WO-400 | 0.204 | 0.6152 | 2.917 | 0.9536 |
| WO-600 | 0.464 | – | 0.018 | 0.9805 |
| $WO_{2.9}$ | 0.883 | 0.9966 | 0.293 | 0.9694 |

#### 6.2.4.1 Adsorption Equilibrium Studies

To characterize the equilibrium interactions in the Rh6G–$WO_{3-x}$ adsorption system presented in this study, a variety of adsorption isotherm models have been established, each offering a distinct conceptual perspective on adsorbate–adsorber interaction at solid–liquid interface. Among the many different models, the Freundlich,[346] Langmuir,[347] Temkin,[348] Sips,[349] and Dubinin–Radushkevich (D–R)[350] isotherms are routinely applied, to probe and characterize adsorption mechanisms, surface heterogeneity, and adsorbate binding strength. Collectively, these models serve as indispensable tools for interpreting adsorption behavior and evaluating the performance of novel adsorbent systems. In this study, the Rh6G adsorption equilibrium experiments were performed for the $WO_{3-x}$ NCs annealed at 400°C in the dark at 20°C (at neutral pH) using 50 mL of aqueous Rh6G dye solutions with 5–30 mg/L dye concentration. To characterize the equilibrium nature and mechanism of Rh6G adsorption at solid-liquid interface for the $WO_{3-x}$–Rh6G system, we implemented the Langmuir, Freundlich, and D-R isotherm models. These non-linear equations relate the quantity of adsorbed species at thermodynamic equilibrium per unit weight of adsorbate ($q_e$) and the equilibrium concentration of the solute remaining in the solution ($C_e$). The Langmuir and Freundlich isotherms (Figure 6.11a,b) assume formation of a monomolecular

layer or multilayer of adsorbates at solid–liquid interfaces, respectively, and are expressed in equations 6.19 and 6.20, respectively:

$$\frac{C_e}{q_e} = \frac{C_e}{q_{max}} + \frac{t}{K_L q_{max}} \tag{6.19}$$

$$ln(q_e) = ln(K_F) - \frac{1}{n} ln(C_e) \tag{6.20}$$

where $q_{max}$ (mg/g) and $K_L$ (l/mg) are the theoretical maximum (monolayer) adsorption capacity and Langmuir equilibrium adsorption constant, respectively. $K_F$ (mg/g) and $n$ in equation 6.20 are, respectively, the Freundlich adsorption isotherm constant and heterogeneity factor characterizing the adsorption intensity (Table 6.2).

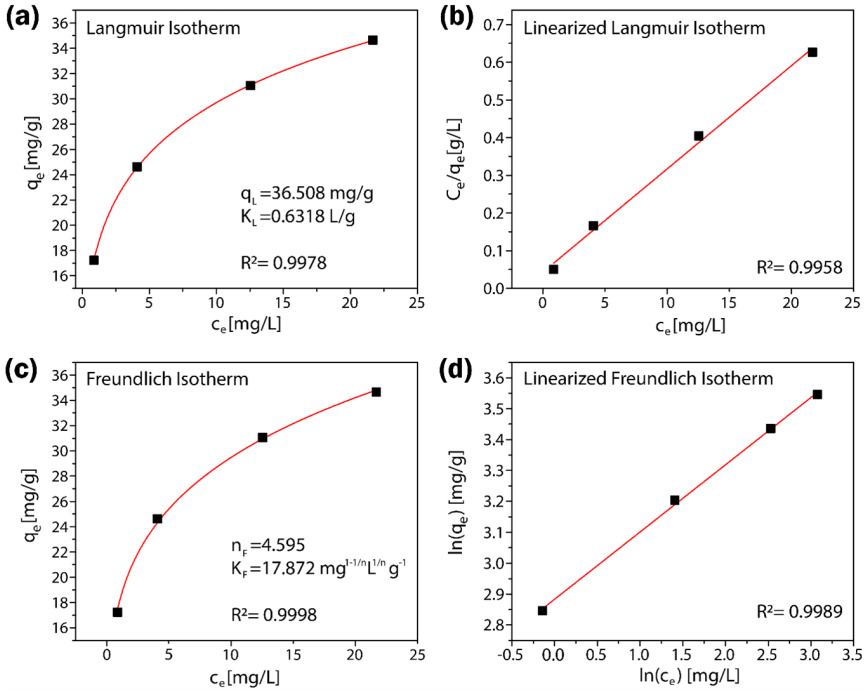



Figure 6.11: Adsorption isotherms and their corresponding linearized forms using Langmuir (a,b) and Freundlich (c,d) models, respectively, for $WO_{3-x}$ NCs annealed at 400°C for 2 hours. (Measurements were carried out at 20°C in dark). Fitting parameters can be seen in bottom right corner of each panel.

Notably, both the Langmuir (Figure 6.11a,b) and Freundlich (Figure 6.11c,d) isotherm models yielded an excellent fitting for the experimental data, indicating the complexity of the adsorption processes. Based on the isotherm fittings, a $q_{max}$ of ∼36.51 mg/g (Figure 6.11a), furthermore, $K_F$ of ∼17.87 L/g and $n_F$ of ∼4.60 (Figure 6.11c), respectively, were found for the present $WO_{3-x}$–Rh6G adsorption system. Importantly, the fact that the heterogeneity factor ($n_F$) found in this study for $WO_{3-x}$ NCs exceeds unity (*i.e.*, $n_F > 1$) provides strong evidence for the multilayer formation of Rh6G on the NC surface.

Apart from the Langmuir and Freundlich isotherms, we also implemented the D–R model (Figure 6.12) to further investigate the adsorption mechanism of Rh6G dye on $WO_{3-x}$ NCs. In general, D–R isotherms can be used to describe adsorption processes governed by pore-filling mechanisms at solid–gas or solid–liquid interfaces and are particularly useful for differentiating between physisorption and chemisorption, using Polanyi's adsorption potential theory.[338] Similarly to Langmuir and Freundlich models, D-R isotherms can also be linearized, as presented in equation 6.21:

$$ln(q_e) = ln(X_m) - \beta\epsilon^2 \tag{6.21}$$

where $X_m$ (mg/g), $\theta$ ($mol^2/kJ^2$), and $\epsilon$ (kJ/mol) are D-R monolayer sorption capacity, activity coefficient, and Polanyi potential parameters (Figure 6.12), respectively. Equation 6.22 can be used to quantify $\epsilon$, as follows:

$$\epsilon = RT \cdot ln(\frac{1}{C_e}) \tag{6.22}$$

where $R$ (8.314 $J \cdot mol^{-1}K^{-1}$) and $T$ are the universal gas constant and the thermodynamic temperature, respectively. Then, one can plot and linearly fit $ln(q_e)$ vs $\epsilon^2$ (Figure 6.12) to get $\beta$ (slope) and $X_m$ (y intercept). Finally, equation 6.23 can be used to quantify sorption energy ($E, kJ/mol$), as follows:

$$E = \frac{1}{\sqrt{-2\beta}} \tag{6.23}$$

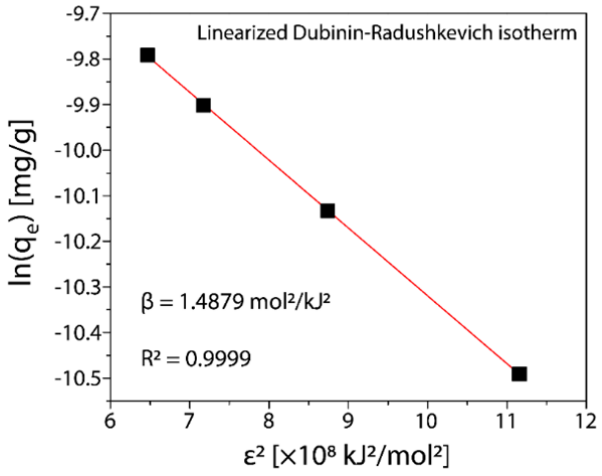



Figure 6.12: Linearized Dubinin–Radushkevich (D-R) isotherm model for $WO_{3-x}$ NCs annealed at 400°C for 2 hours. (Measurements were carried out at 20°C in dark).

Table 6.2: Summary of Isotherm Fitting Parameters Presented in Figure 6.11-12.

| Isotherm Models | Parameter values | | |
|---|---|---|---|
| Langmuir (non-linearized) | $q_{max}$ [mg/g] | $K_L$ [L/mg] | $R^2$ |
| | 36.5081 | 0.6318 | 0.9978 |
| Freundlich (non-linearized) | $K_F$ [L/g$^{-1}$] | $n_F$ | $R^2$ |
| | 17.8723 | 4.5950 | 0.9998 |
| Dubinin–Radushkevich (D–R) (linearized) | $\beta$ [mol$^2$/kJ$^2$] | $E$ [kJ/mol] | $R^2$ |
| | 1.4879 | 0.5797 | 0.9999 |

### 6.2.5 ESI-MS Study

While the adsorption profiles generally provide an insight into binding efficiency, they do not reveal a mechanism of transformation of the dye adsorbate at the molecular level. Therefore, to assess the coexistence of and mutual correlation between adsorption and plasmon-induced photocatalytic degradation, we monitored the formation of Rh6G degradation products formed after adsorption conducted in the dark. Using electrospray ionization-mass spectrometry (ESI–MS), we sought to determine whether and through what pathways Rh6G dye degrades by the $WO_{3-x}$ samples upon adsorption. The ESI–MS spectra of the solutions (post-adsorption) for the as-synthesized and 400°C annealed $WO_{3-x}$ samples are shown in the upper and middle panels of Figure 7, respectively (the spectrum

of Rh6G solution is shown in the bottom panel for comparison). The ESI–MS data for Rh6G displays numerous ions across the mass range, including

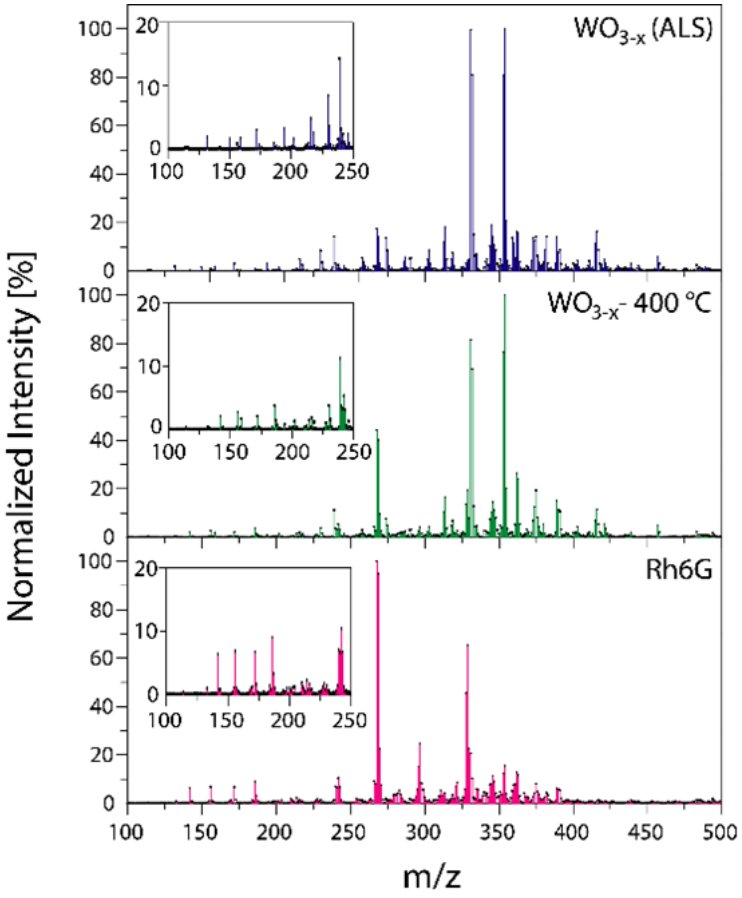



Figure 6.13: ESI–MS spectra showing the molecular fragments of Rh6G degraded by the ligand-stripped $WO_{3-x}$ NCs (top panel), and $WO_{3-x}$ annealed at 400°C and (middle panel). ESI–MS spectrum of pure Rh6G dye (bottom panel) is shown as a reference. Insets show regions of the corresponding spectra between 100–250 $m/z$.

prominent molecular ions at $m/z$ 329 and 268, associated with known fragments of Rh6G. Both ESI-MS data involving $WO_{3-x}$ as a plasmonic photocatalyst show evidence of Rh6G degradation with the change in prominent mass fragments to $m/z$ 354 and 329. There are numerous fragments observed in the spectra; the vast majority are above $m/z$ 250, which are associated with fragments that do not correspond to the cleavage of the chromophore group.[351] However, there is evidence of some small $m/z$ fragments which may indicate

significant degradation using $WO_{3-x}$ as a photocatalyst to drive degradation of organic dyes to small organic molecules.[351] While the results here provide evidence of the coupling of the adsorption and photothermal catalytic processes in $WO_{3-x}$, further work is needed to examine the complete photocatalytic pathway and mechanism.

### 6.2.6 Conclusion

In this study, I investigated the photocatalytic activity of colloidal plasmonic $WO_{3-x}$ NCs synthesized *via* thermal decomposition method. Using Rh6G dye as a model compound, a poor photocatalytic activity was observed for the as-synthesized NCs, owing to the presence of OLAC coordinating ligands on NC surface. Using NOBF4-based post-synthetic ligand stripping, OLAC ligands were successfully removed from NC surface, as evidenced by FTIR measurements, thus enabling greater accessibility of the surface sites. As result, the ligand-stripped NCs exhibited a significant improvement (∼3.3 times) in photocatalytic activity compared to the as-synthesized NCs. To modulate the level of oxygen deficiency and thus free carrier density, the NCs were post-synthetically annealed in air at elevated temperatures. In the annealing series, NCs annealed at 350 and 400°C exhibited the largest BET surface area (56.6 $m^2/g$ and 41.60 $m^2/g$, respectively). While the NCs in the annealing series showed negligible (WO-600 and WO-800°C) or appreciable adsorption capacity (WO-350°C), the WO-400°C sample showed remarkably strong and rapid adsorption for Rh6G dye, as evidenced by the adsorption kinetic and equilibrium studies. Characteristic ESI-MS signals suggested the presence of Rh6G fragments for both ligand-stripped and WO-400°C samples, indicating dye degradation to concurrently proceed with adsorption processes.

# Chapter 7

## Conclusions and Future Work

## 7.1 Conclusions

In this thesis, I investigated the electronic structure, magneto-optical, and photonic properties of colloidal plasmonic oxygen-deficient tungsten oxide ($WO_{3-x}$) and Cs-doped hexagonal tungsten oxide (hex-Cs:$WO_{3-x}$) NCs. The $WO_{3-x}$ NCs were synthesized *via* the thermal decomposition of $W(CO)_6$ at elevated temperatures (300°C, 2h) in a mixture of oleic acid and oleylamine. The NCs were found to possess monoclinic crystal structure and elongated rod-like morphology and shape uniformity, as evidenced by XRD and TEM measurements, respectively. In Chapter 3, I investigated the magneto-optical properties of plasmonic $WO_{3-x}$ NCs, using variable-field (5 K, 1-7 T) and variable-temperature (7T, 5-300 K) MCD measurements. Variable-field MCD spectra and the magnetic field dependence of monochromatic MCD intensities revealed that the broad optical (visible–NIR) absorption bands, formerly attributed to LSPR absorption in fact originates from two fundamentally different spectroscopic phenomena: (*i*) intraionic d-d ligand-field transitions in $W^{5+}$ ($d^1$) at higher energies in the visible region (∼500-650 nm), and (*ii*) LSPR absorption at lower energies (>750 nm) due to collective oscillations of free electrons in the conduction band. Based on these results, I deconvoluted the low-temperature (5 K, 0 T) optical absorption spectrum of plasmonic $WO_{3-x}$ NCs into a ligand field (and polaronic) and LSPR bands, which enabled the correct determination of free carrier density in the NCs.

To develop deeper understanding of the excitonic (interband) absorption region of plasmonic alkali tungsten bronze NCs, I investigated the impact of NC geometry on the intrinsic plasmon-exciton interactions in plasmonic semiconductor metal oxide NCs (Chapter

4). For this study, I used hex-Cs:$WO_{3-x}$ nanoprisms, which exhibit dual-band dipolar LSPR absorption in the visible–NIR region arising from $LSPR_{\parallel}$ and $LSPR_{\perp}$. I synthesized shape- and size uniform colloidal hex-Cs:$WO_{3-x}$ NCs with varying aspect ratios (AR=height/width), using a solvent mixture of oleic acid and oleylamine in specific molar ratios to modulate AR. Using variable-field MCD spectroscopy, I demonstrated that the AR of hex-Cs:$WO_{3-x}$ NCs plays a crucial role in excitonic Zeeman splitting mechanism. Namely, while the nanoplatelets (low AR nanostructures) exhibited strongly saturating magneto-optical response, the excitonic MCD spectra of the nanorods (high AR nanostructures) showed purely linear behavior. These observations were attributed to the interplay of strong carrier localization on the basal (a-b) plane and carrier delocalization along the prismatic (c-axis) plane. Hence, the nanoplatelets (with the basal plane as the dominant facet with strongly localized carriers) exhibit spin-induced (anomalous) Zeeman splitting, while the nanorods (with the prismatic plane as dominant facet with delocalized carriers along c-axis) exhibit cyclotron-free-carrier–induced excitonic Zeeman splitting.

In Chapter 5, I sought to investigate the potential of both non-stoichiometric and doped plasmonic transition metal oxide NCs for enhancing the response of NIR photodetection. For this study, colloidal plasmonic $WO_{3-x}$ nanorods and hex-Cs:$WO_{3-x}$ nanoprisms (AR=1.7) drop-cast on the interdigitated active surface area of epitaxially-grown planar InGaAs MSM photodetector, were used. In the presence of the NCs, significant enhancement in photoresponsivity (EQE≈7%-60%) was observed, indicating the active role of plasmonic NC in NIR light absorption. Although the experimental data collected did not provide sufficient evidence for elucidating the actual mechanism, in our study three possible mechanisms were considered for the enhanced photoresponsivity observed: (*i*) the LSPR modes of NCs create stronger electric fields in the top InGaAs layer of the MSM device, facilitating the generation of charge carriers at a higher rate, (*ii*) as a result of LSPR absorption, the energetic hot carriers can be injected into the CB of InGaAs layer across the Schottky barrier at the heterointerface, and (*iii*) photon collection from scattering is increased due to the NC films forming an anti-reflective coating.

Finally, I investigated the plasmonic photocatalytic activity of a series of post- synthetically annealed and surface-modified colloidal $WO_{3-x}$ NCs, using Rh6G xanthene dye as model compound. As-synthesized colloidal plasmonic NCs are typically stabilized with long-chain organic ligands, impeding dye adsorption and hindering catalytic interactions at the NC surface. Using $NOBF_4$-based post-synthetic ligand stripping, I successfully removed oleic acid (OLAC) coordinating ligands from the surface of OLAC@$WO_{3-x}$ NCs and demonstrated that surface modification not only improves dye adsorption but also sig-

nificantly enhances the photocatalytic degradation rate and apparent rate constant. Furthermore, to modulate the level of oxygen-deficiency and thus LSPR properties, colloidal $WO_{3-x}$ NCs were annealed in air at elevated temperatures (350-800°C, 2 h). Through systematic adsorption equilibrium experiments, I observed a strong and fast adsorption of Rh6G dye within relatively short timescale (minutes), which, in the literature, is often erroneously attributed to photocatalytic activity. Using electrospray-ionization mass spectrometry (ESI-MS) experiments, I investigated the potential degradation of Rh6G aiming to disentangle and quantify the individual contributions of adsorption and photocatalysis.

## 7.2 Future Work

While the research presented in this dissertation has contributed valuable insights, several interesting questions regarding the LSPR tunability, understanding of electronic structure, magneto-optical properties, and functional integration of plasmonic semiconductor metal oxide NCs remain open for future exploration.

One of the interesting and important extensions of the work presented in **Chapter 3** would be to investigate the electronic structure and magneto-optical properties of other plasmonic transition metal oxide NCs, particularly non-stoichiometric molybdenum (VI) oxide ($MoO_{3-x}$) and rhenium (VI) oxide ($ReO_3$) NCs. For this project, the colloidal synthesis protocol of $ReO_3$ NCs reported by Gosh et al. could be implemented, which uses an ether-based reduction of $Re_2O_7$ under inert atmosphere at 100-260°C. Owing to the $d^1$ valence electron configuration of $Re^{6+}$ and the predominant Re d-orbital character of the conduction band, the Fermi level of $ReO_3$ NCs lies within the conduction band, resulting in metallic behavior characterized by an LSPR peak near 600 nm and the onset of excitonic transitions around 350 nm. Interestingly, in the range of 370-470 nm, a pronounced shoulder emerges in the optical extinction spectrum of $ReO_3$ NCs, which could originate from high-energy intraionic (d-d) ligand-field transitions. However, regarding the $MoO_{3-x}$ NCs, first a precise synthesis protocol for size and shape uniform colloidal plasmonic $MoO_{3-x}$ NCs needs to be established. In my preliminary research, I investigated the optimal synthetic conditions for shape and size unform $MoO_{3-x}$ NCs, modulating, for instance, the OLAC/OLAM and $Mo(CO)_6$ precursor ratios. Interestingly, adapting the same synthesis conditions described in Chapter 3 for the colloidal plasmonic $WO_{3-x}$ NCs did not yield colloidal $MoO_{3-x}$ NCs. Although a few studies have reported the magneto-optical properties of non-uniform plasmonic $MoO_{3-x}$ NCs, those are limited to room-temperature MCD experiments under constant magnetic field strengths ($\pm$ 1.6 T). In this project extension, I propose that variable-field MCD measurements would en-

able probing the magnetic field dependence of polaronic transitions (visible-NIR region), as well as polaron-exciton and polaron-LSPR interactions (UV-visible region) in $MoO_{3-x}$ NCs. Given the fact that polarons are quasiparticles arising from charge carrier oscillations coupled to phonons (quanta of lattice vibration), I propose that temperature-dependent and helicity-resolved Raman spectroscopy and variable-temperature MCD measurements would be essential to gain insight into the temperature-dependent nature of polaronic transitions and polaron-exciton-LSPR interactions in plasmonic semiconductor NCs. Another interesting and important research direction in this project would be to perform ultrafast transient absorption measurements to investigate the spatiotemporal evolution of polaronic transitions and its exchange interactions with the exciton and plasmons.

One of the interesting extensions of the research project presented in **Chapter 4** could be to investigate the dual-band plasmon–exciton interactions in Cs:$WO_{3-x}$ NCs of higher aspect ratios. For the synthesis of these NCs, the work of Cheref et al. and Oh et al. can be adapted. Contrary to the Cs:$WO_{3-x}$ nanoplatelets ($\sim 0.3 <$AR$<\sim 0.5$) or iso-prisms (AR$\approx$1.0), in Cs:$WO_{3-x}$ NCs of higher aspect ratios the longitudinal LSPR resonance ($LSPR_{\parallel}$) undergoes a bathochromic shift while the LSPR resonance ($LSPR_{\perp}$) remains nearly invariant in energy, potentially leading to a higher spatial overlap of the $LSPR_{\perp}$ with the exciton. Variable-field MCD measurements could be used to investigate the magneto-optical response of the $LSPR_{\perp}$–exciton interactions. Another interesting research direction of this project could be to synthesize other plasmonic compound semiconductor NCs exhibiting dual-band dipolar or even higher order (e.g., quadrupolar or octopolar) LSPR resonances and investigate their intrinsic plasmon-exciton exchange interactions using MCD spectroscopy. For this study, F,Sn:$In_2O_3$ (FITO) nanocubes exhibiting shape-dependent multimodal LSPR assigned to corner- and edge-centered LSPR modes could be an excellent model system (see Section 1.2.2.2.). According to current models existing in the literature, the angular momentum transfer from cyclotron-related free carriers to excitons in plasmonic semiconductor NCs is proposed to be mediated via a chiral phonon coupling mechanism. This model, however, remains to be examined in greater detail, giving path for further extension of the research presented in both **Chapter 3** and **Chapter 4.**

In **Chapter 5**, I presented the applicability of colloidal plasmonic $WO_{3-x}$ and Cs:$WO_{3-x}$ NCs as photoactive materials in NIR photodetector devices, pursued as a collaborative project with Prof. Jonathan Baugh's research group at IQC at University of Waterloo. One of the important extensions of this project would be to perform ligand stripping of the $WO_{3-x}$ and Cs:$WO_{3-x}$ NCs to remove the OLAC capping ligand shell, which functions as an electrically insulating layer. Although $NOBF_4$-based ligand stripping method (see Ex-

perimental Section in Chapter 6) could potentially be used for ligand stripping. However, a major drawback with this method is that the post-synthetic surface modified NCs are dispersed in polar solvents (e.g., DMF), which usually possess lower vapor pressure than toluene (solvent generally used for suspending as-synthesized $WO_{3-x}$ or Cs:$WO_{3-x}$ NCs) and surface wettability, thus making the drop-casting procedure potentially more complicated. Instead of drop-casting, spin-coating of the ligand-stripped colloidal plasmonic NCs could be implemented, which allows for a smoother and more controlled deposition of the NCs on the detector surface. Another important set of experiments would be to investigate the NIR photoenhancement in the devices using the Cs:$WO_{3-x}$ nanoplatelets or iso-prisms presented in **Chapter 4** or Cs:$WO_{3-x}$ NCs of higher aspect ratio. Owing to the LSPR band splitting (*i.e.*, spectral separation of the $LSPR_{\parallel}$ and $LSPR_{\perp}$) in Cs:$WO_{3-x}$ nanoplatelets and longer nanorods, the $LSPR_{\parallel}$ or $LSPR_{\perp}$-induced photoenhancement could be decoupled.

In **Chapter 6**, I presented the applicability of colloidal ligand-stripped $WO_{3-x}$ NCs as plasmonic catalysts and $WO_{3-x}$ NCs annealed in air as dye adsorbers. This research project has several interesting and important directions to branch into. For instance, further rigorous analysis of the ESI-MS spectra (Figure 6.12) would be one of the first steps towards understanding the Rh6G dye degradation mechanism and pathway. Using this, a model for the degradation mechanism of other xanthene dyes (e.g., Rhodamine B, Fluorescein, Eosin) could also be potentially developed.

Another, currently ongoing, set of complementary experiments of this project is the investigation of dye degradation under continuous wave (CW) NIR laser excitation. For this work, however, several parameters need to be optimized. This includes, for instance, achieving sufficient laser beam cross section on the cuvette using a beam diffuser, and immersing the cuvette into a temperature-controlled water bath in order to maintain the desired experimental temperature and prevent boiling of the solvent. Additional control experiments also need to be performed to see whether the dye itself undergoes any photodegradation in the absence of the photocatalyst (NCs). Beyond the CW laser illumination, photocatalysis using pulsed laser excitation could also be an intriguing research direction. For such experiments, I propose using ultrafast (femtosecond) transient absorption spectroscopy setup, which, apart from providing ultrashort laser pulses as photon source, would also allow for probing the excitation dynamics and spatiotemporal evolution of plasmons, ultrafast generation of plasmon-induced hot carriers, and the mechanism of hot carrier injection into the adsorbed dye species.

# Letters of Copyright Permission

# Copyright Permission

AMERICAN CHEMICAL SOCIETY LICENSE TERMS AND CONDITIONS

This Agreement between Gyorgy Jaics ("You") and American Chemical Society ("American Chemical Society") consists of your license details and the terms and conditions provided by American Chemical Society and Copyright Clearance Center.

| | |
|---|---|
| License Number | **6178460938263** |
| License date | Dec 29, 2025 |
| Licensed Content Publisher | American Chemical Society |
| Licensed Content Publication | The Journal of Physical Chemistry C |
| Licensed Content Title | **Revisiting Plasmonic Properties of Complex Semiconductor Nanocrystals Using Magnetic Circular Dichroism Spectroscopy: A Cautionary Tale** |
| Licensed Content Author | Aaron Kenny-Wilby, Gyorgy Jaics, Chenwei Zhang, et al |
| Licensed Content Date | Jan 1, 2023 |
| Licensed Content Volume | 127 |
| Licensed Content Issue | 2 |
| Volume number | 127 |
| Issue number | 2 |
| Type of Use | Thesis/Dissertation |
| Requestor type | Author (original work) |
| Format | Print and Electronic |
| Portion | Full article |
| Title of new work | **Investigation of Magneto-Optical and Photonic Properties of Plasmonic Tungsten Oxide and Alkali Tungsten Bronze Nanocrystals** |
| Institution name | University of Waterloo, ON, Canada |
| Expected presentation date | Mar 2026 |
| The Requesting Person / Organization to Appear on the License | Gyorgy J. Jaics<br>Mr. Gyorgy J. Jaics |
| Billing Address | University of Waterloo, 200 University Avenue West, Waterloo, ON N2L 3G1, Canada |

# Copyright Permission

AMERICAN CHEMICAL SOCIETY LICENSE TERMS AND CONDITIONS

This Agreement between Gyorgy Jaics ("You") and American Chemical Society ("American Chemical Society") consists of your license details and the terms and conditions provided by American Chemical Society and Copyright Clearance Center.

| | |
|---|---|
| License Number | **6178460442322** |
| License date | Dec 29, 2025 |
| Licensed Content Publisher | American Chemical Society |
| Licensed Content Publication | Chemistry of Materials |
| Licensed Content Title | **Aspect-Ratio-Controlled Excitonic Zeeman Effects in Alkali Tungsten Bronze Nanocrystals Revealed by Magnetic Circular Dichroism Spectroscopy** |
| Licensed Content Author | Gyorgy Jaics, Aaron Kenny-Wilby, Emily S. Wedde, et al |
| Licensed Content Date | Jul 1, 2025 |
| Licensed Content Volume | 37 |
| Licensed Content Issue | 13 |
| Volume number | 37 |
| Issue number | 13 |
| Type of Use | Thesis/Dissertation |
| Requestor type | Author (original work) |
| Format | Print and Electronic |
| Portion | Full article |
| Title of new work | **Investigation of Magneto-Optical and Photonic Properties of Plasmonic Tungsten Oxide and Alkali Tungsten Bronze Nanocrystals** |
| Institution name | University of Waterloo, ON, Canada |
| Expected presentation date | Mar 2026 |
| The Requesting Person / Organization to Appear on the License | Gyorgy J. Jaics<br>Mr. Gyorgy J. Jaics |
| Billing Address | University of Waterloo, 200 University Avenue West, Waterloo, ON N2L 3G1, Canada |

# Copyright Permission



CC BY 4.0

## Attribution 4.0 International

**Deed**

**Canonical URL:** https://creativecommons.org/licenses/by/4.0/legalcode.en

**You are free to:**

**Share** — copy and redistribute the material in any medium or format for any purpose, even commercially.

**Adapt** — remix, transform, and build upon the material for any purpose, even commercially.

The licensor cannot revoke these freedoms as long as you follow the license terms.

**Under the following terms:**

**Attribution** — You must give appropriate credit, provide a link to the license, and indicate if changes were made. You may do so in any reasonable manner, but not in any way that suggests the licensor endorses you or your use.

**No additional restrictions** — You may not apply legal terms or technological measures that legally restrict others from doing anything the license permits.

**Notices:**

You do not have to comply with the license for elements of the material in the public domain or where your use is permitted by an applicable exception or limitation.

No warranties are given. The license may not give you all of the permissions necessary for your intended use. For example, other rights such as publicity, privacy, or moral rights may limit how you use the material.

---

**Notice**

This deed highlights only some of the key features and terms of the actual license. It is not a license and has no legal value. You should carefully review all of the terms and conditions of the actual license before using the licensed material.

Creative Commons is not a law firm and does not provide legal services. Distributing, displaying, or linking to this deed or the license that it summarizes does not create a lawyer-client or any other relationship.

Creative Commons is the nonprofit behind the open licenses and other legal tools that allow creators to share their work. Our legal tools are free to use.

- Learn more about our work
- **Learn more about CC Licensing**
- Support our work
- Use the license for your own material.
- Licenses List
- Public Domain List

https://creativecommons.org/licenses/by/4.0/

# References


[1] Aftab, M.; Mansha, M. S.; Iqbal, T.; Farooq, M. *Plasmonics* **2024**, *19*, 1701–1719.

[2] Masson, J.-F. *The Analyst* **2020**, *145*, 3776–3800.

[3] Luther, J. M.; Jain, P. K.; Ewers, T.; Alivisatos, A. P. *Nature Materials* **2011**, *10*, 361–366.

[4] Agrawal, A.; Cho, S. H.; Zandi, O.; Ghosh, S.; Johns, R. W.; Milliron, D. J. *Chemical Reviews* **2018**, *118*, 3121–3207.

[5] Migas, D. B.; Shaposhnikov, V. L.; Borisenko, V. E. *Journal of Applied Physics* **2010**, *108*, 093714.

[6] Zydlewski, B. Z.; Lu, H.-C.; Celio, H.; Milliron, D. J. *The Journal of Physical Chemistry C* **2022**, *126*, 14537–14546.

[7] Kim, J.; Agrawal, A.; Krieg, F.; Bergerud, A.; Milliron, D. J. *Nano Letters* **2016**, *16*, 3879–3884.

[8] Machida, K.; Okada, M.; Adachi, K. *Journal of Applied Physics* **2019**, *125*, 103103.

[9] Machida, K.; Adachi, K. *Scientific Reports* **2024**, *14*, 6549.

[10] Zhang, N.; Xiong, Y. *Advanced Sensor and Energy Materials* **2023**, *2*, 100047.

[11] Agrawal, A.; Johns, R. W.; Milliron, D. J. *Annual Review of Materials Research* **2017**, *47*, 1–31.

[12] Diroll, B. T.; Gordon, T. R.; Gaulding, E. A.; Klein, D. R.; Paik, T.; Yun, H. J.; Goodwin, E.; Damodhar, D.; Kagan, C. R.; Murray, C. B. *Chemistry of Materials* **2014**, *26*, 4579–4588.

[13] Yin, P.; Tan, Y.; Fang, H.; Hegde, M.; Radovanovic, P. V. *Nature Nanotechnology* **2018**, *13*, 463–467.

[14] Hartstein, K. H.; Schimpf, A. M.; Salvador, M.; Gamelin, D. R. *The Journal of Physical Chemistry Letters* **2017**, *8*, 1831–1836.

[15] Yin, P.; Chen, S.; Radovanovic, P. V. *The Journal of Physical Chemistry Letters* **2022**, *13*, 5545–5552.

[16] Shi, L.; Chen, K.; Zhai, A.; Li, G.; Fan, M.; Hao, Y.; Zhu, F.; Zhang, H.; Cui, Y. *Laser & Photonics Reviews* **2021**, *15*, 2000401.

[17] Panchenko, E.; Cadusch, J. J.; Avayu, O.; Ellenbogen, T.; James, T. D.; Gómez, D.; Roberts, A. *Advanced Materials Technologies* **2018**, *3*, 1700196.

[18] Carlin, C. C.; Dai, A. X.; Al-Zubeidi, A.; Simmerman, E. M.; Oh, H.; Gross, N.; Lee, S. A.; Link, S.; Landes, C. F.; Da Jornada, F. H.; Dionne, J. A. *Chemical Physics Reviews* **2023**, *4*, 041309.

[19] Han, B.; Gao, X.; Lv, J.; Tang, Z. *Advanced Materials* **2020**, *32*, 1801491.

[20] Heo, S.; Cho, S. H.; Dahlman, C. J.; Agrawal, A.; Milliron, D. J. *ACS Energy Letters* **2020**, *5*, 2662–2670.

[21] Yoshio, S.; Okada, M.; Adachi, K. *Journal of Applied Physics* **2018**, *124*, 063109.

[22] Locarno, M.; Brinks, D. *American Journal of Physics* **2023**, *91*, 538–546.

[23] Liu, X.; Swihart, M. T. *Chem. Soc. Rev.* **2014**, *43*, 3908–3920.

[24] Kriegel, I.; Scotognella, F.; Manna, L. *Physics Reports* **2017**, *674*, 1–52.

[25] Faucheaux, J. A.; Stanton, A. L. D.; Jain, P. K. *The Journal of Physical Chemistry Letters* **2014**, *5*, 976–985.

[26] Stockman, M. I. *Optics Express* **2011**, *19*, 22029.

[27] Nithyananda Kumar, R. S.; Martulli, A.; Lizin, S.; Deferme, W. *Progress in Materials Science* **2025**, *153*, 101479.

[28] Hinman, S. S.; McKeating, K. S.; Cheng, Q. *Analytical Chemistry* **2018**, *90*, 19–39.

[29] Mayer, K. M.; Hafner, J. H. *Chemical Reviews* **2011**, *111*, 3828–3857.

[30] Ma, S.-C.; Gupta, R.; Ondevilla, N. A. P.; Barman, K.; Lee, L.-Y.; Chang, H.-C.; Huang, J.-J. *Biomedical Optics Express* **2023**, *14*, 182.

[31] Alonso Calafell, I.; Cox, J. D.; Radonjić, M.; Saavedra, J. R. M.; García De Abajo, F. J.; Rozema, L. A.; Walther, P. *npj Quantum Information* **2019**, *5*, 37.

[32] Bozhevolnyi, S. I.; Mortensen, N. A. *Nanophotonics* **2017**, *6*, 1185–1188.

[33] Lotfiani, A.; Ghanaatshoar, M.; Mohseni, S. M. *IEEE Transactions on Electron Devices* **2019**, *66*, 5215–5220.

[34] Yu, Y.; Zhong, F.; Li, R.; Cui, Y.; Wu, J.; Zhang, J. *2D Materials* **2023**, *10*, 025012.

[35] Balitskii, O. *Materials Today Energy* **2021**, *20*, 100629.

[36] Gellé, A.; Jin, T.; De La Garza, L.; Price, G. D.; Besteiro, L. V.; Moores, A. *Chemical Reviews* **2020**, *120*, 986–1041.

[37] Zhou, L.; Huang, Q.; Xia, Y. *Chemical Reviews* **2024**, *124*, 8597–8619.

[38] Willets, K. A.; Van Duyne, R. P. *Annual Review of Physical Chemistry* **2007**, *58*, 267–297.

[39] Solis, D. M.; Taboada, J. M.; Landesa, L.; Rodriguez, J. L.; Obelleiro, F. *Progress In Electromagnetics Research* **2015**, *154*, 35–50.

[40] Shahbazyan, T. V., Stockman, M. I., Eds. *Plasmonics: Theory and Applications*; Challenges and Advances in Computational Chemistry and Physics; Springer Netherlands: Dordrecht, 2013; Vol. 15.

[41] Yin, P.; Radovanovic, P. V. *ChemSusChem* **2020**, *13*, 4885–4893.

[42] Jain, P. K. *The Journal of Physical Chemistry Letters* **2014**, *5*, 3112–3119.

[43] Rabbani, A.; Rudacille, R.; Hasegawa, K. *The Journal of Physical Chemistry C* **2024**, *128*, 19210–19221.

[44] Lu, Z.; Ji, J.; Ye, H.; Zhang, H.; Zhang, S.; Xu, H. *Nature Communications* **2024**, *15*, 8803.

[45] Horvath, H. *Journal of Quantitative Spectroscopy and Radiative Transfer* **2009**, *110*, 787–799.

[46] Balderas-Cabrera, C.; Castillo, R. *The Journal of Chemical Physics* **2024**, *161*, 084903.

[47] Gans, R. *Annalen der Physik* **1912**, *342*, 881–900.

[48] Alves, R. A.; Guerreiro, A.; Navarro-Cía, M. *Physical Review B* **2020**, *101*, 235412.

[49] Kan, C. *Plasmonic Metal Nanostructures: Preparation, Characterization, and Applications*, 1st ed.; Wiley, 2024.

[50] Sun, J.; Goldys, E. M. *The Journal of Physical Chemistry C* **2008**, *112*, 9261–9266.

[51] Wang, H.; Fan, S. *Annalen der Physik* **2025**, *537*, e00156.

[52] Roman, B. J.; Shubert-Zuleta, S. A.; Milliron, D. J. *MRS Bulletin* **2024**, *49*, 1032–1044.

[53] Tandon, B.; Yadav, A.; Khurana, D.; Reddy, P.; Santra, P. K.; Nag, A. *Chemistry of Materials* **2017**, *29*, 9360–9368.

[54] Fang, H.; Hegde, M.; Yin, P.; Radovanovic, P. V. *Chemistry of Materials* **2017**, *29*, 4970–4979.

[55] Yin, P.; Tan, Y.; Ward, M. J.; Hegde, M.; Radovanovic, P. V. *The Journal of Physical Chemistry C* **2019**, *123*, 29829–29837.

[56] Tandon, B.; Gibbs, S. L.; Zydlewski, B. Z.; Milliron, D. J. *Chemistry of Materials* **2021**, *33*, 6955–6964.

[57] Lu, I.-T.; Zhou, J.-J.; Park, J.; Bernardi, M. *Physical Review Materials* **2022**, *6*, L010801.

[58] Tandon, B.; Ghosh, S.; Milliron, D. J. *Chemistry of Materials* **2019**, *31*, 7752–7760.

[59] Doiron, B.; Mota, M.; Wells, M. P.; Bower, R.; Mihai, A.; Li, Y.; Cohen, L. F.; Alford, N. M.; Petrov, P. K.; Oulton, R. F.; Maier, S. A. *ACS Photonics* **2019**, *6*, 240–259.

[60] Gibbs, S. L.; Staller, C. M.; Milliron, D. J. *Accounts of Chemical Research* **2019**, *52*, 2516–2524.

[61] Staller, C. M.; Gibbs, S. L.; Saez Cabezas, C. A.; Milliron, D. J. *Nano Letters* **2019**, *19*, 8149–8154.

[62] Segui Barragan, V.; Roman, B. J.; Shubert-Zuleta, S. A.; Berry, M. W.; Celio, H.; Milliron, D. J. *Nano Letters* **2023**, *23*, 7983–7989.

[63] Garcia, G.; Buonsanti, R.; Runnerstrom, E. L.; Mendelsberg, R. J.; Llordes, A.; Anders, A.; Richardson, T. J.; Milliron, D. J. *Nano Letters* **2011**, *11*, 4415–4420.

[64] Tandon, B.; Gibbs, S. L.; Dean, C.; Milliron, D. J. *Nano Letters* **2023**, *23*, 908–915.

[65] Liu, Y.; Liu, M.; Swihart, M. T. *The Journal of Physical Chemistry C* **2017**, *121*, 13435–13447.

[66] Madkhali, O. *Physica Scripta* **2024**, *99*, 022004.

[67] Coughlan, C.; Ibáñez, M.; Dobrozhan, O.; Singh, A.; Cabot, A.; Ryan, K. M. *Chemical Reviews* **2017**, *117*, 5865–6109.

[68] Lukashev, P.; Lambrecht, W. R. L.; Kotani, T.; Van Schilfgaarde, M. *Physical Review B* **2007**, *76*, 195202.

[69] Xie, Y.; Riedinger, A.; Prato, M.; Casu, A.; Genovese, A.; Guardia, P.; Sottini, S.; Sangregorio, C.; Miszta, K.; Ghosh, S.; Pellegrino, T.; Manna, L. *Journal of the American Chemical Society* **2013**, *135*, 17630–17637.

[70] Dorfs, D.; Härtling, T.; Miszta, K.; Bigall, N. C.; Kim, M. R.; Genovese, A.; Falqui, A.; Povia, M.; Manna, L. *Journal of the American Chemical Society* **2011**, *133*, 11175–11180.

[71] Wang, X.; Swihart, M. T. *Chemistry of Materials* **2015**, *27*, 1786–1791.

[72] Calzolari, A.; Ruini, A.; Catellani, A. *ACS Photonics* **2014**, *1*, 703–709.

[73] Lounis, S. D.; Runnerstrom, E. L.; Llordés, A.; Milliron, D. J. *The Journal of Physical Chemistry Letters* **2014**, *5*, 1564–1574.

[74] Tandon, B.; Ashok, A.; Nag, A. *Pramana* **2015**, *84*, 1087–1098.

[75] Runnerstrom, E. L.; Bergerud, A.; Agrawal, A.; Johns, R. W.; Dahlman, C. J.; Singh, A.; Selbach, S. M.; Milliron, D. J. *Nano Letters* **2016**, *16*, 3390–3398.

[76] Manthiram, K.; Alivisatos, A. P. *Journal of the American Chemical Society* **2012**, *134*, 3995–3998.

[77] Lee, Y.-J.; Lee, T.; Soon, A. *Chemistry of Materials* **2019**, *31*, 4282–4290.

[78] Wriedt, H. A. *Bulletin of Alloy Phase Diagrams* **1989**, *10*, 368–384.

[79] Wang, W.; Janotti, A.; Van De Walle, C. G. *Journal of Materials Chemistry C* **2016**, *4*, 6641–6648.

[80] Gonçalves, S.; Quitério, P.; Freitas, J.; Ivanou, D.; Lopes, T.; Mendes, A.; Araújo, J. P.; Sousa, C. T.; Apolinário, A. *ACS Applied Materials & Interfaces* **2024**, *16*, 64389–64409.

[81] Prusty, G.; Lee, J. T.; Seifert, S.; Muhoberac, B. B.; Sardar, R. *Journal of the American Chemical Society* **2020**, *142*, 5938–5942.

[82] Davis Jr, G. A.; Wyatt, B. C.; Muhoberac, B. B.; Sardar, R. *Chemistry of Materials* **2025**, *37*, 610–623.

[83] Lee, J. T.; Hati, S.; Fahey, M. M.; Zaleski, J. M.; Sardar, R. *Chemistry of Materials* **2022**, *34*, 3053–3066.

[84] Nayak, S. S.; Sadashivamurthy, N.; Labrugère-Sarroste, C.; Duttine, M.; Maho, A.; Rougier, A. *Chemistry of Materials* **2025**, *37*, 8764–8774.

[85] Guo, J. *Solid State Ionics* **1992**, *53-56*, 305–314.

[86] Dickens, P. G.; Whittingham, M. S. *Quarterly Reviews, Chemical Society* **1968**, *22*, 30.

[87] Conroy, L. E.; Sienko, M. J. *Journal of the American Chemical Society* **1952**, *74*, 3520–3522.

[88] Lee, K.-S.; Seo, D.-K.; Whangbo, M.-H. *Journal of the American Chemical Society* **1997**, *119*, 4043–4049.

[89] Hussain, A.; Gruehn, R.; Rüscher, C. *Journal of Alloys and Compounds* **1997**, *246*, 51–61.

[90] Fang, M.; Song, Y.; Pang, S.; Pu, D.; Guo, J.; Gao, Q.; Chao, M.; Liang, E. *Solid State Ionics* **2024**, *414*, 116632.

[91] Wu, C.-M.; Naseem, S.; Chou, M.-H.; Wang, J.-H.; Jian, Y.-Q. *Frontiers in Materials* **2019**, *6*, 49.

[92] Lee, Y.; Lee, T.; Jang, W.; Soon, A. *Chemistry of Materials* **2016**, *28*, 4528–4535.

[93] Yang, C.; Chen, J.-F.; Zeng, X.; Cheng, D.; Cao, D. *Industrial & Engineering Chemistry Research* **2014**, *53*, 17981–17988.

[94] Mattox, T. M.; Bergerud, A.; Agrawal, A.; Milliron, D. J. *Chemistry of Materials* **2014**, *26*, 1779–1784.

[95] Yoshio, S.; Adachi, K. *Materials Research Express* **2018**, *6*, 026548.

[96] Ágoston, P.; Erhart, P.; Klein, A.; Albe, K. *Journal of Physics: Condensed Matter* **2009**, *21*, 455801.

[97] Hwang, J. *Solid State Ionics* **2000**, *129*, 135–144.

[98] Bhachu, D. S.; Scanlon, D. O.; Sankar, G.; Veal, T. D.; Egdell, R. G.; Cibin, G.; Dent, A. J.; Knapp, C. E.; Carmalt, C. J.; Parkin, I. P. *Chemistry of Materials* **2015**, *27*, 2788–2796.

[99] Schimpf, A. M.; Ochsenbein, S. T.; Buonsanti, R.; Milliron, D. J.; Gamelin, D. R. *Chemical Communications* **2012**, *48*, 9352.

[100] Lim, J. H.; Lee, S. M.; Kim, H.-S.; Kim, H. Y.; Park, J.; Jung, S.-B.; Park, G. C.; Kim, J.; Joo, J. *Scientific Reports* **2017**, *7*, 41992.

[101] Shim, M.; Guyot-Sionnest, P. *Journal of the American Chemical Society* **2001**, *123*, 11651–11654.

[102] Sachet, E.; Shelton, C. T.; Harris, J. S.; Gaddy, B. E.; Irving, D. L.; Curtarolo, S.; Donovan, B. F.; Hopkins, P. E.; Sharma, P. A.; Sharma, A. L.; Ihlefeld, J.; Franzen, S.; Maria, J.-P. *Nature Materials* **2015**, *14*, 414–420.

[103] Ye, X.; Fei, J.; Diroll, B. T.; Paik, T.; Murray, C. B. *Journal of the American Chemical Society* **2014**, *136*, 11680–11686.

[104] Kang, Y.; Van De Walle, C. G. *Applied Physics Letters* **2017**, *111*, 152107.

[105] Furdyna, J. K. *Journal of Applied Physics* **1988**, *64*, R29–R64.

[106] Lounis, S. D.; Runnerstrom, E. L.; Bergerud, A.; Nordlund, D.; Milliron, D. J. *Journal of the American Chemical Society* **2014**, *136*, 7110–7116.

[107] Crockett, B. M.; Jansons, A. W.; Koskela, K. M.; Johnson, D. W.; Hutchison, J. E. *ACS Nano* **2017**, *11*, 7719–7728.

[108] Jansons, A. W.; Hutchison, J. E. *ACS Nano* **2016**, *10*, 6942–6951.

[109] Zandi, O.; Agrawal, A.; Shearer, A. B.; Reimnitz, L. C.; Dahlman, C. J.; Staller, C. M.; Milliron, D. J. *Nature Materials* **2018**, *17*, 710–717.

[110] Agrawal, A.; Kriegel, I.; Runnerstrom, E. L.; Scotognella, F.; Llordes, A.; Milliron, D. J. *ACS Photonics* **2018**, *5*, 2044–2050.

[111] Agrawal, A.; Singh, A.; Yazdi, S.; Singh, A.; Ong, G. K.; Bustillo, K.; Johns, R. W.; Ringe, E.; Milliron, D. J. *Nano Letters* **2017**, *17*, 2611–2620.

[112] Roman, B. J.; Shubert-Zuleta, S. A.; Shim, G.; Kyveryga, V.; Faris, M.; Milliron, D. J. *The Journal of Physical Chemistry C* **2023**, *127*, 2456–2463.

[113] Liu, Z.; Zhong, Y.; Shafei, I.; Jeong, S.; Wang, L.; Nguyen, H. T.; Sun, C.-J.; Li, T.; Chen, J.; Chen, L.; Losovyj, Y.; Gao, X.; Ma, W.; Ye, X. *Nano Letters* **2020**, *20*, 2821–2828.

[114] Cho, S. H.; Ghosh, S.; Berkson, Z. J.; Hachtel, J. A.; Shi, J.; Zhao, X.; Reimnitz, L. C.; Dahlman, C. J.; Ho, Y.; Yang, A.; Liu, Y.; Idrobo, J.-C.; Chmelka, B. F.; Milliron, D. J. *Chemistry of Materials* **2019**, *31*, 2661–2676.

[115] Cho, S. H.; Roccapriore, K. M.; Dass, C. K.; Ghosh, S.; Choi, J.; Noh, J.; Reimnitz, L. C.; Heo, S.; Kim, K.; Xie, K.; Korgel, B. A.; Li, X.; Hendrickson, J. R.; Hachtel, J. A.; Milliron, D. J. *The Journal of Chemical Physics* **2020**, *152*, 014709.

[116] Agrawal, A.; Kriegel, I.; Milliron, D. J. *The Journal of Physical Chemistry C* **2015**, *119*, 6227–6238.

[117] Mason, W. R. *A practical guide to magnetic circular dichroism spectroscopy*; Wiley-Interscience: Hoboken, N.J, 2007.

[118] Pineider, F.; Campo, G.; Bonanni, V.; De Julián Fernández, C.; Mattei, G.; Caneschi, A.; Gatteschi, D.; Sangregorio, C. *Nano Letters* **2013**, *13*, 4785–4789.

[119] Yin, P.; Hegde, M.; Tan, Y.; Chen, S.; Garnet, N.; Radovanovic, P. V. *ACS Nano* **2018**, *12*, 11211–11218.

[120] Shao, Q.; Tandon, B.; Yin, P.; Radovanovic, P. V. *Chemistry of Materials* **2024**, *36*, 3908–3917.

[121] Beaulac, R.; Archer, P. I.; Ochsenbein, S. T.; Gamelin, D. R. *Advanced Functional Materials* **2008**, *18*, 3873–3891.

[122] Zada, A.; Muhammad, P.; Ahmad, W.; Hussain, Z.; Ali, S.; Khan, M.; Khan, Q.; Maqbool, M. *Advanced Functional Materials* **2020**, *30*, 1906744.

[123] Masouleh, F. F.; Das, N. In *Advances in Optical Communication*; Das, N., Ed.; InTech, 2014.

[124] Chang, W. J.; Roman, B. J.; Green, A. M.; Truskett, T. M.; Milliron, D. J. *ACS Nano* **2024**, *18*, 20636–20647.

[125] Çaktü Güler, K.; Göktürk, I.; Yılmaz, F.; Araz, A.; Denizli, A. *Essential Chem* **2024**, *1*, 1–19.

[126] De La Encarnación, C.; Jimenez De Aberasturi, D.; Liz-Marzán, L. M. *Advanced Drug Delivery Reviews* **2022**, *189*, 114484.

[127] Schlicke, H.; Maletz, R.; Dornack, C.; Fery, A. *Small* **2024**, *20*, 2403502.

[128] Yan, N.; Qiu, Y.; He, X.; Tang, X.; Hao, Q.; Chen, M. *Materials* **2023**, *16*, 3216.

[129] Podder, S.; Pal, A. R. *Journal of Applied Physics* **2019**, *126*, 083108.

[130] Su, J.; Hou, X.; Dai, N.; Li, Y. *Frontiers of Physics* **2024**, *19*, 63501.

[131] Martyniuk, P.; Antoszewski, J.; Martyniuk, M.; Faraone, L.; Rogalski, A. *Applied Physics Reviews* **2014**, *1*, 041102.

[132] Omnes, F. In *Optoelectronic Sensors*, 1st ed.; Decoster, D., Harari, J., Eds.; Wiley, 2009; pp 1–14.

[133] Hidayat, W.; Usman, M. *Physica Scripta* **2024**, *99*, 112002.

[134] Imran, A.; Sulaman, M.; Yang, S.; Bukhtiar, A.; Qasim, M.; Elshahat, S.; Khan, M. S. A.; Dastgeer, G.; Zou, B.; Yousaf, M. *Surfaces and Interfaces* **2022**, *29*, 101772.

[135] Lee, Y.; Hassan, Z.; Yam, F.; Abdullah, M.; Ibrahim, K.; Barmawi, M.; Sugianto; Budiman, M.; Arifin, P. *Applied Surface Science* **2005**, *249*, 91–96.

[136] Soole, J.; Schumacher, H. *IEEE Journal of Quantum Electronics* **1991**, *27*, 737–752.

[137] Asar, T.; Özçelik, S.; Özbay, E. *Journal of Applied Physics* **2014**, *115*, 104502.

[138] Yerino, C. D.; Liang, B.; Huffaker, D. L.; Simmonds, P. J.; Lee, M. L. *Journal of Vacuum Science & Technology B, Nanotechnology and Microelectronics: Materials, Processing, Measurement, and Phenomena* **2017**, *35*, 010801.

[139] Soole, J.; Schumacher, H.; LeBlanc, H.; Bhat, R.; Koza, M. *IEEE Photonics Technology Letters* **1989**, *1*, 250–252.

[140] Nolte, D. *Applied Physics Letters* **1989**, *54*, 2277–2277.

[141] Kong, T.; Liao, A.; Xu, Y.; Qiao, X.; Zhang, H.; Zhang, L.; Zhang, C. *RSC Advances* **2024**, *14*, 17041–17050.

[142] Jiang, W.; Low, B. Q. L.; Long, R.; Low, J.; Loh, H.; Tang, K. Y.; Chai, C. H. T.; Zhu, H.; Zhu, H.; Li, Z.; Loh, X. J.; Xiong, Y.; Ye, E. *ACS Nano* **2023**, *17*, 4193–4229.

[143] Zhang, X.; Chen, Y. L.; Liu, R.-S.; Tsai, D. P. *Reports on Progress in Physics* **2013**, *76*, 046401.

[144] Dong, Y.; Hu, C.; Xiong, H.; Long, R.; Xiong, Y. *ACS Catalysis* **2023**, *13*, 6730–6743.

[145] Hamans, R. F.; Kamarudheen, R.; Baldi, A. *Nanomaterials* **2020**, *10*, 2377.

[146] Guo, Y.; Yin, H.; Hu, J.; Yang, B.; Wang, J. *The Journal of Physical Chemistry C* **2024**, *128*, 5777–5797.

[147] Han, C.; Gómez, D. E.; Xiao, Q.; Xu, J. *Journal of Catalysis* **2021**, *397*, 205–211.

[148] Zhang, Z. *Nanomaterials* **2023**, *13*, 1427.

[149] Schirato, A.; Moretti, L.; Yang, Z.; Mazzanti, A.; Cerullo, G.; Pileni, M.-P.; Maiuri, M.; Della Valle, G. *The Journal of Physical Chemistry C* **2022**, *126*, 6308–6317.

[150] Mascaretti, L.; Naldoni, A. *Journal of Applied Physics* **2020**, *128*, 041101.

[151] Ahlawat, M.; Mittal, D.; Govind Rao, V. *Communications Materials* **2021**, *2*, 114.

[152] Yan, Y.; Spear, N. J.; Cummings, A. J.; Khusainova, K.; Macdonald, J. E.; Haglund, R. F. *Science Advances* **2025**, *11*, eadv1822.

[153] Ding, W.; Hsu, L.-Y.; Heaps, C. W.; Schatz, G. C. *The Journal of Physical Chemistry C* **2018**, *122*, 22650–22659.

[154] Gao, Y.; Diederich, J.; Xie, Y.; Zhu, Q.; Höhn, C.; Harbauer, K.; Fan, F.; Li, C.; Van De Krol, R.; Friedrich, D. *Nature Communications* **2025**, *16*, 10410.

[155] Schirato, A.; Sanders, S. K.; Proietti Zaccaria, R.; Nordlander, P.; Della Valle, G.; Alabastri, A. *ACS Nano* **2024**, *18*, 18933–18947.

[156] Yin, X.; Gao, D.; Zhang, J.; García, H.; Yu, J.; Yu, H. *Journal of the American Chemical Society* **2025**, *147*, 34881–34890.

[157] Zhang, W.; Xiao, Q.; Wen, J. *The Journal of Physical Chemistry Letters* **2025**, *16*, 6073–6080.

[158] Koya, A. N. et al. *Applied Physics Reviews* **2023**, *10*, 021318.

[159] Zhang, P.; Wang, T.; Chang, X.; Gong, J. *Accounts of Chemical Research* **2016**, *49*, 911–921.

[160] Vanzan, M.; Gil, G.; Castaldo, D.; Nordlander, P.; Corni, S. *Nano Letters* **2023**, *23*, 2719–2725.

[161] Mubeen, S.; Hernandez-Sosa, G.; Moses, D.; Lee, J.; Moskovits, M. *Nano Letters* **2011**, *11*, 5548–5552.

[162] Chen, Y.; Wu, S.; Gao, S. *The Journal of Physical Chemistry C* **2025**, *129*, 12804–12813.

[163] Jiang, Z.; Zhou, Y.; Zhou, Z.; Li, H.; Yang, Y.; Song, J.; Jia, M.; Hu, H.; Cai, Y.; Govorov, A.; Zhang, W.; Yang, J.; Lan, X. *Nature Communications* **2025**, *16*, 11702.

[164] Ostovar, B.; Lee, S. A.; Mehmood, A.; Farrell, K.; Searles, E. K.; Bourgeois, B.; Chiang, W.-Y.; Misiura, A.; Gross, N.; Al-Zubeidi, A.; Dionne, J. A.; Landes, C. F.; Zanni, M.; Levine, B. G.; Link, S. *Science Advances* **2024**, *10*, eadp3353.

[165] Li, J.; Cushing, S. K.; Meng, F.; Senty, T. R.; Bristow, A. D.; Wu, N. *Nature Photonics* **2015**, *9*, 601–607.

[166] Cushing, S. K.; Li, J.; Bright, J.; Yost, B. T.; Zheng, P.; Bristow, A. D.; Wu, N. *The Journal of Physical Chemistry C* **2015**, *119*, 16239–16244.

[167] Chen, J.; Ye, Z.; Yang, F.; Yin, Y. *Small Science* **2021**, *1*, 2000055.

[168] Giannini, V.; Fernández-Domínguez, A. I.; Heck, S. C.; Maier, S. A. *Chemical Reviews* **2011**, *111*, 3888–3912.

[169] Xi, G.; Ouyang, S.; Li, P.; Ye, J.; Ma, Q.; Su, N.; Bai, H.; Wang, C. *Angewandte Chemie International Edition* **2012**, *51*, 2395–2399.

[170] Yan, J.; Wang, T.; Wu, G.; Dai, W.; Guan, N.; Li, L.; Gong, J. *Advanced Materials* **2015**, *27*, 1580–1586.

[171] Paik, T.; Cargnello, M.; Gordon, T. R.; Zhang, S.; Yun, H.; Lee, J. D.; Woo, H. Y.; Oh, S. J.; Kagan, C. R.; Fornasiero, P.; Murray, C. B. *ACS Energy Letters* **2018**, *3*, 1904–1910.

[172] Tang, H.; Tang, Z.; Bright, J.; Liu, B.; Wang, X.; Meng, G.; Wu, N. *ACS Sustainable Chemistry & Engineering* **2021**, *9*, 1500–1506.

[173] Shi, K.; Wang, F.; Li, X.; Huang, W.; Lu, K.; Yu, C.; Yang, K. *Journal of Materials Science* **2023**, *58*, 16309–16321.

[174] Cheng, H.; Kamegawa, T.; Mori, K.; Yamashita, H. *Angewandte Chemie International Edition* **2014**, *53*, 2910–2914.

[175] Yin, H.; Kuwahara, Y.; Mori, K.; Cheng, H.; Wen, M.; Huo, Y.; Yamashita, H. *The Journal of Physical Chemistry C* **2017**, *121*, 23531–23540.

[176] Sahoo, P. K.; Kalyan Kamal, S.; Premkumar, M.; Jagadeesh Kumar, T.; Sreedhar, B.; Singh, A.; Srivastava, S.; Chandra Sekhar, K. *International Journal of Refractory Metals and Hard Materials* **2009**, *27*, 784–791.

[177] Dong, A.; Ye, X.; Chen, J.; Kang, Y.; Gordon, T.; Kikkawa, J. M.; Murray, C. B. *Journal of the American Chemical Society* **2011**, *133*, 998–1006.

[178] Cheref, Y.; Lochon, F.; Daugas, L.; Cleret De Langavant, C.; Larquet, ; Baron, A.; Gacoin, T.; Kim, J. *Chemistry of Materials* **2022**, *34*, 9795–9802.

[179] Kenny-Wilby, A.; Jaics, G.; Zhang, C.; Yin, P.; Radovanovic, P. V. *The Journal of Physical Chemistry C* **2023**, *127*, 1087–1096.

[180] Naik, G. V.; Shalaev, V. M.; Boltasseva, A. *Advanced Materials* **2013**, *25*, 3264–3294.

[181] Comin, A.; Manna, L. *Chem. Soc. Rev.* **2014**, *43*, 3957–3975.

[182] Kramer, N. J.; Schramke, K. S.; Kortshagen, U. R. *Nano Letters* **2015**, *15*, 5597–5603.

[183] Sturaro, M.; Della Gaspera, E.; Michieli, N.; Cantalini, C.; Emamjomeh, S. M.; Guglielmi, M.; Martucci, A. *ACS Applied Materials & Interfaces* **2016**, *8*, 30440–30448.

[184] Abb, M.; Wang, Y.; Papasimakis, N.; De Groot, C. H.; Muskens, O. L. *Nano Letters* **2014**, *14*, 346–352.

[185] Niezgoda, J. S.; Yap, E.; Keene, J. D.; McBride, J. R.; Rosenthal, S. J. *Nano Letters* **2014**, *14*, 3262–3269.

[186] Gordon, T. R.; Cargnello, M.; Paik, T.; Mangolini, F.; Weber, R. T.; Fornasiero, P.; Murray, C. B. *Journal of the American Chemical Society* **2012**, *134*, 6751–6761.

[187] Gan, X. Y.; Keller, E. L.; Warkentin, C. L.; Crawford, S. E.; Frontiera, R. R.; Millstone, J. E. *Nano Letters* **2019**, *19*, 2384–2388.

[188] Della Gaspera, E.; Chesman, A. S. R.; Van Embden, J.; Jasieniak, J. J. *ACS Nano* **2014**, *8*, 9154–9163.

[189] De Trizio, L.; Buonsanti, R.; Schimpf, A. M.; Llordes, A.; Gamelin, D. R.; Simonutti, R.; Milliron, D. J. *Chemistry of Materials* **2013**, *25*, 3383–3390.

[190] Huang, Q.; Hu, S.; Zhuang, J.; Wang, X. *Chemistry – A European Journal* **2012**, *18*, 15283–15287.

[191] Ghosh, S.; Lu, H.-C.; Cho, S. H.; Maruvada, T.; Price, M. C.; Milliron, D. J. *Journal of the American Chemical Society* **2019**, *141*, 16331–16343.

[192] Biswas, K.; Rao, C. N. R. *The Journal of Physical Chemistry B* **2006**, *110*, 842–845.

[193] Ferretti, A.; Rogers, D.; Goodenough, J. *Journal of Physics and Chemistry of Solids* **1965**, *26*, 2007–2011.

[194] Urso, C.; Barawi, M.; Gaspari, R.; Sirigu, G.; Kriegel, I.; Zavelani-Rossi, M.; Scotognella, F.; Manca, M.; Prato, M.; De Trizio, L.; Manna, L. *Journal of the American Chemical Society* **2017**, *139*, 1198–1206.

[195] Gabka, G.; Bujak, P.; Ostrowski, A.; Tomaszewski, W.; Lisowski, W.; Sobczak, J. W.; Pron, A. *Inorganic Chemistry* **2016**, *55*, 6660–6669.

[196] Kowalik, P.; Bujak, P.; Penkala, M.; Kotwica, K.; Kmita, A.; Gajewska, M.; Ostrowski, A.; Pron, A. *Journal of Materials Chemistry C* **2019**, *7*, 6246–6250.

[197] Farvid, S. S.; Hegde, M.; Radovanovic, P. V. *Chemistry of Materials* **2013**, *25*, 233–244.

[198] Farvid, S. S.; Sabergharesou, T.; Hutfluss, L. N.; Hegde, M.; Prouzet, E.; Radovanovic, P. V. *Journal of the American Chemical Society* **2014**, *136*, 7669–7679.

[199] Ju, L.; Sabergharesou, T.; Stamplecoskie, K. G.; Hegde, M.; Wang, T.; Combe, N. A.; Wu, H.; Radovanovic, P. V. *Journal of the American Chemical Society* **2012**, *134*, 1136–1146.

[200] Farvid, S. S.; Ju, L.; Worden, M.; Radovanovic, P. V. *The Journal of Physical Chemistry C* **2008**, *112*, 17755–17759.

[201] Garnet, N. S.; Ghodsi, V.; Hutfluss, L. N.; Yin, P.; Hegde, M.; Radovanovic, P. V. *The Journal of Physical Chemistry C* **2017**, *121*, 1918–1927.

[202] Cho, H. D.; Yoon, I. T.; Chung, K. B.; Kim, D. Y.; Kang, T. W.; Yuldashev, S. *Journal of Luminescence* **2018**, *195*, 344–347.

[203] Shpak, A.; Korduban, A.; Medvedskij, M.; Kandyba, V. *Journal of Electron Spectroscopy and Related Phenomena* **2007**, *156-158*, 172–175.

[204] Li, Y.-Y.; Zhong, C.-Y.; Li, M.-X.; Zhang, Q.-Y.; Chen, Y.; Liu, Z.-Q.; Zhang, J. Z. *Journal of Materials Chemistry C* **2021**, *9*, 1614–1621.

[205] Su, C.-Y.; Lin, H.-C. *The Journal of Physical Chemistry C* **2009**, *113*, 4042–4046.

[206] Lever, A. B. P.; Rice, S. A. *Physics Today* **1969**, *22*, 77–77.

[207] Walton, R.; Crouch, P.; Brisdon, B. *Spectrochimica Acta Part A: Molecular Spectroscopy* **1968**, *24*, 601–609.

[208] Balitskii, O. A.; Moszyński, D.; Abbas, Z. *RSC Advances* **2016**, *6*, 59050–59054.

[209] Yin, P.; Hegde, M.; Garnet, N. S.; Tan, Y.; Radovanovic, P. V. *Nano Letters* **2019**, *19*, 6695–6702.

[210] Maier, S. A. *Plasmonics: fundamentals and applications*, repr. ed.; Springer: New York, NY, 2007.

[211] Mattox, T. M.; Ye, X.; Manthiram, K.; Schuck, P. J.; Alivisatos, A. P.; Urban, J. J. *Advanced Materials* **2015**, *27*, 5830–5837.

[212] Buonsanti, R.; Llordes, A.; Aloni, S.; Helms, B. A.; Milliron, D. J. *Nano Letters* **2011**, *11*, 4706–4710.

[213] Ghini, M.; Curreli, N.; Camellini, A.; Wang, M.; Asaithambi, A.; Kriegel, I. *Nanoscale* **2021**, *13*, 8773–8783.

[214] Araujo, J. J.; Brozek, C. K.; Liu, H.; Merkulova, A.; Li, X.; Gamelin, D. R. *ACS Nano* **2021**, *15*, 14116–14124.

[215] Merino, Z. D.; Jaics, G.; Jordan, A. W. M.; Shetty, A.; Yin, P.; Tam, M. C.; Wang, X.; Wasilewski, Z. R.; Radovanovic, P. V.; Baugh, J. *Nanotechnology* **2025**, *36*, 015201.

[216] Zhu, Y.; Lu, W.; Gu, T.; Gao, X.; Yu, N.; Ketkov, S. Y.; Zhang, Z. *ACS Applied Nano Materials* **2023**, *6*, 11104–11114.

[217] Xu, J.; Zhang, Y.; Zhai, T.-T.; Kuang, Z.; Li, J.; Wang, Y.; Gao, Z.; Song, Y.-Y.; Xia, X.-H. *ACS Nano* **2018**, *12*, 6895–6903.

[218] Gu, H.; Guo, C.; Zhang, S.; Bi, L.; Li, T.; Sun, T.; Liu, S. *ACS Nano* **2018**, *12*, 559–567.

[219] Liang, Y.; Cao, S.; Guo, J.; Zeng, R.; Zhao, J.; Zou, B. *ACS Applied Electronic Materials* **2022**, *4*, 5109–5118.

[220] Heo, S.; Kim, J.; Ong, G. K.; Milliron, D. J. *Nano Letters* **2017**, *17*, 5756–5761.

[221] Patil, M. K.; Gaikwad, S. H.; Mukherjee, S. P. *The Journal of Physical Chemistry C* **2020**, *124*, 21082–21093.

[222] Tan, X.; Melkersson, J.; Wu, S.; Wang, L.; Zhang, J. *ChemPhysChem* **2016**, *17*, 2630–2639.

[223] Kriegel, I.; Rodríguez-Fernández, J.; Wisnet, A.; Zhang, H.; Waurisch, C.; Eychmüller, A.; Dubavik, A.; Govorov, A. O.; Feldmann, J. *ACS Nano* **2013**, *7*, 4367–4377.

[224] Gordon, T. R.; Paik, T.; Klein, D. R.; Naik, G. V.; Caglayan, H.; Boltasseva, A.; Murray, C. B. *Nano Letters* **2013**, *13*, 2857–2863.

[225] Hsu, S.-W.; On, K.; Tao, A. R. *Journal of the American Chemical Society* **2011**, *133*, 19072–19075.

[226] Machida, K.; Adachi, K.; Sato, Y. K.; Terauchi, M. *Journal of Applied Physics* **2020**, *128*, 083108.

[227] Kenny-Wilby, A.; Wedde, E. S.; Zorn, S.; Gojsevic, M.; Radovanovic, P. V. *Journal of the American Chemical Society* **2024**, *146*, 17986–17994.

[228] Tandon, B.; Radovanovic, P. V. *ACS Nano* **2023**, *17*, 14069–14078.

[229] Okada, M.; Ono, K.; Yoshio, S.; Fukuyama, H.; Adachi, K. *Journal of the American Ceramic Society* **2019**, *102*, 5386–5400.

[230] Suzuki, N.; Yabuki, K.; Oshimura, N.; Yoshio, S.; Adachi, K. *The Journal of Physical Chemistry C* **2022**, *126*, 15436–15445.

[231] Yoshio, S.; Sato, K.; Adachi, K. *Journal of Applied Physics* **2021**, *130*, 123102.

[232] Salje, E.; Carley, A.; Roberts, M. *Journal of Solid State Chemistry* **1979**, *29*, 237–251.

[233] Adachi, K.; Ota, Y.; Tanaka, H.; Okada, M.; Oshimura, N.; Tofuku, A. *Journal of Applied Physics* **2013**, *114*, 194304.

[234] Kilty, P. A.; Nicholls, D. *Journal of the Chemical Society (Resumed)* **1965**, 4915.

[235] Fowles, G.; Hoodless, R.; Walton, R. *Journal of Inorganic and Nuclear Chemistry* **1965**, *27*, 391–396.

[236] Ando, K. In *Magneto-Optics*; Cardona, M., Fulde, P., Von Klitzing, K., Queisser, H.-J., Merlin, R., Störmer, H., Sugano, S., Kojima, N., Eds.; Springer Berlin Heidelberg: Berlin, Heidelberg, 2000; Vol. 128; pp 211–244, Series Title: Springer Series in Solid-State Sciences.

[237] Van Stappen, C.; Maganas, D.; DeBeer, S.; Bill, E.; Neese, F. *Inorganic Chemistry* **2018**, *57*, 6421–6438.

[238] Mollet, H. F.; Gerstein, B. C. *The Journal of Chemical Physics* **1974**, *60*, 1440–1446.

[239] Rogalski, A.; Antoszewski, J.; Faraone, L. *Journal of Applied Physics* **2009**, *105*, 091101.

[240] Gunapala, S. D.; Bandara, S. V.; Liu, J. K.; Mumolo, J. M.; Rafol, S. B.; Ting, D. Z.; Soibel, A.; Hill, C. *IEEE Journal of Selected Topics in Quantum Electronics* **2014**, *20*, 154–165.

[241] Zhong, Z.-M.; Peng, F.; Ying, L.; Huang, Z.-Q.; Zhong, W.-K.; Yu, G.; Cao, Y.; Huang, F. *Chinese Journal of Polymer Science* **2023**, *41*, 1629–1637.

[242] Zhu, Y.; Chen, H.; Han, R.; Qin, H.; Yao, Z.; Liu, H.; Ma, Y.; Wan, X.; Li, G.; Chen, Y. *National Science Review* **2024**, *11*, nwad311.

[243] Li, Z.; He, Z.; Xi, C.; Zhang, F.; Huang, L.; Yu, Y.; Tan, H. H.; Jagadish, C.; Fu, L. *Advanced Materials Technologies* **2023**, *8*, 2202126.

[244] Ramakrishnan, K.; Ajitha, B.; Ashok Kumar Reddy, Y. *Sensors and Actuators A: Physical* **2023**, *349*, 114051.

[245] Wang, L.; Wang, B.; Zhang, Y.; Meng, L.; Sun, H.; Liu, T.; Zhang, N.; Jiang, Z.; Hu, H. *Optics Express* **2021**, *29*, 12941.

[246] Bansal, S. *Results in Optics* **2023**, *12*, 100425.

[247] Brouckaert, J.; Roelkens, G.; Van Thourhout, D.; Baets, R. *IEEE Photonics Technology Letters* **2007**, *19*, 1484–1486.

[248] Unal, D. H.; Demir, I. *Results in Optics* **2023**, *13*, 100581.

[249] Kuhl, D.; Hieronymi, F.; Bottcher, E.; Wolf, T.; Bimberg, D.; Kuhl, J.; Klingenstein, M. *Journal of Lightwave Technology* **1992**, *10*, 753–759.

[250] Salem, A.; Brennan, K. *IEEE Journal of Quantum Electronics* **1995**, *31*, 944–953.

[251] Wohlmuth, W. A.; Arafa, M.; Mahajan, A.; Fay, P.; Adesida, I. *Applied Physics Letters* **1996**, *69*, 3578–3580.

[252] Aliberti, K.; Wraback, M.; Stead, M.; Newman, P.; Shen, H. *Applied Physics Letters* **2002**, *80*, 2848–2850.

[253] Kim, J.; Johnson, W.; Kanakaraju, S.; Calhoun, L.; Lee, C. *IEEE Transactions on Electron Devices* **2004**, *51*, 351–356.

[254] Smiri, B.; Ben Arbia, M.; Ilkay, D.; Saidi, F.; Othmen, Z.; Dkhil, B.; Ismail, A.; Sezai, E.; Hassen, F.; Maaref, H. *Materials Science and Engineering: B* **2020**, *262*, 114769.

[255] Berini, P. *Laser & Photonics Reviews* **2014**, *8*, 197–220.

[256] Dorodnyy, A.; Salamin, Y.; Ma, P.; Vukajlovic Plestina, J.; Lassaline, N.; Mikulik, D.; Romero-Gomez, P.; Fontcuberta I Morral, A.; Leuthold, J. *IEEE Journal of Selected Topics in Quantum Electronics* **2018**, *24*, 1–13.

[257] Zhang, J.; Wang, Y.; Li, D.; Sun, Y.; Jiang, L. *ACS Materials Letters* **2022**, *4*, 343–355.

[258] Butun, S.; Cinel, N. A.; Ozbay, E. *Nanotechnology* **2012**, *23*, 444010.

[259] Azizur-Rahman, K. M.; LaPierre, R. R. *Nanotechnology* **2016**, *27*, 315202.

[260] Goosney, C. J.; Jarvis, V. M.; Wilson, D. P.; Goktas, N. I.; LaPierre, R. R. *Semiconductor Science and Technology* **2019**, *34*, 035023.

[261] Yang, T.; Hertenberger, S.; Morkötter, S.; Abstreiter, G.; Koblmüller, G. *Applied Physics Letters* **2012**, *101*, 233102.

[262] Zhu, Y.; Xu, H.; Yu, P.; Wang, Z. *Applied Physics Reviews* **2021**, *8*, 021305.

[263] Lee, W.-Y.; Lee, J.; Kwon, H.-J.; Kim, K.; Kang, H.; Jang, J. *Applied Surface Science* **2024**, *654*, 159563.

[264] Cushing, S. K.; Wu, N. *Interface magazine* **2013**, *22*, 63–67.

[265] Huang, J.; Luo, L. *Advanced Optical Materials* **2018**, *6*, 1701282.

[266] Ji, Y.; Xu, W.; Li, D.; Zhou, D.; Chen, X.; Ding, N.; Li, J.; Wang, N.; Bai, X.; Song, H. *Nano Energy* **2019**, *61*, 211–220.

[267] Li, J.; Lou, Z.; Li, B. *Journal of Materials Chemistry A* **2021**, *9*, 18818–18835.

[268] Alqanoo, A. A.; Ahmed, N. M.; Hashim, M.; Almessiere, M. A.; Taya, S. A.; Zyoud, S. H. *Sensors and Actuators A: Physical* **2022**, *347*, 113942.

[269] Rajkumari, R.; Ngangbam, C.; Singh, N. K. *IEEE Electron Device Letters* **2022**, *43*, 470–473.

[270] Zheng, L.; Yang, Y.; Bowen, C. R.; Jiang, L.; Shu, Z.; He, Y.; Yang, H.; Xie, Z.; Lu, T.; Hu, F.; Yang, W. *Journal of Materials Chemistry C* **2023**, *11*, 6227–6238.

[271] Maity, S.; Sarkar, K.; Kumar, P. *Nanoscale* **2023**, *15*, 16068–16079.

[272] Liu, Y.; Cheng, R.; Liao, L.; Zhou, H.; Bai, J.; Liu, G.; Liu, L.; Huang, Y.; Duan, X. *Nature Communications* **2011**, *2*, 579.

[273] Wu, Y.; Sun, X.-J.; Jia, Y.-P.; Li, D.-B. *Chinese Physics B* **2018**, *27*, 126101.

[274] Tian, C.; Jiang, D.; Li, B.; Lin, J.; Zhao, Y.; Yuan, W.; Zhao, J.; Liang, Q.; Gao, S.; Hou, J.; Qin, J. *ACS Applied Materials & Interfaces* **2014**, *6*, 2162–2166.

[275] Kunwar, S.; Pandit, S.; Jeong, J.-H.; Lee, J. *Nano-Micro Letters* **2020**, *12*, 91.

[276] Senanayake, P.; Hung, C.-H.; Shapiro, J.; Lin, A.; Liang, B.; Williams, B. S.; Huffaker, D. L. *Nano Letters* **2011**, *11*, 5279–5283.

[277] Lin, K.-T.; Lin, H.; Jia, B. *Nanophotonics* **2020**, *9*, 3135–3163.

[278] Daugas, L.; Lahlil, K.; De Langavant, C. C.; Florea, I.; Larquet, E.; Henry, H.; Kim, J.; Gacoin, T. *Advanced Functional Materials* **2023**, *33*, 2212845.

[279] Nütz, T.; Felde, U. Z.; Haase, M. *The Journal of Chemical Physics* **1999**, *110*, 12142–12150.

[280] Wang, T.; Radovanovic, P. V. *The Journal of Physical Chemistry C* **2011**, *115*, 406–413.

[281] Dai, X.; Tchernycheva, M.; Soci, C. *Semiconductors and Semimetals*; Elsevier, 2016; Vol. 94; pp 75–107.

[282] Ahmadivand, A.; Karabiyik, M.; Pala, N. *Photodetectors*; Elsevier, 2016; pp 157–193.

[283] Bao, G.; Li, D.; Sun, X.; Jiang, M.; Li, Z.; Song, H.; Jiang, H.; Chen, Y.; Miao, G.; Zhang, Z. *Optics Express* **2014**, *22*, 24286.

[284] Escalante, G.; López, R.; Demesa, F. N.; Villa-Sánchez, G.; Castrejón-Sánchez, V. H.; Vivaldo De La Cruz, I. *AIP Advances* **2021**, *11*, 055103.

[285] Houweling, Z. S.; Geus, J. W.; De Jong, M.; Harks, P.-P. R.; Van Der Werf, K. H.; Schropp, R. E. *Materials Chemistry and Physics* **2011**, *131*, 375–386.

[286] Chen, S.; Xiao, Y.; Xie, W.; Wang, Y.; Hu, Z.; Zhang, W.; Zhao, H. *Nanomaterials* **2018**, *8*, 553.

[287] Popescu, A. G. M.; Tudose, I. V.; Romanitan, C.; Popescu, M.; Manica, M.; Schiopu, P.; Vladescu, M.; Suchea, M. P.; Pachiu, C. *Nanomaterials* **2024**, *14*, 1227.

[288] Triantafyllou, S.; Christidis, P.; Lioutas, C. *Journal of Solid State Chemistry* **1997**, *133*, 479–485.

[289] Mohammadi, M.; Negreiros, F. R.; Radlinger, T.; Edelmayer, P.; Netzer, F. P.; Surnev, S. *The Journal of Physical Chemistry C* **2022**, *126*, 3289–3300.

[290] Masuda, T.; Yao, H. *The Journal of Physical Chemistry C* **2020**, *124*, 15460–15467.

[291] Breitenstein, O.; Altermatt, P.; Ramspeck, K.; Green, M.; Zhao, J.; Schenk, A. Interpretation of the Commonly Observed I-V Characteristics of C-SI Cells Having Ideality Factor Larger Than Two. 2006 IEEE 4th World Conference on Photovoltaic Energy Conference. Waikoloa, HI, 2006; pp 879–884.

[292] Chistokhin, I. B.; Aksenov, M. S.; Valisheva, N.; Dmitriev, D. V.; Marchishin, I. V.; Toropov, A. I.; Zhuravlev, K. S. *Technical Physics Letters* **2019**, *45*, 180–184.

[293] Bhattacharya, G.; Venimadhav, A. *Journal of Physics D: Applied Physics* **2022**, *55*, 435101.

[294] Chen, J.; Wang, J.; Li, X.; Chen, J.; Yu, F.; He, J.; Wang, J.; Zhao, Z.; Li, G.; Chen, X.; Lu, W. *Sensors* **2022**, *22*, 677.

[295] Li, X.; Zhang, J.; Yue, C.; Tang, X.; Gao, Z.; Jiang, Y.; Du, C.; Deng, Z.; Jia, H.; Wang, W.; Chen, H. *Scientific Reports* **2022**, *12*, 7681.

[296] Bansal, S.; Prakash, K.; Sharma, K.; Sardana, N.; Kumar, S.; Gupta, N.; Singh, A. K. *Nanotechnology* **2020**, *31*, 405205.

[297] Duan, R.; Qi, W.; Li, P.; Tang, K.; Ru, G.; Liu, W. *Research* **2023**, *6*, 0195.

[298] Abdulhalim, I. *Nanophotonics* **2018**, *7*, 1891–1916.

[299] Tian, Y.; Tatsuma, T. *Journal of the American Chemical Society* **2005**, *127*, 7632–7637.

[300] Luo, J.; Wu, Q.; Zhou, L.; Lu, W.; Yang, W.; Zhu, J. *Photonics Insights* **2023**, *2*, R08.

[301] Katagiri, K.; Yamazaki, S.-i.; Inumaru, K.; Koumoto, K. *Polymer Journal* **2015**, *47*, 190–194.

[302] Zeb, S.; Sun, G.; Nie, Y.; Xu, H.; Cui, Y.; Jiang, X. *Materials Advances* **2021**, *2*, 6839–6884.

[303] Brissaud, C.; Besteiro, L. V.; Piquemal, J.-Y.; Comesaña-Hermo, M. *Solar RRL* **2023**, *7*, 2300195.

[304] Warren, S. C.; Thimsen, E. *Energy Environ. Sci.* **2012**, *5*, 5133–5146.

[305] Lee, J.; Mubeen, S.; Ji, X.; Stucky, G. D.; Moskovits, M. *Nano Letters* **2012**, *12*, 5014–5019.

[306] Gellé, A.; Moores, A. *Pure and Applied Chemistry* **2017**, *89*, 1817–1827.

[307] Awazu, K.; Fujimaki, M.; Rockstuhl, C.; Tominaga, J.; Murakami, H.; Ohki, Y.; Yoshida, N.; Watanabe, T. *Journal of the American Chemical Society* **2008**, *130*, 1676–1680.

[308] Zhang, X.; Ke, X.; Yao, J. *Journal of Materials Chemistry A* **2018**, *6*, 1941–1966.

[309] DePuccio, D. P.; Botella, P.; O'Rourke, B.; Landry, C. C. *ACS Applied Materials & Interfaces* **2015**, *7*, 1987–1996.

[310] Prakash, J.; Swart, H. *Physica B: Condensed Matter* **2023**, *669*, 415297.

[311] Tada, H.; Fujishima, M.; Naya, S.-i. *ACS ES&T Engineering* **2024**, *4*, 506–524.

[312] Amirjani, A.; Firouzi, F.; Haghshenas, D. F. *Plasmonics* **2020**, *15*, 1077–1082.

[313] Kang, H.; Buchman, J. T.; Rodriguez, R. S.; Ring, H. L.; He, J.; Bantz, K. C.; Haynes, C. L. *Chemical Reviews* **2019**, *119*, 664–699.

[314] Jiang, N.; Zhuo, X.; Wang, J. *Chemical Reviews* **2018**, *118*, 3054–3099.

[315] Waketola, A. G.; Tegegne, N. A.; Hone, F. G. *Plasmonics* **2024**, *20*, 5521–5556.

[316] Jain, P. K.; Huang, X.; El-Sayed, I. H.; El-Sayed, M. A. *Accounts of Chemical Research* **2008**, *41*, 1578–1586.

[317] Zheng, J.; Cheng, X.; Zhang, H.; Bai, X.; Ai, R.; Shao, L.; Wang, J. *Chemical Reviews* **2021**, *121*, 13342–13453.

[318] Liu, J.; Pennell, K. G.; Hurt, R. H. *Environmental Science & Technology* **2011**, *45*, 7345–7353.

[319] Zafari, M.; Shariatmadar Tehrani, F. *Scientific Reports* **2025**, *15*, 14624.

[320] Zhang, S.; Zhang, L.; Fang, S.; Zhou, J.; Fan, J.; Lv, K. *Environmental Research* **2021**, *199*, 111259.

[321] Etafa Tasisa, Y.; Kumar Sarma, T.; Krishnaraj, R.; Sarma, S. *Results in Chemistry* **2024**, *11*, 101850.

[322] Dadiani, T.; Tchabukiani, T.; Jishiashvili, D.; Daraselia, D.; Japaridze, D.; La Mattina, F.; Shengelaya, A. *Journal of Superconductivity and Novel Magnetism* **2025**, *38*, 58.

[323] Han, B.; Popov, A. L.; Shekunova, T. O.; Kozlov, D. A.; Ivanova, O. S.; Rumyantsev, A. A.; Shcherbakov, A. B.; Popova, N. R.; Baranchikov, A. E.; Ivanov, V. K. *Journal of Nanomaterials* **2019**, *2019*, 1–13.

[324] Chinde, S.; Grover, P. *Mutation Research/Genetic Toxicology and Environmental Mutagenesis* **2017**, *819*, 1–13.

[325] Li, X.-L.; Liu, J.-F.; Li, Y.-D. *Inorganic Chemistry* **2003**, *42*, 921–924.

[326] Adhikari, S.; Mandal, S.; Sarkar, D.; Kim, D.-H.; Madras, G. *Applied Surface Science* **2017**, *420*, 472–482.

[327] Hkiri, K.; Mohamed, H. E. A.; Abodouh, M. M.; Maaza, M. *Scientific Reports* **2024**, *14*, 26991.

[328] Arteaga-Jiménez, A.; Trejo-Pérez, M. G.; García-García, A. L.; González-Jasso, E.; Vidales-Hurtado, M. A. *Environmental Technology* **2022**, *43*, 2620–2636.

[329] Deblock, L.; Goossens, E.; Pokratath, R.; De Buysser, K.; De Roo, J. *JACS Au* **2022**, *2*, 711–722.

[330] Heuer-Jungemann, A. et al. *Chemical Reviews* **2019**, *119*, 4819–4880.

[331] De Roo, J.; Van Den Broeck, F.; De Keukeleere, K.; Martins, J. C.; Van Driessche, I.; Hens, Z. *Journal of the American Chemical Society* **2014**, *136*, 9650–9657.

[332] Helendra; Istiqomah, N. I.; Sabarman, H.; Suharyadi, E. *Sensors International* **2025**, *6*, 100295.

[333] Lattuada, M.; Hatton, T. A. *Langmuir* **2007**, *23*, 2158–2168.

[334] Schneider, J. T.; Firak, D. S.; Ribeiro, R. R.; Peralta-Zamora, P. *Physical Chemistry Chemical Physics* **2020**, *22*, 15723–15733.

[335] Tran, H. D.; Nguyen, D. Q.; Do, P. T.; Tran, U. N. P. *RSC Advances* **2023**, *13*, 16915–16925.

[336] Kumar, A.; Dutta, S.; Kim, S.; Kwon, T.; Patil, S. S.; Kumari, N.; Jeevanandham, S.; Lee, I. S. *Chemical Reviews* **2022**, *122*, 12748–12863.

[337] Revellame, E. D.; Fortela, D. L.; Sharp, W.; Hernandez, R.; Zappi, M. E. *Cleaner Engineering and Technology* **2020**, *1*, 100032.

[338] Shah, B.; Shah, A.; Jadav, P. *Journal of the Serbian Chemical Society* **2013**, *78*, 1055–1077.

[339] Liu, Y.; Shen, L. *Langmuir* **2008**, *24*, 11625–11630.

[340] Chu, K. H.; Bollinger, J.-C.; Kierczak, J. *Environmental Surfaces and Interfaces* **2025**, *3*, 191–195.

[341] Tseng, R.-L.; Wu, F.-C.; Juang, R.-S. *Journal of the Taiwan Institute of Chemical Engineers* **2010**, *41*, 661–669.

[342] Ho, Y.; McKay, G. *Process Biochemistry* **1999**, *34*, 451–465.

[343] Wang, J.; Guo, X. *Chemosphere* **2022**, *309*, 136732.

[344] Weber, W. J.; Morris, J. C. *Journal of the Sanitary Engineering Division* **1963**, *89*, 31–59.

[345] Hu, Q.; Ma, S.; He, Z.; Liu, H.; Pei, X. *Journal of Water Process Engineering* **2024**, *60*, 105241.

[346] Skopp, J. *Journal of Chemical Education* **2009**, *86*, 1341.

[347] Islam, M. A.; Chowdhury, M. A.; Mozumder, M. S. I.; Uddin, M. T. *ACS Omega* **2021**, *6*, 14481–14492.

[348] Chu, K. H. *Industrial & Engineering Chemistry Research* **2021**, *60*, 13140–13147.

[349] Debord, J.; Harel, M.; Cheknane, B.; Bollinger, J.-C.; Bouras, O. *RSC Advances* **2016**, *6*, 66266–66274.

[350] Travis, C. C.; Etnier, E. L. *Journal of Environmental Quality* **1981**, *10*, 8–17.

[351] Rasheed, T.; Bilal, M.; Iqbal, H. M. N.; Hu, H.; Zhang, X. *Water, Air, & Soil Pollution* **2017**, *228*, 291.

# APPENDICES

# Chapter A

## Supplementary Data for Chapter 3

## A.1 Stead-State Photoluminescence of $WO_{3-x}$ NCs

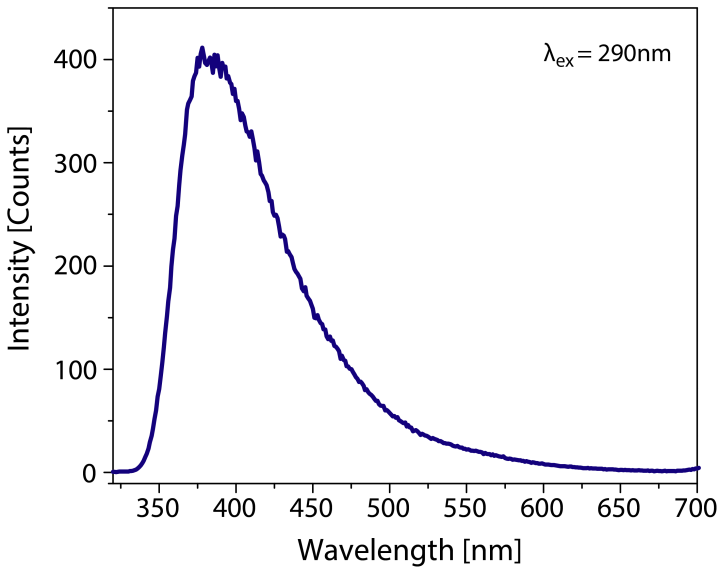



Figure A.1: Steady-state photoluminescence emission spectrum (300 K) of as-synthesized $WO_{3-x}$ NCs dispersed in TCE.

## A.2 Variable-Temperature MCD Spectra of $WO_{3-x}$ NCs

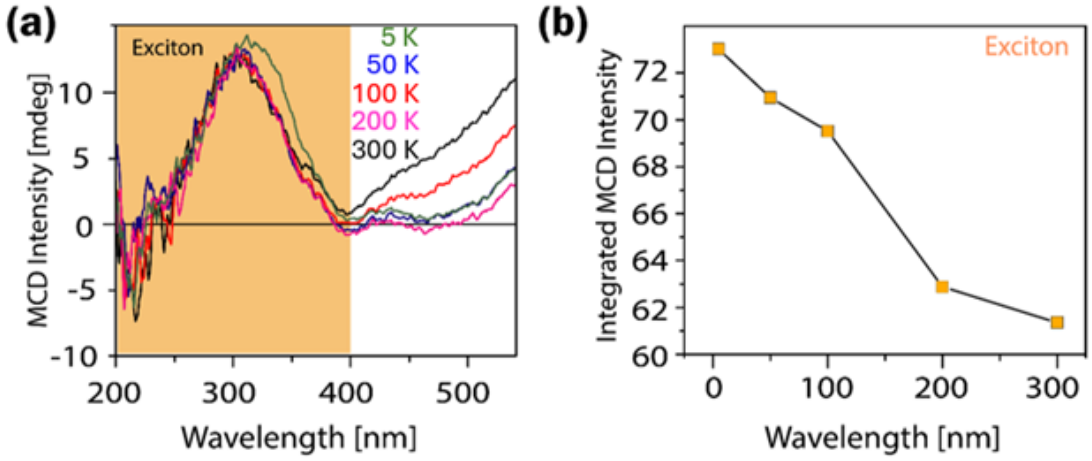



Figure A.2: (a) Variable-temperature excitonic MCD spectra collected at 7 T for the colloidal plasmonic $WO_{3-x}$ NCs presented in Chapter 3. (b) Integrated excitonic MCD intensity as a function of wavelength determined from (a).

## A.3 Low-Temperature CD Extinction Spectra of $WO_{3-x}$ NCs

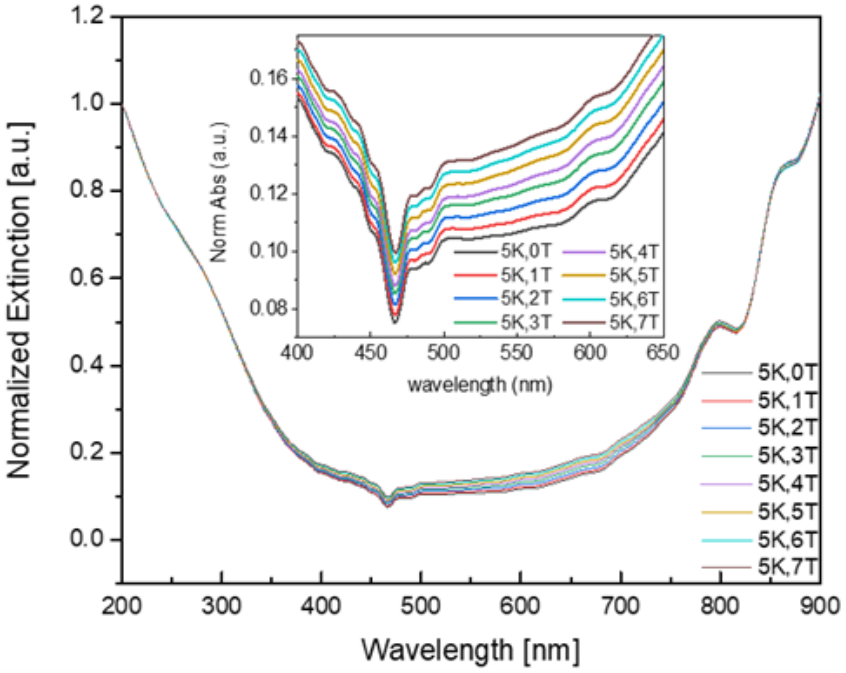



Figure A.3: Normalized CD extinction spectra for colloidal $WO_{3-x}$ NC thin films. Spectra were collected at 5 K in the range of 0-7 T.

## A.4 Magnetization Measurements of $WO_{3-x}$ NCs

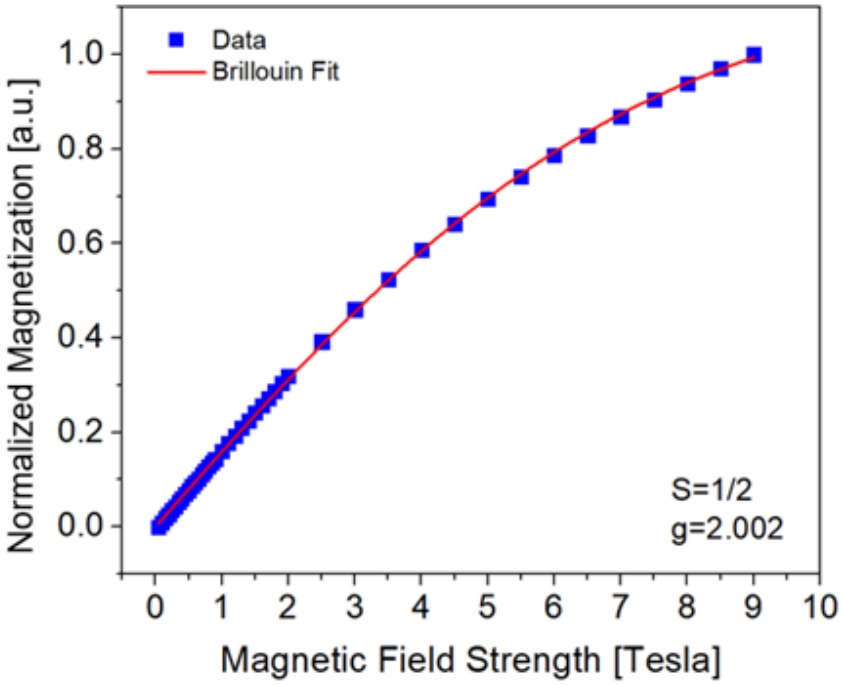



Figure A.4: Saturation magnetization curve of $WO_{3-x}$ NCs. Experimental data were collected at 5 K in the range of 0-9 T and fitted with Brillouin function.

# Chapter B

## Supplementary Data for Chapter 4

## B.1 Optical Extinction Spectra of Cs:$WO_{3-x}$ Nanoplatelets

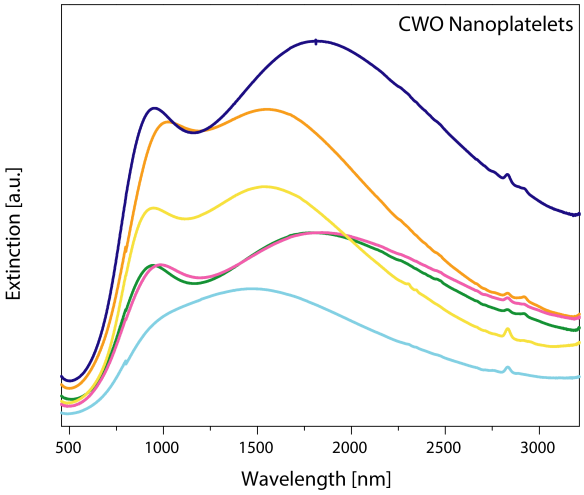



Figure B.1: Optical extinction spectra of colloidal Cs:$WO_{3-x}$ nanoplatelets dispersed in TCE.

# Chapter C

## Supplementary Data for Chapter 5

## C.1 Spectral Responsivity Normalization and Incident Power

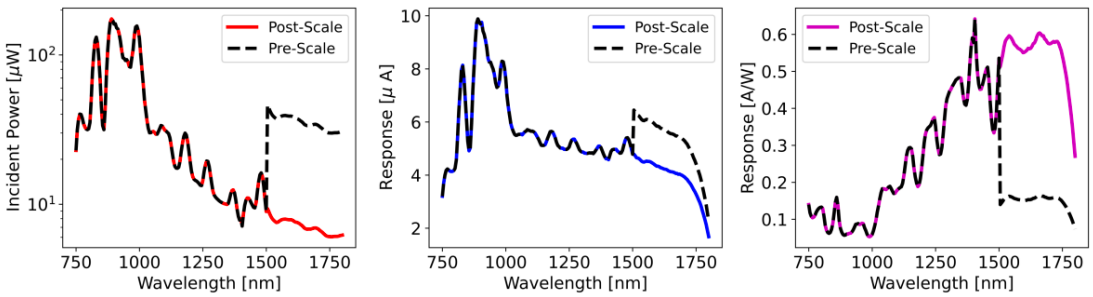



Figure C.1: Example showing how the power spectrum and photocurrent data are processed to account for changes in power transmission through different diffraction gratings used in the monochromator. Two gratings are used over the range of wavelength values selected; the grating change occurs at 1500 nm.

## C.2 Enhancement of Photoresponse for InGaAs Infrared Photodetectors

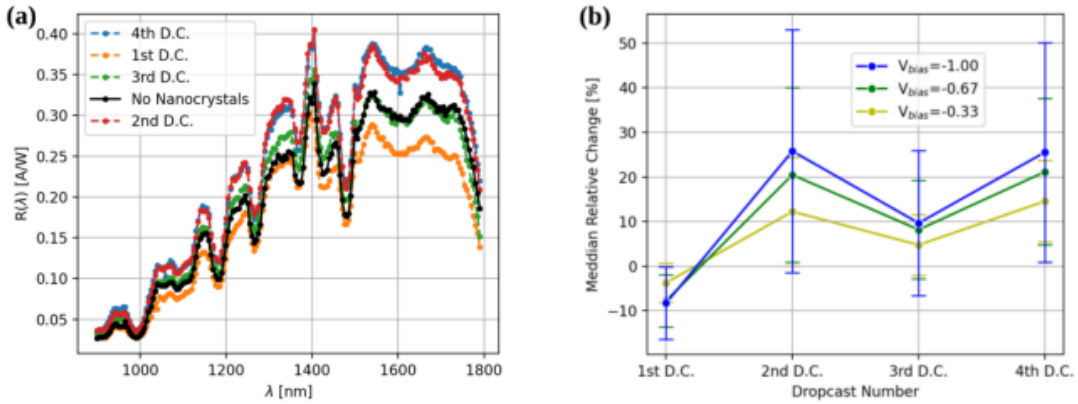



Figure C.2: The effect of successive drop-casts of $Cs_yWO_{3-x}$ NCs using a concentration of 135g/L. (a) Responsivity as a function of wavelength for successive drop-casts. (b) Relative percent difference in responsivity for successive drop-casts, measured at several bias voltages. The median (data points) and standard deviation (bars) of the relative percent difference are calculated over the full wavelength range shown in (a).

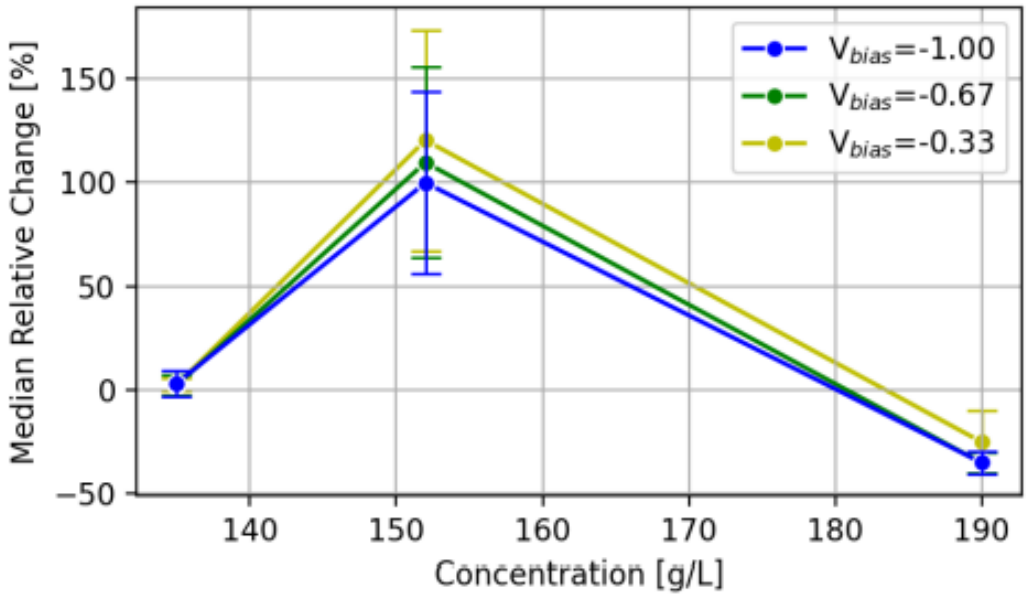



Figure C.3: The effect of drop-cast concentration on the change in responsivity (RPD) for $Cs_yWO_{3-x}$ NCs. Samples were diluted in hexane. The RPD is measured over the full spectrum (900-1800 nm) and the median value plotted (bars indicate the standard deviation).

# Chapter D

## Supplementary Data for Chapter 6

### D.1 Recycling of Plasmonic $WO_{3-x}$ NC Photocatalysts

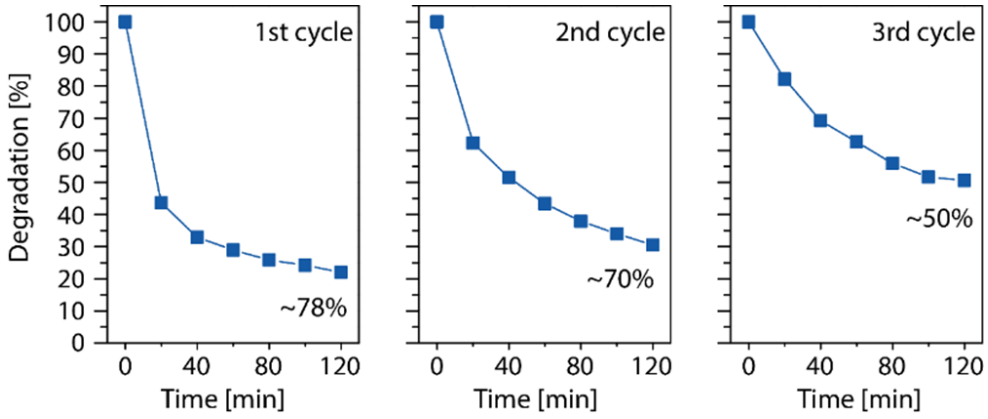



Figure D.1: Plots showing the reusability of colloidal ligand-stripped $WO_{3-x}$ NC photocatalysts (12 mg). The measurements were performed in the dark at 20°C.

## D.2 BET Specific Surface Area Measurements

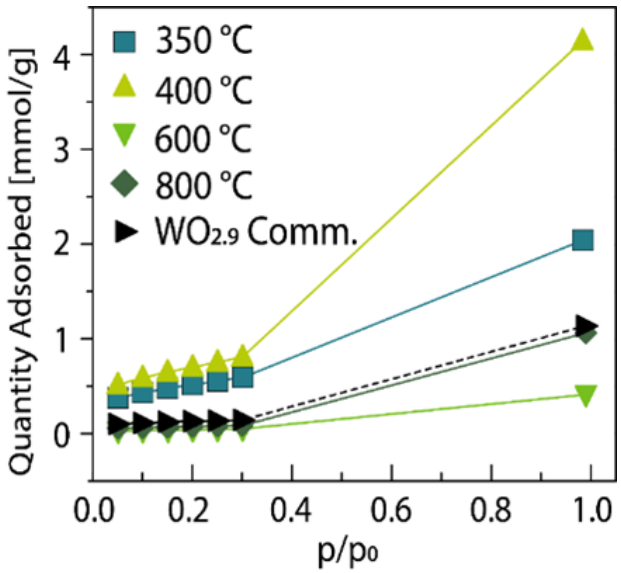



Figure D.2: BET specific surface area measurements of the $WO_{3-x}$ NCs annealed at different temperatures for 2h.

Table D.1: BET specific surface area data of the $WO_{3-x}$ NCs annealed at different temperatures for 2h.

| Sample | BET surface area [$m^2/g$] |
|---|---|
| Bulk $WO_{2.9}$ | 10.08 |
| WO–350°C | 41.60 |
| WO–400°C | 56.57 |
| WO–600°C | 3.44 |
| WO–800°C | 5.92 |

## D.3 XRD Patterns of Annealed $WO_{3-x}$ NCs

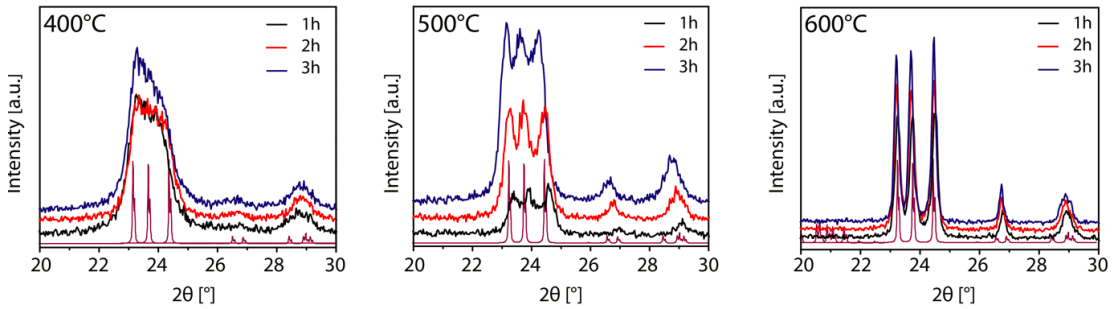



Figure D.3: X-ray diffractograms of $WO_{3-x}$ NCs annealed in air for 1-3 hours at 400°C (left panel), 500°C (middle panel), and 600°C (right panel).